Christiane Janke

Novel Ammoxidation Catalysts based on Vanadium Containing Oxynitrides

Impact of Structure on the Catalytic Performance

Cuvillier Verlag Göttingen
Internationaler wissenschaftlicher Fachverlag

Novel Ammoxidation Catalysts based on Vanadium Containing Oxynitrides - Impact of Structure on the Catalytic Performance

Novel Ammoxidation Catalysts based on Vanadium Containing Oxynitrides - Impact of Structure on the Catalytic Performance

Dissertation
zur
Erlangung des akademischen Grades
doctor rerum naturalium (Dr. rer. nat.)
der Mathematisch-Naturwissenschaftlichen Fakultät
der Universität Rostock

vorgelegt von
Christiane Janke, geb. am 06.12.1982 in Potsdam
aus Rostock
Rostock, den 29.11.2011

Bibliografische Information der Deutschen Nationalbibliothek
Die Deutsche Nationalbibliothek verzeichnet diese Publikation in der Deutschen Nationalbibliographie; detaillierte bibliografische Daten sind im Internet über http://dnb.d-nb.de abrufbar.
1. Aufl. - Göttingen: Cuvillier, 2012
Zugl.: Rostock, Univ., Diss., 2012

978-3-95404-037-7

Gutachter:

1. Prof. Dr. A. Brückner (Leibniz-Institut für Katalyse an der Universität Rostock e.V.)

2. Prof. Dr. R. Stößer (Humboldt-Universität zu Berlin)

Tag der Verteidigung: 24.01.2012

Nonnenstieg 8, 37075 Göttingen
Telefon: 0551-54724-0
Telefax: 0551-54724-21
www.cuvillier.de

1. Auflage, 2012
Gedruckt auf säurefreiem Papier

978-3-95404-037-7

Acknowledgements

This work has been carried out under supervision and guidance of Prof. Dr. Angelika Brückner at the Leibniz Institute for Catalysis at the University of Rostock between August 2008 and November 2011.

I would particularly like to acknowledge my supervisor, Prof. Dr. Angelika Brückner, not only for the interesting research project, but also for her kind scientific advices. Her persistent support and feedback was always a great inspiration for me.

I would like thank also Dr. habil. Andreas Martin for his remarkable scientific support and sharing his expertise with me.

I also thank each past and present member of the analytical group at Likat for the outstanding atmosphere in our group. Special thanks are due to Dr. Radnik, Dr. Bentrup, Dr. Pohl, Dr. Schneider and Dr. J. Rabeah. I really appreciated each discussion and advice. I also would like to acknowledge the experimental support of U. Marx, A. Simmula, W. Winkler and B. Friedrich. I am grateful to my coworkers in Groß Lüsewitz, Karin Struve and Neetika Madaan. Special thank and appreciation go to R. Eckelt and Dr. Bartoszek for sharing their world of chemistry with me.

I also thank the house workshop at Likat, W. Wilhelm (†), G. Ackermann, J. Dewart and T. Rall, who make technical ideas of PhD students become real. I thank in particular W. Wilhelm for his outstanding commitment in Groß Lüsewitz.

I am indebted to PD Dr. Scholz at the Humboldt-University of Berlin for the solid state NMR measurements. I thank Dr. F. Emmerling and Maria Klimakow at BAM in Berlin for the measurements at BESSY and their time they dedicated to mixed solid solutions.

I would also like to say merci beaucoup to Dr. Millet, Dr. Loridant and J. Bilde for inviting me to research one month at IRCELYON. I thank especially for the scientific discussions and guidances during this research stay. I learned so much during that time.

I gratefully acknowledge the financial support of DFG, ANR and Dechema for the Max Buchner scholarship.

Finally, I thank my family and friends for their love, patience and never-ending encouragement.

Rostock, 29.11.2011

Dedicated to my family

Abbreviations

A$_{EPR}$	Double integral intensity of as received EPR signal
A$_{P}$	Gaussian peak area
A$_{\parallel}$	Parallel component of the hyperfine coupling tensor
A$_{\perp}$	Perpendicular component of the hyperfine coupling tensor
A$_{R}$	Area of a defined reflection
ATR	Attenuated Total Reflectance
B$_{C}$	Carbon balance
β_2^{*2}	In plane delocalization coefficient
c	Elemental surface concentration derived by XPS
CT transition	Charge Transfer transition
3-CP	3-cyanopyridine
d$_{P}$	Diameter of catalyst particles
E$_{B}$	Binding energy derived from XPS
EDX spectroscopy	Energy-dispersive X-ray spectroscopy
E$_{g}$	Absorption edge energy
EPR	Electron paramagnetic resonance
EtOH	Ethanol
FTIR spectroscopy	Fourier transform infrared spectroscopy
GC	Gas Chromatography
g$_{e}$	Free electron g value
g$_{iso}$	Isotropic g value
g$_{\parallel}$	Parallel component of the g tensor
g$_{\perp}$	Perpendicular component of the g tensor
GHSV	Gas Hourly Space Velocity
hfs	hyperfine structure
ICDD	International Center of Diffraction Data
ICP-OES	Inductively Coupled Plasma-Optical Emission Spectrometry
IVCT transition	Inter valence Charge transfer transition
MAS	Magic Angle Spinning
MS	Mass Spectrometry
Ox	Oxidation
3-PIC	3-picoline

R_{CL}	Intensity ratio of EPR signals I(623K)/I(295K)
Red	Reduction
RT	Room temperature
S_{BET}	Surface area according to Brunauer, Emmett and Teller
S_{3-CP}	Selectivity of 3-cyanopyridine
STY	Space-time yield
TAP	Temporal-Analysis-of-Products
T_{B}	Measured bed temperature in a reactor
TEM	Transmission Electron Microscopy
T_{N}	Temperature during nitridation
T_{O}	Adjusted oven temperature
TPO	Temperature Programmed Oxidation
UV/Vis-DRS	Ultraviolet/Visible-Diffuse Reflectance Spectroscopy
X_{3-PIC}	Conversion of 3-picoline
XPS	X-ray Photoelectron Spectroscopy
XRD	X-ray Diffraction
Y_{3-CP}	Yield of 3-cyanopyridine

Contents

1. Introduction and Objectives

Aliphatic, aromatic and heteroaromatic nitriles are important intermediates for producing pharmaceuticals, agricultural pesticides, dyestuffs and textiles.

One economically and ecologically efficient route to synthesize a variety of different nitriles is the ammoxidation of aliphatic or methyl-substituted aromatic and heteroaromatic hydrocarbons in the presence of ammonia and air in the gas phase using suitable solid catalysts. This reaction would be most sustainable, energy-efficient and eco-friendly if it was possible to achieve a nitrile selectivity of 100 % and high space-time yields (STY).

Up to now, this goal is not yet reached. Although conventional catalysts based on mixed oxides of transition metals provide high selectivities at fairly high conversion for selected nitriles such as benzonitrile and 3-cyanopyridine [1], the STY bear still enough potential for improvement.

In the late 1990s, a new class of vanadium oxynitrides (VAlON) has been discovered, which however, was only used for ammoxidation of propane to acrylonitrile [2, 3]. Although the nitrile selectivity was somewhat lower compared to MoVTeNbO usually used for this reaction, 5 - 10 times higher STY have been reached with the new VAlON catalysts [4–6].

During my preceding diploma work, VAlON and VZrON oxynitrides were very successfully tested for the ammoxidation of 3-picoline (3-PIC) to 3-cyanopyridine (3-CP) [7]. The obtained STY exceeded the state of the art by a factor of three [8], though at slightly lower selectivity according to [1]. These promising results inspired us to perform a more comprehensive exploration of V containing oxynitrides for ammoxidation of aromatic hydrocarbons.

It is the aim of this work to elucidate structure-reactivity relationships of vanadium containing oxynitrides in the ammoxidation of 3-PIC to 3-CP, which has been chosen as a model reaction by an integrated approach of catalytic test and characterization studies including in situ spectroscopy. The ultimate goal was to optimize the catalytic performance towards high selectivity and STY.

To this end, the following sub-tasks have been considered in the thesis:

- Development of novel VZrAlON catalysts by combination of the most active (VZrON) and selective (VAlON) catalysts,

- Investigation of the influence of incorporation of phosphorus into VZrON catalysts,
- Examination of the influence of mixing VMON and $\mathrm{Mo}_x\mathrm{O}_y\mathrm{N}_z$ catalysts (M = Al or Zr),
- Evaluation of the impact of redox-active M in VMON catalysts (M = Mo or Sb).

2. State of the Art

The ammoxidation belongs to the class of heterogeneous catalytic gas phase reactions and has been investigated for more than 60 years [9, 10]. In presence of ammonia, air and a suitable catalyst alkanes and alkenes as well as methyl-substituted aromatics and heteroaromatics R-CH_3 are transferred into nitriles at temperatures higher than 300 °C. The ammoxidation can be regarded as oxidative ammonolysis. Besides the desired nitrile only water is produced as by-product at 100 % selectivity according to the reaction:

$$R - CH_3 \quad + \quad 3/2\, O_2 \quad + \quad NH_3 \quad \xrightarrow{catalyst,\, T > 300°C} \quad R - CN \quad + \quad 3\, H_2O. \qquad (2.1)$$

Conventional catalysts contain supported or unsupported redox active transition metals such as V, Mo, or Cr as key components in the form of pure oxides [11–14], oxyfluorides [15–17] or phosphor containing oxides [18–22].

In Table B.3 a short overview is given on some heteroaromatic ammoxidation reactions to clarify the still persistent research interest in this kind of reaction. In particular, active and selective catalysts for the ammoxidation of dimethoxytoluene to dimethoxybenzonitrile are still missing up to now. In addition, the synthesis of aliphatic dinitriles such as adiponitrile via ammoxidation is of great interest. Processes starting from cyclohexane, cyclohexene or methylcyclohexane are reported, but conversions and selectivities did not exceed 40 % [23–25].

On the contrary, a story of success possesses the oxidative ammonolysis of propene to acrylonitrile, which was the first industrially implemented and commercialized ammoxidation technology [26, 27]. From the late 1950s still up to now, the worldwide demand on polyacrylonitrile fibers is almost covered by the production of acrylonitrile via this process [11], but an efficient alternative route for producing acrylonitrile is needed due to e.g. the advancing scarcity of propene [28]. One promising route seems to be the ammoxidation of propane to acrylonitrile. However, the development of functional, highly active and selective catalysts for activation of an alkane is experimentally challenging due to its higher activation energy [29–31].

One active class of catalysts for this reaction is the oxynitride VAlON [2,3]. Propane conversions around 60-80 % and selectivities to acrylonitrile about 50 - 65 % are reported at high space velocities (GHSV). Although the nitrile selectivity was somewhat lower compared to MoVTeNbO, higher STY (up to 10 times) have been reached with the new VAlON catalysts [4–6,32].

Recently, it was found that VAlON and VZrON oxynitrides also bear a high activity and STY in the ammoxidation of heteroaromatics, e.g. 3-picoline (3-PIC) to 3-cyanopyridine (3-CP) [7,8]. However, the latter ammoxidation was already industrialized in 1983 by Degussa [33]. A vanadium containing long-term stable catalyst with the general formula $Sb_aV_bTi_cX_d$ supported on SiO_2 (X = alkali metal) is used. A selectivity to 3-CP (S_{3-CP}) of 95.8 % at nearly full conversion of 3-PIC (X_{PIC}) is obtained at 370 °C with a maximum STY of 156 g/lh [1,34].

In contrast to acrylonitrile being a bulk chemical 3-CP belongs to fine chemicals. The latter compound is used as intermediate to produce nicotinic acid and amide by hydrolysis (see Fig. 2.1). 14 000 ton of nicotinic acid and 8000 ton of the related nicotinic amide were globally manufactured in 1995 [35]. In 2006 the worldwide production of both increased to about 35 000 to 40 000 ton [18]. Up to now, the direct oxidation of 3-PIC to nicotinic acid in the gas phase is not established (see Fig. 2.1) since sufficient catalysts are missing and side-reactions like decarboxylation are occurring. Also, the low sublimation temperature of nicotinic acid may be a problem in implementation of an industrial process [35].

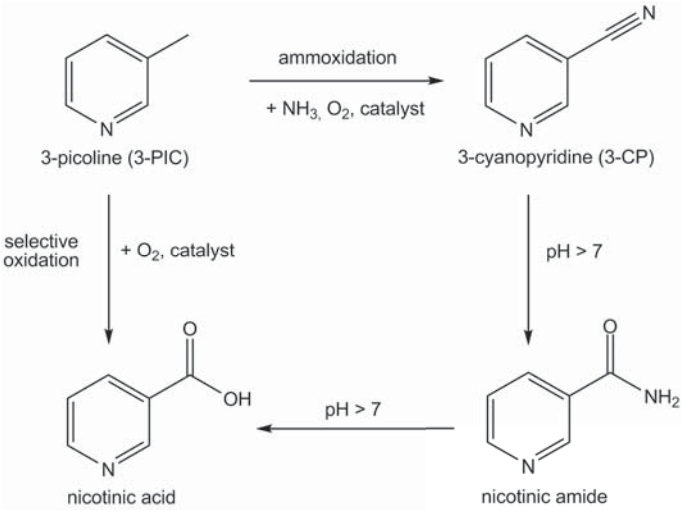

Figure 2.1.: Heterogeneous catalytic gas phase routes to nicotinic acid starting from 3-PIC [35]

Nicotinic acid and its derivates are needed in different fields. Most notably, nicotinic acid is applied as additive. In animal nutrition it is supposed to improve the natural capability of productive livestocks, and it is also added to beverage, food and cosmetic products. Humans can not produce nicotinic acid (vitamin B_3) and amide on its own; and the importance of nicotinic acid ingestion was not recognized until 2nd decade in 1900. Thitherto, many humans suffered from the disease called pellagra due to an insufficient ingestion of vitamin B_3, resulting mostly from undernourishment. However, nowadays this disease is still not extinct [36, 37].

The mechanism of heteroaromatic ammoxidation over oxide catalysts has been investigated for several years, starting with the early work of Andersson et al. [38], while no such studies are available for oxynitrides.

For oxide catalysts it has been proposed that the ammoxidation starts with adsorption of the aromatic ring followed by hydrogen abstraction from the alkyl group, formation of a benzyl-like intermediate and in situ generation of an -OH group that converts gaseous NH_3 to NH_4^+ by proton transfer. In due course, it was suggested that NH_4^+ is supposed to react with the benzyl-like intermediate to a benzylamine species, which is transformed to the nitrile and desorbs from the surface of the catalyst. A Mars-van Krevelen mechanism proceeds during this reaction including participation of lattice oxygen [39–45]. Also, imido =NH or amido -NH_2 species on the catalyst surface are considered as active N-insertion species, however their role in the aromatic ammoxidation is still not fully elucidated [41, 46, 47].

From extensive studies of toluene ammoxidation over phosphor and vanadium containing oxide catalysts it was proposed that highly active and selective catalysts must fulfill four crucial features: i) They should provide chain- or layer-like surface vandyl units; ii) These units should be located at a proper distance to enable adsorption of the aromatic ring and reaction of the methyl group at the neighboring site, iii) The mean surface V valence state should be close to +4 and iv) the catalyst must be able to incorporate NH_3 from the gas phase [40].

The activation of NH_3 from the gas feed via transient incorporation into the catalyst lattice during toluene ammoxidation has been evidenced by isotopic labeling experiments using the Temporal-Analysis-of-Products (TAP) reactor and $^{15}NH_3$ as gaseous feed component [48]. For VAlON catalysts, TAP experiments with labeled $^{15}NH_3$ in the ammoxidation of propane have shown, too, that N insertion into hydrocarbons occurs via surface N sites [49]. Thus, the insertion of N as well as O via a double Mars-van Krevelen mechanism is considered to be responsible for their high catalytic performance in the ammoxidation of propane. The structure-reactivity relationship proposed for ammoxidation of 3-PIC to 3-CP over VZrON and VAlON catalysts also confirms that such N insertion process is of great importance in the ammoxidation of 3-PIC [8]. This structure-reactivity relationship is described in-depth later on.

In general, transition metal oxide catalysts are only capable of catalyzing selective oxidation reaction via a Mars-van Krevelen redox cycle if oxygen anions of the lattice are highly mobile and migrate. Thus, a well-directed incorporation of anionic defects and vacancies (point defects as well as 2-D and 3-D defects) in transition metal oxides might not only support electron migration and therefore influence the redox-activity of the transition metal site but also support the migration of O and N containing species.

Moreover, it was considered that the surface acidity of V containing catalysts has a crucial impact on the catalytic performance in the partial oxidation of heteroaromatics [50]. This is also true for the ammoxidation of heteroaromatics since a benzyl-like intermediate is formed. Different strategies are known to influence the surface acidity and basicity of a solid material. One common way is to dope oxide compounds with basic ions such as Na^+ or K^+ [51, 52]. A second strategy is based on the idea to modify the anionic lattice via introduction of anions such as fluoride [53] or nitride [54–56].

Metal nitrides and oxynitrides are accessible via nitridation of the corresponding metal oxide precursor [57, 58]. This reaction in pure ammonia implies the substitution of three oxygen anions by two nitride anions leaving one vacancy in the anionic lattice according to the following equation:

$$3\,O^{2-} \quad + \quad 2\,NH_3 \quad \rightleftharpoons \quad 2\,N^{3-} \quad + \quad 3\,H_2O. \tag{2.2}$$

A high flow of ammonia is generally used to remove the water from the equilibrium and adjust the balance state to the right site of the reaction. In principle, the nitridation of metal oxide precursors might be an excellent route to synthesize effective ammoxidation catalysts since this reaction introduces anionic defects and nitrogen containing sites such as N^{3-} into the catalyst, modifies the surface acidity and reduces the valence state of redox-active metal sites.

Moreover, nitrides and oxynitrides are promising materials in various fields of applications due to their outstanding physical and chemical properties [58]. Compared to oxides, metal nitrides possess superior physical properties such as hardness, mechanical and tensile strength and high melting points. In addition, they provide electronic and magnetic properties resembling those of metals, such as electronic conductivity, Hall coefficient, magnetic susceptibility and heat capacity [59]. Their extreme hardness and excellent corrosion resistance make them suitable as cutting tools and hard coatings [60–62]. Among nitrides and oxynitrides also non-metal compounds such as phosphorus nitride and carbon nitrides CN_x have attracted considerable attention. L. Chen et al. [63] succeed the synthesis of amorphous P_3N_5 hollow spheres, which might have a great potential for encapsulation and delivery in drugs. CN_x coatings are used in thin film-Schottky-solar cells and computer hard discs of IBM, as layers in humidity sensors and electrochemical gas detectors [64].

As already indicated, transition metal nitrides and oxynitrides have also received considerable attention in the field of heterogeneous catalysis. In ammonia synthesis [65,66], Fischer-Tropsch [67], hydrodenitrogenation [68,69], hydrodesulfurization [70] and ammoxidation [4–6], they are proved to be active, and in some cases they possess superior selectivity, stability and resistance to poisoning. For example, the decomposition of hydrazine being traditionally catalyzed over iridium supported on alumina, is also efficiently catalyzed over $\mathrm{MoN}_x\mathrm{O}_y$ catalysts [71]. Nitrides and oxynitrides are proved to be active in photo catalytic water splitting to hydrogen, too [72,73].

Structure-reactivity relationship of VAlON and VZrON in the ammoxidation of 3-PIC VAlON and VZrON catalysts synthesized via co-precipitation and nitridation were proved to be active in the ammoxidation of 3-PIC to 3-CP [7,8]. Results for the catalytic testings showed that the catalytic performance of these two systems differ significantly. VAlON catalysts are less active, but more selective than VZrON catalysts. A maximum STY of 399 g/lh was reached using VZrON catalysts with a ratio of V/Zr = 0.25. In comparison to the benchmark catalyst with the general formula $\mathrm{Sb}_a\mathrm{V}_b\mathrm{Ti}_c\mathrm{X}_d/\mathrm{SiO}_2$ ($\mathrm{X} = \mathrm{K}^+$) STY could be triplicated using VZrON oxynitrides. Both catalyst classes, VZrON and VAlON, suffer from a lower selectivity compared to the latter benchmark catalyst.

By a multitude of ex situ characterization techniques such as XPS and UV/Vis-DRS and in situ EPR spectroscopy, it was possible to elucidate the structural differences in these two catalyst classes under working state and to build up structure-reactivity relationship.

In contrast to VAlON catalysts, VZrON oxynitrides are characterized by a higher polymerisation degree of VO^{2+} sites indicated by results derived from EPR spectroscopy, UV/Vis-DRS and XPS. The chemical composition calculated from XPS suggested a surface enrichment of V for VZrON, but not for VAlON. Additionally a higher mean oxidation state of V was observed for VZrON, which was close to V^{5+}. In contrast, two different V sites could be detected by XPS for VAlON catalyst. Both V sites in VAlON differ in their mean V oxidation state, one V valence close to +3 and the second close to +4. Additionally, only for VAlON with V/Al $\geq$ 0.25 a nitrogen site with a binding energy being typical for N^{3-} could be detected by XPS. As opposed to this, the near surface region of VZrON catalyst was N-free.

Moreover in situ EPR investigations on VZrON and VAlON suggested that the latter catalyst can provide a significant higher amount of VO^{2+} under reaction conditions. In combination with results derived from UV/Vis-DRS and XPS, it was concluded, that the main amount of V in VZrON catalysts must be present as V^{5+} and not as V^{3+} or V^{4+} under reaction conditions.

Development of strategies Based on the knowledge gained from the structure-reactivity relationship of VAlON and VZrON different strategies were followed to improve the selectivity and to increase the conversion and STY in the ammoxidation of 3-PIC.

Firstly, three different routes were investigated to generate N containing surface sites in highly active VZrON catalysts to improve the selectivity of this catalyst class without losing the activity:

- Since for VAlON catalysts nitride sites could be detected on the surface, it was assumed that adding Al in VZrON might help to stabilize surface nitrogen species. For this reason, VZrAlON catalysts were synthesized by simultaneous co-precipitation of V, Al and Zr.
- VPO catalysts are well known for their superior catalytic performance in the ammoxidation of heteroaromatics [18–22]. Moreover, it is well known from literature, that ZrPON oxynitrides possess a variety of nitrogen surface sites in contrast to VZrON catalysts [55, 74]. For these reasons the impact of adding phosphor into VZrON was investigated.
- Different types of molybdenum nitrides are known. VMO (M = Al or Zr) precursors mechanically mixed with MoO_3 were nitrided by a defined nitridation protocol described in literature to form molybdenum nitrides besides VZrON and VAlON, respectively [75–77]. With the help of this route a defined amount of nitride site was supposed to be introduced into VMON catalysts.

Secondly, it was additionally focused on novel VMON oxynitrides. Since active ammoxidation catalysts contain beside V as redox-active site also Sb [34, 78], it was decided to elucidate the potential of VSbON catalysts in the ammoxidation of 3-PIC. Finally, the two redox-active metal sites, V and Mo, were combined via an aqueous route to investigate the impact of VMoON catalysts in the ammoxidation of heteroaromatics.

3. Results

3.1. Combining VAlON and VZrON to VZrAlON catalysts

As described in section 2, the high activity and low selectivity of VZrON compared to VAlON catalysts is mainly attributed to three structural features: VZrON catalysts possess an almost N-free surface and a higher polymerisation degree of VO_x sites, moreover they provide a lower amount of reduced V sites under reaction conditions compared to VAlON catalysts. With this knowledge it was decided to investigate whether a combination of VZrON and VAlON catalysts leads to an improvement of the catalytic performance. The combination of V, Zr and Al was realized by co-precipitation. Thus obtained oxide precursors are denoted in the following discussion as VZrAlO. These oxide precursors were nitrided afterwards and are abbreviated with VZrAlON. Different V/(Al+Zr) ratios were adjusted during co-precipitation ranging from 0.15 up to 0.60. The respective V/(Al+Zr) ratio is enclosed behind the formula VZrAlO and VZrAlON, respectively. The Al/Zr ratio was fixed to 1.5. However, one sample was prepared with Al/Zr = 0.8 and V/(Al+Zr) = 0.5 to elucidate the impact of the Al/Zr ratio.

In the following section the structural and catalytic properties of these VZrAlON catalysts are discussed and compared with results received previously for VZrON and VAlON catalysts [8].

3.1.1. Catalytic performance

Catalytic data for the VZrAlON oxynitride series with Al/Zr = 1.5 are depicted as function of the bulk $V/(Al+Zr)_{ICP}$ ratio in Fig. 3.1 A and B. Conversions X_{3-PIC}, selectivities S_{3-CP} and yields Y_{3-CP} received at a bed temperature T_B = 360 °C are presented for two different space velocities GHSV = 2713 h^{-1} and 5728 h^{-1} in these figures.[1] It should be noted that no change of the catalytic performance was observed with time on stream for VZrAlON catalysts.

---

[1] The catalytic performance of VAlON catalysts was measured at GHSV = 2713 h^{-1}. Due to the high activity of VZrON catalysts, no catalytic data could be obtained at GHSV = 2713 h^{-1} since the stability of the temperature in the catalyst bed was not ensured. For this reason the GHSV was increased to 5728 h^{-1} for this catalyst class [7, 8]. For comparison VZrAlON catalysts were tested for both GHSV values.

Generally, equal trends can be observed for both space velocities, but a higher GHSV value reduces X_{3-PIC} slightly. By rising the V/(Al+Zr) ratio, initially the conversion increases up to a ratio of 0.5. At a ratio of 0.6 the conversion decreases by 20 % for GHSV = 2713 h^{-1} and by 32 % for GHSV = 5728 h^{-1}, respectively. However, for both space velocities S_{3-CP} increases as a function of the V concentration. This outstanding behaviour of the selectivity was already observed in the VAlON series, but not for the VZrON series [8].

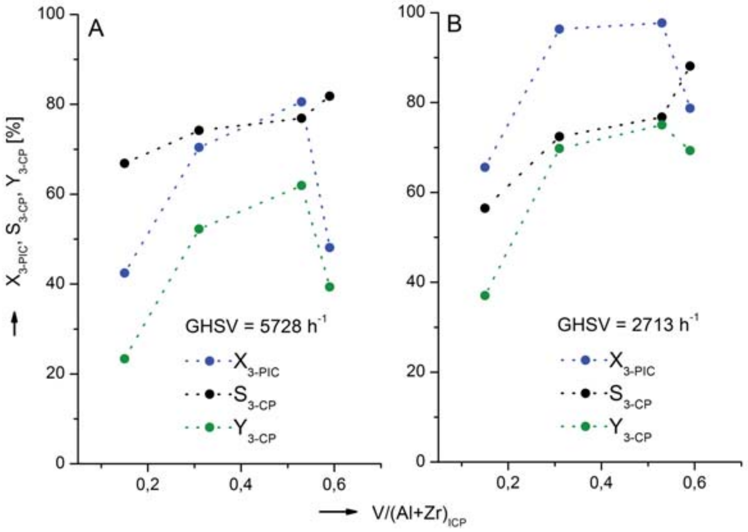

Figure 3.1.: Catalytic performance of VZrAlON catalysts (Al/Zr = 1.5) at T_B = 360 °C depending on the V/(Al+Zr) ratio derived by ICP-OES analysis for A) GHSV = 5728 h^{-1} and B) GHSV = 2713 h^{-1}

Since the bulk V/(Al+Zr)$_{ICP}$ ratios differ dramatically from the surface V/(Al+Zr)$_{XPS}$ ratios (see Tab. 3.2 in section 3.1.2), the catalytic performance of the VZrAlON, VAlON and VZrON series are given in Fig. 3.2 A and B as a function of the surface metal ratios derived by XPS.

By comparing the conversion of the VZrAlON series with VAlON as a function of the surface ratios at GHSV = 2713 h^{-1} (see Fig. 3.2 A), it must be concluded that VZrAlON catalysts are more active than VAlON catalysts. In contrast, VZrAlON catalysts are less active than VZrON catalysts at GHSV = 5728 h^{-1}.

By rising the V/(Zr+Al)$_{XPS}$ up to 0.2 in VZrAlON catalysts, S_{3-CP} increases continuously for both space velocities in agreement with the correlations given in Fig. 3.1 A and B.

At V/(Al+Zr)$_{XPS}$ $\approx$ 0.2 almost identical selectivities are observed in the VZrAlON catalyst series for both space velocities. Thus, for the VZrAlON catalysts with V/(Al+Zr)$_{XPS}$ $\approx$ 0.2 the selectivity is almost independent of the space velocity (see Fig. 3.2 B).

Moreover, the values of S_{3-CP} of VZrAlON catalysts are higher than those for the VZrON catalysts at each V/(Zr+Al)$_{XPS}$ ratio. Not until the ratio V/(Zr+Al)$_{XPS}$ reaches a value of > 0.1, an improvement of S_{3-CP} is observed compared to VAlON catalysts.

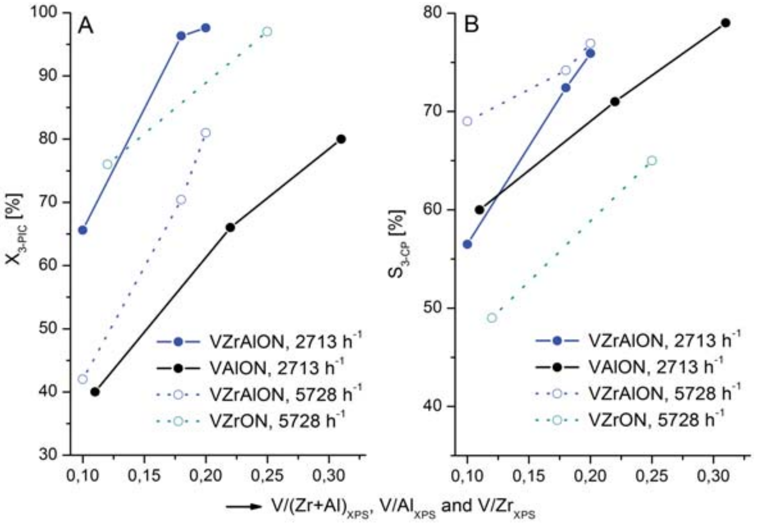

Figure 3.2.: Catalytic performance of VZrAlON series at T_B = 360 °C compared to VAlON and VZrON catalysts [7, 8] as function of the V/M$_{XPS}$ ratio; A) X_{3-PIC} and B) S_{3-CP}

To elucidate the potential of VZrAlON catalysts the impact of the bed temperature T_B on the catalytic performance was investigated for the VZrAlON series (Al/Zr = 1.5) for both GHSV values. The results of this study are plotted in Fig. A.1. At low and at high GHSV the conversion increases with rising bed temperature for each V/(Zr+Al) ratio. The maximum value of X_{3-PIC} is detected for the VZrAlON with a V/(Al+Zr) ratio of 0.5 at each T_B. Moreover, values of selectivities are almost constant over a wide temperature range at GHSV = 5728 h^{-1} for each of the VZrAlON catalysts. At a lower GHSV the selectivity increases slightly for the samples with V/(Zr+Al) $\geq$ 0.25, while for the catalyst with the lowest V/(Zr+Al) ratio a dramatic decrease of S_{3-CP} can be detected by rising T_B. The best catalytic performance with respect to STY was found for the catalyst VZrAlON-0.5. At $T_B \approx$ 380 °C a value of STY 488 g/lh is reached.

A comparison of the catalytic performance as function of T_B of the best catalysts in the VZrON and VZrAlON series is depicted in Fig. 3.3 A. As clearly indicated by this plot, the conversion increases from 50 % to 100 % for the VZrON-0.25 catalyst, when increasing T_B from 320 to 360 °C. In this course S_{3-CP} decreases from 74 to 65 %. Conversion values above 90 % for the VZrAlON-0.5 catalyst are not reached below T_B = 375 °C.

In contrast to VZrON-0.25, the VZrAlON-0.5 catalyst possesses an almost constant selectivity over a wide temperature range. Due to the latter unique catalytic property of the VZrAlON-0.5 catalyst a STY of 488 g/lh can be reached at T_B = 380 °C, whereby the maximum STY for the VZrON-0.25 catalyst is merely close to 400 g/lh at T_B = 360 °C.

Additionally, it can be seen by the comparison in Fig. 3.3 A that at equal values of X_{3-PIC} for VZrON-0.5 and VZrAlON-0.5 the latter catalyst has a higher selectivity. For these reasons, it can be concluded that the combination of VZrON and VAlON catalysts leads to a new material which has indeed better catalytic properties in the ammoxidation than the corresponding pure catalysts VAlON and VZrON.

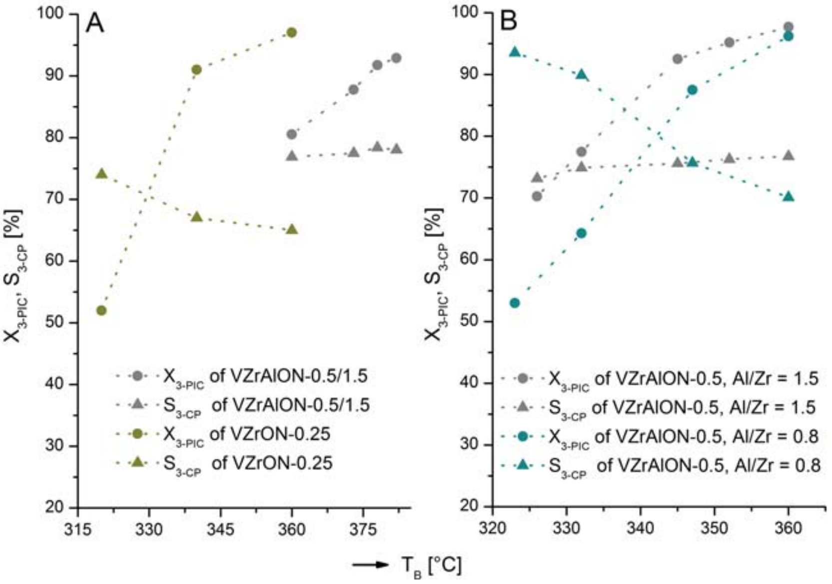

Figure 3.3.: Catalytic performance of VZrAlON-0.5 as function of the bed temperature T_B in comparison to A) VZrON-0.25 at GHSV = 5728 h^{-1} [7] and B) VZrAlON-0.5 (Al/Zr = 0.8) at GHSV = 2713 h^{-1}

Finally, the impact of the Al/Zr ratio of VZrAlON oxynitrides on the catalytic performance was studied. A comparison of the catalytic performance of two VZrAlON-0.5 catalysts with Al/Zr = 1.5 and 0.8 is shown in Fig. 3.3 B as a function of T_B. For the catalyst with Al/Zr = 0.8 the conversion also increases with rising T_B and approaches the one for the catalyst with Al/Zr = 1.5 at T_B = 360 °C. But S_{3-CP} is slightly lower for the catalyst with Al/Zr = 0.8. Consequently, the catalytic performance cannot be improved significantly by decreasing the Al/Zr ratio and rising the Zr content in VZrAlON, respectively.

In conclusion it can be stated:

- The conversion and the selectivity increase continuously with rising V/(Al+Zr)$_{ICP}$ ratio from 0.1 to 0.5. The VZrAlON-0.5 catalyst (X_{3-PIC} = 98 %, S_{3-CP} = 77 %, Y_{3-CP} = 75 %) is more active and selective than the VZrAlON-0.1 catalyst (X_{3-PIC} = 66 %, S_{3-CP} = 57 %, Y_{3-CP} = 38 %) at T_B = 360 °C & GHSV = 2713 h^{-1}.
- Based on the surface V/Al$_{XPS}$ and V/(Al+Zr)$_{XPS}$ ratios VAlZrON catalysts are more active and slightly more selective than VAlON catalysts at T_B = 360 °C & GHSV =

2713 h^{-1}. However, the selectivity of the best VAlON-0.5 catalyst (X_{3-PIC} = 80 %, S_{3-CP} = 79 %, Y_{3-CP} = 63 %) is slightly higher than for the best VZrAlON-0.5 catalyst (X_{3-PIC} = 98 %, S_{3-CP} = 77 %, Y_{3-CP} = 75 %).

- Based on the surface V/Zr_{XPS} and $V/(Al+Zr)_{XPS}$ ratios, VZrAlON are more selective and less active than VZrON catalysts at T_B = 360 °C & GHSV = 5728 h^{-1}. Almost equal yields are reached for the best VZrON-0.25 catalyst (X = 97 %, S_{3-CP} = 65 %, Y_{3-CP} = 63 %) and best VZrAlON-0.5 catalyst (X_{3-PIC} = 82 %, S_{3-CP} = 77 %, Y_{3-CP} = 63 %).
- For T_B > 360 °C the conversion increases continuously for VZrAlON-0.5 with an almost constant selectivity (e.g. X_{3-PIC} = 93 %, S_{3-CP} = 78 % and Y_{3-CP} = 73 % at T_B = 382 °C) resulting in a maximum STY of 488 g/lh. In comparison, the conversion also increases continuously for VZrON-0.25 with rising T_B, but this goes along with a decrease of the selectivity. Therefore, a maximum STY of 399 g/lh is reached for VZrON-0.25 at T_B = 360 °C.
- It was found that also the Al/Zr ratio has an impact on the catalytic performance of VZrAlON catalysts. But no significant improvement of the catalytic performance at T_B = 360 °C and GHSV = 2713 h^{-1} is observed by changing the Al/Zr ratio from 1.5 to 0.8.

Finally, these results illustrate that the combination of VAlON and VZrON to VZrAlON leads to an improvement of the catalytic performance.

3.1.2. Comparison of structural properties of VZrAlON with those of VAlON and VZrON catalysts

Chemical composition and BET surface areas The chemical compositions of fresh and used VZrAlON catalysts as well as the N/V and V/(Al+Zr) ratios derived by ICP-OES and CHN analysis are given in Tab. 3.1. In addition, the surface areas S_{BET} and the N content in wt.-% are listed for each sample. Several trends for VZrAlON can be derived from this table. For the fresh catalysts with Al/Zr = 1.5 the N content increases up to a V/(Al+Zr) ratio of 0.5. Also the values of S_{BET} increase up to a ratio of 0.5 and then drop dramatically for larger ratios. This dramatic loss of surface area by 100 m^2/g for VZrAlON-0.6 might be one possible reason for the loss of conversion compared to VZrAlON-0.5 (see Fig. 3.1 A and B).

Moreover, by comparing the chemical composition and the N content given in wt.-% for each fresh and used sample it is easily seen, that the bulk N content decreases after use. This effect was also detected for VAlON and VZrON catalysts. No general trend can be derived from the N/V bulk ratio - neither for the fresh nor for the used VZrAlON catalysts implying that not only V sites are nitrided. For VAlON catalysts it was observed that the N/V ratio was almost constant with overall V/Al ratios, indicating that V might be preferentially nitried. Also for VZrON catalysts no general trend was observed for the N/V ratio when rising the V/Zr ratio in the VZrON catalyst series.

Table 3.1.: Chemical compositions, N contents, N/V and V/(Zr+Al) ratios as well as surface areas S_{BET} of fresh and used VZrAlON catalysts

VZrAlON sample	Chemical composition	N [wt.-%]	N/V	V/(Al+Zr)	S_{BET} [m^2/g]
0.1, fresh	$V_{0.39}ZrAl_{1.55}O_{5.60}N_{0.27}$	1.51	0.68	0.15	199.0
0.1, used	$V_{0.40}ZrAl_{1.54}O_{7.39}N_{0.16}$	0.84	0.41	0.16	167.4
0.25, fresh	$V_{0.77}ZrAl_{1.50}O_{6.25}N_{0.40}$	2.04	0.53	0.31	154.4
0.25, used	$V_{0.78}ZrAl_{1.54}O_{7.10}N_{0.35}$	1.70	0.46	0.31	112.0
0.5, fresh	$V_{1.32}ZrAl_{1.51}O_{7.12}N_{0.71}$	3.07	0.54	0.54	152.8
0.5, used	$V_{1.32}ZrAl_{1.52}O_{8.45}N_{0.45}$	1.84	0.34	0.52	110.0
0.6, fresh	$V_{1.48}ZrAl_{1.53}O_{7.39}N_{0.55}$	2.32	0.38	0.58	55.4
0.6, used	$V_{1.49}ZrAl_{1.53}O_{8.75}N_{0.47}$	1.85	0.31	0.59	46.9
0.5, fresh	$V_{0.99}ZrAl_{0.77}O_{5.50}N_{0.57}$	3.11	0.58	0.56	119.0
0.5, used	$V_{1.00}ZrAl_{0.77}O_{6.92}N_{0.35}$	1.76	0.35	0.57	95.4

The change of the Al/Zr ratio from 1.5 to 0.8 in VZrAlON affects mainly the surface area, which is about 33 m^2/g lower for the fresh sample with Al/Zr = 0.8 compared to the sample with Al/Zr = 1.5. Moreover it can be seen that the N/V ratios and the N content are almost in the same range for both samples - as well as in the fresh and used catalyst.

Surface analysis by XPS More information about the surface composition was derived by XPS. Among the VZrAlON samples in Tab. 3.1 the fresh catalysts with Al/Zr = 1.5 and $0.1 \leq V/(Al+Zr) \leq 0.5$ were investigated via XPS. Additionally the used catalyst VZrAlON-0.1 and VZrAlON-0.5 (Al/Zr = 1.5) were analyzed to clarify the impact of the ammoxidation on the surface composition and the N sites.

First of all, relevant surface ratios are summarized for fresh and used samples in Tab. 3.2. Marked differences are seen for the surface and bulk composition of the fresh VZrAlON catalysts as indicated by the elemental ratios given in Tab. 3.1 and Tab. 3.2. For each fresh sample the surface V/(Al+Zr) ratio is lower than the corresponding bulk ratio. Moreover, the deviation between the bulk and surface V/(Zr+Al) ratios becomes more pronounced with rising the V concentration in the VZrAlON series. This means that vanadium is enriched in the bulk. Also the bulk and surface N/V ratios differ strongly indicating that N is partly enriched in the bulk as well. Finally the surface Al/Zr ratios are higher than the bulk Al/Zr ratios which are around 1.5 according to the chemical compositions given in Tab. 3.1. This means that in each of the fresh VZrAlON samples Al is enriched on the surface.

Table 3.2.: Relevant surface ratios of fresh and used VZrAlON catalysts with Al/Zr = 1.5 derived by XPS

sample	V/(Al+Zr)	N/V	Al/Zr	V/Zr	V/Al
fresh VZrAlON-0.1	0.10	0.00	1.99	0.20	0.15
fresh VZrAlON-0.25	0.18	0.22	1.79	0.50	0.28
fresh VZrAlON-0.5	0.20	0.35	1.96	0.59	0.30
used VZrAlON-0.1	0.09	0.70	1.85	0.26	0.14
used VZrAlON-0.5	0.28	0.32	2.17	0.90	0.41

Also the chemical nature of the surface differs in the fresh and used VZrAlON series and depends strongly on the adjusted V/(Zr+Al) ratio as evident from E_B values and elemental surface concentrations c, which are listed in Tab. 3.3 for the fresh samples and in Tab. 3.4 for the used samples.

To compare the mean surface V oxidation state in VZrAlON catalysts, ΔE_B values instead of E_B(V2p3/2) are used and were calculated from $\Delta E_B = E_B(O1s) - E_B(V2p3/2)$. This equation considers the change of surface oxygen state according ref. [79] and gives a more precise information about the V surface valence. The correlation between ΔE_B values and the mean V surface oxidation state found for V_xO_y samples is depicted in Fig. 3.4 [79]. Own calculated ΔE_B values for fresh and used VZrAlON catalysts are arranged in this figure to illustrate the changes of V surface valence. At low V/(Al+Zr) ratios merely one V site (labeled with V^1) is detected for the fresh catalysts (see Tab. 3.3). Its ΔE_B value points to a mean surface V oxidation state close to + 4.3 as it is seen from Fig. 3.4. As indicated by a decrease of ΔE_B for the site V^1 the mean surface vanadium oxidation state rises from + 4.3 to 5.0 with rising the V/(Al+Zr) ratio in the fresh VZrAlON catalyst series. Moreover, for the fresh VZrAlON-0.5 catalyst an additional V site (labeled with V^2) can be detected being the dominant V surface site according to the elemental surface concentration. Its ΔE_B value indicates that the mean oxidation state of this site is close to + 3.5 (see Fig. 3.4).

Interestingly, for all fresh VZrAlON catalysts two types of Al species can be detected. Both of these Al sites possess binding energies, which clearly deviate from the Al2p binding energy of Al_2O_3 (E_B = 74.5 - 75.6 eV) [80, 81]. [2] Remarkably, a binding energy of around 69 eV for the Al_1 site is extremely low and to our knowledge such low binding energy was never observed for an Al containing surface site. Even for elemental Al merely binding energies of 72.7 eV are

---

[2] For the fresh VAlON series one Al2p signal was found at 74.4 eV for V/Al $\leq$ 0.25; merely at V/Al = 0.5 a second Al site with E_B = 71.9 eV could be detected. It was assigned to Al-N-V units, since also in the V2p3/2 region a second V site with a considerable low E_B value of 513.9 eV was observed [7, 8].

Table 3.3.: Binding energies E_B and elemental surface concentrations c [at.-%] of fresh VZrAlON catalysts derived by XPS

		fresh VZrAlON-0.1		fresh VZrAlON-0.25		fresh VZrAlON-0.5	
XPS peak	site	E_B [eV]	c [at.-%]	E_B [eV]	c [at.-%]	E_B [eV]	c [at.-%]
V2p3/2	V^1	517.1	3.62	517.4	5.83	518.2	2.77
V2p3/2	V^2	-	-	-	-	516.8	3.8
Al2p	Al^1	69.5	4.91	69.9	3.88	69.8	8.69
Al2p	Al^2	72.8	19.53	73.5	17.19	73.8	12.68
Zr3d3/2	Zr^1	181.1	12.3	181.7	11.75	182.0	10.92
O1s	O^1	530.7	59.6	530.8	46.12	531.1	49.23
O1s	O^2	-	-	532.6	8.25	532.5	5.38
N1s	N^1	-	-	397.3	0.38	397.6	1.08
N1s	N^2	-	-	400.3	0.32	401.0	0.58
N1s	N^3	-	-	402.9	0.57	403.4	0.63

Table 3.4.: Binding energies E_B and elemental surface concentrations c [at.-%] of used VZrAlON catalysts derived by XPS

		used VZrAlON-0.1		used VZrAlON-0.5	
XPS peak	site	E_B [eV]	c [at.-%]	E_B [eV]	c [at.-%]
V2p3/2	V^1	516.6	2.8	517.4	1.20
V2p3/2	V^2	-	-	514.8	1.91
Al2p	Al^1	70.3	4.44	71.2	8.31
Al2p	Al^2	73.8	15.54	74.7	8.03
Zr3d	Zr^1	181.8	10.81	182.5	7.54
O1s	O^1	526.5	4.82	527.1	4.96
O1s	O^2	529.9	42.92	529.6	46.37
N1s	N^2	399.5	1.97	399.2	1.20
N1s	N^3	-	-	400.8	0.98

reported in literature [82]. However, the binding energy value of the second Al species (labeled with Al^2) might hint to the presence of Al-N-M bonds (M = Al, Zr or V), since it is close to those observed for aluminum nitrides (73.5 to 73.6 eV) [83, 84].

In contrast, only one Zr surface species could be detected by XPS in the fresh VZrAlON series, for which E_B rises from 181.1 to 182.0 eV with increasing V/(Zr+Al) ratio. According to literature, the position of the $Zr3d_{3/2}$ peak in ZrO_2 is found at 182.4 eV [85, 86]. [3] This suggests a surface reduction of Zr^{4+} to Zr^{3+} by nitridation at least at low V/(Al+Zr) ratios since binding energies of the $Zr3d_{3/2}$ peak for the samples VZrAlON-0.1 and VZrAlON-0.5 differ about 1 eV.

---

[3] In the series of fresh VZrON catalysts E_B of $Zr3d_{3/2}$ peak was found to be 182.2 eV for each adjusted V/Zr ratio, which ranges from 0.1 to 0.5. This indicates that Zr surface sites are not reduced. Also a substitution of O by N can be excluded in the coordination sphere of Zr sites [7, 8].

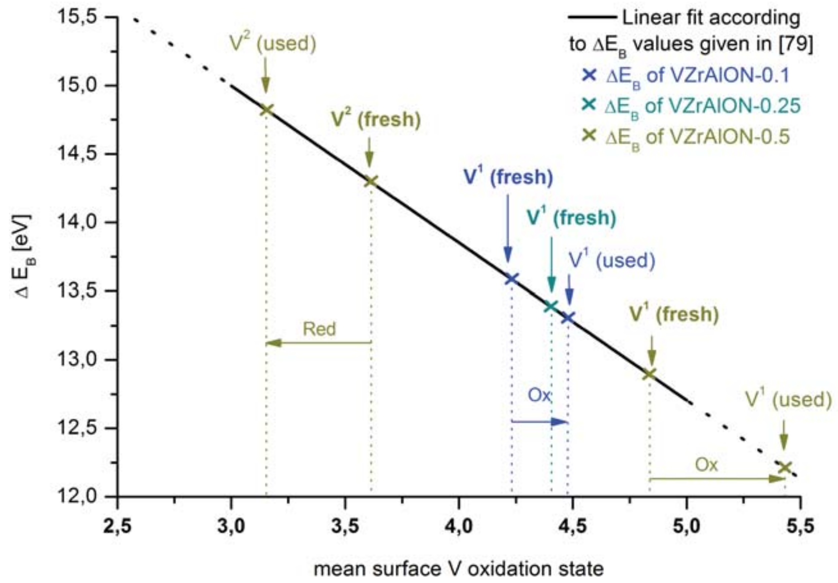

Figure 3.4.: Changes of the surface V valence in fresh and used VZrAlON catalysts (Al/Zr = 1.5) according to the linear plot of mean surface V oxidation state vs. ΔE_B values found for V_xO_y [79]

Additionally, a partial reduction of Zr in the fresh VZrAlON-0.1 sample could explain the low E_B value of the corresponding Al^2 site. Generally, the binding energy of an atom is influenced by its environment; the more electron-rich, the lower E_B. Thus, a Zr^{3+} species is supposed to attract the electrons in a Zr-O-Al surface unit weaker than a Zr^{4+} species. Therefore, the electron density around the Al atom in a Zr^{3+}-O-Al^{3+} environment is supposed to be higher than in a Zr^{4+}-O-Al^{3+} environment which in turn might lead to lower E_B values expected for the Al^2 site.

While the surface of the VZrAlON-0.1 catalyst initially does not contain any nitrogen, which was also the case for VZrON series [8], the surface of fresh VZrAlON catalysts with higher V/(Al+Zr) ratios shows the presence of three N species with E_B between 397.3 and 403.4 eV. Based on literature data, site N^1 can be attributed to nitride ($N1s^{ZrN}$ = 397.3 - 397.6 eV [87,88], $N1s^{AlN}$ = 396.5 eV [83,84,89] and $N1s^{VN}$ = 397.4 eV [90]). The species N^2 with E_B values of 400 - 401 eV are most probably due to NH_x (x = 1 or 2) [91]. The species N^3 might be assigned to NH_4^+, but consider that the N^3 site might be also attributed to bimolecular-like -N=N- sites according to [6,86,91]. However, ATR results being in detail discussed in the next chapter confirm the presence NH_4^+ sites in the fresh VZrAlON catalysts since a typical band of NH_4^+ can be detected for each sample ranging from 1441 to 1419 cm^{-1}(see Fig. 3.6 A). No hints for an N=N vibration could be found.

The surface concentration of each N site and the overall sum of N surface sites N_s are plotted as a function of the surface $V/(Al+Zr)_{XPS}$ ratio in Fig. 3.5. In general, the concentration of each N site increases with rising V surface concentration in fresh VZrAlON catalysts indicating that V plays a crucial role for the formation of these N species. The concentrations of N^2 and N^3 increase linearly with V/(Al+Zr) ratio suggesting that the sites N^2 and N^3 are mainly located in the coordination environment of V sites. For the nitride-like site an exponential growth can be observed, which indicates that not only V sites are nitrided. This is also supported by a non-constant bulk and surface N/V ratio (see Tab. 3.1 and Tab. 3.2). It might be possible that also Al sites possess N in their coordination sphere since the E_B value of the Al2p peak with 73.8 eV is too low for Al-O bonds.

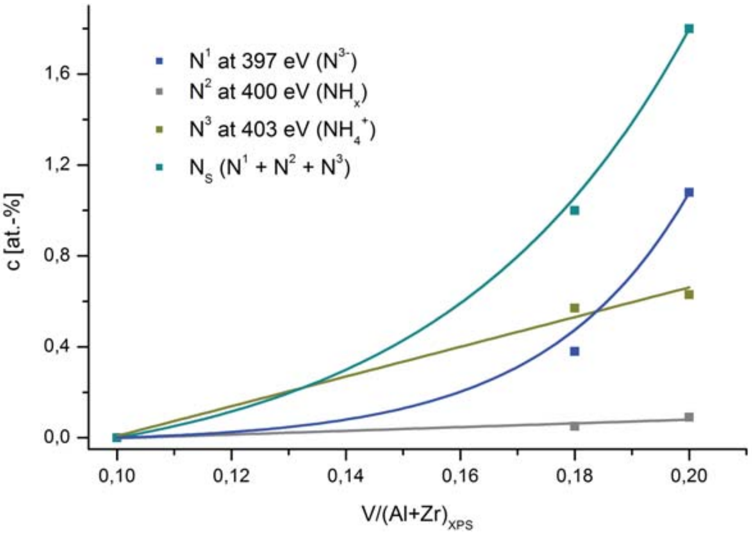

Figure 3.5.: Surface concentrations c [at.-%] of N species as a function of the surface V/(Zr+Al)$_{XPS}$ ratio in fresh VZrAlON catalysts (Al/Zr = 1.5)

Significant changes of the surface composition and surface sites are observed in VZrAlON samples after ammoxidation (compare results in Tab. 3.3 and Tab. 3.4). While the total surface N content for sample VZrAlON-0.5 remains almost constant, the N^{3-} species (N^1) is no longer seen in the used catalyst. Rather the concentration of the remaining NH_x species (N^2 and N^3) increases. In the sample VZrAlON-0.1 an NH_x species (N^2) appears on the surface for the first time. Simultaneously, the bulk N content decreases for both samples after use (see Tab. 3.1).

This suggests that N^{3-} species from the bulk are moving to the surface under reaction conditions where they are partly transformed into NH_x species N^2 and N^3. Alternatively, nitrides N^{3-} can be converted to molecular N_2. This has been experimentally observed during TPO experiments upon heating VMo oxynitrides in air (see chapter 3.4) and was also assumed by Wiame et al. and L. Le Gendre et al., who investigated the thermal oxidative decomposition of several metal oxynitrides [92, 93]. The electrons released during this reaction can be taken up either by a neighboring V site, which is reduced in turn or by O_2 from the gas phase which forms O^{2-} via the sequence [94]:

$$O_2 \xrightarrow{+e^-} O_2^- \xrightarrow{+e^-} O_2^{2-} \rightarrow 2\,O^- \xrightarrow{+2e^-} 2\,O^{2-}. \tag{3.1}$$

The O^{2-} species might fill the vacancies in the lattice while O^- species in the neighborhood of a reduced V site can be converted to O^{2-} upon oxidation of the former. Note that the ΔE_B value of site V^1 decreases (indicating oxidation) while the one of site V^2 increases (indicating reduction) for the VZrAlON-0.5 catalyst during ammoxidation (see Fig. 3.4). Obviously, the net release of nitride species from the catalyst during ammoxidation gives rise to a complex system of dynamic changes. However, it is indicated that in the used VZrAlON-0.5 catalysts the site V^1 might be located in a matrix of Zr sites while site V^2 is rather connected to Al containing species since the surface ratio of V^2/V^1 = 1.6 is equal to the adjusted bulk Al/Zr (see again Tab. 3.1). This assignment also means that Zr containing V sites (V^1) are oxidized during ammoxidation while Al containing V sites (V^2) are reduced (see also Fig. 3.4) in the course of ammoxidation. This assignment will be later on supported by results of in situ EPR spectroscopy.

ATR spectroscopy and surface acidity ATR spectroscopy was additionally applied to get more information about the chemical nature of N sites. The spectra for the fresh and used VZrAlON series with Al/Zr = 1.5 are given in Fig. 3.6 A and B.

Two distinct bands can be observed for fresh VZrAlON samples at around 1441 and 1629 cm^{-1} being typical for $\delta(NH_4^+)$ and $\delta(H_2O)$ vibration [95], respectively. Moreover, a shift of the $\delta(NH_4^+)$ vibration to lower wavenumber is detected with rising V/(Al+Zr) ratio, which points to the fact that the oxidation state of the metal site to which NH_4^+ sites are bound differ.

For the fresh VZrAlON-0.5 sample additional bands are detected at 896 and 1068 cm^{-1}. The band at 1068 cm^{-1} is assigned to the ν(V=O) vibration of VO_x species. For isolated VO_x sites in supported VO_x/Al_2O_3 and VO_x/ZrO_2 this band appears around 1040 cm^{-1} [96]. However, this band is shifted to higher wavenumber for the VZrAlON-0.5 oxynitride, indicating that the chemical environment of V=O has changed via nitridation. The band at 896 cm^{-1} might originate from M-N-M (M = Al, Zr or Al) units.

ATR spectra of all used VZrAlON are given in Fig. 3.6 B. They are mainly characterized by one intense vibration at around 1424 cm^{-1} and a broad band ranging from 1551 to 1665 cm^{-1}. This might indicate that besides $\delta(NH_4^+)$ and $\delta(H_2O)$ vibrations also vibrations of NH_x sites ($x < 4$) contribute to the ATR spectra. Note that e.g. the $\delta(NH_2)$ band is expected in the same region [97]. For the used VZrAlON-0.5 sample two distinct N containing sites could be also detected by XPS.

Remarkably, the intensity of both bands in the δ(N-H) region increases upon use suggesting that more of such surface species are formed during reaction. This agrees properly with the higher surface concentration of N^2 and N^3 species detected by XPS in the used catalysts (see Tab. 3.4), which arise from NH_x (x = 1-4) species as well.

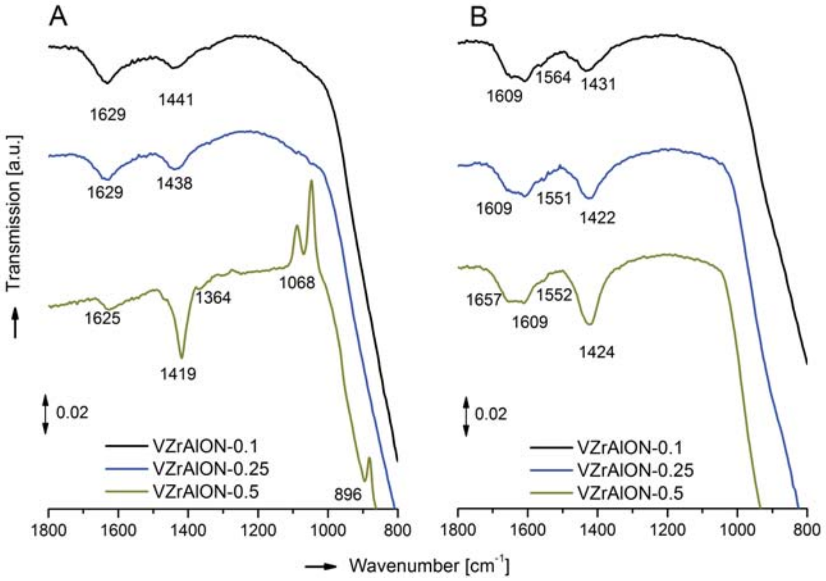

Figure 3.6.: ATR spectra of VZrAlON catalysts with Al/Zr = 1.5 at RT as function of the V/(Al+Zr) ratio, Al/Zr = 1.5; A) Fresh samples, B) Used samples

To elucidate the surface acidity of VZrAlON oxynitrides the adsorption of pyridine followed by FTIR spectroscopy was applied. Both Brønstedt and Lewis acid sites can be detected by this method [98]. No typical bands for these two sites are detected by FTIR spectroscopy for the fresh VZrAlON series with $0.12 \leq$ V/(Al+Zr) ≤ 0.53 and Al/Zr = 1.5. Also for VZrON catalysts acid sites were not observed by this method [7, 8]. Only for VAlON oxynitrides at low V/Al-ratios typical vibration bands for Lewis acid sides could be seen. Hence, the formation of Lewis acid sites at low V concentrations can be suppressed by using a mixture of V, Zr and Al.

XRD analysis The fresh and used catalysts of the VZrAlON series with Al/Zr = 0.8 and 1.5 are almost X-ray amorphous as indicated by the powder XRD pattern given in Fig. A.2. Only for the used catalyst VZrAlON-0.1 very broad peaks can be detected indicative of a crystalline structure might start to form in this sample. A reliable assignment to a certain phase is impossible. This agrees with previous observations showing that also VAlON catalysts are almost X-ray amorphous [7, 8]. In contrast, VZrON catalysts showed typical reflection for slightly disordered crystalline ZrO_2 [7, 8]. Hence, from the XRD point of view VZrAlON catalysts are more similar the VAlON oxynitrides. This suggests that the formation of crystalline ZrO_2 can be suppressed by adding Al indicating that Zr and Al are forming a highly disordered network in the solid.

3.1.3. In situ experiments using EPR spectroscopy

In situ EPR studies of VZrAlON catalysts during nitridation The nitridation of the VZrAlO-0.5 oxide precursor (Al/Zr = 1.5) was followed by in situ EPR spectroscopy using a diluted NH_3 stream.

The in situ investigation during nitridation was designed in the following way: The sample was first heated from RT to 120 °C in N_2 and was cooled down to RT again after 1 h. Then it was switched to 20 % NH_3/N_2 at RT and stepwise heated to 410 °C. After cooling the sample from 410 °C to RT in NH_3/N_2, it was finally switched at RT to N_2. The sample was exposed to latter condition for 14 h. Spectra at elevated temperatures were recorded as a function of time for at least 30 min.

In Fig. 3.7 A the EPR spectrum for the untreated precursor at RT and the EPR spectrum after heating in N_2 at 120 °C are depicted. The EPR spectrum of the untreated oxide precursor shows a hyperfine structure (hfs) signal due to isolated VO^{2+} sites, which is superimposed on a broad background signal arising from interacting V^{4+} sites within cluster-like moieties. Upon switching from N_2 to NH_3 flow at 120 °C the hfs signal of VO^{2+} increases slightly indicating beginning reduction of V^{5+} (see Fig. 3.7 B).

By rising the nitridation temperature to 300 °C not only the EPR signal intensity increases with time, but also the shape of the signal changes (see Fig. 3.7 C). The increase of the EPR signal intensity points to a further reduction of V^{5+} to V^{4+} while the change of the shape implies that new isolated and polymerized V sites are created at this temperature. At 410 °C the EPR signal intensity decreases (see Fig. 3.7 D), and an additional sharp line can be seen possessing no hfs and a g value close to two (see Fig. A.3 B). Probably, this signal arises from F-centers.

In Fig. A.3 A EPR spectra derived at RT after the in situ nitridation are depicted. The brown signal was directly measured after in situ nitridation, while the green signal was obtained after exposure of the sample to N_2 at RT for 14 h. However, the access of N_2 leads to an increase of the EPR signal intensity. Since the N_2 is for sure not completely oxygen-free, a partial reoxidation of V^{3+} to V^{4+} can be assumed indicating that V^{3+} is partially oxidized to V^{4+} under ambient conditions. The corresponding 2nd derivatives of these two spectra given in Fig. A.3 C and D illustrate that in both spectra a sharp isotropic line typical of F-centers is hidden under the hfs signal of VO^{2+}. Therefore, a stability of these defects against reoxidation is proved.

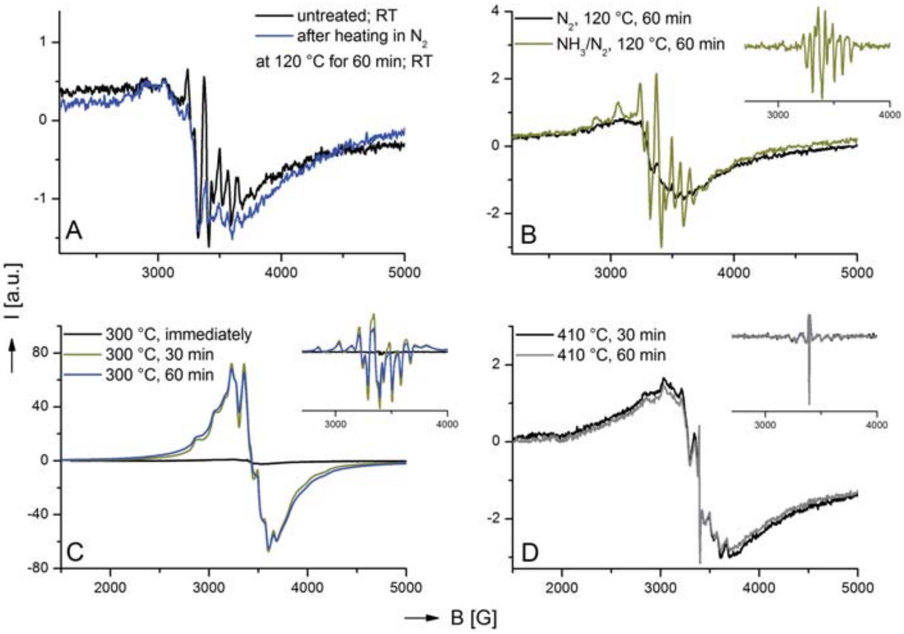

Figure 3.7.: In situ EPR signals for nitridation of the VZrAlO-0.5 oxide precursor; A) Untreated and after heating in N_2 at RT; B) Heating in N_2 or NH_3/N_2 at 120 °C for 1 h; C) NH_3/N_2, 300 °C; D) NH_3/N_2, 410 °C; insets: 2nd derivative of the EPR signal

By comparing the 2nd derivatives of the EPR signals given as insets in Fig. 3.7 B - D, it can be concluded that F-centers are not formed until reaching a nitridation temperature close to 400 °C. These results clearly indicate that the thermal ammonia treatment of the VZrAlO-0.5 oxide precursor results in the formation of vacancies according to the nitridation reaction. This reaction formally predicts the substitution of three O^{2-} anions by two N^{3-} anions and one anionic vacancy. To clarify the stability and the contribution of these introduced vacancies to the catalytic properties, in situ EPR spectroscopy was also used during ammoxidation.

In situ EPR studies of VZrAlON catalysts during ammoxidation The in situ investigation during ammoxidation was designed in the following way: Spectra were recorded at RT before any treatment and after in situ ammoxidation at RT. After heating the catalysts in air/NH_3 (4.5 : 1) to 350 °C water was added to the air/NH_3 stream at 350 °C. Subsequently it was switched to the complete feed at 350 °C (air/NH_3/H_2O/3-PIC). This was followed by stopping the 3-PIC stream, so that the catalyst was again exposed to air/NH_3 at 350 °C. Then the gaseous stream was changed again from air/NH_3 to N_2 (10 ml/min) and finally the sample was cooled from 350 °C to RT in N_2. EPR spectra recorded at elevated temperature were measured for each condition with time on stream until a steady state was reached.

First of all, the EPR signals for the ex situ nitrided fresh VZrAlON oxynitrides measured at RT should be compared in Fig. 3.8 A as a function of the V/(Zr+Al) ratio. Additionally, the EPR signals after the in situ ammoxidation experiment measured at RT are depicted for this series in Fig. 3.8 B. The 2nd derivative of each EPR signal is given in Fig. 3.8 A’ - B’. Generally, the EPR signal intensity decreases with rising V concentration for the untreated VZrAlON series. This trend was also observed for the VAlON series [7]. The corresponding EPR signals for the VAlON series as a function of the V/Al ratio are given in Fig. 3.9 A and B including the 2nd derivatives of each signal.

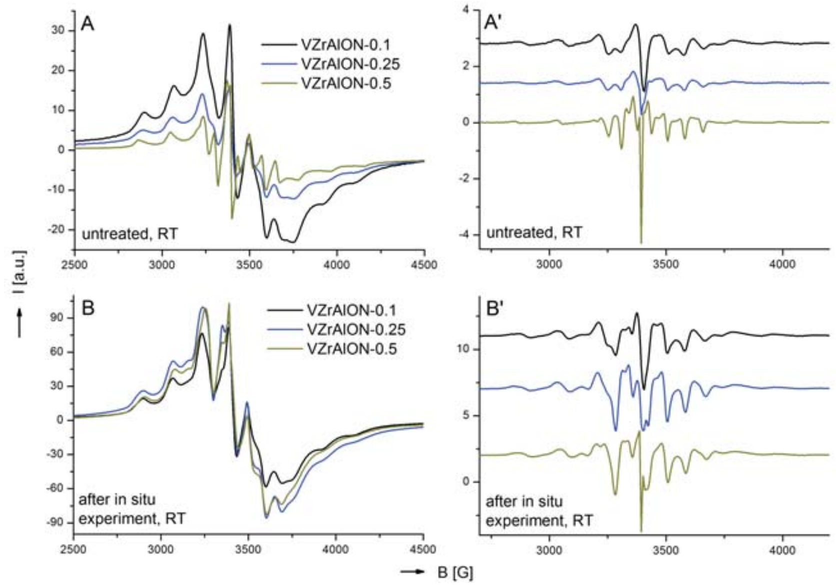

Figure 3.8.: EPR signals and their 2nd derivatives (’) for VZrAlON depending on the V/(Zr+Al) ratio at RT; A/A’) Untreated catalysts; B/B’) After in situ ammoxidation experiment

By comparing the EPR signals for both series, it can be concluded that the signal intensity is higher for the VAlON than for the VZrAlON. This is also supported by the correlation given in Fig. 3.9 C, which shows the double integral intensities A_{EPR} for both series depending on the bulk V/(Al+Zr) and V/Al ratios, respectively. This suggests that the degree of V reduction is higher for VAlON than for VZrAlON samples as already indicated by XPS results. The shape of the EPR signal of the VZrAlON samples is closer to that of VAlON than to that of VZrON catalysts. A EPR spectrum for VZrON-0.25 is given in Fig. 3.9 D. In contrast to VAlON and VZrAlON, a hfs is hardly seen for the VZrON sample pointing to a high amount of polymerized VO^{2+} sites. Thus, aggregation of isolated VO^{2+} sites to $V^{4+}O_x$ clusters can be suppressed by combining VZrON and VAlON to VZrAlON.

More information about an additional signal of vacancies for the oxynitride series can be obtained by comparing the 2nd derivatives of the EPR signals (see Fig. 3.8 A’ - B’ and Fig. 3.9 B). Without doubt, an additional sharp signal can be seen in the EPR spectrum of the untreated VZrAlON

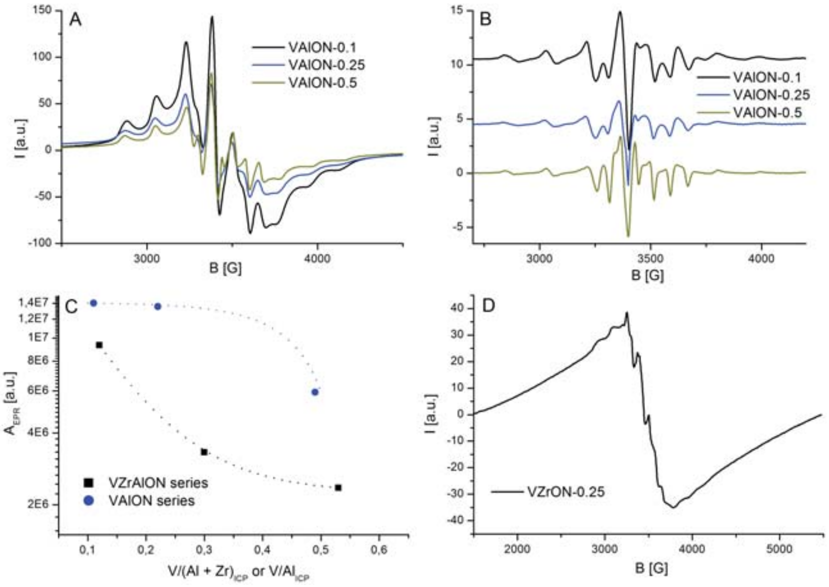

Figure 3.9.: Additional information to Fig. 3.8; A) EPR signals for untreated VAlON series at RT; B) 2nd derivatives of EPR signals in A; C) Double integral intensities (A_{EPR}) for EPR signals measured at RT for VZrAlON and VAlON; D) EPR signal for VZrON-0.25 measured at RT

catalyst with V/(Zr+Al) = 0.5 and weakly for the 0.25 ratio. For the ratio 0.1 the sharp isotropic signal is not seen. It might be weak and therefore hidden under the strong signals of isolated and polymeric VO^{2+} sites, or it is missing because vacancies are simply not formed. Additionally, also for the VAlON and VZrON series no typical signal for a paramagnetic defect can be detected (see Fig. 3.9 B) indicating that the formation of vacancies in a high amount is only favored for VZrAlON oxynitrides. Comparing the EPR signals of the VZrAlON series for the untreated oxynitrides with the EPR signals derived after in situ ammoxidation at RT, clearly the sharp line is still visible for the highest V/(Zr+Al) ratio. Moreover, for each VZrAlON catalyst an increase of the EPR signal can be observed during in situ ammoxidation (see Fig. 3.8 A and B), which implies a change of the V oxidation state during ammoxidation.

The fact that the defect signal is properly seen only in the VZrAlON-0.5 catalyst with the highest V content suggests that these defects might be located close to the coordination sphere of vanadium. This raises the question at which vanadium site it is exactly located and which is the valence of this site. These questions are hard to answer. However, the electron spin of the trapped electron does not couple with the spin of a V^{4+} site. Otherwise it would not be seen anymore. Therefore, it seems to be reasonable that the sharp electron line must be caused by a defect site which is located near to the coordination sphere of V^{5+}. Furthermore, the structure of the fresh VZrAlON-0.5 catalyst seems to differ from all samples. By comparing the normalized EPR spectra measured at RT for this sample before and after use in the in situ experiment (see

Fig. A.4 A and B), clearly marked changes of the hfs can be observed for the highest ratio of V/(Zr+Al) while the structure of the vanadyl site for VZrAlON-0.1 catalyst stays almost the same. This effect will be discussed in more detail in the following chapter.

In situ studies of VZrAlON catalysts in the presence of ammoxidation feed components
To elucidate the impact of the catalyst structure on the catalytic performance for VZrAlON as well as the reason and the moment of the observed structure change of the VZrAlON-0.5 catalyst, EPR spectra taken at elevated temperatures will be discussed below. For comparison, also the data for the VZrAlON-0.1 catalyst are incorporated since the catalytic performance differs significantly for the V/(Zr+Al) ratios 0.1 (X_{3-PIC} = 66 % ;S_{3-CP} = 57 %) and 0.5 (X_{3-PIC} = 98 % ;S_{3-CP} = 77 %).

In Fig. 3.10 A and B EPR signals derived at RT are compared with those measured in air/NH_3 at 350 °C for the two catalysts VZrAlON-0.1 and -0.5. Several trends are indicated by this comparison. First of all, according to Curie's law, the loss of EPR signal intensity for the sample VZrAlON-0.1 must be regarded as thermal effect since the expected ratio of I_{CL} = I(623K)/I(295K) amounts to 0.5. As opposed to this, the EPR signal intensity increases for the sample VZrAlON-0.5, which points to a partial reoxidation of V^{3+} to V^{4+} (I_{CL} = 9.7).

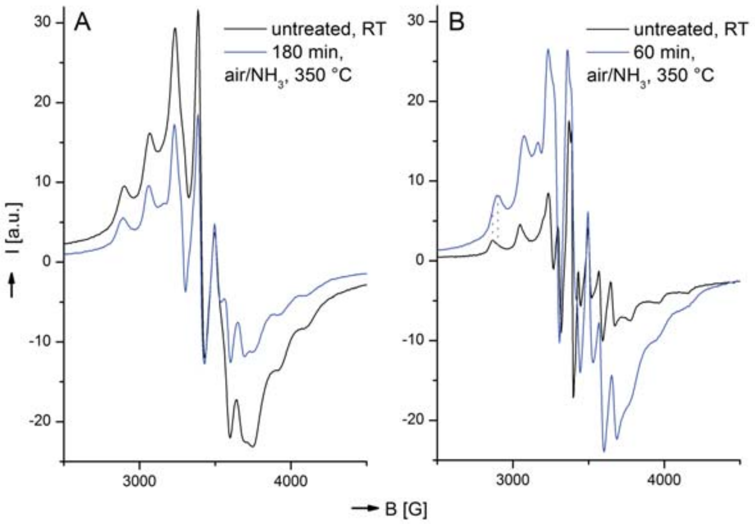

Figure 3.10.: EPR signals for VZrAlON under air/NH_3 at 350 °C with time on stream compared to EPR signal derived for untreated sample at RT; A) VZrAlON-0.1, I_{CL} = 0.5; B) VZrAlON-0.5, I_{CL} = 9.7

Moreover, while the hfs of the isolated VO^{2+} sites for VZrAlON-0.1 stays almost the same, significant changes can be observed for the VZrAlON-0.5 oxynitride. First of all, the typical sharp signal for the defect sites decreases and secondly the hfs parameters change. This is already indicated by the change of the line positions with respect to the spectrum of the untreated sample (exemplified by dotted lines in Fig. 3.10 B). By spectra simulation (discussed below) it could be shown that the EPR spectrum of the VZrAlON-0.5 sample at RT might consists of four different paramagnetic sites: a defect signal, a signal for cluster-like $V^{4+}O_x$ sites, and two signals for two types of isolated VO^{2+} sites. The superposition of two isolated sites in the EPR spectrum of the untreated catalysts is especially well seen by the asymmetric signal in the low field range. Unfortunately, the resolution of these two isolated sites is not sufficient to observe two separated peaks. However, heating this catalyst in an air/NH_3 stream results in a high amount of one isolated site while the afore predominant second isolated site is hardly detectable (see dotted lines in Fig. 3.10 A).

More detailed information about the local structure of the isolated VO^{2+} sites can be derived by calculating the spin Hamiltonian parameters for the EPR signals using the program SIM14S. Also the relative ratio of the paramagnetic sites is accessible by this method. In principle three types of paramagnetic sites (V_{single}, V_{poly} & defect) must be superimposed for the EPR signal of the VZrAlON-0.5 catalyst to obtain a satisfactory fit, while for the signal of VZrAlON-0.1 sample the superposition of two types of paramagnetic sites was sufficient (V_{single} & V_{poly}). A comparison of simulated spectra with experimental spectra is shown in Fig. A.5. The spin Hamiltonian parameters ($A_{\|}$, $A_{\perp}$, $g_{\|}$ and $g_{\perp}$), the parameters $\Delta g_{\|}/\Delta g_{\perp}$ and β_2^{*2}, and the ratios of the paramagnetic species $C_S : C_P : C_D$ are presented in Tab. 3.5 not only for VZrAlON-0.5, but for the VZrAlON-0.1 catalyst too.[4]

The parameter $\Delta g_{\|}/\Delta g_{\perp}$ can be regarded as a measure for the total axial distortion of VO^{2+} species in powder samples. It can be derived from the following relation:

$$\frac{\Delta g_{\|}}{\Delta g_{\perp}} = \frac{g_{\|} - g_e}{g_{\perp} - g_e}. \tag{3.2}$$

The higher $\Delta g_{\|}/\Delta g_{\perp}$ the shorter the V=O bond or longer the bonds in the equatorial plane of the VO^{2+} sites become [99]. The so-called in-plane delocalization coefficient β_2^{*2} reflects the extent to which the free electron is delocalized towards the ligands in the basal plane of the VO^{2+} species and is given by:

$$\beta_2^{*2} = \frac{7}{6}\Delta g_{\|} - \frac{5}{12}\Delta g_{\perp} - \frac{7}{6}[(A_{\|} - A_{\perp})/P] \quad \text{with} \quad P = 184.5\,G. \tag{3.3}$$

β_2^{*2} becomes 1 for a pure VO^{2+} ion and decreases with rising covalent character of the bonds in the basal plane.

---

[4] For the spectrum of the untreated catalyst VZrAlON-0.5 the amount of both isolated sites was added ($C_S = C_{S_1} + C_{S_2}$).

As already indicated by EPR spectra given in Fig. 3.10 and A.4 two different VO^{2+} sites can be detected for the untreated VZrAlON-0.5 catalyst at RT, but not for VZrAlON-0.1. The two isolated sites in the VZrAlON-0.5 catalyst differ clearly in their spin Hamiltonian parameters (see Tab. 3.5). The calculated ratio of $C_{S_1} : C_{S_2} = 1 : 1.6$ suggests that the concentration of S_2 is higher than for S_1. It is almost identical to the adjusted Al/Zr bulk ratio in this sample (see Tab. 3.1) indicating that S_1 might be rather connected to Zr and S_2 to Al containing VO^{2+} sites.

In Tab. 3.6 the spin Hamiltonian parameters and their $\Delta g_{\|}/\Delta g_{\perp}$ and β_2^{*2} are given for different prepared VZr as well as VAl containing samples [7, 100–106]. In general, VO_x/ZrO_2 samples possess a higher value of $\Delta g_{\|}/\Delta g_{\perp}$ than VO_x/Al_2O_3. This supports the assignment of S_1 and S_2 in the fresh VZrAlON-0.5 catalyst.

Moreover, reduction in H_2 of VO_x/Al_2O_3 compounds weakens the V=O bond in isolated VO^{2+} sites and decreases β_2^{*2} values, but also relaxes the tetragonal distortion as evident from $\Delta g_{\|}/\Delta g_{\perp}$ values (see Tab. 3.6). However, distinct structural differences are observed for S_1 and S_2 in VZrAlON-0.5 compared to VO^{2+} sites in VO_x/Al_2O_3, VO_x/ZrO_2 and V_2O_5/Al_2O_3-ZrO_2 samples. The spin Hamiltonian parameters of S_1 assigned to VO^{2+} sites being in a matrix of Zr are less distorted than VO^{2+} sites in VO_x/ZrO_2 and even do not resemble those calculated from the EPR spectrum of VZrON-0.25. Additionally, β_2^{*2} of S_1 is higher than those for reduced or nitrided samples indicating that the ligand coordination sphere for the isolated site S_1 is free of nitrogen. As opposed to this, the β_2^{*2} and $\Delta g_{\|}/\Delta g_{\perp}$ values of VO^{2+} in S_2 deviate strongly from those given for calcined and reduced VO_x/Al_2O_3 as well as from those for V_2O_5/Al_2O_3-ZrO_2. This might be a hint that the oxygen ligands of the VO^{2+} sites in the basal plane are partly substituted by nitrogen.

Moreover, the spin Hamiltonian parameters of the VO^{2+} site in the VZrAlON-0.1 sample (RT, untreated) are more related to those found for pure $AlVO_x$ (see Tab. 3.6). This suggests that the VO^{2+} sites possess no nitrogen in their coordination sphere. This is also supported by XPS results, which suggest that the surface of the latter sample is initially almost free of nitrogen.

When the VZrAlON-0.1 catalyst is heated to 350 °C in air/NH_3, no significant changes of the spin Hamiltonian parameters for VO^{2+} sites are detected. In contrast, heating the catalyst VZrAlON-0.5 in air/NH_3 to 350 °C, only the second isolated VO^{2+} site S_2 remains while S_1 diminishes possibly due to oxidation to pentavalent VO^{3+}. According to the previous assignment of S_1 and S_2, Zr containing VO^{2+} sites are oxidized to VO^{3+} . This assumption is supported by the fact that for pure VZrON catalysts the mean V surface oxidation state was close to +5 (proved by XPS and EPR results) [8] indicating that the close proximity of V and Zr sites favor

Table 3.5.: Spin Hamiltonian parameters, $\Delta g_{\parallel}/\Delta g_{\perp}$ and β_2^{*2} for EPR signals of VZrAlON-0.1 and -0.5

Spin Hamiltonian parameters of EPR spectra of VZrAlON-0.1(Al/Zr = 1.5)									
type of site	V_{single}						V_{poly}	defect	Intensity ratio
parameters	$A_{\parallel}$ [G]	$A_{\perp}$ [G]	$g_{\parallel}$	$g_{\perp}$	$\Delta g_{\parallel}/\Delta g_{\perp}$	β_2^{*2}	g_{iso}	g_e	$C_S : C_P$
untreated, RT	175.9	53.9	1.936	1.962	1.65	0.71	1.956	-	1 : 16.2
air/NH_3, 350 °C, 180 min	176.0	54.9	1.935	1.968	1.94	0.70	1.957	-	1 : 10.1
feed, 350 °C, 10 min	181.2	68.0	1.927	1.972	2.51	0.64	1.972	-	1 : 7.7
feed, 350 °C, 60 min	187.2	65.8	1.923	1.978	3.20	0.69	1.977	-	1 : 7.1
air/NH_3, 350 °C, 60 min	176.9	55.2	1.935	1.968	1.94	0.70	1.958	-	1 : 6.4
N_2, 350 °C, 60 min	176.6	57.8	1.933	1.970	2.14	0.68	1.971	-	1 : 8.9
RT, post in situ experiment	176.5	53.1	1.939	1.962	1.58	0.72	1.957	-	1 : 8.8

Spin Hamiltonian parameters of EPR spectra of VZrAlON-0.5 (Al/Zr = 1.5)									
type of site	V_{single}						V_{poly}	defect	Intensity ratio
parameters	$A_{\parallel}$ [G]	$A_{\perp}$ [G]	$g_{\parallel}$	$g_{\perp}$	$\Delta g_{\parallel}/\Delta g_{\perp}$	β_2^{*2}	g_{iso}	g_e	$C_S : C_P : C_D$
untreated, RT, S_1 (Zr)	193.6	61.4	1.920	1.968	2.41	0.75	1.975	2.00	$1.0 : 12.4 : 1.49 \cdot 10^{-2}$
untreated, RT, S_2 (Al)	180.3	72.2	1.930	1.966	2.01	0.61	-	-	$C_{S_1} : C_{S_2} = 1 : 1.6$
air/NH_3, 350 °C, 60 min	181.3	63.8	1.921	1.976	3.10	0.66	1.972	2.00	$1.0 : 13.9 : 2.57 \cdot 10^{-3}$
feed, 350 °C, 10 min	181.8	63.5	1.921	1.975	2.93	0.66	1.973	2.00	$1.0 : 11.4 : 2.82 \cdot 10^{-3}$
feed, 350 °C, 60 min	183.3	64.5	1.920	1.976	3.10	0.67	1.973	2.00	$1.0 : 16.0 : 2.30 \cdot 10^{-3}$
air/NH_3, 350 °C, 60 min	183.6	63.7	1.920	1.973	3.10	0.67	1.973	2.00	$1.0 : 13.7 : 2.54 \cdot 10^{-3}$
N_2, 350 °C, 60 min	176.2	63.0	1.914	1.972	3.28	0.65	1.970	2.00	$1.0 : 15.0 : 1.00 \cdot 10^{-2}$
RT, post in situ experiment	181.9	60.5	1.921	1.973	2.73	0.69	1.962	2.00	$1.0 : 10.7 : 3.15 \cdot 10^{-3}$

Table 3.6.: Characteristic parameters of VO^{2+} species found in EPR spectra of V containing solids

sample	$A_\parallel$ [G]	$A_\perp$ [G]	$g_\parallel$	$g_\perp$	$\Delta g_\parallel/\Delta g_\perp$	β_2^{*2}
VO_x/ZrO_2 [100] impregnation	188.0	64.0	1.926	1.979	3.27	0.70
VO_x/ZrO_2 [101] slurry method	179.6	64.5	1.925	1.977	3.05	0.65
VO_x/ZrO_2 [101, 102] impregnation	185.6	61.2	1.930	1.979	3.10	0.71
K-doped VO_x/ZrO_2 [103] impregnation, non-calcined	186.2	62.5	1.925	1.974	2.70	0.70
VZrON-0.25 [7] co-precipitation, nitridation	182.4	61.9	1.940	1.980	2.79	0.70
VO_x/Al_2O_3 [104] impregnation, as received, monolayer	191.0	63.0	1.942	1.974	2.1	0.75
VO_x/Al_2O_3 [104] impregnation, reduced, monolayer	179.0	73.0	1.947	1.950	1.1	0.63
VO_x/Al_2O_3 [104] impregnation, as received, doublelayer	194.0	66.0	1.938	1.979	2.8	0.75
VO_x/Al_2O_3 [104] impregnation, reduced, doublelayer	181.0	78.0	1.946	1.953	1.1	0.61
VO_x/γ-Al_2O_3 [105] impregnation, reduced	177.0	63.0	1.933	1.975	2.54	0.65
$AlVO_x$ [107] citrate-method	177.9	56.9	1.935	1.969	2.00	0.70
2.5 wt.-% V_2O_5/Al_2O_3-ZrO_2 [106] impregnation	196.0	71.0	1.972	1.989	2.28	0.76
20 wt.-% V_2O_5/Al_2O_3-ZrO_2 [106] impregnation	177.0	61.3	1.986	1.989	1.23	0.72

an oxidation state close to + 5. Simultaneously, the concentration of the defect signal decreases and the remaining isolated site S_2 possesses an outstanding high $\Delta g_\perp/\Delta g_\parallel$ ratio indicating that the axial distortion increases for VO^{2+} site in S_2. This suggests that N sites in the equatorial plane of VO^{2+} in S_2 are partly transformed by heating the catalyst in air/NH_3 to 350 °C leaving to NH_x sites. The anionic defects being linked to V^{5+} sites might be replaced by O^{2-} or NH_x.

In Fig. A.6 A and B the impact of adding water to the air/NH_3 stream at 350 °C on the EPR signals is depicted. When adding water to the air/NH_3 stream at 350 °C almost no changes on the EPR signals can be observed for both samples. Also for VAlON catalysts it was observed that water has no impact on the catalytic performance or catalyst structure [7, 8].

As opposed to this, when switching to the complete feed including 3-PIC for both catalysts, VZrAlON-0.1 and VZrAlON-0.5, the EPR signal intensities increase with time (see Fig. 3.11

A and B) and decrease again when switching the 3-Pic component off (see Fig. 3.12 A and B). This points to the reducing impact of 3-PIC. Remarkably, the hfs signal is more pronounced in the EPR spectra of VZrAlON-0.1, indicating that the percentage of isolated VO^{2+} sites is much higher in this sample under working state than for the sample with V/(Al+Zr) = 0.5. Interestingly, only for VZrAlON-0.1 the hfs parameters are slightly changed under working state, while those of VZrAlON-0.5 stay almost the same (see Tab. 3.5).

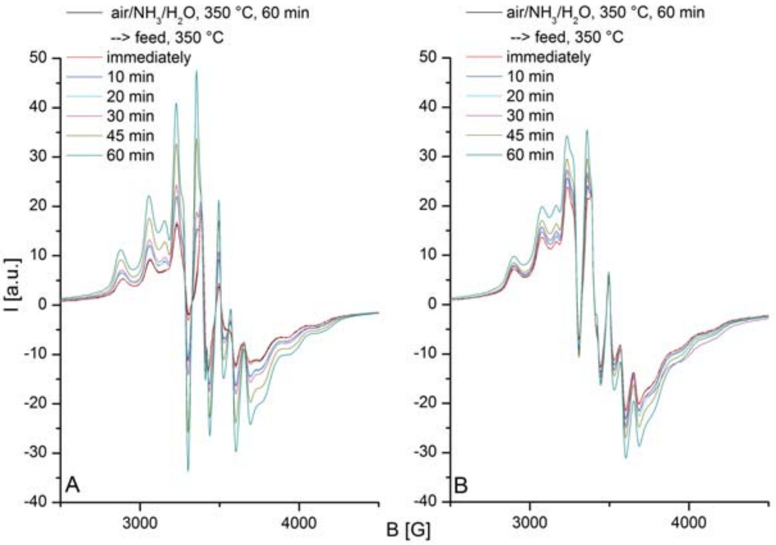

Figure 3.11.: EPR signals for VZrAlON derived under feed conditions at 350 °C with time on stream; A) VZrAlON-0.1; B) VZrAlON-0.5

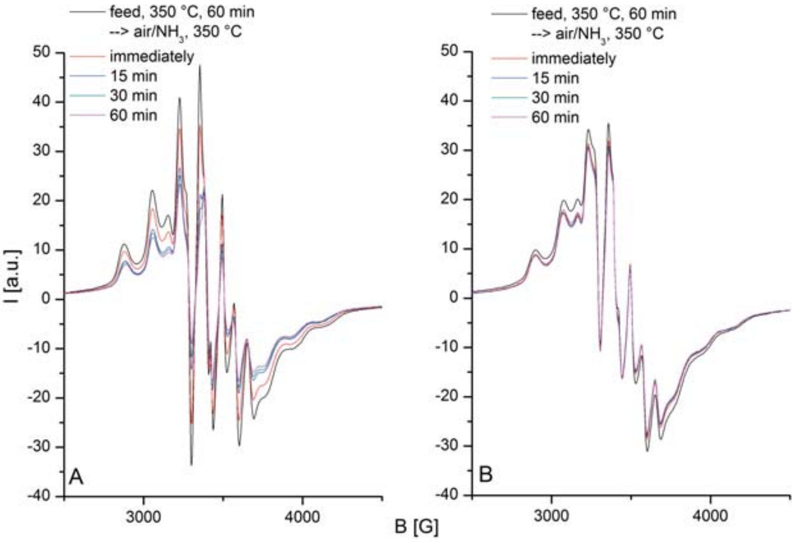

Figure 3.12.: EPR signals for VZrAlON derived after stopping 3-PIC stream at 350 °C; A) VZrAlON-0.1; B) VZrAlON-0.5

A comparison of the EPR signals derived at 350 °C under feed conditions for the VZrAlON series with Al/Zr = 1.5 is given as a function of the V/(Al+Zr) ratio for two different times on stream in Fig. A.7 A - B. In addition, their 2nd derivatives are shown in Fig. A.7 A' - B'. As indicated also by this comparison, the parallel components $A_{\|}$ and $g_{\|}$ of the hfs signal change stronger with time on stream at low V/(Zr+Al) ratios (see also Tab. 3.5). This implies that the V=O bond of the VO^{2+} sites seems to be prone to the reaction stream in the sample VZrAlON-0.1. Thus it seems that the higher the amount of V in VZrAlON catalysts the lower the degree of V=O distortion under working state. Indeed, from Tab. 3.5 it is evident that the structure of VO^{2+} sites in catalyst with the lowest V/(Al+Zr) ratio seems to be less distorted at RT and at elevated temperatures under air/NH_3. Not until switching to the entire feed composition, $\Delta g_{\|}/\Delta g_{\perp}$ increases significantly from 1.70 to 3.20 with time on stream for the latter sample. When switching off the 3-PIC component in the feed the distortion of VO^{2+} sites is only reversible for VZrAlON-0.1, but not for VZrAlON-0.5 sample. This implies that the distortion of VO^{2+} sites in the VZrAlON-0.1 catalyst is mainly introduced in the course of the ammoxidation reaction, possibly due to a reversible adsorption of 3-PIC on VO^{2+} sites.

When switching finally from air/NH_3 to N_2, the EPR signal intensity stays almost the same for both samples (see Fig. A.8). As it is evident from Tab. 3.5 the composition and structure of paramagnetic sites of VZrAlON-0.5 changes again. While the hfs of the perpendicular component of VO^{2+} sites stays almost the same, it can be seen that the hfs of the parallel component changes. This suggests that transient vacancies are formed close to the coordination sphere of VO^{2+} since NH_3 and O_2 are missing in the gaseous stream. Additionally, the sharp signal for the defect site (related to V^{5+} species) becomes more pronounced in the EPR signal. The increase of this defect signal intensity upon switching from air/NH_3 to N_2 might be due to the fact that paramagnetic oxygen is missing in the stream and therefore the magnetically interaction between O_2 and the defect site diminishes. This implies that defect sites are indeed located on the surface of the VZrAlON-0.5 catalyst.

Conclusively, results of in situ investigations clearly indicate that the two catalysts VZrAlON-0.1 and -0.5 work differently during ammoxidation due to the fact that they expose already initially different types of N and V containing sites on their surface. Although X_{3-PIC} is close to 100 % for VZrAlON-0.5 and about 32 % higher than for VZrAlON-0.1 (360 °C, GHSV = 2713 h^{-1}), the latter catalyst is significantly less selective. This might be due to the fact that the catalyst VZrAlON-0.1 provides initially only N-free V containing sites on its surface. This is not only proved by EPR results, but also by results from XPS. The nitridation of the VZrAlO-0.1 oxide precursor does not lead to the formation of surface N^{3-} species or defect sites. Defect sites and N^{3-} surface species are detected only in a significant concentration for the fresh

VZrAlON-0.5 catalyst. These nitride sites are located near to the VAl containing species while VZr containing sites seems to be free of nitride-like sites. Although these N^{3-} anions are missing after ammoxidation for the latter catalyst, it seems that, thanks to their introduction by nitridation, defect sites in the near coordination sphere of V^{5+} sites are formed, which might be replaced by O or/and N containing species originating from the gas phase during the ammoxidation. Due to the loss of N^{3-} in the course of ammoxidation additional transient vacancies might be formed, which might be also refilled in a sense of a double Mars-van Krevelen mechanism by O and/or N containing species. This is also supported by the fact that two N sites are detected by XPS for the used VZrAlON-0.5 catalyst, but not for the used VZrAlON-0.1 catalyst. This suggests that these transient formed vacancies are refilled by both, O and N sites, which originate from the gas feed. At least it is clear that the defect concentration is much higher for VZrAlON-0.5 than for VZrAlON-0.1. Finally, these effects might lead to the outstanding better selectivity of the VZrAlON-0.5 in comparison to the VZrAlON-0.1 catalyst.

3.1.4. Conclusions on VZrAlON catalysts in relation to VZrON and VAlON

The combination of VZrON and VAlON oxynitrides to VZrAlON leads to a new material with androgynous properties with respect to the structural and catalytic characteristics.

Compared to VZrON catalysts, S_{3-CP} could be significantly improved at T_B = 360 °C, but also a loss of X_{3-PIC} was observed. Compared to VAlON catalysts, VZrAlON catalysts are more active and slightly more selective at T_B = 360 °C (see Fig. 3.2). By investigating the catalytic performance of VZrON and VZrAlON as a function of T_B, it can be concluded that VZrAlON catalysts provide improved catalytic performance. In contrast to VZrON catalysts, S_{3-CP} is almost constant over a wide T_B range for VZrAlON catalysts, so that at $T_B > 360$ °C the conversion is continuously increasing at almost constant selectivity. The latter trend was also observed for VAlON catalysts, but not for VZrON catalysts [7].

Interestingly, structural investigation showed that VZrAlON catalysts are completely X-ray amorphous before and after use in ammoxidation. This was also observed for VAlON catalysts, but not for VZrON catalysts, in which a significant amount of crystalline ZrO_2 could be detected. Hence, by combining Al and Zr, the formation of crystalline ZrO_2 can be suppressed indicating that the fraction of Zr, being a part of the highly disturbed V containing network, is much higher in VZrAlON materials than in VZrON. Moreover, by combining Zr and Al different N containing sites could be detected in the near surface region by XPS. While VZrON catalysts possess an almost N-free surface despite a high bulk N content, VAlON catalysts provide nitrogen on the surface in form of nitride sites N^{3-} [8].

For VZrAlON catalysts with V/(Al+Zr) $\geq$ 0.25 three different N containing sites could be initially detected by XPS. Results of EPR spectroscopy and XPS suggest that the mean V surface oxidation state of VZrAlON catalysts ranges between those found for VAlON and VZrON catalysts. Furthermore, a strong VO_x site polymerization observed for VZrON catalysts is suppressed by combining VAlON and VZrON materials. This might contribute to the improved selectivity for mixed VZrAlON catalysts. Moreover, the enrichment of V in the bulk increases with rising V/(Zr+Al) ratio. The latter trend was also observed for VAlON, but not for VZrON materials [7, 8]. All catalyst classes VZrON, VAlON and VZrAlON are mainly free of surface acid sites as proved by adsorption and desorption experiments using FTIR spectroscopy and pyridine as probe molecule.

By in situ EPR spectroscopy under ammoxidation and nitridation conditions a novel structural property could be identified for VZrAlON catalysts which was not observed for VZrON or VAlON catalysts. A significant concentration of paramagnetic defects (probably F centers) could be identified for catalysts with V/(Al+Zr) $\geq$ 0.25, which seems to be related to V^{5+} species in VZrAlON and which participate during ammoxidation. Results of in situ nitridation and XPS suggests that these defects are introduced beside nitride-like sites during nitridation. Additionally, XPS and in situ EPR investigations showed that in fact N^{3-} anions are released under ammoxidation conditions, but the resulting transient vacancies as well as paramagnetic defects might be quickly refilled by O and/or N containing sites from the gas phase. In principle, by comparing the in situ results for VZrAlON-0.1 and VZrAlON-0.5 catalysts this process is only possible when initially a high concentration of N^{3-} sites are introduced into the coordination sphere of catalytically active V species.

Unfortunately, no further improvement of the catalytic performance could be observed when changing the V/(Al+Zr) ratio from 0.5 to 0.6 in the VZrAlON series so far. A dramatic reduction of the surface area might be the main reason for the observed decrease of X_{3-PIC}. Therefore, a systematic exploration of the synthesis parameters during nitridation and co-precipitation might be useful keeping a ratio of Al/Zr = 1.5; such a study could be helpful for a further improvement of the catalytic performance of VZrAlON catalysts.

3.2. VZrPON catalysts

As mentioned in section 2, it was assumed that the addition of P to VZrON might improve the selectivity of VZrON catalysts while maintaining their high activity. Since it was reported in literature that ZrPON materials with Zr/P = 0.9 possess a variety of different N sites on their surface [55, 74], it was decided also to adjust the P/Zr ratio to 0.9. The introduction of V into ZrPO in different concentration (V/Zr = 0.1 - 0.9) was realized by adding NH_4VO_3 to the synthesis of ZrPO, which was done according to literature by the citrate method [108]. The latter synthesis method requires a calcination step before nitridation to remove the carbon.

Thus, the impact of nitridation on structure and performance of the calcined oxide has been studied as well. The precalcined oxide are labeled VZrPO-x.x while the precalcined nitrided samples are called VZrPON-x.x in the following chapter. x.x denotes the V/Zr ratio. The structural and catalytic properties of VZrPON samples are compared with those of VZrPO and VZrON samples. In addition, structural data for the used VZrPON oxynitrides and used VZrPO oxides are discussed when needed. As already indicated, both the structure and the catalytic performance of VZrPO and VZrPON catalysts were investigated as a function of the V/Zr ratio whereby the Zr/P ratio was kept constant at 0.9.

3.2.1. Catalytic performance

In Fig. 3.13 the catalytic performances are plotted as functions of the V/Zr ratio for VZrPON and VZrPO catalysts. Additionally, the catalytic performance of the VZrON series is given [7, 8].

First of all, VZrPO and VZrPON catalysts with equal V content show identical conversion values, which pass through a maximum at a medium ratio of V/Zr = 0.56. S_{3-CP} for VZrPO catalysts is slightly higher than for the VZrPON catalysts at lower V content but falls below the selectivity of the latter at the highest V/Zr ratio. Compared to P containing VZrPON, the P-free VZrON catalysts are much more active at low V/Zr ratios while S_{3-CP} is comparable to that of VZrPON catalysts. Thus it turns out that the introduction of P into the VZrON structure does not lead to the desired improvement of the catalytic performance. This is surprising since, based on literature data over VPO catalysts, a positive effect on the catalytic performance was expected. Also a better selectivity of the VZrPO catalyst series compared to the VZrPON series is unexpected since it was assumed that nitridation leads to the formation of surface N sites, which can participate in the ammoxidation and lead to a better selectivity. However, catalytic data for VZrPON and VZrPO catalysts suggest that the introduced N sites in VZrPON catalysts carries no function during catalysis or/and are changed during ammoxidation.

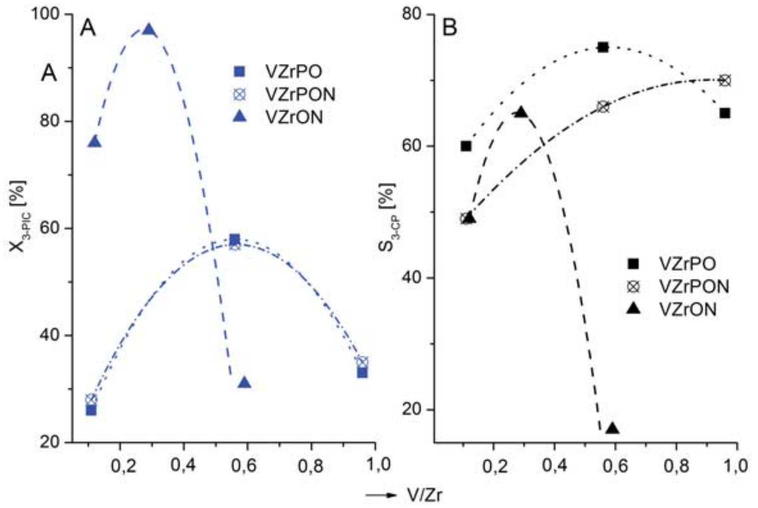

Figure 3.13.: Catalytic performance of VZrPO and VZrPON compared to VZrON at T_B = 360 °C; GHSV(VZrPO) = 3242 h^{-1}, GHSV(VZrPON) = 3242 h^{-1}; GHSV(VZrON) = 5728 h^{-1}

Therefore, additional catalytic studies of the best catalyst in the VZrPON series (VZrPON-0.53) were done to clarify whether VZrPON catalysts are changing under stream on time and whether this change is related to a structure change. The catalytic performance of this catalyst depending on the reaction time is depicted in Fig. 3.14 A.

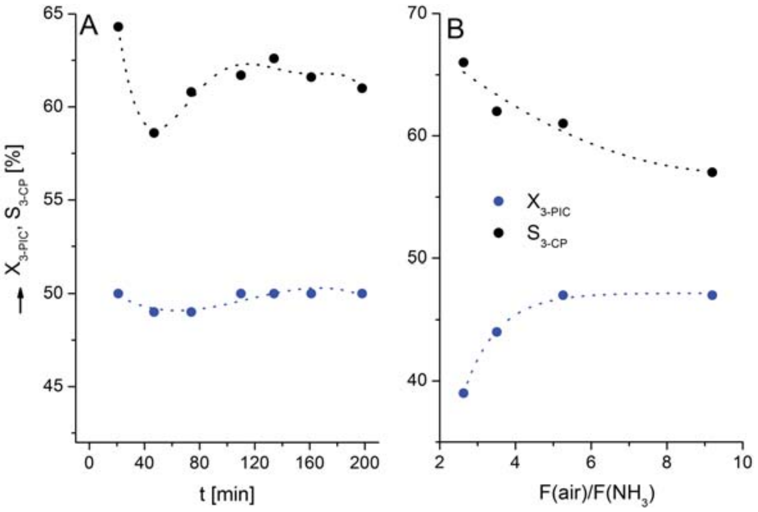

Figure 3.14.: Catalytic performance for VZrPON-0.53; A) As a function of time on stream at 360 °C; B) As a function of the flow ratio F(air)/F(NH_3) for a reaction time of ca. 1 h for each ratio

While X_{3-PIC} is nearly constant, S_{3-CP} is slightly changing with time on stream. Starting from 65 %, S_{3-CP} drops after 40 min to a minimum of 59 % and returns afterwards to ca. 62 %. Apparently, the structure of the VZrPON catalyst is changing during the initial reaction period. This already indicates that the nature or/and the relative concentration of surface N sites is rapidly changed during the initial reaction period.

Moreover, the variation of the air/NH_3 ratio should clarify the impact of the gaseous NH_3 concentration on S_{3-CP} for VZrPON catalysts. In Fig. 3.14 B the catalytic performance of VZrPON-0.53 is depicted as a function of the air/ammonia feed ratio F(air)/F(NH_3). It can be seen that X_{3-PIC} increases with rising air content in the feed up to a ratio of F(air)/F(NH_3) = 5 and then remains virtually constant while S_{3-CP} decreases continuously upon lowering the NH_3 content. This shows clearly that a high NH_3 concentration is essential to maintain high selectivity while high activity is mainly related to a high oxygen content.

3.2.2. Structural characterization of VZrPON by ex situ analysis in comparison to VZrPO and VZrON

Chemical composition, BET surface areas and XPS The bulk compositions and surface areas S_{BET} of the fresh VZrPO and VZrPON catalysts are compared in Tab. 3.7. In addition, the N contents derived from CHN analysis for the fresh and used samples are listed in the latter table. Relevant bulk and surface ratios are shown in Tab. 3.8 whereby the surface ratios are given in brackets.

Table 3.7.: Surface areas S_{BET} and bulk compositions of fresh VZrPO and VZrPON samples in addition to N content given in wt.-% for fresh and used samples

sample	S_{BET} [m^2/g]	composition	N [wt.-%], fresh	N [wt.-%], used
VZrPO-0.1	192	$ZrV_{0.11}P_{1.18}O_{6.23}$	0	2.67
VZrPO-0.5	75	$ZrV_{0.56}P_{1.22}O_{7.86}$	0	1.86
VZrPO-0.9	52	$ZrV_{0.96}P_{1.19}O_{7.59}$	0	0.51
VZrPON-0.1	122	$ZrV_{0.11}P_{1.16}O_{6.71}N_{0.59}$	3.35	2.94
VZrPON-0.5	65	$ZrV_{0.56}P_{1.21}O_{6.15}N_{0.53}$	2.83	2.60
VZrPON-0.9	25	$ZrV_{0.97}P_{1.17}O_{7.40}N_{0.47}$	2.91	1.61

The Zr/P ratio in the fresh oxide series VZrPO is close to 0.9 as desired. This does not change by nitridation. Therefore, a loss of phosphorous via the formation of volatile phosphine during ammonia treatment does not occur at a nitridation temperature of 500 °C. [5] The Zr/P ratio on the surface is slightly lower than in the bulk for all fresh VZrPO and VZrPON samples indicating that P is slightly enriched on the surface. The Zr/V ratio is almost the same in the surface and in the bulk, except for VZrPO-0.1 and the corresponding oxynitride. In these samples V is enriched on the surface as reflected by a markedly lower Zr/V surface ratio.

---

[5] Fripiat et al. emphasized that at nitridation temperatures beyond 800 °C a release of P probably via PH_3 occur for ZrPON materials [55].

Table 3.8.: Relevant bulk and surface ratios for fresh and used VZrPO and VZrPON catalysts; values given in brackets: surface ratios

	fresh samples				used samples			
sample	Zr/V	Zr/P	N/V	N/P	Zr/V	Zr/P	N/V	N/P
VZrPO-0.1	9.10	0.84	0	0	-	-	-	-
	(5.88)	(0.76)	0	0	(2.26)	(0.81)	(1.20)	(0.36)
VZrPO-0.5	1.78	0.82	0	0	-	-	-	-
	(2.00)	(0.64)	0	0	-	-	-	-
VZrPO-0.9	1.04	0.84	0	0	-	-	-	-
	(0.86)	(0.62)	0	0	-	-	-	-
VZrPON-0.1	9.10	0.86	5.36	0.51	-	-	-	-
	(6.67)	(0.65)	(2.00)	(0.19)	(5.48)	(0.69)	(1.89)	(0.24)
VZrPON-0.5	1.78	0.83	0.95	0.44	-	-		-
	(1.74)	(0.63)	(0.71)	(0.26)	(1.65)	(0.67)	(0.78)	(0.32)
VZrPON-0.9	1.03	0.85	0.48	0.40	-	-	-	
	(1.25)	(0.61)	(0.43)	(0.21)	(1.03)	(0.64)	(0.55)	(0.34)

Remarkably, the total N content (see Tab. 3.7) and the N/V ratios in the VZrPON series decrease with rising V content, while the N/P ratios remain nearly constant (see Tab. 3.8). This suggests that P-O bonds may be more prone to nitridation than V-O bonds and incorporation of N into the VZrPO oxides is rather linked to the P content. Compared to the bulk N/V ratios, the surface N/V ratios of the fresh VZrPON catalysts are lower indicating that N is enriched to some extent in the bulk. Incorporation of N into the oxides does not only occur during nitridation but also upon using the VZrPO oxides directly as catalysts in the ammoxidation as can be seen in Tab. 3.7. As likewise observed for fresh VZrPON catalysts, the total N content decreases for the used VZrPO oxides with rising V content. In contrast to the oxides the VZrPON oxynitrides loose N during use in the ammoxidation. However, the remaining N concentration in the structure is still higher than in the used VZrPO samples. Additional results derived from XPS investigations on fresh and used VZrPO and VZrPON samples are given in Tab. 3.9.

Besides the binding energies E_B for each element ΔE_B and the percentage of nitrogen N are listed in this table too. In the XP spectra the P2p peak is found at a binding energy of ca. 132.6 eV for all samples, which is very similar to the E_B values in VPO compounds [109]. However, differences were observed for the N1s and V2p$_{3/2}$ peaks. The ΔE_B values are essentially the same for all fresh oxynitrides and amount to 14.1. A slight decrease in ΔE_B values from 14.1 to 13.6 is observed for the entire catalyst series VZrPON after use in the ammoxidation, which points to a slight increase in the surface V valence state from 4.0 to 4.3. ΔE_B values of fresh oxides VZrPO are also almost similar, ranging between 13.5 and 13.7 eV, which corresponds to a mean surface V valence state of ca. 4.3. From the comparison of the ΔE_B values of the fresh

Table 3.9.: Binding energies E_B and ΔE_B values for fresh and used VZrPO and VZrPON catalysts as a function of V/Zr ratio and the percentage of nitrogen N on the surface

sample	E_B [eV]				N [%]	ΔE_B [eV]
	O1s	P2p	$V2p_{3/2}$	N1s		
			Fresh catalysts			
VZrPO-0.1	530.4	132.6	516.7	-	-	13.7
VZrPO-0.5	530.4	132.6	516.8	-	-	13.6
VZrPO-0.9	530.3	132.7	516.8	-	-	13.5
VZrPON-0.1	530.0	132.6	515.8	400.4; 398.2	29.5; 70.5	14.2
VZrPON-0.5	529.8	132.6	515.6	400.9; 398.4	4.2; 95.8	14.1
VZrPON-0.9	529.8	132.7	515.7	400.6; 398.6	14.3; 85.7	14.1
			Used catalysts			
VZrPO-0.1	530.5	132.6	516.4	399.8	100	14.1
VZrPON-0.1	530.4	132.6	516.8	400.7; 398.8	51.3; 48.7	13.6
VZrPON-0.5	530.3	132.6	516.7	400.7; 399.0	67.9; 32.1	13.6
VZrPON-0.9	530.3	132.6	516.7	401.0; 399.6	45.5; 54.5	13.6

and used VZrPO-0.1 oxide with those of the corresponding VZrPON-0.1 oxynitride, it can be concluded that the surface of the oxide is slightly reduced during ammoxidation while that of the oxynitrides is slightly oxidized.

Two different XPS peaks were detected in the N1s region for all fresh and used VZrPON catalysts ranging from 400.4 - 401.0 and 398.2 - 399.6 eV, respectively. Fripiat et al. observed three different N1s peaks in ZrPON oxynitrides with Zr/P = 0.9 [110]. They assigned these peaks to nitride anions N^{3-} (397.7 eV), surface NH_x species with $1 \leq x \leq 4$ (399.2 eV), and NH_4^+ ions (400.4 eV). Based on this work, we attribute the peaks at 399.8 - 401.0 eV to NH_4^+ ions and the peaks at 398.2 - 399.6 eV to $-NH_2$ and/or -NH surface groups. Wiame et al. have studied the influence of nitridation temperature T_N on the nitrogen environment in VAlON catalysts using also XPS [91]. They found surface species of the latter type already at temperatures of T_N = 250 °C, while nitride species in the vicinity of V began to form only at 500 °C and their amount increased with rising T_N. In contrast to VAlON or VZrAlON catalysts [8], the formation of nitridic V-N surface species can be excluded since no peaks at typical binding energies like in VAlON or VZrAlON catalysts ($\approx$ 397.5 eV) are detected. Thus, it is likely that the second N surface site in VZrPON is rather connected to P or Zr which, however, does not change the position of the P2p peak. This may be due to the rather low amount of surface N species. The N/P surface ratio merely amounts to 0.19 - 0.34. This means that nominally only one of the four P-O bonds is replaced by P-N. Most probably this is not enough to cause a P binding energy shift that differs significantly from experimental error, which is 0.1 - 0.2 eV. Inspection of Tab. 3.9 shows that E_B values for the two N1s signals do not differ much for all fresh and used VZrPON catalysts; however their relative intensity changes. In general, the percentage of NH_x (x = 1 or/and 2) surface species dominates in the fresh VZrPON catalysts, in particular for higher V/Zr ratios, while the percentage of NH_4^+ species increases after use in the ammoxidation. Interestingly, the used oxide VZrPO-0.1 contains only NH_4^+ surface species reflected by a single N1s peak at 399.8 eV.

XRD, TEM and MAS NMR investigations Results obtained from XRD suggest that the structure of VZrPON oxynitrides differ significantly compared to P-free VZrON catalysts.

The powder patterns for fresh and used VZrPO and VZrPON are shown in Fig. 3.15 A - D.

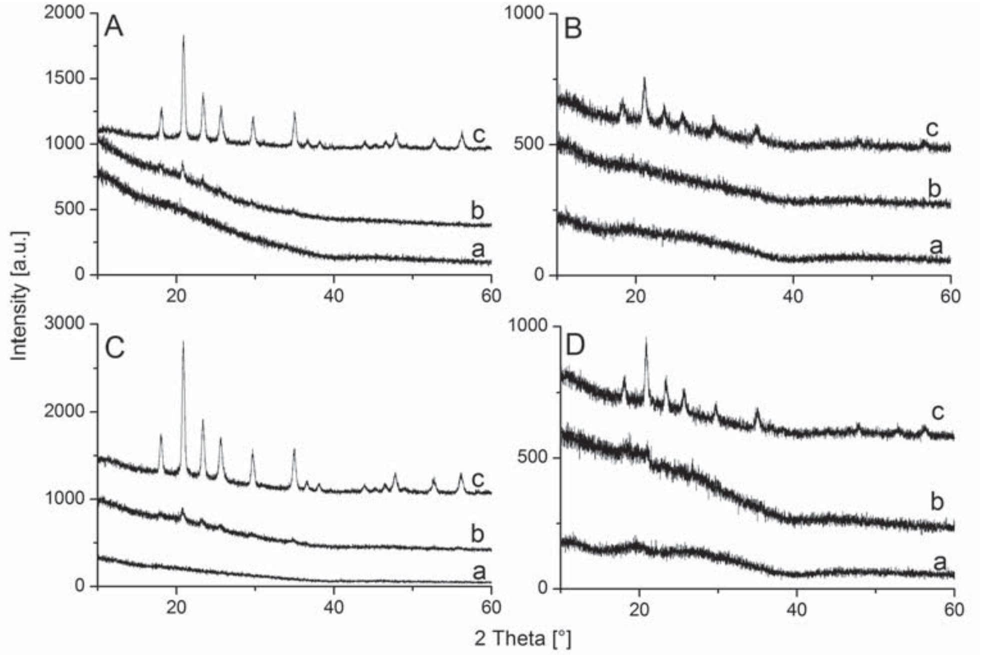

Figure 3.15.: Powder patterns for fresh and used VZrPO and VZrPON catalysts as a function of the V/Zr ratio; A) Fresh VZrPO; B) Fresh VZrPON; C) Used VZrPO and D) Used VZrPON; (a = 0.9; b = 0.5 and c = 0.1)

Below a ratio of 0.5 calcined VZrPO catalysts are almost X-ray amorphous. At a ratio higher than 0.5 the formation of a crystalline phase can be observed for VZrPO catalysts. Through nitridation of the oxides the reflection intensity of the latter crystalline phase decreases considerably. Hence, the crystalline phase is partly destroyed by the thermal ammonia treatment. The position and the intensity ratios of the detected reflections do not coincide with those of phases listed in the ICDD database. Nevertheless the position and the intensity ratio of the reflections suggest that the observed crystalline phase is related to the pure phases ZrV_2O_7 and ZrP_2O_7 (see assignment in Fig. A.9). Due to this relation it was assumed that the latter reflections might be caused by the solid solution $ZrV_{2-x}P_xO_7$.

Beside numerous publications on the binary ZrP_2O_7 and ZrV_2O_7 phases [111–115], only a few papers are published on the mixed phase $ZrV_{2-x}P_xO_7$ [116]. Nevertheless, MAS NMR spectroscopy was proved to be especially suitable to characterize the solid solutions $ZrV_{2-x}P_xO_7$.

Own MAS NMR results of the oxides and oxynitrides with V/Zr = 0.9 are summarized in Fig. 3.16. In the ^{31}P MAS NMR spectrum of VZrPO-0.9 two peaks can be seen. The signal at -28.9 ppm originates from V-O-P units, while the second signal at -41.7 ppm is caused by P-O-P bridges. Accordingly, the detected peak at -822 ppm in the ^{51}V MAS NMR spectrum can be assigned to V-O-P units [116]. The additional signal at -612 ppm is characteristic for V_2O_5 [117].

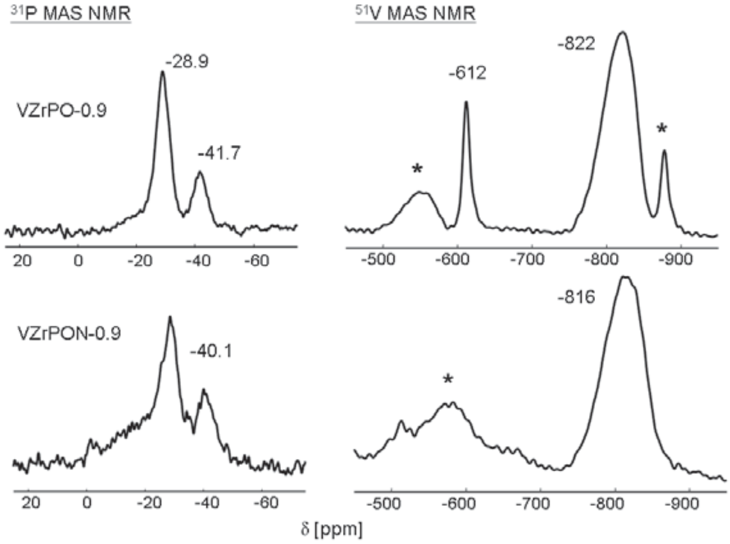

Figure 3.16.: ^{31}P (left) and ^{51}V (right) MAS NMR spectra for VZrPO-0.9 and VZrPON-0.9 at RT; *: spinning side bands

The latter phase was not observed in the conventional XRD powder pattern (see Fig. 3.15 A), but it can be well seen in the XRD pattern recorded using synchrotron radiation (see Fig. A.9) indicating that V_2O_5 has a nanocrystalline character. [6] In the MAS NMR spectrum of the corresponding nitrided sample VZrPON-0.9 the signal for V_2O_5 is missing. Reduced V sites are not visible by solid state NMR. This suggests that V_2O_5 has been reduced by the ammonia treatment. Despite a higher accumulation time for the measurements of the oxyitride, the intensity of the signal assigned to VPO_7^{4-} decreases in both the ^{31}P and ^{51}V spectrum. Additionally, a small shift of the ^{51}V signal from -822 to -816 ppm and of the ^{31}P signal from -41.7 ppm to -40.1 ppm can be seen by comparing the spectra of VZrPO and VZrPON.

---

[6] XRD patterns recorded at BESSY with synchrotron radiation provides a much higher sensitivity to nanocrystalline phases.

Also in the corresponding XRD pattern, a small shift of all reflections to higher theta values can be observed. These shiftings indicate a slight change of the unit cell of the crystalline phase and may originate from a structure, which possesses N sites. Moreover, TEM-EDX investigations on the VZrPO series were performed to confirm the presence of the $ZrVPO_7$ and to obtain information about the morphology of these samples. The results of this study are given in Fig. A.10 to Fig. A.12. In the image of VZrPO (V/Zr = 0.9) there are domains, in which lattice plans can be observed (see Fig. A.10). The local chemical composition in these domains detected by EDX has an atomic ratio of V:Zr:P = 1:1:1. Hence, the detected reflections in the pattern of VZrPO-0.9 originate certainly from the solid solution $ZrV_{2-x}P_xO_7$. Also for the oxide sample VZrPO-0.5 traces of the latter crystalline phase can be detected by TEM-EDX and XRD measurements (see Fig. A.11). For the oxide sample with the lowest V content (V/Zr = 0.1) no hints can be found for this phase using X-ray and TEM-EDX methods (see Fig. A.12 and 3.15).

Analysis of the structure and surface acidity by FTIR spectroscopy More detailed information about structural changes upon nitridation can be obtained by comparing the ATR spectra given in Fig. 3.17. Bands from 1500 - 1200 cm^{-1} (ν(P=O)), 1200 - 900 cm^{-1} (ν(P-O)) and 650 - 300 $cm-1$ (δ(O-P-O)) are characteristic for phosphorous oxide compounds [118].

The spectrum of the fresh VZrPO-0.1 sample shows a broad P-O band at 999 cm^{-1} (see Fig. 3.17 A, spectrum a). The V=O vibration being typical for vanadyl sites VO^{3+} is expected at around 1030 cm^{-1} [96] and can not be observed in the spectrum of the latter sample. The V content might be too low for this vibration. Only in the spectra of VZrPO-0.5 and -0.9 with markedly higher V content, the V=O vibration is superimposed on the P-O band. In the spectrum of VZrPO-0.5, additional bands appear below 1000 cm^{-1}, which can be considered as a fingerprint of the crystalline $ZrV_{2-x}P_xO_7$ phase. In agreement with XRD data given in Fig. 3.15, the bands of the latter phase become more pronounced for VZrPO-0.9, in which this phase is dominating. In principle, bands in this range arise from ν(M-O-M) vibrations [119, 120]. Thus, P-O-P bridging groups in sodium pyrophosphate $Na_4[P_2O_7]$ give rise to stretching vibrations ν_{as} = 915 cm^{-1} and ν_s = 730 $cm-1$ [121], while V-O-V units in sodium pyrovanadate $Na_4[V_2O_7]$ vibrate at ν_{as} = 710 cm^{-1} and ν_s = 533 cm^{-1} [122]. Based on these data, bands at 874 and 650 cm^{-1} for the spectra given in Fig. 3.17 A are assigned to ν(P-O-P) and those at 715 cm^{-1} and 533 cm^{-1} to ν(V-O-V) vibrations. The band around 800 cm^{-1}, which is especially strong in sample VZrPO-0.9 containing the mixed $ZrV_{2-x}P_xO_7$ as main component, may come from a V-O-P stretching mode.

The very weak band around 1620 cm^{-1} arises from a $\delta(H_2O)$ vibration. Thermal treatment in NH_3 gives rise to a new band at around 1430 cm^{-1}, which is typical for NH_4^+ species [123]

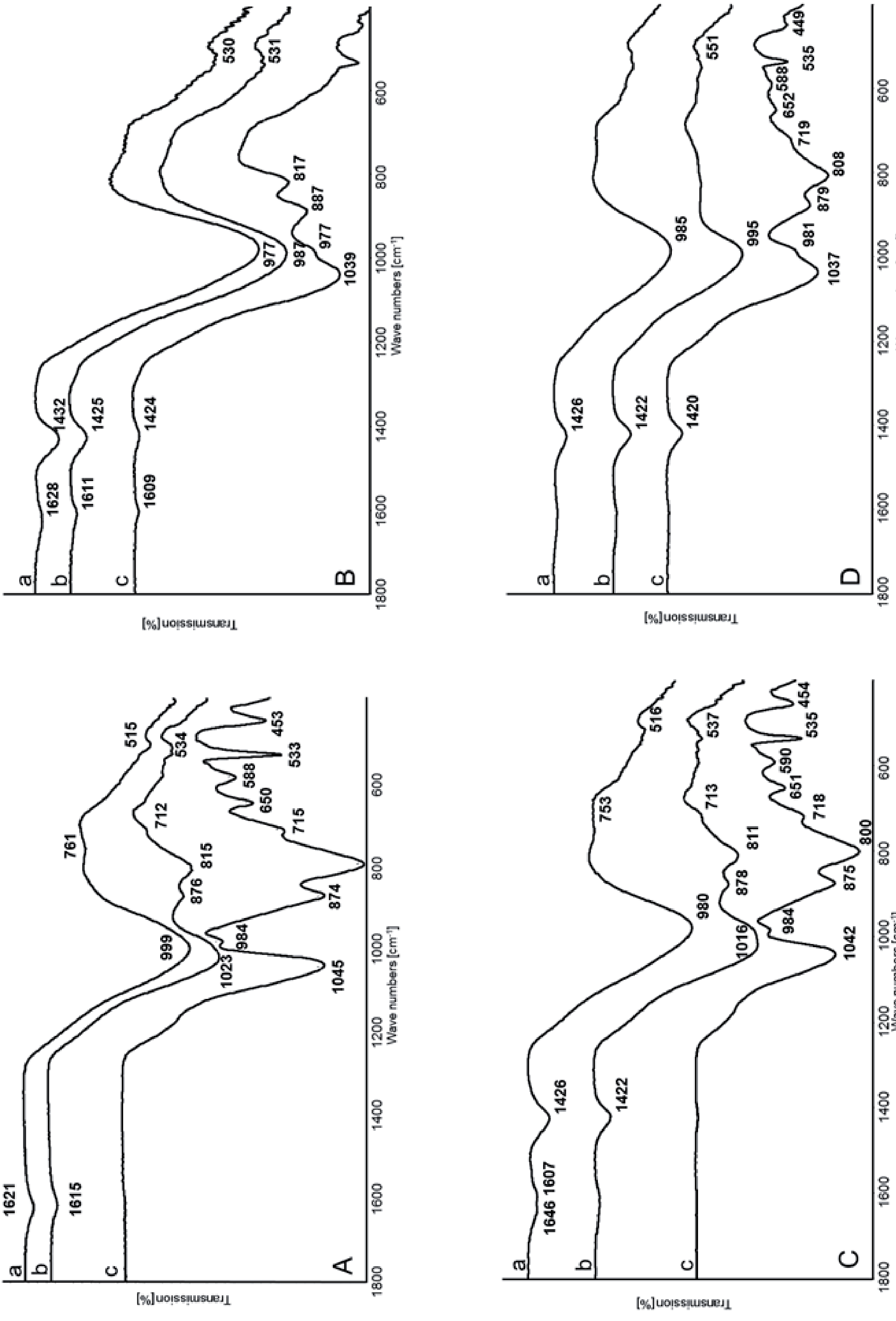

Figure 3.17.: ATR spectra of fresh VZrPO (A), fresh VZrPON (B), used VZrPO (C) and used VZrPON (D) catalysts depending on V/Zr ratio; a = 0.1, b = 0.5, c = 0.9

(compare spectra in Fig 3.17 B). Moreover, the bands assigned to the crystalline $\mathrm{ZrV}_{2-x}\mathrm{P}_x\mathrm{O}_7$ phase disappear completely in sample VZrPON-0.5 and widely in VZrPON-0.9, in agreement with XRD and MAS NMR data. For VZrPON-0.9, new bands at 977, 887 and 817 cm^{-1} can be observed, which presumably hide those of the residual crystalline $\mathrm{ZrV}_{2-x}\mathrm{P}_x\mathrm{O}_7$ phase. Obviously, the M-O-M sites (M = P and/or V) in the latter phase are splitted by nitridation, which makes the sample widely X-ray amorphous. Bands at 887 and 817 cm^{-1} may originate from condensed P-N units, while the shoulder at 977 cm^{-1} can be attributed to P-O(H) groups [118]. Possibly, P-O-M bonds (M = P or V) undergo ammonolysis according to the equation:

$$P-O-M \quad + \quad NH_3 \rightarrow P-NH_2 \quad + \quad HO-M. \tag{3.4}$$

The ATR spectra of all samples after use in the ammoxidation are shown in Fig. 3.17 C - D. By comparing the spectra of the VZrPO oxides before and after use it is clearly seen that position and shape of the bands do almost not change during treatment in the ammoxidation flow. The only difference is a NH_4^+ band that arises in the spectra at lower V concentration, but is hardly seen in the used sample VZrPO-0.9. Interestingly, the fingerprint of the crystalline $\mathrm{ZrV}_{2-x}\mathrm{P}_x\mathrm{O}_7$ phase is still well visible in the spectra of the used oxide with V $\geq$ 0.5, indicating a high stability of this phase under ammoxidation conditions. In the spectrum of the used VZrPON-0.9 sample, the $\mathrm{ZrV}_{2-x}\mathrm{P}_x\mathrm{O}_7$ fingerprint signals at 879, 808 and 719 cm^{-1} gain intensity after use (compare spectra c in Fig. 3.17 B and D), suggesting that this phase is restored during ammoxidation. Also bands of NH_4^+ at 1425 cm^{-1} appear again, but their intensities are almost equal in the series of used VZrPON catalysts and do not correlate with the V concentration.

To support the identification of different N containing sites in VZrPON series, additional FTIR spectra of self-supporting wafers for fresh VZrPON were recorded at 300 °C in vacuum. These spectra are given in Fig. 3.18.

For comparison, IR bands of phosphordiamidic acid used as reference are presented in Tab. B.1 [97].

On this basis, the band at 1558 cm^{-1} is assigned to P-NH_2 vibrations, while the band at 1420 cm^{-1} is typical for $\delta(\mathrm{NH}_4^+)$ vibration. This band has also been observed in the ATR spectra of fresh and used VZrPON samples recorded under ambient conditions. Moreover, the presence of NH_4^+ surface species is confirmed by the XPS results. No bridging P-NH-P unit can be identified, since bands around 3074 cm^{-1} are missing. Vibrations of doubly bound -P=N-P- units formed by condensation of neighbouring P-NH_2 and M-OH groups according to equation 3.5 are expected in a range from 1420 to 1250 cm^{-1} (ν_{as}) and 950 to 800 cm^{-1} (ν_s) [123].

$$P - NH_2 \quad + \quad HO - M \rightarrow -P = N - M \quad + \quad H_2O; \quad M \; = \; P \; or \; Zr. \qquad (3.5)$$

A band at 1372 cm^{-1}, which might arise from ν_{as} (-P=N-P-) vibrations, is well seen in the spectrum of sample VZrPON-0.9 (see spectrum c in Fig. 3.18). In agreement with XPS data, this suggests that N is preferentially incorporated in the vicinity of P.

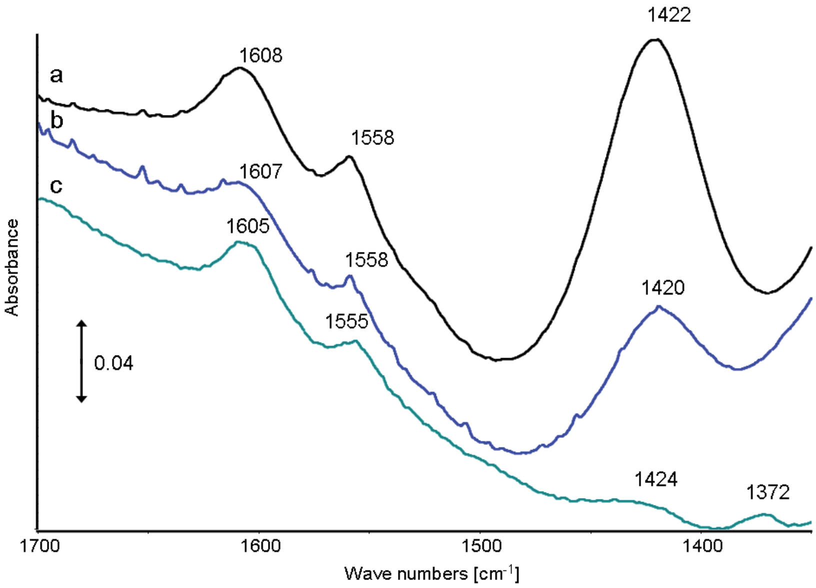

Figure 3.18.: FTIR spectra of fresh VZrPON catalysts with different V/Zr ratios measured in transmission mode at 300 °C in vacuum; a = 0.1, b = 0.5 and c = 0.9

The surface acidity of fresh and used VZrPO and VZrPON catalysts with V/Zr = 0.1 was investigated by adsorption of pyridine. Typical signals of Lewis and Brønsted surface sites could be detected at elevated temperature. However, even the relative quantification is not possible, since the characteristic band of Lewis acid sites at 1445 cm^{-1} in the fresh oxynitride VZrPON-0.1 is partly superimposed by a second broad band, which may be assigned to NH_4^+ sites (compare spectra given in Fig. A.13). For this reason, only the Brønsted band at 1545 cm^{-1} has been analyzed for evaluating surface acidity. The resulting relative band areas A$_B$ normalized on S$_{BET}$ at 1545 cm^{-1} are shown in Tab. 3.10 for the fresh and used oxide and oxynitride catalysts with V/Zr = 0.1.

From Tab. 3.10, it is evident that the number of Brønsted acid sites increases slightly during ammoxidation for both oxide and oxynitride catalysts. In general, the oxynitride samples possess more Brønsted acidic sites than the corresponding oxide catalysts. The higher concentration of Brønsted acidic sites for VZrPON compared to VZrPO might be a consequence of P-O-M bond breaking according to equation 3.4, which becomes more pronounced in the course of ammoxidation.

Table 3.10.: Relative concentration of Brønsted acid sites [a.u.] for fresh and used oxide and oxynitride with V/Zr = 0.1

Fresh sample	A_B/S_{BET}	Used sample	A_B/S_{BET}
VZrPO-0.1	8.9	VZrPO-0.1	16.8
VZrPON-0.1	12.6	VZrPON-0.1	27.8

3.2.3. In situ experiments

Nitridation of VZrPO catalysts followed by coupled in-situ-EPR/Raman/UV-Vis spectroscopy

To gain more detailed insight in the structural changes during nitridation, calcined VZrPO oxides were additionally investigated by coupling EPR, UV/Vis and Raman spectroscopy in situ at elevated temperatures. By coupling these spectroscopic techniques changes of the V oxidation state and chemical environment can be followed simultaneously during nitridation.

The nitridation was investigated in situ for VZrPO samples with V/Zr ratios ranging from $0.1 \leq x \leq 0.9$.

First of all, samples were heated in N_2 at 120 °C for 90 min, followed by a treatment in a diluted NH_3/N_2 stream at a maximum temperature of 410 °C. However, spectra were measured at RT before any treatment as well as after treatment in N_2 and NH_3/N_2 flow and cooling in the same atmosphere, since this led to spectra with higher quality.

In Fig. 3.19, normalized EPR spectra are presented to visualize changes of the spectral shape. The as-received intensities are given in form of their double integrals A_{EPR} written on the right side of each EPR spectrum. All spectra show a well-resolved hfs which arises from isolated VO^{2+} sites in square-pyramidal or octahedral coordination. Two single VO^{2+} species labeled with S_1 and S_2 and a broad isotropic singlet caused by cluster-like magnetically interacting VO^{2+} sites denoted as C must be superimposed to reproduce the experimental EPR spectra (see Tab. 3.11). A comparison of the experimental and simulated spectra is given in Fig. A.14. Spin Hamiltonian parameters for both isolated sites in sample VZrPO-0.1 before any treatment (spectrum a in Fig. 3.19) and for all VZrPO samples after heating in NH_3/N_2 flow are listed in Tab. 3.11. Additionally the parameters $\Delta g_{\|}/\Delta g_{\perp}$ and β_2^{*2} are given, as well as the intensity ratios of the single and cluster site signals, $S_1 : C : S_2$.

For the untreated oxides the double integral intensities A_{EPR} increase with rising V content as expected (see spectra a-c in Fig. 3.19). However, the signal intensity grows strongly after treatment in NH_3/N_2 flow, which goes along with an increase in the relative contribution of the cluster signal. Interestingly, the gain in total intensity upon switching from N_2 to NH_3/N_2 flow, which reflects the reduction of V^{5+} to V^{4+} is most pronounced for the sample with the lowest V content VZrPO-0.1, while it is almost negligible for VZrPO with the highest V content VZrPO-0.9. The reason might be, that the partial reduction of V to EPR-silent V^{3+} occurs with rising V concentration. This is also supported by UV/Vis data, which will be discussed later.

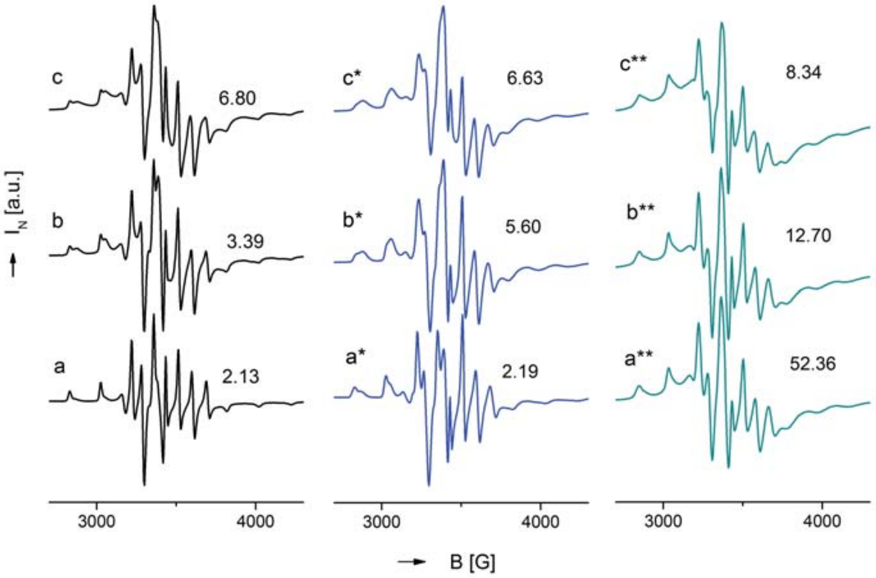

Figure 3.19.: Normalized in situ EPR spectra of VZrPO oxides with different V/Zr ratios (a = 0.1, b = 0.5 and c = 0.9) measured at RT; a-c: untreated VZrPO; a*-c*: after heating in N_2 for 90 min at 120 °C; a**-c**: after heating in NH_3/N_2 for 30 min at 410 °C; numbers: A_{EPR} derived by double integration of the experimental EPR signal

Spin Hamiltonian parameters of the two isolated VO^{2+} species provide more information about the local environment. The g and A parameters of species S_1 are very close to those of partially reduced $VOPO_4 \cdot 2H_2O$ [124, 125], containing single VO^{2+} defects ($g_{\|}$ = 1.938, $g_{\perp}$ = 1.982, $A_{\|}$ = 192 G and $A_{\perp}$ = 69 G). The structure of the latter vanadyl site consists of VO_5 chains linked via PO_4 tetrahedral resulting in polymeric $(VOPO_4)_n$ layers.

The axial geometry of the second isolated VO^{2+} species S_2 in VZrPON-0.1 is less distorted, as can be concluded from the smaller $\Delta g_{\|}/\Delta g_{\perp}$ ratio. The spin Hamiltonian parameters of this site are similar to those derived for the corresponding P free VZrON catalysts ($g_{\|}$ = 1.940, $g_{\perp}$ = 1.980, $A_{\|}$ = 182.4 G and $A_{\perp}$ = 69.9 G). Therefore, species S_2 might be attributed to isolated VO^{2+} sites connected via oxygen bridges to Zr rather than to P. From Tab. 3.11, it is evident that the two isolated species S_1 and S_2 are equally abundant in the untreated sample VZrPO-0.1, while the intensity of species S_2 decreases in relation to that of species S_1 in VZrPON-0.1 after

Table 3.11.: Spin Hamiltonians for EPR signals of in situ formed VZrPON catalysts and VZrPO-0.1

EPR spectrum	VZrPO-0.1 (a)		VZrPON-0.1 (a**)		VZrPO-0.5 (b**)		VZrPON-0.9 (c**)	
species	S_{1a}	S_{2a}	S_{1a**}	S_{2a**}	S_{1b**}	S_{2b**}	S_{1c**}	S_{2c**}
$A_{\|\|}$ [G]	202.3	198.5	192.8	181.8	190.5	184.4	188.0	188.5
$A_{\perp}$ [G]	74.1	69.5	69.0	54.4	68.7	53.9	67.3	53.8
$g_{\|\|}$	1.923	1.933	1.937	1.939	1.940	1.938	1.942	1.939
$g_{\perp}$	1.978	1.976	1.981	1.972	1.981	1.972	1.981	1.971
$\Delta g_{\|\|}/\Delta g_{\perp}$	3.26	2.63	3.08	2.09	2.98	2.12	2.83	1.98
β_2^{*2}	0.73	0.75	0.72	0.74	0.71	0.76	0.70	0.79
$S_1 : C : S_2$	1 : 3.7 : 1		1 : 5.1 : 0.8		1:11.6:0.7		1 : 18.9 : 0.6	

NH_3 treatment. This suggests that VO^{2+} species connected to Zr (site S_2) are easier reduced to EPR silent V^{3+} than those connected to P (site S_1) during nitridation.

With rising V content, $A_{||}$ parameters of site S_1 and site S_2 become more similar and finally converge to $\approx$ 188 G for the sample VZrPO-0.9. The latter sample contains P, V and Zr in almost equal amounts. Given that a rather homogeneous distribution of V is established throughout the structure, this would imply that both V sites S_1 and S_2 should be connected via oxygen bridges to both P and Zr. This may average to some extent the differences in their local environment.

Comparing $\Delta g_{||}/\Delta g_{\perp}$ and β_2^{*2} values of VZrPON with those of VAlON catalysts [7] or VZrAlON catalysts possessing V-N bonds, significant differences are evident for nitrided VZrPON samples. This suggests that a partial substitution of V-O by V-N moieties observed for VAlON and VZrAlON (see Tab. 3.5) can be excluded for VZrPON catalysts. In other words, the first coordination sphere of V sites in the latter catalysts is most probably almost N^{3-} free. This agrees properly with results of XPS and FTIR spectroscopy, which also suggest that N might be preferentially linked to P and not to V sites.

UV/Vis spectra after treatment in N_2 recorded along with the EPR spectra are shown in Fig. 3.20 A. All three spectra of VZrPON samples are characterized by a broad band in the low wavelength range caused by CT transitions of V^{5+} [96, 126–130]. The adsorption edge energy E_g additionally given in Fig. 3.20 decreases with rising V content in the VZrPO series.[8] As expected, this points to increasing formation of vanadyl clusters, which is also evident from the broad isotropic signal in the EPR spectra of magnetically interacting cluster-like VO^{2+} sites. Upon heating in an NH_3/N_2 flow, the intensity of the CT below 400 nm decreases while it rises strongly in the visible range above 500 nm, where d-d transitions of V^{3+} and V^{4+} sites are expected (see Fig. 3.20 B) [96, 126–130]. It is clearly seen, that the increase in absorbance above 500 nm is highest for

---

[7] Values of VAlON-0.5 samples were found to be β_2^{*2} = 0.67 - 0.69 and $\Delta g_{||}/\Delta g_{\perp}$ = 3.30 - 3.46.

[8] The absorption edge energy E_g for this transition was determined by finding the intercept of the straight line in the low-energy rise of a plot of $[F(R)h\nu]^2$ against $h\nu$, where $h\nu$ is the incident photon energy.

the sample VZrPO-0.9 with the highest V content. This suggests a stronger reduction during nitridation. Most probably, this leads to a certain percentage of EPR silent V^{3+}, beside EPR visible V^{4+}.

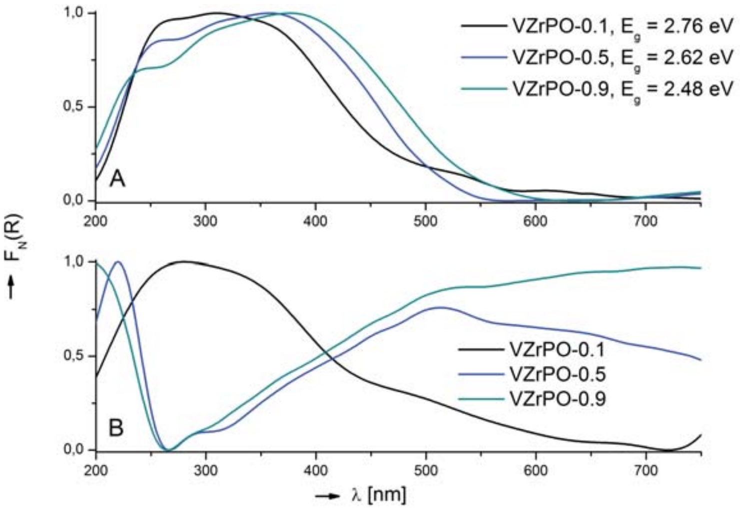

Figure 3.20.: Normalized in situ UV/Vis spectra measured at RT for VZrPO oxides as a function of V/Zr ratios; A) After heating in N_2 flow for 90 min at 120 °C; B) After heating in NH_3/N_2 flow for 30 min at 410 °C

In situ Raman spectra recorded along with EPR and UV/Vis spectra are plotted in Fig. A.15 only for the sample VZrPO-0.9 with the highest V content before and after treatment in NH_3/N_2 flow, since for the other samples the signal-to-noise ratio was not sufficient. Bands at 994, 702, 525, 486, 405 and 285 cm^{-1} are assigned to nanocrystalline V_2O_5, which are obviously to small to be detected by XRD (see Fig. 3.15), but can be seen using ^{51} MAS NMR spectroscopy (see Fig. 3.16). Bands at 883 and 817 cm^{-1} may be assigned to V-O-P vibrations, while the signal at 1045 cm^{-1} might originate from V=O vibrations of single V^{5+} species. Most probably these bands belong to the crystalline $ZrV_{2-x}P_xO_7$ phase. By comparing the Raman spectra in Fig. A.15 it can be concluded, that the intensities of all bands decrease during NH_3 treatment. This is caused by reduction of V^{5+}. However, it is also seen, that the bands of V_2O_5 nanocrystals decrease faster than those of $ZrV_{2-x}P_xO_7$, indicating that the latter phase is more stable against reduction by NH_3.

3.2.4. Structure-reactivity relationships in VZrPON catalysts

Compared to VZrON catalysts, an improvement of the catalytic performance was not reached by adding P into VZrON catalysts. The highest achievable conversion of 3-PIC obtained over

VZrPON catalysts is only about half as high, while S_{3-CP} of VZrPON-0.9 exceeds that of the best P-free VZrON-0.25 catalysts only slightly.

Marked structural changes caused by incorporation of P might be responsible for this different catalytic behavior. This is confirmed by a variety of characterization methods. For VZrON catalysts, a pronounced formation of crystalline ZrO_2, though containing some dispersed V sites in Zr lattice positions, forces agglomeration of the majority of V within V_xO_y clusters in which V takes markedly higher mean valence state. Moreover, the surface of the P free VZrON catalysts remained essentially free of N, since the latter was almost completely enriched in the bulk structure. The incorporation of P leads first of all to higher dispersion of V in VZrPON oxynitrides. This is shown by the EPR spectra, which possess a well resolved hfs at each V/Zr ratio. Moreover, the formation of a crystalline $ZrV_{2-x}P_xO_7$ phase suppresses the agglomeration of VO_x species. This phase, in which V is tetrahedrally coordinated by O, is confirmed by results derived from XRD, TEM-EDX, MAS NMR and ATR spectroscopy. Both effects, high V site isolation and low O coordination, are known to diminish catalytic activity but improve selectivity in selective oxidation reactions [131, 132]. Additionally, a high percentage of V^{5+} increases activity, though at the expense of selectivity, while deep reduction to V^{3+} deactivates ammoxidation catalysts [40]. Coupled in-situ-EPR/UV-Vis results suggest that in the VZrPON-0.9 catalyst with the highest V content, a marked reduction to inactive V^{3+} takes place during nitridation, which might account for the drop in activity compared to VZrON catalysts. Surprisingly, the selectivity values are not much higher than for VZrON catalysts at low V content. This suggests that factors other than V dispersion might govern the 3-CP selectivity. For VZrON and VAlON oxynitrides, the close vicinity of V and N sites within V-N-M moieties (M = Al or Zr) as well as negligible surface acidity was found to be beneficial for the high catalytic performance, besides high V dispersion. While V sites are highly dispersed also in VZrPON and VZrPO catalysts, XPS, FTIR and EPR results suggest that N in these catalysts, although being present on the surface, is preferentially linked to P but not incorporated in the vicinity of V. This possibly disfavors a concerted oxidation/N-insertion mechanism catalyzed by -O-V-N-M-O- sites, which might lower the 3-CP selectivity.

Comparing VZrPO and VZrPON catalysts, initially N free VZrPO oxides take up N when exposed to ammoxidation conditions, while the corresponding VZrPON catalysts loose N under the same conditions. A similar effect has been observed by Florea et al. for VAlO and VAlON catalysts in the ammoxidation of propane [2, 3, 91]. In their experiments, the equilibrated N content established during reaction was governed by the NH_3/O_2 ratio in the feed. Moreover it was found, that the selectivity to acrylonitrile increased with the total N content in the catalysts, while the propane conversion was not influenced. In the series of the used VZrPON catalysts, a similar dependence of the 3-CP selectivity is found, yet not on the total N content but on the surface N content reflected by the N/P ratio derived from XPS. This is not only evident within the series of VZrPON catalysts, but also from a comparison of S_{3-CP} and surface N/P ratio of the used VZrPO catalyst series, in which N originates exclusively from the reaction feed. This suggests that the same surface N species are formed in VZrPO as well as in VZrPON catalysts under reaction conditions, as supposed accordingly by Florea et al. for the VAlO/VAlON system.

Besides the N content, it was supposed that the surface acidity may influence the S_{3-CP} as well, since the incorporation of P in the surface of VZrPON catalysts might lead to Brønsted acidity by formation of P-OH bonds and to Lewis acidity arising from empty 3d orbitals of P. Acidic surface sites can hinder fast desorption of the basic 3-CP and thus diminish selectivity as a consequence of deep oxidation. From FTIR spectroscopy of adsorbed pyridine, the characteristic band of pyridine adsorbed on Lewis acid sites is not accessible, since the relevant wave number range is masked by an NH_4^+ band. However, a band being characteristic of Brønsted sites is clearly seen in both VZrPO and VZrPON catalysts, which is essentially missing in the spectra of VZrON catalysts. From catalytic results it is evident, that S_{3-CP} for non-acidic VZrON is lower compared to VZrPO catalysts and almost identical to VZrPON catalysts at low V/Zr ratios. This suggests that a certain amount of surface N species being present for VZrPO but not for VZrON, might have a higher impact on the selectivity than surface acidity. The surface concentration of Brønsted sites is higher for VZrPON-0.1 than for VZrPO-0.1 and so VZrPO-0.1 catalyst is more selective. This is most probably due to a higher N/P ratio of VZrPO-0.1 sample. This dominating impact of the N/P ratio on S_{3-CP} can be also seen within the catalysts of the VZrPON series. S_{3-CP} and N/P surface ratios increase simultaneously with rising V/Zr ratio in the VZrPON series. Finally, the selectivity improving impact of N is also supported by catalytic tests with varying the air/NH_3 flow, in which highest S_{3-CP} values were found for the lowest air/NH_3 ratio. However, during nitridation N seems to be preferentially incorporated in the vicinity of P resulting in mainly P-NH_2 and P=N-M (M = P or Zr) groups, while the formation of surface nitride-like -V-N-M- moieties, considered to be essential for an effective ammoxidation following a concerted oxidation/N-insertion mechanism, seems to be suppressed for both VZrPO and VZrPON catalysts, despite nitridation of the latter material.

3.3. VMON/Mo$_x$O$_y$N$_z$ catalysts (M = Zr or Al)

In order to generate additional N surface sites in VAlON and VZrON catalysts, both corresponding oxide precursors VMO (M = Al or Zr) with V/Al = 0.5 and V/Zr = 0.25 were mixed with MoO_3. These mixtures were subsequently nitrided according to a nitridation protocol to form high-surface nitrides of Mo [75–77]. MoO_3 was selected for its ability to introduce additional redox-active sites and because of its easy conversion into nitrile.

Different ratios of the VMO oxide precursor to MoO_3 were adjusted. The nitrided compounds are called in the following discussion VMON/Mo$_x$O$_y$N$_z$. Additionally, the corresponding pure compounds VAlON-0.5, VZrON-0.25 and Mo$_x$O$_y$N$_z$ were synthesized and characterized to clarify if the nitridation of mechanical mixed VMO/MoO_3 leads to the formation of new chemical bonds. The V/M ratios were chosen to be 0.5 for VAlON and 0.25 for VZrON, since in previous studies it was found, that these catalysts possess the best catalytic performance in the VAlON and VZrON series [7, 8]. Among described metal nitrides in literature, the compound Mo_2N was chosen since for this kind of nitride comprehensive nitridation studies were done resulting in an elaborated nitridation procedure, which provides the synthesis of a high-surface nitride, starting from conventional MoO_3 [75,76]. Therefore, the as-received untreated VMO compounds synthesized via co-precipitation were mechanically mixed with MoO_3 and subsequently nitrided, since it was expected that this might lead to chemical bonds between VMON and Mo$_x$O$_y$N$_z$.

In the next chapter the results for catalytic performance and structural analysis of VMON/Mo$_x$O$_y$N$_z$ will be discussed in comparison to pure VMON catalysts. This chapter also explains why the formula Mo$_x$O$_y$N$_z$ is used instead of Mo_2N.

3.3.1. Catalytic performance

The catalytic performance (X_{3-PIC} and S_{3-CP}) is shown for both VMON/Mo$_x$O$_y$N$_z$ series as a function of the VMO content on MoO_3 in Fig. 3.21 A and B. For comparison the catalytic performance of the pure VZrON-0.25 and VAlON-0.5 samples are added as well, whereby X_{3-PIC} and S_{3-CP} are labeled with open symbols for these two catalysts.

First of all, there is a clear difference in the catalytic performance of pure VZrON-0.25 and VAlON-0.5 compared to the Mo containing samples. Interestingly, the catalysts of the VAlON/Mo$_x$O$_y$N$_z$ series possess almost identical selectivity values, which are slightly higher than that of the pure VAlON-0.5 catalyst. The conversion for the latter series increases continuously with rising amount of VAlON-0.5 and seems to approach the value of X_{3-PIC} measured for the pure VAlON-0.5 catalyst. However, the trend in the catalytic performance of

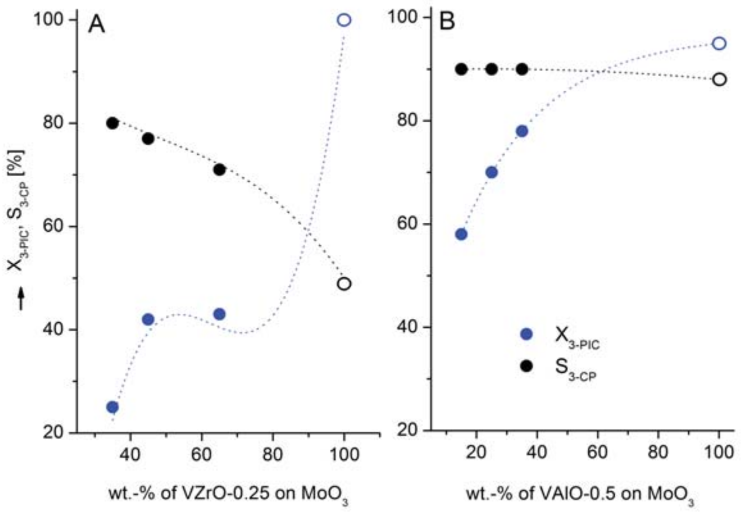

Figure 3.21.: Catalytic performance of VMON/Mo$_x$O$_y$N$_z$ catalysts as a function of the VMON content and catalytic performance of pure VMON catalysts (T$_B$ = 360 °C and GHSV = 2713 h^{-1}); A)VZrON-0.25/Mo$_x$O$_y$N$_z$ (closed symbols) and pure VZrON-0.25 (open symbols) B) VAlON-0.5/Mo$_x$O$_y$N$_z$ (closed symbols) and pure VAlON-0.5 (open symbols)

the VZrON/Mo$_x$O$_y$N$_z$ series is contrary to that of the VAlON/Mo$_x$O$_y$N$_z$ series. In this case S$_{3-CP}$ decreases continuously and approaches to the value obtained for pure VZrON-0.25. Also the conversion increases initially, but remains constant at 65 wt.-% VZrO-0.25/MoO$_3$ suggesting that the conversion, which is reached for the pure VZrON-0.25 sample cannot be achived by increasing the amount of VZrON in the VZrON/Mo$_x$O$_y$N$_z$ catalyst series. It seems, that with rising VZrON-0.25 content a deactivation of the catalytic performance takes place for VZrON/Mo$_x$O$_y$N$_z$, but not for VAlON/Mo$_x$O$_y$N$_z$.

3.3.2. Structural comparison of VMON/Mo$_x$O$_y$N$_z$ samples with the corresponding VMON catalysts (M = Al or Zr)

Information by XRD First of all, the XRD pattern for the sample derived by nitridation of pure MoO$_3$ is discussed, since different nitrides of Mo are known and can form [133, 134]. The XRD pattern of the nitrided MoO$_3$ is given in Fig. 3.22. It is mainly characterized by two broad reflections around 40 ° and one narrow peak at ca. 26 °. The comparison with ICDD database suggests, that a mixture of different N and O containing Mo phases is formed. MoO$_2$ and tetragonal as well as monoclinic Mo$_2$N are expected as main phases. Surprisingly, the intensity ratio of the two reflections around 40 ° does not fit with those of monoclinic or tetragonal Mo$_2$N. This indicates that another phase is hidden under the experimental pattern.

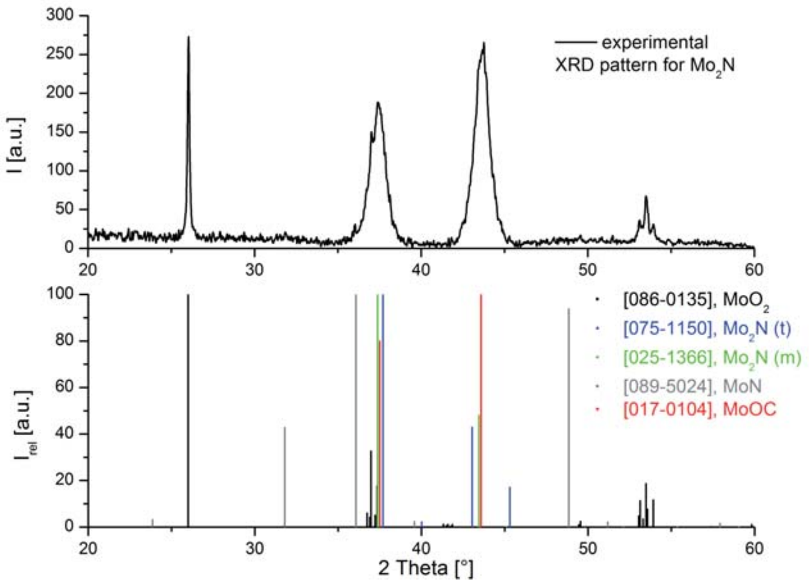

Figure 3.22.: Powder XRD pattern of nitrided MoO_3 including potential attributions according to the ICDD database

It might be an oxynitride phase MoON, which accounts for the experimental XRD pattern. Unfortunately, up to now a XRD pattern for pure MoON is not reported. However, the pattern of MoOC is shown for comparison in Fig. 3.22. By comparing the positions and intensities of the two reflections of the latter phase with those of the experimental pattern, it is clearly seen that MoOC fits to the experimental pattern more precisely. It is very probable that MoON should give rise to a similar pattern. Additionally very small traces of crystalline MoN might be also produced. [9]

When the VAlO-0.5 oxide precursor is added to MoO_3 in different amount by grinding, it can be seen by XRD, that the nitridation leads to almost identical crystalline phases. The corresponding XRD patterns are compared in Fig. 3.23 A as a function of the VAlO/MoO_3 ratio , whereby 100 % means that the pure VMO precursor was nitrided under the same conditions like the VMO/MoO_3 samples. However, pure VAlON-0.5 is amorphous despite rising the maximum nitridation temperature from 610 to 700 °C compared to previous investigated VAlON catalysts [7,8]. When increasing the VAlON amount in the VAlON/$Mo_xO_yN_z$ catalyst series, the reflection intensities of the $Mo_xO_yN_z$ phases rise first up to a loading of 25 wt.-% and decrease again at a ratio higher than 25 wt.-%.

Almost identical trends can be observed for the XRD patterns of the VZrON/$Mo_xO_yN_z$ series, which are shown in Fig. 3.23 B, but in contrast to VAlON/$Mo_xO_yN_z$ additional reflections of a

---

[9] For simplification the abbreviation VMON/$Mo_xO_yN_z$ is used, but it should be kept in mind that indeed at least 5 different crystalline Mo-, N- and/or O-containing phases are present in $Mo_xO_yN_z$.

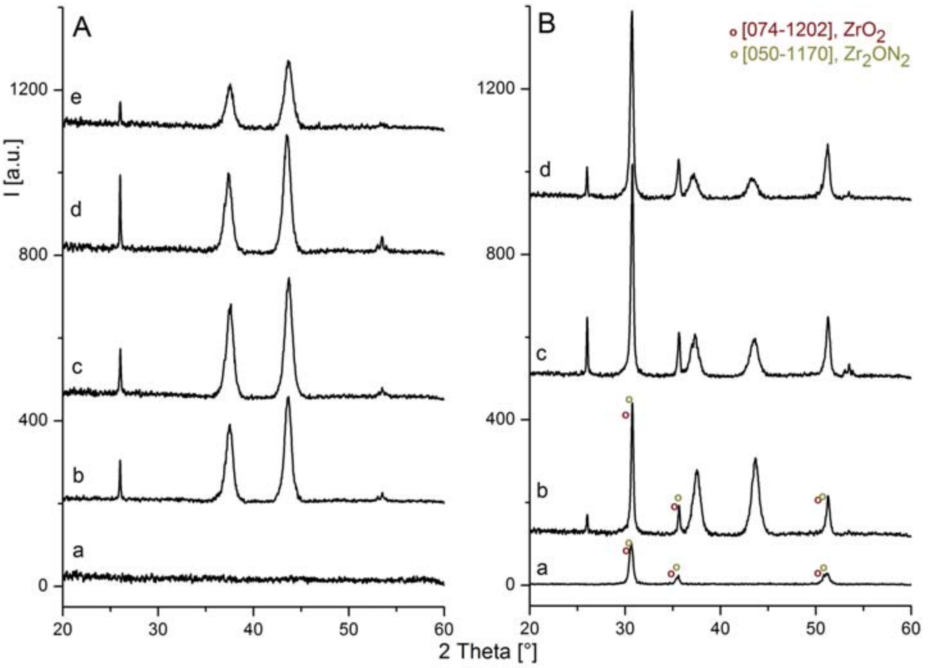

Figure 3.23.: Powder XRD patterns of fresh VMON/$Mo_xO_yN_z$ catalysts; A) VAlON-0.5/$Mo_xO_yN_z$ (a = 100, b = 5, c = 15, d = 25 and e = 35 wt.-%); B) VZrON-0.25/$Mo_xO_yN_z$ (a = 100, b = 35, c = 45 and d = 65 wt.-%)

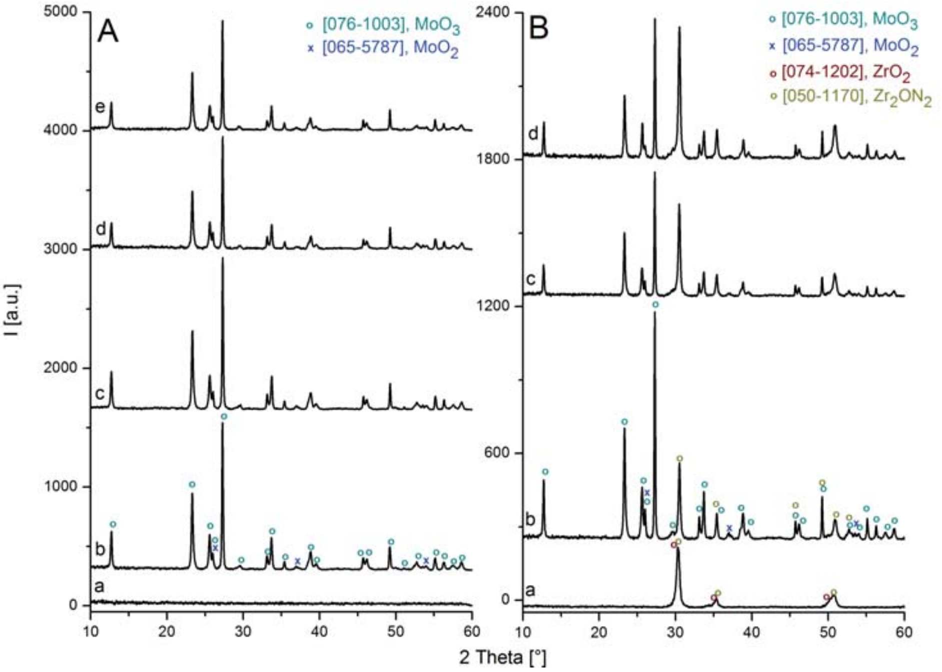

Figure 3.24.: Powder XRD patterns of used VMON/$Mo_xO_yN_z$ catalysts; A) VAlON-0.5/$Mo_xO_yN_z$ (a = 100, b = 5, c = 15, d = 25 and e = 35 wt.-%); B) VZrON-0.25/$Mo_xO_yN_z$ (a = 100, b = 35, c = 45 and d = 65 wt.-%)

structural disturbed Zr containing phase are detected. These reflections are exclusively present in the pure VZrON-0.25 sample, which was nitrided in the same way as to the VZrON/$Mo_xO_yN_z$ catalysts. In Fig. 3.25 A reflections of ZrO_2 and Zr_2ON_2 taken from the ICDD database are shown together with the normalized experimental XRD patterns of fresh and used VZrON-0.25 catalysts. This comparison suggests, that the structural disturbed Zr-containing phase observed in the fresh VZrON-0.25 and VZrON/$Mo_xO_yN_z$ catalysts is more related to the Zr_2ON_2 phase than to the ZrO_2 phase.

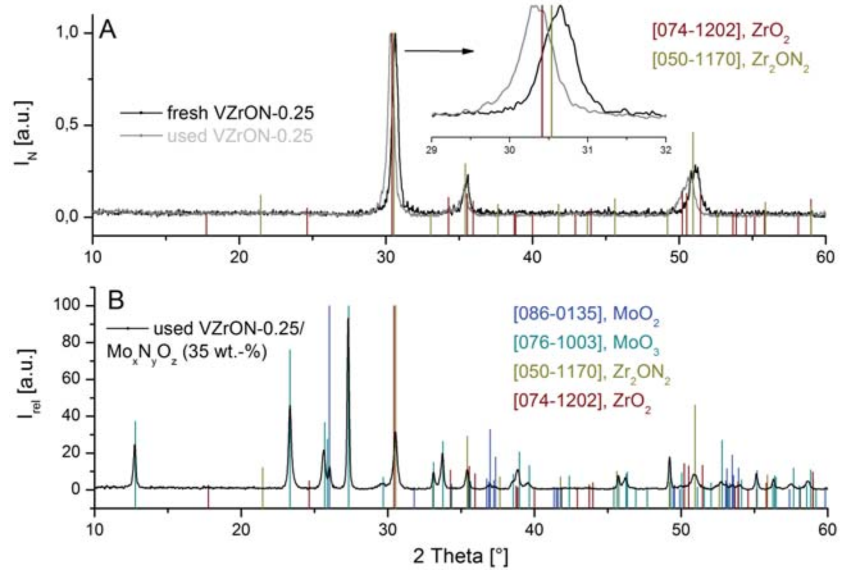

Figure 3.25.: Powder XRD patterns of A) Fresh and used VZrON-0.25 catalysts and B) Used VZrON-0.25/$Mo_xO_yN_z$ catalyst including attributions according to ICDD database

However, no evidence can be found by XRD that a new crystalline V-Mo containing phase is formed suggesting that the two compounds VMON and $Mo_xO_yN_z$ are not interacting structurally, neither in the VAlON/$Mo_xO_yN_z$ nor in the VZrON/$Mo_xO_yN_z$ series.

Moreover, marked changes in both VMON/$Mo_xO_yN_z$ catalyst series can be observed by XRD, when using these catalysts for ammoxidation. The XRD patterns of the used VMON/$Mo_xO_yN_z$ samples are given in Fig. 3.24 A and B. A new crystalline phase can be observed for all Mo containing samples in the XRD patterns, whereby the reflection intensity and position fit well with those of MoO_3. In addition, small traces of MoO_2 are still visible in the patterns of all used Mo-containing catalysts (see also Fig. 3.25 B). Reflections hinting to a N containing Mo phase cannot be observed anymore. For the VZrON/$Mo_xO_yN_z$ series still typical reflections of a structural disturbed Zr containing phase are detected, but in all samples the reflection positions of the latter phase shifts about 0.3 ° to lower angle values. Hence, independent on the percentage of VZrON, the unit cell of this Zr containing phase is changed during ammoxidation for the VZrON/$Mo_xO_yN_z$ series and for the pure VZrON-0.25 catalyst (see also Fig. 3.25 A and B). From Fig. 3.25 A it is clear, that the shift to lower theta values is due to the release of nitrogen, since the pattern of the used catalysts is now more related to ZrO_2 than to Zr_2ON_2. Moreover, by comparing the reflection intensities of the Zr containing phase in the pattern of the used VZrON-0.25 catalyst with those of the used VZrON/$Mo_xO_yN_z$ catalysts (see Fig. 3.24 B), it is evident, that the formation of the inactive crystalline Zr containing phase is much more pronounced for the VZrON/$Mo_xO_yN_z$ catalysts than for the pure VZrON-0.25 catalyst.

Surface areas and chemical composition In Tab. 3.12 the N contents and the surface areas S_{BET} of the used and fresh catalysts for the VMON/$Mo_xO_yN_z$ series as well as for the pure compounds are listed. The pure $Mo_xO_yN_z$ compound possesses a surface area higher than 100 m^2g^{-1} as desired.

Table 3.12.: N contents and surface areas S_{BET} of fresh and used VMON/$Mo_xO_yN_z$ catalysts and the corresponding pure compounds VMON and $Mo_xO_yN_z$

	N [wt.-%]		S_{BET} [m^2g^{-1}]	
sample	fresh	used	fresh	used
pure $Mo_xO_yN_z$	7.2	-	109	-
pure VAlON-0.5	3.8	2.0	90	68
pure VZrON-0.25	4.0	2.1	20	4
5 wt.-% VAlON-0.5/$Mo_xO_yN_z$	7.46	0.50	118	5
15 wt.-% VAlON-0.5/$Mo_xO_yN_z$	6.04	0.54	70	9
25 wt.-% VAlON-0.5/$Mo_xO_yN_z$	6.18	0.83	80	10
35 wt.-% VAlON-0.5/$Mo_xO_yN_z$	4.66	1.00	90	15
35 wt.-% VZrON-0.25/$Mo_xO_yN_z$	4.12	0.60	33	2
45 wt.-% VZrON-0.25/$Mo_xO_yN_z$	3.52	0.65	18	2
65 wt.-% VZrON-0.25/$Mo_xO_yN_z$	3.28	0.72	57	1

For the two VMON/$Mo_xO_yN_z$ catalyst series several effects can be observed. First of all, for both fresh catalyst classes the N content decreases with rising the VMON amount. During ammoxidation both series loose a considerable amount of N indicating that the observed phase transformation of $Mo_xO_yN_z$ to MoO_3 is the main reason for this N loss. Moreover in between both series of the used catalysts the N content increases slightly. This might be due to the fact, that the amount of VMON increases continuously so that also N rises as expected.

Remarkable is the trend of the surface area in these catalyst series. The catalysts in both VMON/$Mo_xO_yN_z$ series loose most of their surface area during ammoxidation. This trend is particularly dramatic for the VZrON/$Mo_xO_yN_z$ and VZrON-0.25 catalysts. Independent of the amount of VZrON-0.25 in the VZrON/$Mo_xO_yN_z$ catalysts, the surface area drops to values ≤ 2

m^2g^{-1}. In contrast, the smallest value for S_{BET} in the used VAlON/$Mo_xO_yN_z$ is observed for the lowest VAlON content. Moreover, the surface area increases continuously with rising VAlON content. Apparently , the loss of N during ammoxidation and therefore the transformation of the $Mo_xO_yN_z$ phases to MoO_3 are affecting the surface area of VAlON/$Mo_xO_yN_z$ and VZrON/$Mo_xO_yN_z$ catalysts in a different manner.

3.3.3. Conclusions on VMON/$Mo_xO_yN_z$ catalysts

The mechanical mixing of VMO precursors with MoO_3 followed by subsequent nitridation leads to VMON/$Mo_xO_yN_z$ solids, which possess initially only at low VMO amount higher surface areas than the corresponding pure VMON compounds. No hints could be found that VMON phases are chemically bound to $Mo_xO_yN_z$. The latter compound is probably a mixture of several phases such as Mo_2N, MoON, MoN and MoO_2. Thus, VMON and $Mo_xO_yN_z$ might rather exist in separated phases.

Catalytic tests as a function of the VMON content in VMON/$Mo_xO_yN_z$ catalysts show that no significant improvement of the catalytic performance was reached compared to the pure VMON catalysts. Results from XRD indicate clearly that Mo_2N, MoON and MoN are not stable under ammoxidation conditions and are retransformed to well crystallized MoO_3. The loss of N and the crystallization to MoO_3 in the course of ammoxidation have different impacts on the structure and catalytic performance of the two VMON/$Mo_xO_yN_z$ series. For the VZrON/$Mo_xO_yN_z$ catalyst series a dramatic drop of the surface area during ammoxidation can be observed. However, this effect is also observed for the pure VZrON-0.25 catalyst. Nevertheless, the latter catalyst is more active than VZrON/$Mo_xO_yN_z$ catalysts, although the values of S_{BET} of the used samples are in the same range. XRD investigations of the used VZrON/$Mo_xO_yN_z$ hint to a higher concentration of inactive crystalline ZrO_2 compared to that in the used VZrON-0.25 catalyst. Thus, in the VZrON/$Mo_xO_yN_z$ catalysts a considerable number of active V species might be covered by MoO_3 or/and ZrO_2, which are not accessible anymore during ammoxidation. On the contrary, the surface area increases with rising VAlON content in the used VAlON/$Mo_xO_yN_z$ series. Interestingly, the loss of surface area is more pronounced than the loss of activity. In this case, both effects, the decrease of S_{BET} and the covering of active V sites with MoO_3 might be the reason for the loss of activity in the VAlON/$Mo_xO_yN_z$ series compared to the pure VAlON-0.5 catalyst.

3.4. VMoON catalysts

In the following chapter the potential of VMo containing oxynitrides will be discussed. Different V/Mo ratios were adjusted ranging from 0.25 up to 2.0. In contrast to previously described VMON/$Mo_xO_yN_z$ catalysts VMo containing solids were synthesized via an aqueous route, in which both V and Mo containing salts were pre-mixed in solution and subsequently precipitated together, with the aim to prevent separation of the two redox-active elements V and Mo as it observed in the above described VMON/$Mo_xO_yN_z$ samples. Precalcined oxides are called VMoO-x.x and oxynitrides calcined prior nitridation are abbreviated as VMoON-x.x. x.x denotes the V/Mo ratio. At this point it should be emphasized again, that the VMoON catalysts being nitrided at 500 °C were precalcined under identical conditions like VMoO catalysts. On the contrary, the maximum nitridation temperature of 700 °C was used for VMON/$Mo_xO_yN_z$ samples. A lower nitridation temperature for VMoON samples was chosen to avoid the formation of $Mo_xO_yN_z$ phases. Structure and catalytic performance of the VMoON catalysts are discussed in the following chapter in comparison to their calcined VMoO oxides.

3.4.1. Catalytic performance

The catalytic performance of the VMoON oxynitrides is depicted in Fig. 3.26 as a function of the V/Mo ratio.

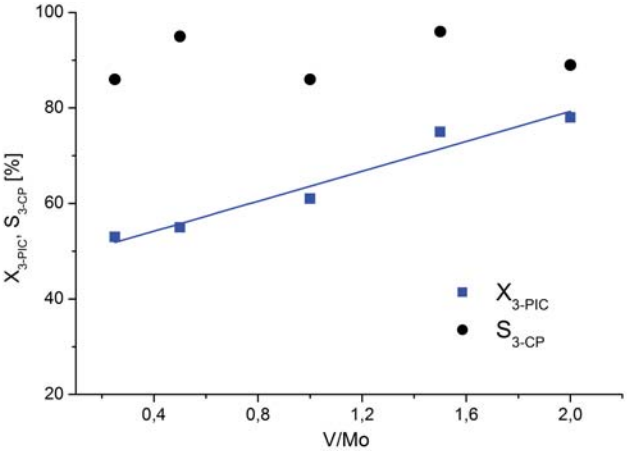

Figure 3.26.: Catalytic performance VMoON oxynitrides as a function of the V/Mo ratio at T_B = 360 °C and GHSV = 2713 h^{-1}

It can be seen, that the conversion increases with rising V/Mo-ratio for VMoON oxynitride catalysts, while the values of the selectivity range between 86 and 96 %. [10] The best catalytic performance can be reached using a ratio V/Mo = 1.5.

---

[10] This effect is significant, as it will be clarified by following results.

Interestingly, a short activation period is observed for the VMoON catalysts with V/Mo ≥ 1.0. As depicted in Fig. 3.27 A the conversion as well as the selectivity increase rapidly with time on stream for the catalyst VMoON-1.5 and VMoON-2.0. This catalytic behavior was not observed for the corresponding calcined oxide catalysts VMoO-1.5 and VMoO-2.0, which possess a constant selectivity and conversion with time on stream. This indicates that the structure VMoON catalyst changes rapidly during ammoxidation.

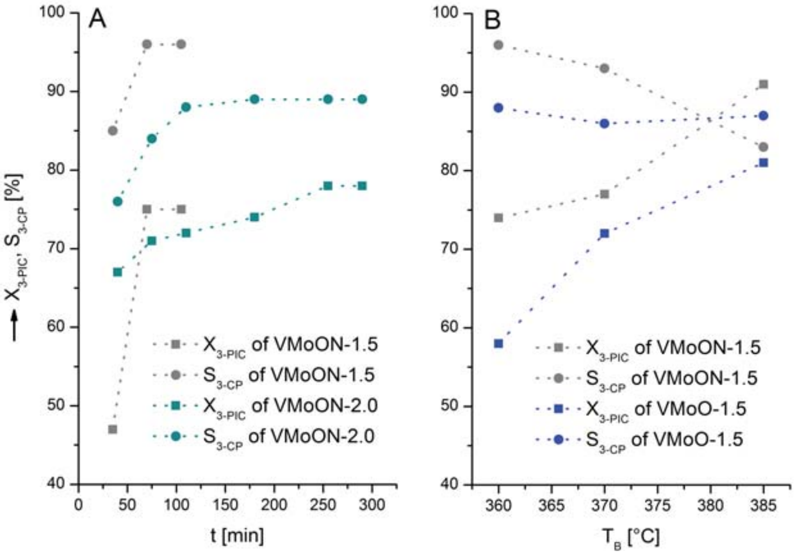

Figure 3.27.: A) Catalytic performance with time on stream of VMoON-1.5 and VMoON-2.0 at T_B = 360 °C and GHSV = 2713 h^{-1}; B) Catalytic performance of VMoON-1.5 and VMoON-2.0 as a function of T_B (GHSV = 2713 h^{-1})

Moreover, the conversions and selectivities of the VMoON-1.5 oxynitride and calcined VMoO-1.5 oxide are compared in Fig. 3.27 B for different bed temperatures T_B. As it is evident from this comparison, the oxynitride is more selective and more active, especially at a bed temperature of 360 °C. For both catalysts the conversion increases with rising bed temperature. However, the oxynititride looses selectivity with increasing T_B. At T_B = 385 °C conversions above 90 % at S_{3-CP} = 84 % are reached with the oxynitride, while the conversion of the oxide catalysts is 10 % lower, yet with almost similar selectivity of S_{3-CP} = 86 %.

3.4.2. Ex situ characterization of VMoO and VMoON catalysts

Chemical composition and surface area of VMo catalysts The chemical compositions and the surface areas S_{BET} of fresh and used VMo oxides and oxynitrides are given in Tab. 3.13.

From the chemical composition in the fresh calcined VMoO oxide series it can be seen, that the desired V/Mo was achieved in each catalyst, and this ratio does almost not change by nitridation. The surface area of the fresh calcined VMoO oxide decrease with rising V/Mo ratio, while no trend can be derived from the surface area in the series of the fresh VMoON catalysts. By nitridation of the calcined oxides to the oxynitrides VMoON nitrogen is incorporated. The highest N content can be observed for the sample VMoON-1.5. However, the N/V ratio for the fresh VMoON samples scatters strongly and shows no correlation to the bulk V content. Also for the surface area of the latter series no general trend can be deduced. Remarkably, a dramatic loss of the incorporated N can be observed for the oxynitride series during ammoxidation, which is especially high for the sample VMoON-1.5 with the highest N concentration. These trends suggest, that N does not correlate with the bulk V content, rather with another species.

Table 3.13.: Chemical compositions, N/V bulk ratios and surface areas S_{BET} of fresh and used VMoON oxynitrides and VMoO oxides derived by ICP-OES and CHN analysis

	Chemical compositions		N/V-ratio		S_{BET} [m^2g^{-1}]	
catalyst name	fresh	used	fresh	used	fresh	used
VMoO-0.25	$V_{0.28}MoO_{3.82}$	-	-	-	7.0	-
VMoO-0.5	$V_{0.46}MoO_{4.57}$	-	-	-	6.9	-
VMoO-1.0	$V_{0.96}MoO_{4.76}$	-	-	-	5.7	-
VMoO-1.5	$V_{1.50}MoO_{7.20}$	$V_{1.48}MoO_{6.56}N_{0.09}$	-	0.06	3.2	5.1
VMoO-2.0	$V_{1.96}MoO_{8.31}$	$V_{2.00}MoO_{8.08}N_{0.11}$	-	0.06	4.0	4.3
VMoON-0.25	$V_{0.25}MoO_{3.21}N_{0.12}$	$V_{0.25}MoO_{3.43}N_{0.07}$	0.48	0.30	10.0	6.3
VMoON-0.5	$V_{0.48}MoO_{3.90}N_{0.24}$	$V_{0.45}MoO_{4.10}N_{0.12}$	0.50	0.27	4.2	4.1
VMoON-1.0	$V_{0.99}MoO_{5.16}N_{0.26}$	$V_{0.97}MoO_{5.03}N_{0.08}$	0.27	0.08	3.7	5.8
VMoON-1.5	$V_{1.45}MoO_{5.76}N_{0.97}$	$V_{1.48}MoO_{7.00}N_{0.08}$	0.67	0.04	16.1	4.4
VMoON-2.0	$V_{1.96}MoO_{6.38}N_{0.54}$	$V_{1.97}MoO_{8.11}N_{0.18}$	0.27	0.09	19.0	3.7

Information by XRD The powder XRD patterns of the fresh calcined VMoO samples are given in Fig. 3.28 A as a function of the V/Mo ratio. Several trends can be derived from this investigation.

At low V/Mo ratios like 0.25 and 0.5 crystalline MoO_3 is detected as main crystalline phase beside traces of crystalline V_2MoO_8. The most intense peaks in the patterns of VMoO-0.25 and -0.5 originate from MoO_3 (see dotted green line). The amount of crystalline V_2MoO_8 increases with rising V/Mo ratio, but not continuously as it can be seen by comparing the most intense undisturbed reflection of V_2MoO_8 at around 22° for each XRD pattern in the VMoO series (see dotted blue line). Remarkably, for the oxide sample with V/Mo = 1.5 only reflections of crystalline V_2MoO_8 are observed, indicating that this catalyst contains only one crystalline phase.

For a ratio V/Mo = 2.0 additional reflections assigned to V_2O_5 and MoO_3 can be detected beside V_2MoO_8, indicating that the solid reaction between MoO_3 and V_2O_5 to V_2MoO_8 has not been completed. This would explain, why the crystalline amount of V_2MoO_8 is much lower in the sample VMoO-2.0 compared to VMoO-1.5. Although, the VMoO catalysts were synthesized and calcined under more or less identical conditions, it can be seen from XRD results, that the mixed crystalline phase V_2MoO_8 forms to a different extent.

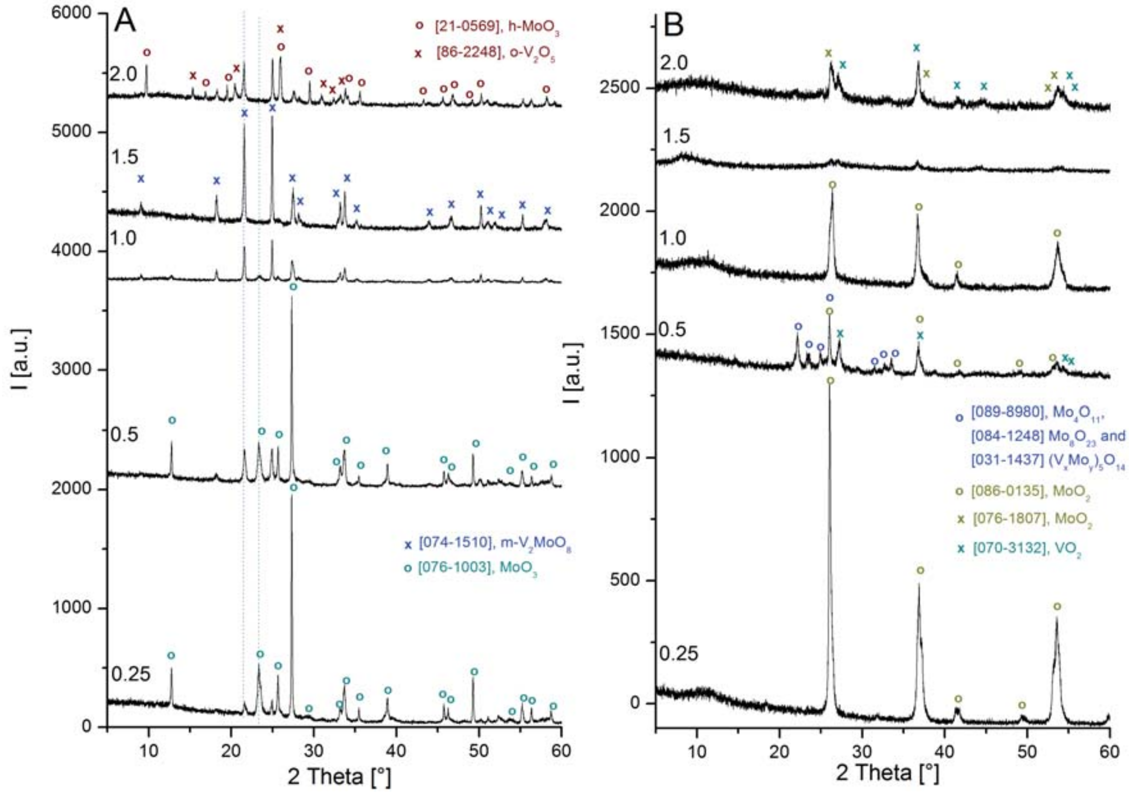

Figure 3.28.: Powder XRD pattern of A) Fresh VMoO catalysts and B) Fresh VMoON catalysts as function of the V/Mo ratio as indicated

To quantify the relative amount of crystalline V_2MoO_8 in the fresh VMoO oxides, the area A_R of the reflection at 21.6 ° was taken as a measure for the concentration of crystalline V_2MoO_8. For each pattern a baseline correction in the range from 20 to 22.5° was done on the untreated experimental XRD pattern. It was found, that a pseudo-Voigt-1 function reproduces the shape of the experimental reflection most reliably. A plot of A_R versus the experimental V/Mo ratio in VMoO catalysts is given in Fig. 3.29.

Remarkably, this relation seems to be related to the selectivity behavior derived from catalytic test in the VMoON catalyst series, which is given in Fig. 3.26. This indicates that the concentration of crystalline V_2MoO_8 in VMoO catalysts has an important impact on the selectivity found for VMoON oxynitrides.

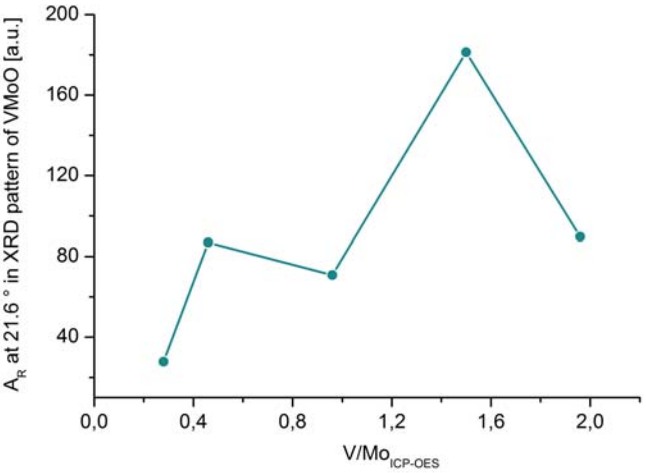

Figure 3.29.: Reflex area A_R at 21.6 ° in the XRD pattern of the fresh VMoO oxide series

The corresponding XRD patterns of the fresh VMoON oxynitrides are given as a function of the V/Mo ratio in Fig. 3.28 B. Apparently, the nitridation of the calcined VMoO oxides has a dramatic impact on the crystalline phases (compare patterns in Fig. 3.28 A and B). Two border cases can be distinguished. For the oxynitride sample with the lowest V/Mo ratio intense reflections assigned to crystalline MoO_2 are detected. For the sample with a ratio V/Mo = 1.5 almost no peaks are observed, merely weak and broad signals indicate that MoO_2 might be present, yet in very low amount. Conclusively, crystalline MoO_3 in VMoO samples is reduced by the nitridation merely to crystalline MoO_2. The formation of crystalline Mo containing oxynitride or nitride compounds is not indicated by XRD. This is not surprising, since the maximum nitridation temperature for VMoO samples is about 200 °C lower in comparison to that for VMO/$Mo_xO_yN_z$ samples. Interestingly, crystalline V_2MoO_8 is obviously totally destroyed during nitridation. Also V_2O_5, being exclusively present in the calcined VMoO-2.0 sample is not seen anymore in the corresponding XRD pattern of the fresh oxynitride. Instead reflections of VO_2 are detected. This indicates that V_2O_5 is reduced to VO_2.

Since the crystalline amount of V_2MoO_8 does not continuously increase with the V/Mo ratio and also the N content seems to be not related to the entire bulk V content in fresh VMoON samples, the idea arose to correlate the N content in the fresh VMoON series with the amount of crystalline V_2MoO_8 in fresh calcined oxides.

This was done for the calcined VMoO samples with $0.25 \leq V/Mo \leq 1.5$. In Fig. 3.30 A the concentration of N is plotted against the experimental V/Mo ratio of the corresponding VMoON samples. This plot shows, that the N content does not continuously increase with the V/Mo ratio in the fresh VMoON series. Instead, the N concentration of the fresh VMoON samples increases more or less continuously with the amount of crystalline V_2MoO_8 in the oxide VMoO, suggesting that it is V_2MoO_8 which is preferentially nitrided upon treatment of the VMoO oxides in NH_3 flow. (see Fig. 3.30 B). Therefore, traces of an amorphous V containing phase must be present in each VMoO sample with different amount relative to crystalline V_2MoO_8. This amorphous V containing phase seems to be less prone to nitridation and seems to be especially high for the VMoO-1.0 sample. Further kinetic studies on VMoO catalysts using UV/Vis-DRS are presented in the next chapter and support this idea.

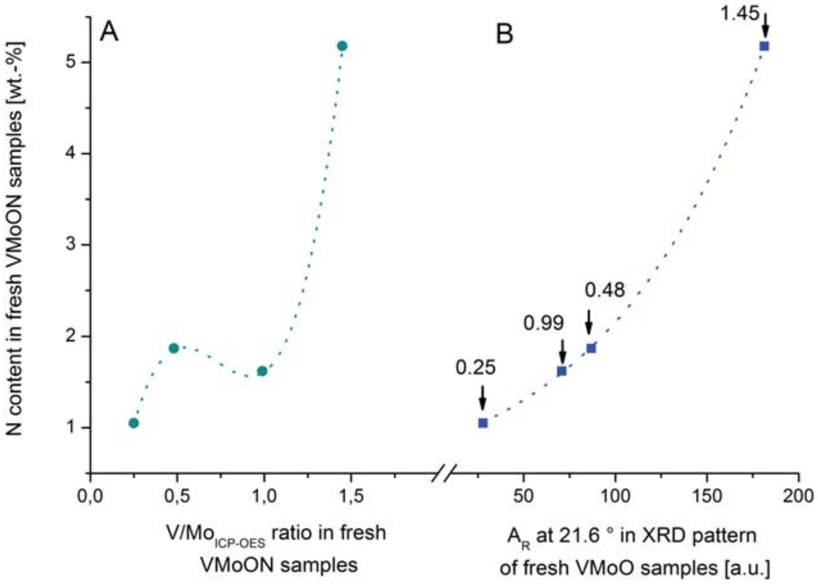

Figure 3.30.: A) N content in fresh VMoON samples as a function of their V/Mo$_{ICP-OES}$ ratios
B) N content of fresh VMoON samples as a function of the peak area A_R of the V_2MoO_8 peak at 2Θ = 21.6 °; numbers: V/Mo$_{ICP-OES}$ ratios of VMoON catalysts

The sample VMoO-2.0 is not included in the plot of Fig. 3.30 B, since the nitrogen content of the nitrided sample VMoO-2.0 is slightly higher than expected from the correlation in Fig. 3.30 B (2.47 wt.-%/89.7 a.u.). Note that this calcined oxide VMoO-2.0 contains some crystalline V_2O_5, which might be prone to nitridation as well. Probably, the additional nitrogen was taken up by V_2O_5.

When using the oxynitrides of the VMoON series for ammoxidation again dramatic changes of the crystalline phases are detected. The XRD patterns of the used oxynitrides VMoON are depicted in Fig. 3.31 A for V/Mo ranging from 0.5 to 2.0, plotted with those of ICDD database in Fig. 3.31 B - D. Again, the XRD pattern of used sample with the ratio 1.5 is of exceptional importance in the VMoON series, since according to the ICDD database three more or less structurally equal phases $VMoO_5$, $V_4Mo_6O_{25}$ and $V_6Mo_4O_{25}$ describe the experimental reflections in the pattern of the latter sample (see Fig. 3.31 B - D) most precisely.

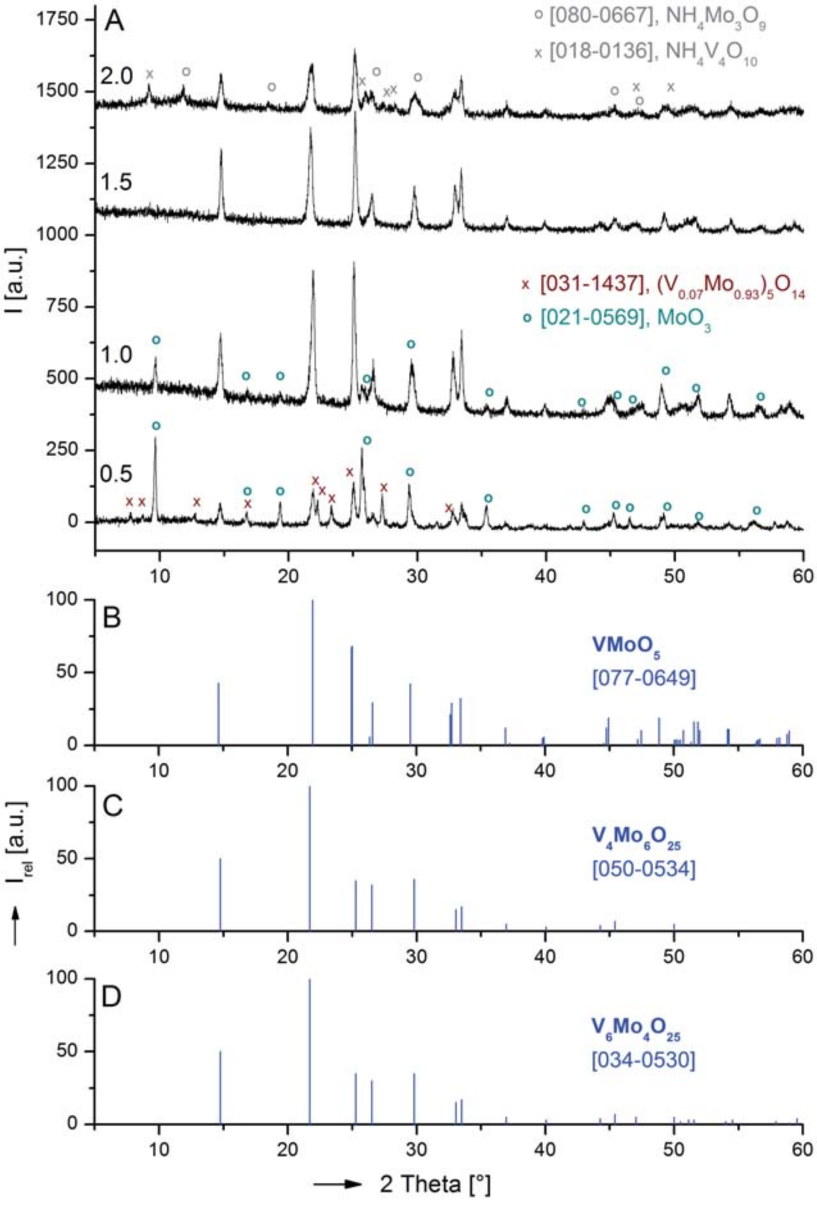

Figure 3.31.: A) Powder XRD pattern of used VMoON oxynitrides as a function of the V/Mo ratios as indicated; B) - D) XRD pattern of $VMoO_5$, $V_4Mo_6O_{25}$ and $V_6Mo_4O_{25}$ from the ICDD database

Without doubt, $V_4Mo_6O_{25}$ and $V_6Mo_4O_{25}$ can not be distinguished by XRD, since these two phases possess almost equal reflection positions and intensity ratios (see Fig. 3.31 C and D). For simplification these two kinds of solid solutions are abbreviated in the following discussions with $V_{4/6}Mo_{6/4}O_{25}$.

Also the XRD pattern of non-stoichiometric $VMoO_5$ is closely related to the two $V_{4/6}Mo_{6/4}O_{25}$ oxide phases, merely the reflection at 25 ° and around 33 ° are more intense. Comparing the intensity ratios and the peak positions of these three phases with the experimental pattern of the used VMoON-1.5 catalyst, it has to be considered that, besides $V_{4/6}Mo_{6/4}O_{25}$, also non-stoichiometric $VMoO_5$ may be formed during ammoxidation, since the reflections of the experimental pattern at 25 ° and around 33 ° are slightly to intense.

The XRD patterns of the catalysts with V/Mo = 0.5 and 1.0 contain a number of additional peaks assigned to MoO_3 and $(V_xMo_y)O_{14}$, beside those belonging to the mixture of $V_{4/6}Mo_{6/4}O_{25}$ and $VMoO_5$.

Also the pattern of the used VMoON-2.0 catalysts shows additional reflections, which belong to $NH_4Mo_3O_{14}$ and $NH_4V_4O_{10}$. This is expected, since in the corresponding XRD patterns of fresh catalysts (calcined VMoO-2.0 and nitrided VMoON-2.0) V_xO_y and Mo_xO_y phases are detected due to an incomplete reaction of V_2O_5 and MoO_3 to V_2MoO_8.

Finally, the XRD pattern of the used oxide catalysts with V/Mo = 1.5 is compared with that of the fresh oxide catalyst in Fig. A.16. Remarkably, almost no changes two XRD pattern are observed. This indicates that a phase transformation similar to that in the corresponding VMoON catalysts does not take place in the VMoO oxides.

UV/Vis-DRS and EPR studies of the fresh calcined VMoO oxide series UV/Vis spectra of the fresh VMoO samples are shown in Fig. 3.32 A and A'. In general, below 500 nm intense bands due to CT transitions of V^{5+} and Mo^{6+} are expected, while weak bands for reduced metal sites such as V^{4+}, V^{3+} and Mo^{5+} occur above 500 nm [96, 126–130].

The most intense signal below 500 nm is measured for the VMoO sample with the lowest V concentration (see Fig. 3.32 A). Upon increase of the V content the intensity of the CT bands decreases in the VMoO series. This might be due to the darkening of the samples with increasing V/Mo ratio, indicating a partial reduction of V^{5+} and possibly also Mo^{6+}. This leads to a dramatic drop of the CT band intensity in the range below 500 nm in favor of an intensity increase above 500 nm, in the range of d-d transitions of reduced V and Mo species occur. This is particularly well seen from the plot of the normalized UV/Vis spectra (see Fig. 3.32 A'), suggesting that the percentage of V and/or Mo reduction rises with increasing V/Mo ratio.

Deconvolutions of the UV/Vis spectra in Fig. 3.32 A' were done using five Gaussian curves to derive additional information about the chemical nature of Mo and V species. The resulting Gaussian areas A_P for each peak are compared in Fig. 3.33 A (see also Tab. B.2). One deconvoluted spectrum of VMoO-0.5 is depicted in Fig. 3.33 B. A first view on the plot given in Fig. 3.33

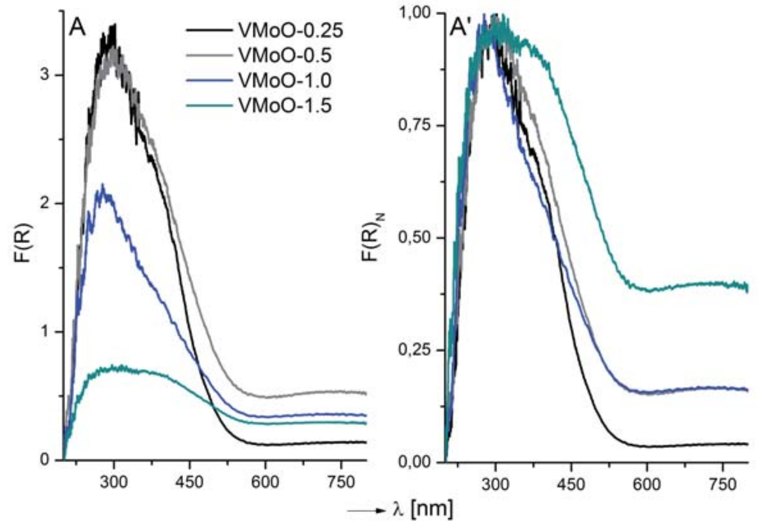

Figure 3.32.: UV/Vis spectra at RT of fresh VMoO oxide as a function of the V/Mo ratio; A) As-received spectra, A') Normalized spectra

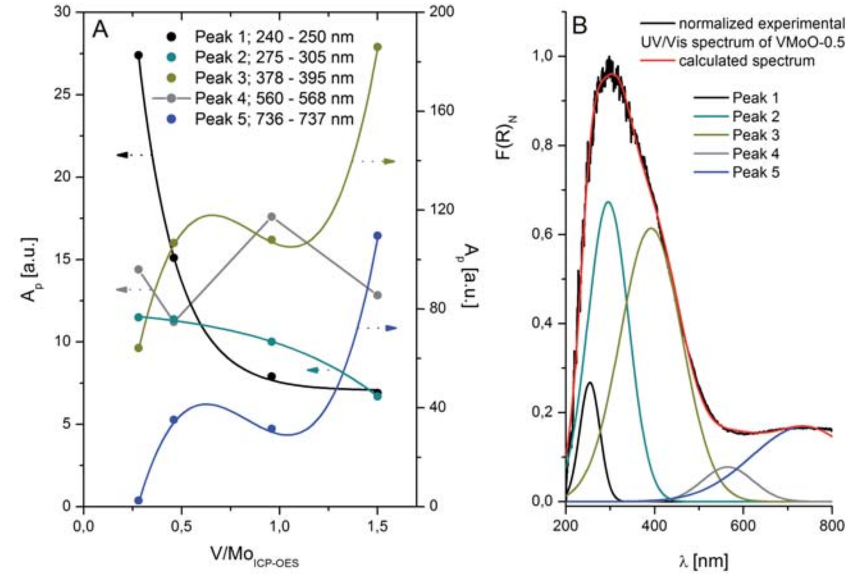

Figure 3.33.: A) Peak areas A_P of Gaussian peaks 1 - 5 derived by deconvolution of UV/Vis spectra of the VMoO series; B) Experimental UV/Vis spectrum at RT of VMoO-0.5 including results of deconvolution

A shows that A_P for each of the five Gaussian peaks rises differently with the V/Mo ratio in the VMoO series. Remarkably, peak 3 (395 - 378 nm) and peak 5 ($\approx$ 737 nm) possess an almost identical curve progression in this plot indicating that these two transitions belong to the same type of metal site. It is very probable that the Gaussian peak 5 reflects the V^{4+} d-d transition in crystalline V_2MoO_8, while the subband 3 might represent CT transitions of V^{5+} and Mo^{6+} in crystalline V_2MoO_8.

Moreover, it is again indicated that the V_2MoO_8 phase is especially prone to the nitridation, since the plot of the bulk N content vs. the V/Mo$_{ICP-OES}$ ratio shows an almost identical trend (see Fig. 3.30 A). This supports additionally the idea, that crystals of V_2MoO_8 are preferentially nitrided in the VMoON series. The peak areas of the Gaussian peak 1 (240 - 250 nm) and peak 2 (275 - 305 nm) decrease with rising V/Mo ratio. For sure, these two signals must be assigned to CT transitions of MoO_3, which was also detected by XRD (see Fig. 3.28 A). [11]

For further comparison of the UV/Vis spectra of the VMoO series the absorption edge energies E_g were determined for each spectrum in the VMoO series. A plot of E_g against V/Mo is given in Fig. 3.34. In principle, the parameter E_g is interpreted in two ways according to literature. A shift of the absorption edge energy to lower energies is often assigned to an increase of the VO_x polymerisation degree in supported VO_x samples [129, 137]. For pure MoO_x samples it is also assigned to the change of the molybdenum oxidation state and coordination sphere, respectively [138].

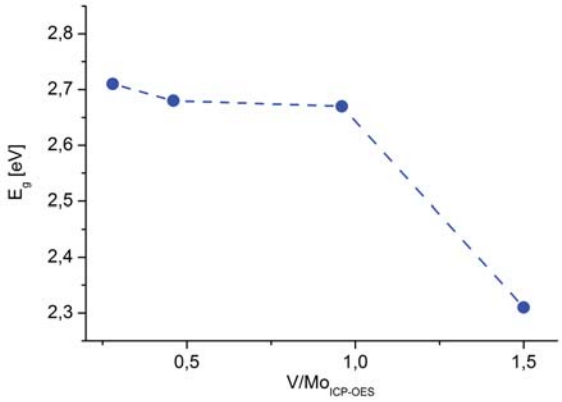

Figure 3.34.: E_g values derived from UV/Vis spectra at RT of fresh VMoO samples

Own calculated E_g values as a function of the V/Mo ratio in the VMoO series show, that the E_g can be regarded as a mirror for the concentration of crystalline V_2MoO_8. The greater the amount of crystalline V_2MoO_8, the smaller the value of E_g.

To evaluate the presence or absence of Mo^{5+} in the fresh VMoO series, EPR spectroscopy was applied at RT and 77 K. These spectra are compared in Fig. 3.35 A - B. The inset in Fig. 3.35 A

---

[11] Commercial MoO_3 shows three distinct bands at 238, 333 and 365 nm, which where determined by spectrum deconvolution of the UV/Vis spectrum measured at RT (see Fig. A.17). According to literature [135, 136], the band at 238 nm might arise from CT transitions in tetrahedrally coordinated molybdenum, whereby the most intense band at 333 nm must be assigned to octahedrally coordinated molybdenum. The presence of the third peak indicates, that this kind of MoO_3 is not defect-free. However, its origin cannot distinctly assigned.

represents the double integral intensity A_{EPR} of the EPR signals as a function of the V/Mo ratio in VMoO samples.

In the EPR signals measured at RT an isotropic line dominates in the spectra for V/Mo ≥ 0.25, which accounts for the presence of magnetically interacting $^{4+}$V-O-V^{4+} sites. The g value is typical for V containing interacting sites. Merely for the ratios 0.25 and 0.5 a typical hfs signal of VO^{2+} contributes additionally to the EPR signal, but its contribution is very low compared to the isotropic signal. The correlation between A_{EPR} and the V/Mo$_{ICP-OES}$ suggests, that the amount of V^{4+} detected by EPR at RT might be mainly attributed to V^{4+} sites in the crystalline V_2MoO_8 phase, since an almost similar curve progression can be derived, when plotting A_R against V/Mo (see Fig. 3.29). Moreover, the curve progression of Gaussian peak 5 in Fig. 3.33 assigned to d-d transitions of V_2MoO_8 resemble that of A_{EPR} vs. V/Mo$_{ICP-OES}$ given in Fig. 3.35 A. The g_{iso} value of 1.96 found for the EPR signal of VMoO-1.5 is characteristic for pure $V^{4+}O_x$ clusters in V_2MoO_8 [139].

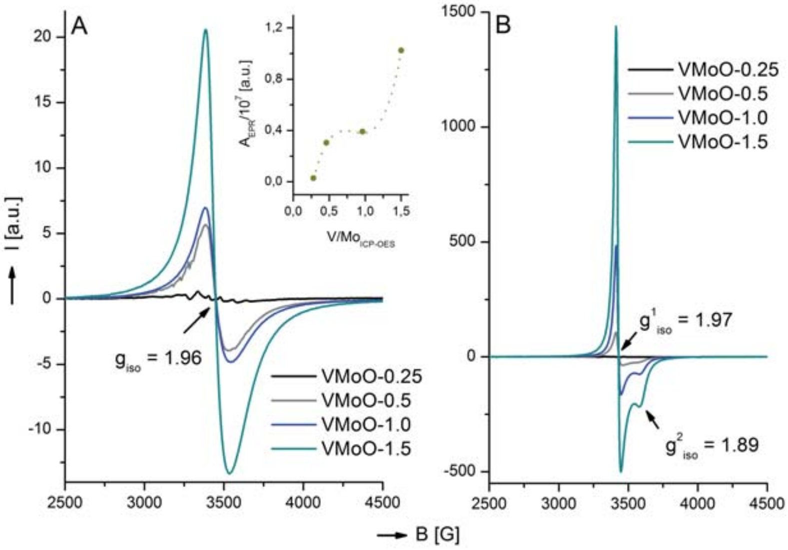

Figure 3.35.: EPR signals of fresh VMoO oxides as a function of the V/Mo ratio; A) Measured at RT; B) Measured at 77 K; inset: plot of A_{EPR} vs. V/Mo$_{ICP-OES}$ for EPR signals derived at RT

The EPR spectra measured at 77 K of the VMoO series (see Fig. 3.35 B) show a narrow intense signal for V/Mo > 0.5. The two g_{iso} values of 1.97 and 1.89 calculated for the spectrum of VMoO-1.5 suggests that besides V^{4+} also traces of Mo^{5+} sites are present in VMoO samples [138–142].

In addition, redox experiments on the VMoO series were performed to evaluate the real reason for the fluctuating selectivities in the VMoON catalyst series (see again Fig. 3.26). For these experiments, initially each VMoO sample was heated in a 9 % O_2/Ar atmosphere to 300 °C. After reaching steady state, the flow was switched to a diluted 9 % H_2/Ar stream. By this treatment a reduction of redox active metal sites (e.g. V^{5+} or/and Mo^{6+} to V^{4+} or/and Mo^{5+}) is induced, which is accompanied by an increase of the absorption above 500 nm. This effect was followed at a fixed wavelength of 700 nm. After reaching steady state again, the gas flow was immediatly switched at 300 °C to a 9 % O_2/Ar atmosphere to evalute which reduced sites can be reoxidized. An example for the time-dependend change of the absorbance during reduction and reoxidation is shown in Fig. 3.36, including the respective fit functions calulated by assuming the kinetic model described in chapter 5.3.

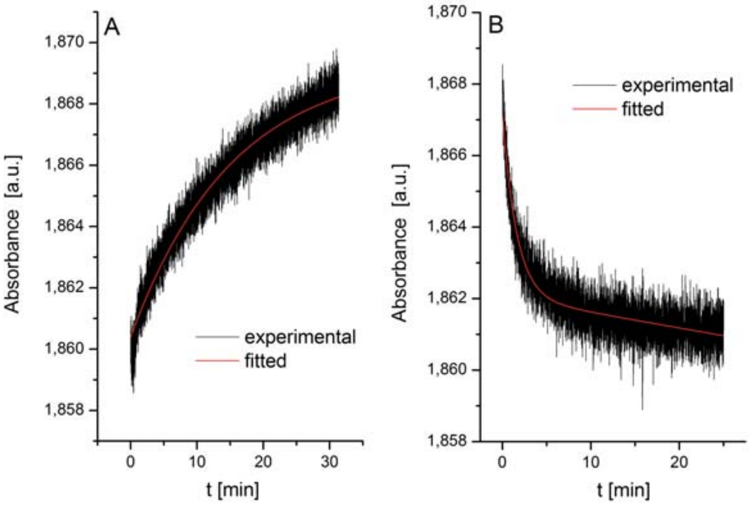

Figure 3.36.: Experimental absorbance functions and fit functions for the treatment of VMoO-1.5 in A) H_2/Ar flow and B) O_2/Ar flow; (λ = 700 nm, T = 300 °C)

As already indicated by the deconvolution of the UV/Vis spectra derived at RT for the VMoO series, two distinct transitions contribute to the absorbance at 700 nm. This is also supported by the fit analysis of the time-dependent reduction and reoxidation curves. Merely by taking two different V sites into account for each VMoO sample the experimental curves of reduction and reoxidation could be successfully fitted using the kinetic model described in chapter 5.3. The resulting relative concentrations of these two sites (abbreviated in this case with site 1 and site 2) for the reduction and reoxidation process are compared in Fig. 3.37. First of all, it can be seen by this plot that site 1 has a much higher relative concentration than site 2. However, the concentration of both sites in the VMoO series correlates somehow. A high concentration of site 1 provokes a low concentration of site 2 and vice versa. Again, an S-shaped correlation can be found for the VMoO series indicating that the predominant site 1 can be attributed to V^{4+} sites in crystalline V_2MoO_8, while the second site 2 might represents the V containing amorphous residuum. Remarkably, the redox behavior of site 1 and 2 differs significantly. Site 1 and therefore V^{4+} sites in crystalline V_2MoO_8 can be completely reoxidized. On the contrary, it is evident from Fig. 3.37, that site 2 stays in its reduced state and cannot be fully reoxidized.

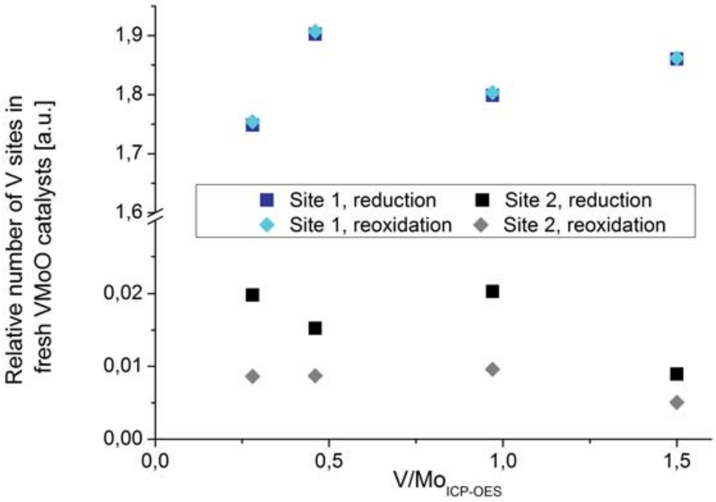

Figure 3.37.: Relative number of V sites estimated via kinetic studies on VMoO samples as a function of the V/Mo ratio using UV/Vis-DRS

Moreover, from a comparison of this plot with the selectivity behavior in Fig. 3.26 it is evident that the two V sites 1 and 2 have an opposite impact on the selectivity of VMoON samples. A low amount of site 2 (V containing amorphous residue) and a high amount of site 1 (V in V_2MoO_8) leads to a better selectivity of VMoON catalysts.

Finally, the UV/Vis spectra of the fresh VMoON series measured at RT are given in Fig. 3.38 A for different V/Mo ratios. Clearly, the nitridation of the calcined VMoO samples changes the oxidation state of the redox-active metal sites, since the spectra of VMoON samples show a much stronger absorbance above 500 nm (compare Fig. 3.32 A and Fig. 3.38 A).

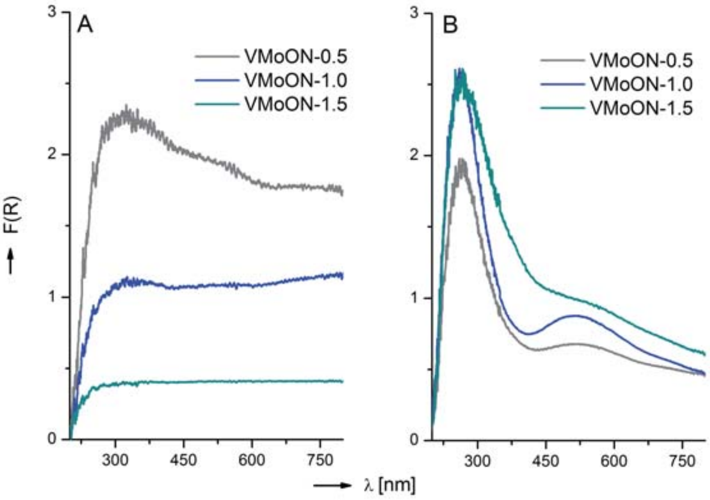

Figure 3.38.: UV/Vis spectra of VMoON catalysts as a function of the V/Mo ratio measured at RT; A) Fresh samples; B) Used samples

This may suggest that the fresh nitided samples contain mainly V^{3+} and V^{4+} as well as probably Mo^{5+}. Interestingly, a strong decrease of absorbance above 500 nm is observed for the same samples after use in the catalytic reaction (see Fig. 3.38 B) and a new distinct band around 525 nm can be observed. This points to a marked reoxidation of reduced V sites under reaction conditions. In the region above 500 nm also inter valence charge transfer transitions (IVCT) are expected [126]. Possibly, the pronounced band at 525 nm is due to an IVCT transition, which could originate from edge-sharing V-O-Mo units. These V-O-Mo species are characteristic for the solid solutions $V_{4/6}Mo_{6/4}O_{25}$ and $VMoO_5$, but almost do not exist in the structure V_2MoO_8 [143–146].

XPS investigations The fresh and used samples of the VMoO-1.5 oxide and VMoON-1.5 oxynitride were additionally investigated by XPS to evaluate the chemical surface composition and the nature of N species on their surface. Binding energies E_B, ΔE_B values and the surface concentration c are listed in Tab. 3.14 for each detected surface element. Useful surface ratios are additionally given in Tab. 3.15 for each sample.

Table 3.14.: Binding energies E_B and surface concentrations c [at.-%] for surface sites of fresh and used VMoO-1.5 and VMoON-1.5 catalysts derived by XPS;
values in brackets: ΔE_B values

		fresh VMoO-1.5		used VMoO-1.5	
XPS peak	site	E_B [eV]	c [at.-%]	E_B [eV]	c [at.-%]
N1s	N^1	-	-	401.6	3.35
V2p	V^1	517.4 (13.3)	7.62	516.8 (13.6)	6.87
V2p	V^2	517.2 (13.0)	2.90	517.4 (13.0)	4.63
O1s	O^1	530.7	61.36	530.4	56.53
Mo3d	Mo^1	233.03	13.61	232.6	10.5
		fresh VMoON-1.5		used VMoON-1.5	
XPS peak	site	E_B [eV]	c [at.-%]	E_B [eV]	c [at.-%]
N1s	N^1	402.3	3.15	401.5	1.5
V2p	V^1	517.8 (13.2)	1.99	516.6 (13.9)	6.13
V2p	V^2	-	-	517.6 (12.9)	9.05
O1s	O^1	531.0	59.57	530.5	65.31
Mo3d	Mo^1	233.1	8.26	232.6	5.70
Mo3d	Mo^2	-	-	233.1	5.06

For the fresh calcined oxide VMoO-1.5 two V surface species can be observed differing slightly in their mean oxidation state, which is close to 4.5 according to their ΔE_B and E_B values.

For the fresh oxynitride only one V surface site can be detected possessing a mean oxidation state close to 4.5. There is no hint for deeply reduced V surface sites although UV/Vis-DRS results suggests, that mainly V^{4+} and possibly also V^{3+} are present in the sample. Since the samples were exposed to ambient atmosphere after nitridation, it is possible that V surface sites are partially reoxidized. However, merely one N site can be seen by XPS with an unusually high binding energy; therefore no nitride-like site is exposed on the surface of VMoON samples. Moreover, the surface N/V ratio (0.22) deviates dramatically from the bulk N/V ratio (0.67) indicating that N sites are mainly located in the bulk and not in the near-surface region. Several N containing sites come into consideration for assigning the E_B value of the N1s signal, e.g. azide-like sites N_3^-, -N≡N- sites or -N=N- sites. However, a reliable assignment merely by the XPS binding energy value is impossible.

Table 3.15.: Experimental surface ratios of fresh and used VMoO-1.5 and VMoON-1.5 samples derived from XPS measurements compared to expected surface ratios of defined stoichiometric VMo solid solutions

ratio	fresh VMoON-1.5	used VMoON-1.5	fresh VMoO-1.5	used VMoO-1.5
V/Mo	1.74	1.41	0.77	1.10
O/V	4.15	4.30	5.83	4.92
O/Mo	7.21	6.07	4.51	5.38
N/V	0.22	0.10	-	0.29

ratio	$V_4Mo_6O_{25}$	$V_6Mo_4O_{25}$	V_2MoO_8	$VMoO_5$
V/Mo	0.7	1.5	2.0	1.0
O/V	6.3	4.2	4.0	5.0
O/Mo	4.2	6.3	8.0	5.0

The nature of the N surface site changes during ammoxidation. In the used VMoON-1.5 oxynitride catalyst a E_B value of 401.5 eV is observed. Moreover, an almost identical E_B value can be detected for the VMoO-1.5 oxide catalyst after use in ammoxidation. This is surprising, since it indicates that the oxide and oxynitride catalysts inserts nitrogen into the benzyl-like intermediate in the same manner. The surface concentration of N in the used VMoO-1.5 oxide is even higher as evident from the surface N/V ratios of the used VMoO-1.5 and VMoON-1.5 samples (see Tab. 3.15), although the oxynitride catalyst is more active and selective than the corresponding oxide catalyst.

Additionally, two distinct V surface sites are detected now for both used samples, but the difference in ΔE_B for V_1 and V_2 is much more pronounced for the used VMoON-1.5 than for the used VMoO-1.5 catalyst. Remarkably, two different Mo surface states are seen for the VMoON-1.5 catalysts after ammoxidation.

By comparing the experimental surface ratios in used VMoON-1.5 and VMoO-1.5 with those of defined binary $V_xMo_yO_z$ solid solutions (see Tab. 3.15) it seems probable that the surface of used VMoON-1.5 is similar to that of $V_6Mo_4O_{25}$ and not to $V_4Mo_6O_{25}$. This is easily understood, since the adjusted bulk V/Mo ratio is also 1.5 for the latter sample. Moreover, the surface ratios of the fresh VMoON-1.5 catalyst seem to be related to V_2MoO_8 with a lack of oxygen. This might hint to a substitution of oxygen by nitrogen.

As already indicated in the previous chapter the substitution of oxygen by nitrogen in VMoO series seems to be related to the amount of crystalline V_2MoO_8. Taking the nitridation reaction into account, a substitution of O by N in V_2MoO_8 according to equation 2.2 would lead to a compound with the theoretical formula $V_2MoO_5N_2^{vac}$. The abbreviation vac in this formula reflects the introduction of an anionic vacancy when substituting three oxygen anions by two nitride-like anions. Unfortunately, neither the bulk chemical composition (see Tab. 3.13) nor the surface composition (see Tab. 3.15) coincide with this theoretical formula. In principle, this might be due to two reasons. Firstly, to obtain an oxynitride with a formula of $V_2MoO_5N_2^{vac}$ a strong resistance to reoxidation must be ensured. This requirement is not necessarily adhered. The high sensitivity to ambient air and formation of a passivation layer, respectively, is already indicated by the fact, that no typical E_B values for nitride-like sites can be detected in the near-surface region of the fresh VMoON-1.5 sample by XPS. Secondly, it must be considered that the adjusted bulk ratio of V/Mo = 1.5 additionally does not agree with the formula $V_2MoO_5N_2^{vac}$. This adjusted bulk V/Mo ratio seems to have also an impact on the surface composition of the fresh VMoO-1.5 sample, since latter does not resemble that of V_2MoO_8, although only well crystallized V_2MoO_8 can be detected by XRD for this compound. This is also true for the used VMoO-1.5 catalyst. In fact, the surface composition of the fresh VMoO-1.5 sample resembles more the theoretical composition of $V_4Mo_6O_{25}$, while the used VMoO-1.5 catalyst is closer to the theoretical composition of $VMoO_5$ (see Tab. 3.15).

Consequently, results obtained by XRD for the fresh and used VMoO and VMoON series doe not mandatorily describe precisely in each case the surface of the latter compounds. However, it should be emphasized that a phase transformation of the fresh VMoON-1.5 catalysts during ammoxidation indicated by XRD leads to the formation of a surface with a similar composition as crystalline $V_6Mo_4O_{25}$. To support this observation, additional in situ investigations of the catalysts VMoON-1.5 and VMoO-1.0 were done. Besides Raman microscopy also EPR spectroscopy as bulk technique was applied in situ on the two compounds VMoO-1.5 and VMoON-1.5.

3.4.3. In situ experiments

Ammoxidation over VMoON and VMoO catalysts followed by in situ EPR spectroscopy
The EPR signals of the untreated catalysts VMoO-1.5 and VMoON-1.5 measured at RT are depicted in Fig. 3.39. Additionally, the resulting EPR signals at RT after the in situ experiments are given for these two samples in the latter figure.

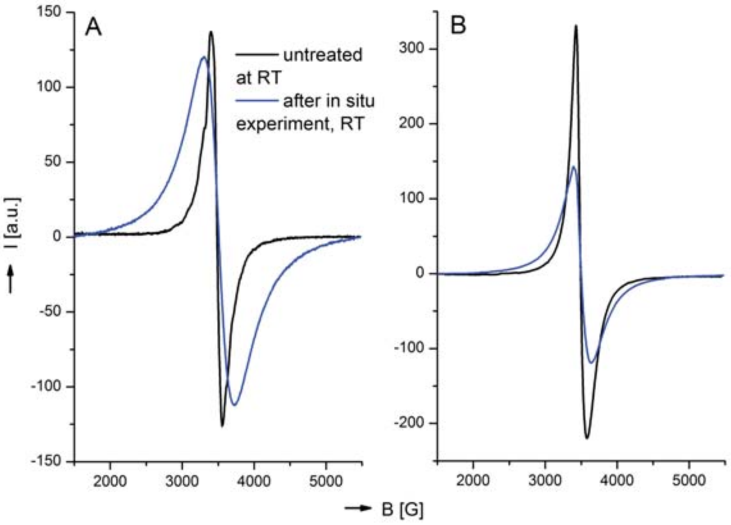

Figure 3.39.: EPR spectra measured at RT before and after in situ ammoxidation experiment using VMo catalysts; A) VMoON-1.5 and B) VMoO-1.5

In all cases, an isotropic signal being characteristic for magnetically interacting $^{4+}$V-O-V^{4+} sites is detected. Neither the EPR signal of the oxynitride nor that of the oxide shows a hfs, indicating the absence of isolated VO^{2+} sites in both samples. All four EPR signals in Fig. 3.39 A and B differ clearly in their line width and intensity. Moreover it can be seen, that the EPR signal of the fresh VMoON-1.5 catalyst has changed through the in situ experiment.

In Fig. A.18 the double integral intensity A$_{EPR}$ is shown for each EPR signal. As evident from this figure, A$_{EPR}$ of the EPR signal of the untreated oxide catalyst VMoO-1.5 is much higher than that of the untreated oxynitride indicating that the amount of cluster-like V^{4+}O$_x$ is lower for the sample VMoON-1.5. Interestingly, it is the other way around for the EPR signals after the in situ experiment. The double integral intensity A$_{EPR}$ is much higher for VMoON-1.5 than for VMoO-1.5 after the in situ experiment. This suggests, that V sites in the VMoO-1.5 catalyst are slightly oxidized from V^{4+} to V^{5+} during ammoxidation, while V species in VMoON-1.5 catalysts are predominantly oxidized from V^{3+} to V^{4+}. However, it has to be considered that Mo^{5+} can also contribute to the EPR signals and that these signals were recorded at RT and do not give a reliable information about the amount of V^{4+} of the catalysts in working state, as it will be seen by next results.

The in situ EPR investigation started with heating the catalyst initially in N_2 to 350 °C. Afterwards, the gas flow was switched from N_2 to a mixture of 2.3 ml/min air and 0.5 ml/min NH_3 at 350 °C. The resulting time-dependent EPR spectra recorded in air/NH_3 stream are given for both catalysts in Fig. 3.40 A and B. For the catalyst VMoO-1.5 the EPR signal shape and intensity stay almost constant, while for the oxynitride the signal intensity increase with time. The gain of the EPR signal intensity for the VMoON-1.5 sample may point to a phase transformation, in the course of which V^{3+} is reoxidezed to V^{4+}. The latter reoxidation process is also supported by the observed change of the UV/Vis spectra of VMoON-1.5 catalyst (compare spectra of VMoON-1.5 in Fig. 3.38 A and B). Comparing the position of the EPR signals with time on stream for VMoON-1.5 catalysts, no significant shift of the signal position can be observed.

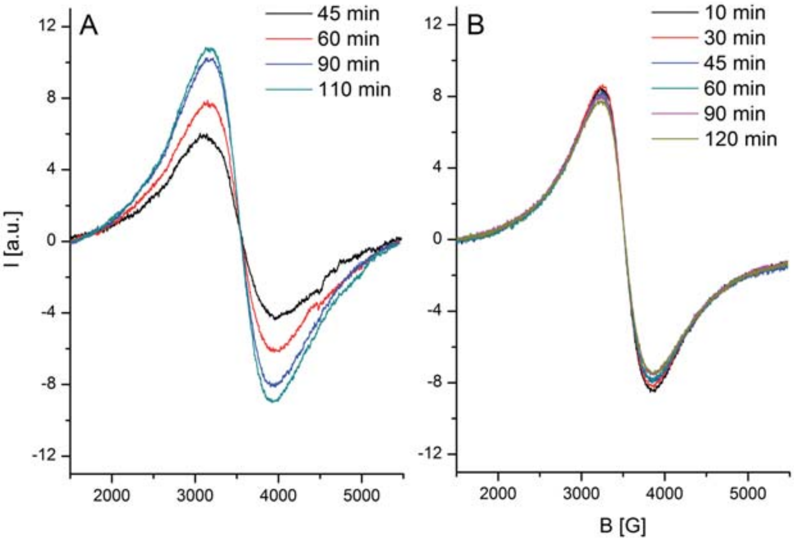

Figure 3.40.: In situ EPR spectra at 350 °C as a function of time; catalyst treatment in air/NH_3; A) VMoON-1.5 catalyst and B) VMoO-1.5 catalyst

When switching from the air/NH_3 mixture at 350 °C to the entire feed air/NH_3/3-PIC the EPR signal of the VMoON-1.5 catalyst increases further, while again almost no changes can be observed under equal conditions for VMoO-1.5 sample (see Fig. 3.41 A and B).

The difference in EPR signal intensity under reaction conditions for the two catalysts might be mainly due to a different concentration of V^{4+}, yet partial reduction to Mo^{5+} can also contribute to the EPR signals. In principle, when these two paramagnetic metal sites would contribute to the experimental isotropic EPR signal, three types of paramagnetic interactions must be taken into account. Besides $^{4+}$V-O-V^{4+} species also $^{4+}$V-O-Mo^{5+} and $^{5+}$Mo-O-Mo^{5+} species have

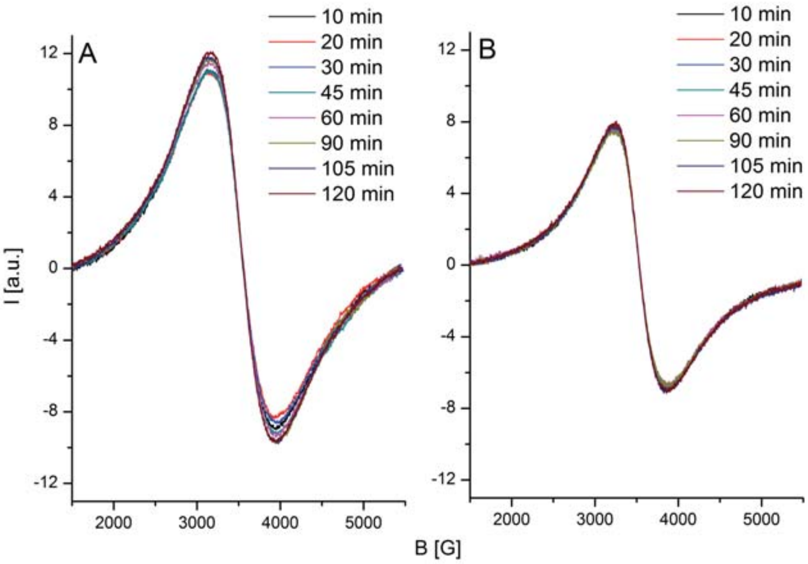

Figure 3.41.: In situ EPR spectra at 350 °C as a function of time; catalyst treatment in air/NH_3/3-PIC; A) VMoON-1.5 catalyst and B) VMoO-1.5 catalyst

to considered. Already from the direct comparison of the two normalized EPR spectra derived at 350 °C after 60 min under feed conditions (see Fig. A.19), it is clear, that the shape of these two signals differs. Therefore, spectra simulations of the EPR signals were done to clarify the situation. The results of the spectra simulations are given in Tab. 3.16. A plot of the calculated and experimental signals is shown in Fig. A.20.

Table 3.16.: Parameters for the species x derived by spectra simulation of the EPR signals of VMoON-1.5 and VMoO-1.5 (feed, 350 °C, 60 min); WIDL = line width; C = relative and percentage contribution; A_{EPR}: percentage double integral of the EPR signal; g_{iso}: isotropic g-value

sample	site x	g_{iso}	C	WIDL	A_{EPR} [a.u.]
VMoO-1.5	1	1.95	1 (30 %)	516	$6.8 \cdot 10^6$
VMoO-1.5	2	1.89	2.28 (70 %)	941	$15.5 \cdot 10^6$
VMoON-1.5	1	1.94	1.1 (30 %)	781	$10.8 \cdot 10^6$
VMoON-1.5	2	1.90	1.66 (44 %)	670	$16.3 \cdot 10^6$
VMoON-1.5	3	2.00	1(26 %)	744	$9.6 \cdot 10^6$

The experimental EPR signal at 350 °C of VMoO-1.5 could be successfully reproduced by taking two types of magnetically interacting sites into account. The isotropic g-values of 1.93 and 1.89 point to the fact, that the EPR signal under reaction conditions consists of cluster-like $^{4+}$V-O-V^{4+} sites and cluster-like $^{5+}$Mo-O-Mo^{5+} sites for the VMoO-1.5 catalyst. The percentage contribution of $V^{4+}O_x$ and $Mo^{5+}O_x$ suggest, that the concentration of reduced Mo^{5+} cluster-like species is much higher than that of V^{4+} under working state.

On the contrary, three different isotropic lines have to be superimposed to describe the experimental EPR spectrum of VMoON-1.5 under reaction conditions. Their g-values differ significantly. The two isotropic signals with g = 1.90 and 1.94 can be detected almost in equal amounts. Site 1 might arise from magnetically interacting V^{4+}-O-V^{4+} clusters, while site 2 may be assigned to magnetically interacting Mo^{5+}-O-Mo^{5+} clusters. Interestingly for both sites the isotropic g value deviates slightly from that reported in literature (g = 1.96 for $V^{4+}O_x$ and g = 1.89 for $Mo^{5+}O_x$) [138–142], indicating that an exchange interaction might influence the two g-values mutually. Surprisingly, the third signal in VMoON-1.5 found by spectra simulation has an isotropic g-value of 2.00, which is in principle somewhat too high for both $V^{4+}O_x$ and $Mo^{5+}O_x$ clusters. Possibly, exchange interaction within mixed V-O-Mo units modifies the internal field which in turn leads to such a g shift. Indeed, electron transfer between V and Mo has been experimentally detected. For edge-shared V-O-Mo units in $V_6Mo_4O_{25}$ an IVCT transition V^{5+}-O-Mo^{5+} $\longleftrightarrow$ V^{4+}-O-Mo^{6+} has been observed, in which one electron is shifted. Hence, the third signal with g = 2.00 might arise from edge-shared V^{4+}-O-Mo^{6+} units, in which the exchange interaction is caused by neighbored V^{4+}-O-Mo^{6+} and/or V^{5+}-O-Mo^{5+} sites. The assignment of these three structure units (Mo^{5+}-O-Mo^{5+}, ${}^{4+}V$-O-V^{4+} and V^{5+}-O-Mo^{5+}/V^{4+}-O-Mo^{6+}) sites demand the presence of two different Mo and at least two different V sites. Results derived by XPS for the used VMoON-1.5 catalyst confirm the presence of such sites.

Moreover, results from spectra simulations suggest, that a higher concentration of cluster-like V^{4+}-O-V^{4+} sites is detected for VMoON-1.5 ($A_{EPR} = 10.8 \cdot 10^6$ a.u.) than for VMoO-1.5 catalysts ($A_{EPR} = 6.78 \cdot 10^6$ a.u.) under ammoxidation conditions; thus the higher selectivity of VMoON-1.5 compared to VMoO-1.5 might be due to a higher concentration of V^{4+} under reaction conditions (see Fig. 3.27 B). However, besides V^{4+}-O-V^{4+} species, probably also edge-shared V^{4+}-O-Mo^{6+} and V^{5+}-O-Mo^{5+} sites may play a significant role during ammoxidation to achieve high a selectivity.

Therefore, in situ Raman microscopy studies on VMoON-1.5 and VMoO-1.5 were done to monitor the changes of the two catalysts during ammoxidation. Results from this study are presented in the next section.

In situ Raman microscopy investigations during ammoxidation using VMoON-1.5 and VMoO-1.5 catalysts In Fig. 3.42 two Raman spectra taken at RT on an object plate are depicted for VMoON-1.5 and VMoO-1.5, as well.

Distinct bands assigned to V_2MoO_8 are detected in the sample VMoO-1.5 [147, 148], while the Raman spectra of the corresponding oxynitride show two broad bands at around 1500 cm^{-1} assigned to a ν(N=N) vibration [149–151]. However, the broad band superimposed on the

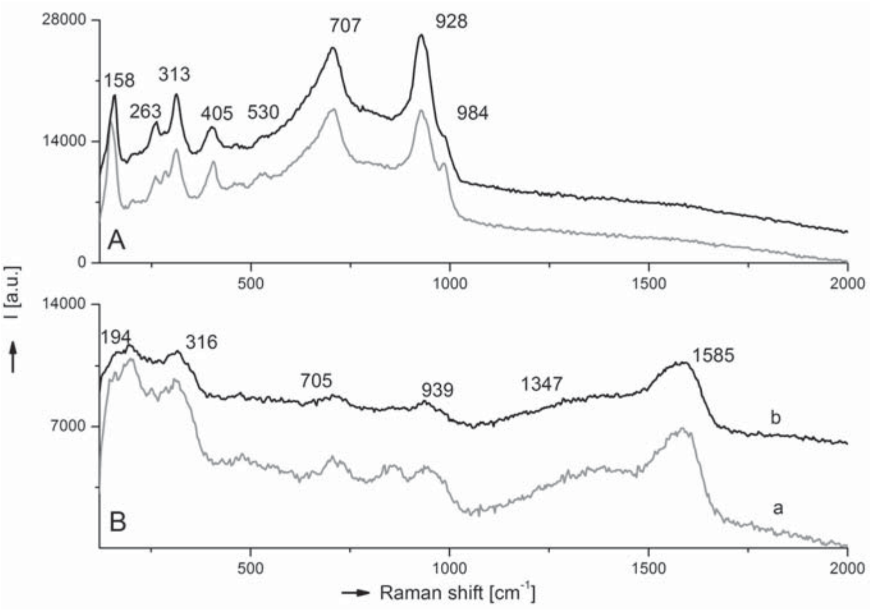

Figure 3.42.: Raman spectra measured at RT on an object plate of A) VMoO-1.5 and B) VMoON-1.5

N=N vibration band indicates that besides N=N species also other nitrogen containing species contribute to the spectrum. In agreement with XRD, XPS and UV-Vis results it can be stated that V_2MoO_8 is destroyed during nitridation.

The in situ Raman microscopy studies during ammoxidation were performed in a fixed bed reactor. First of all, the two samples were heated in He to 200 °C. Then it was switched to NH_3/He at the same temperature, subsequently oxygen was added to the feed and finally it was switched to the entire reaction feed including 3-PIC. After heating to the reaction temperature of 360 °C, spectra were taken with time on stream. 3-PIC and 3-CP were condensed in a cooling trap at the exit of the reactor, while the composition of the rest gas was analyzed via MS.

It turned out that almost no changes were detected for the Raman spectra of VMoO-1.5 catalyst under ammoxidation conditions as it exemplified by the spectra given in Fig. A.21. This is consistent with results from XRD and UV/Vis, which also indicate that the structure of the catalyst is almost stable under ammoxidation conditions.

In contrast, marked changes on the Raman spectra are seen already before switching to the reaction feed during in situ investigations with VMoON-1.5 sample. In Fig. 3.43 A Raman spectra taken at elevated temperature are depicted for the latter sample. As evident from this figure, new bands appear when switching from NH_3/He to an oxygen containing stream at around 240 °C, while the vibration bands assigned to -N=N- units diminish. New narrow intense bands at 707, 849 and 918 cm^{-1} appear for the first time. Simultaneously, less intense bands at around 1682 cm^{-1} occur, which can be assigned to overtone vibrations of the bands at 707, 849 and

918 cm^{-1}. Interestingly, no typical bands of V=O (1030 cm^{-1}) and Mo=O (996 cm^{-1}) units are seen, indicating the absence of these structure units [152]. Bands between 600 and 980 cm^{-1} are characteristic for solid solutions of V and Mo [153]. The assignment of these bands will be discussed below.

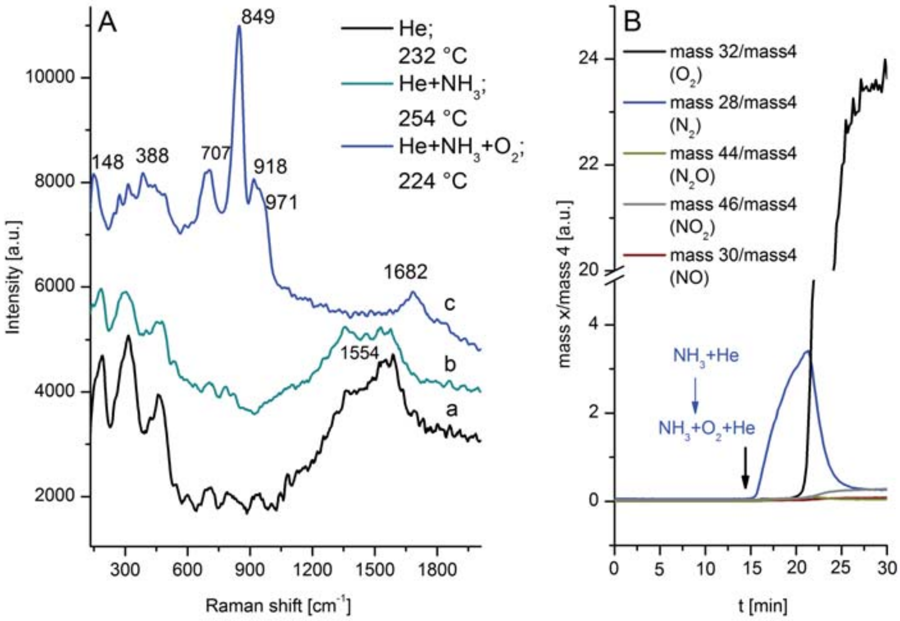

Figure 3.43.: A) In situ Raman spectra of VMoON-1.5, a: in He (25 ml/min) , b: in 16 % NH_3/He, c: in NH_3/O_2/He (1 : 1.25 : 4); B) MS spectra recorded during switching from NH_3/He to NH_3/O_2/He

Moreover, a strong increase of the mass traces being typical for molecular N_2 could be observed in the mass spectrum , when switching from an NH_3/He to NH_3/O_2/He stream. Interestingly, the concentration of O_2 (mass 32) is increasing slowly, while simultaneously the concentration of NO, NO_2 and N_2O does not increase (see Fig. 3.43 B). This suggest that during the change of catalyst structure, in which mainly N_2 is released, also a consumption of oxygen takes place. Note that when oxygen was added to stream, the oven temperature increased from 240 to around 350 °C and decreased again due to an exothermic reaction. This indicates, that the structure of the VMoON-1.5 catalyst is extremely sensitive to an oxygen containing feed at elevated temperatures. The phase transformation occurs already as soon as O_2 is added to stream, which is accompanied by a release of molecular N_2 and an uptake of O_2 from the gas phase.

This is also supported by results of temperature programmed oxidation (TPO) experiments with VMoON-1.5 depicted in Fig. A.22. After desorption of H_2O and NH_3 below 300 °C, an increase of the mass 28 is observed. Simultaneously the sample starts to consume oxygen at around 260 °C.

Moreover, in the course of the in situ Raman microscopy experiment it was switched from a mixture of NH_3/O_2/He to the complete feed containing 3-PIC, H_2O, NH_3, O_2 and He at around 250 °C. Subsequently, it was heated to the reaction temperature of 360 °C.

In Fig. 3.44 in situ Raman spectra of the VMoON-1.5 catalyst are shown recorded with time on reaction stream.

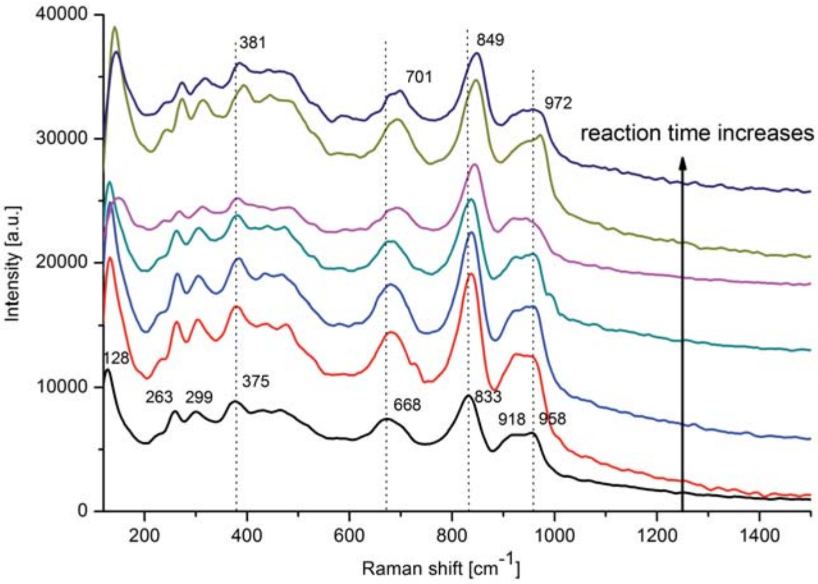

Figure 3.44.: In situ Raman spectra of VMoON-1.5 under feed conditions as function of time; reaction time ≈ 110 min

As evident from this comparison, a significant shift of the main bands from 833 to 849 cm^{-1} is observed. Also bands at 668 cm^{-1} and around 958 cm^{-1} shift to higher wavenumbers with time on reaction stream. This shifting can have several reasons. First of all, this shift is not related to crystal growth, since no decrease of the band width is observed simultaneously. Thus, the shift is caused by another effect. It might be due to a change of the valence state and/or a change of the V content. Supportingly, an increase of the V concentration during ammoxidation in the near-surface region for the VMoON-1.5 catalyst is already indicated by XPS results (compare results of fresh and used VMoON-1.5 catalysts in Tab. 3.14). Since the experimental chemical surface composition of the used VMoON-1.5 catalysts calculated from XPS is close to that of $V_6Mo_4O_{25}$, it is probable, that the Raman bands after ca. 110 min are characteristic for the latter phase. The strong band at 849 cm^{-1} might reflect V-O-Mo bonds, while the two bands at 701 cm^{-1} and 972 cm^{-1} might be mainly attributed to Mo-O-Mo and V-O-V stretching vibrations. However, these Raman bands are also close to those observed for Mo_5O_{14} containing V sites [154, 155].

Finally, the rapid increase of selectivity S_{3-CP} and conversion X_{3-PIC} (see Fig. 3.27 A) with time on stream for VMoON-1.5 catalyst might be caused by the migration of V species from the bulk to the surface and the formation of a surface with a composition and structure close to $V_6Mo_4O_{25}$.

3.4.4. Conclusions on VMoON catalysts

VMoON oxynitride catalysts are highly selective ammoxidation catalysts. In this work, it turned out that a ratio of V/Mo = 1.5 in VMoON catalysts provides the best catalytic performance (X_{3-PIC} = 76 %, S_{3-CP} = 96 % and STY = 228 g/lh at T_B = 360 °C and GHSV = 2713 h^{-1}). On the contrary, the corresponding VMoO-1.5 oxide catalyst is less active and selective. In contrast to VMoO catalysts a short activation period was observed for VMoON catalysts, in which both S_{3-CP} and X_{3-PIC} increase. This suggests that the structure of VMoON catalysts is changed under ammoxidation conditions and that the catalytically active species in the as received oxynitride are at least less active than the catalytically active sites in the structure of the equilibrated formed catalyst.

Results from XRD, XPS and UV/Vis-DRS as well as in situ EPR spectroscopy and in situ Raman microscopy investigations confirm that marked structural changes are observed for VMoON-1.5 catalysts during ammoxidation, while the structure of the VMoO-1.5 catalyst is almost not changed. A mixture consisting of $V_6Mo_4O_{25}$, $V_4Mo_6O_{25}$ and $VMoO_5$ is formed during ammoxidation in the oxynitrides as indicated by XRD.

Interestingly, conversion increases with rising V/Mo ratio in the VMoON series, while the selectivity takes values between 86 and 96 %. By comprehensive analytical studies applied ex situ before and after use in ammoxidation as well as in situ during ammoxidation on VMoON oxynitrides and VMoO oxides, it was found that the selectivity in the VMoON catalyst series is related to the chemical nature of V species formed during calcination of VMoO oxide precursors. VMoO oxides contain crystalline V_2MoO_8 besides an amorphous V containing phase. The correlation between the selectivity of VMoON catalysts and the percentage of crystalline V_2MoO_8 with respect to amorphous V containing phase suggests that the latter does not contribute to a high selectivity. Rather a high amount of crystalline V_2MoO_8 seems to be beneficial to obtain high selectivities in the ammoxidation of 3-PIC with VMoON catalysts. Additionally, it turned out by kinetic UV/Vis-DRS studies, that V_2MoO_8 can be reduced in a reducing atmosphere and fully reoxidzed, while the amorphous V containing phase stays in its reduced state.

Crystalline V_2MoO_8 in VMoO oxides is especially prone to nitridation and an almost X-ray amorphous structure is created by nitridation at 500 °C containing a high percentage of reduced V species as it is suggested by UV/Vis-DRS results and in situ EPR spectroscopy. This effect is especially well seen for the sample with V/Mo = 1.5, which contains the highest content of crystalline V_2MoO_8 among the investigated VMoO samples prior nitridation; thus the corresponding oxynitride also contains the highest N content among the investigated VMoON samples. During ammoxidation a mixture of a new solid solution is formed consisting of $V_6Mo_4O_{25}$, $V_4Mo_4O_{25}$ and $VMoO_5$. It seems that the higher the amount of V_2MoO_8, the higher the amount of the latter mixture. Thus the catalyst VMoON-1.5 shows the highest selectivity to 3-CP in the VMoON series. So it is reasonable, that the selectivity in the VMoON catalyst series is related to the chemical nature of V species formed during calcination of VMoO oxide precursors.

Interestingly, the formation of $V_6Mo_4O_{25}$, $V_4Mo_4O_{25}$ and $VMoO_5$ is accompanied by a reoxidation of V sites and a loss of nitrogen indicating that nitridation plays a crucial role for this phase transformation. Results of in situ Raman microscopy studies coupled with MS as well as TPO results indicate that N sites in VMoON catalysts are released as molecular N_2. In principle, by comparing the oxygen concentration in the solid solution V_2MoO_8 with that in the mixture ($V_6Mo_4O_{25}$, $V_4Mo_4O_{25}$ and $VMoO_5$), it is clear that the mixture contains types of solid solutions which possess less oxygen than V_2MoO_8. This implies indirectly that by nitridation of VMoO and V_2MoO_8, respectively, oxygen anions are replaced by nitrogen and anionic vacancies according to the equation 2.2. In contrast to VZrAlON, VAlON or VZrON catalysts, these vacancies are annealed in VMoON oxynitrides under ammoxidation conditions by formation of a mixture containing $V_{6/4}Mo_{4/6}O_{25}$ and $VMoO_5$, which is accompanied by a release of nitrogen. The latter three solid solutions have one common structural feature in contrast to V_2MoO_8. They provide a high concentration of edge-shared V-O-Mo units, while the structure of V_2MoO_8 is mainly characterized by edge-shared V-O-V units. XPS as well as UV/Vis-DRS results on VMoON-1.5 catalysts after use in ammoxidation suggest, that therefore a distinct IVCT transition can occur in these catalysts, which might facilitate the electron transport from the bulk to the surface and vice versa. This effect probably may account for the higher selectivity of VMoON-1.5 catalyst in comparison to the VMoO-1.5 catalyst. The lower conversion of the latter catalyst is probably mainly due to the fact that the oxide contains a lower amount of V surface sites as it is evident from results of XPS.

Moreover in situ EPR investigation indicates, that the percentage of cluster-like V^{4+}-O-V^{4+} and certainly of V^{5+}-O-$Mo^{5+} \longleftrightarrow V^{4+}$-O-$Mo^{6+}$ units is much higher in VMoON-1.5 catalysts than in VMoO-1.5 catalysts under working state. Moreover, it is evident from XPS that both catalyst classes are able to incorporate nitrogen into their structure during ammoxidation. For both catalysts, the same N site (probably NH_4^+) is observed by XPS, even in higher surface concentration for VMoO-1.5. This suggests that the incorporation of nitrogen into the benzyl-like intermediate proceeds in the same way. Nitrogen species being introduced by nitridation in the VMoON catalysts obviously only support the phase transformation from V_2MoO_8 to $V_6Mo_4O_{25}$, $V_4Mo_4O_{25}$ and $VMoO_5$. Thus, nitrogen sites introduced by nitridation do possibly not contribute to the higher selectivity of VMoON catalysts compared to VMoO catalysts.

Finally, this structure-reactivity relationship suggests, that a catalyst consisting of stable $V_6Mo_4O_{25}$ nanocrystals might be an excellent catalyst for the ammoxidation of heteroaromatics. However, to our knowledge, no literature is published which provides a synthesis procedure for this kind of material.

3.5. VSbON oxynitrides

Beside VAlON, VZrON and VMoON catalysts, it was decided to investigate also the potential of VSbON catalysts. VSbO oxide precursors were synthesized by a long-term refluxing procedure. Different V/Sb ratios were adjusted during this synthesis. These VSbO oxide precursors were treated in three different ways: 1) VSbO oxide precursors were calcined at 500 °C and subsequently nitrided at 500 °C. These samples are called precalcined VSbON-x.x oxynitrides. 2) VSbO oxide precursors were directly nitrided at 500 °C. These samples are called non-precalcined VSbON-x.x* oxynitrides and are labeled with a star. 3) VSbO oxide precursors were calcined at 500 °C. These samples are called calcined VSbO-x.x oxides. x.x denotes the V/Sb ratio, which was adjusted from 0.2 to 2.0. These three types of VSb containing compounds were catalytically and structurally characterized. The major focus of the investigation in this section is on the precalcined VSbON oxynitride series.

3.5.1. Catalytic performance

In Fig. 3.45 A - D the catalytic performance of precalcined VSbON catalysts is depicted as a function of time on stream t for four different V/Sb ratios ranging from 0.2 up to 2.0.

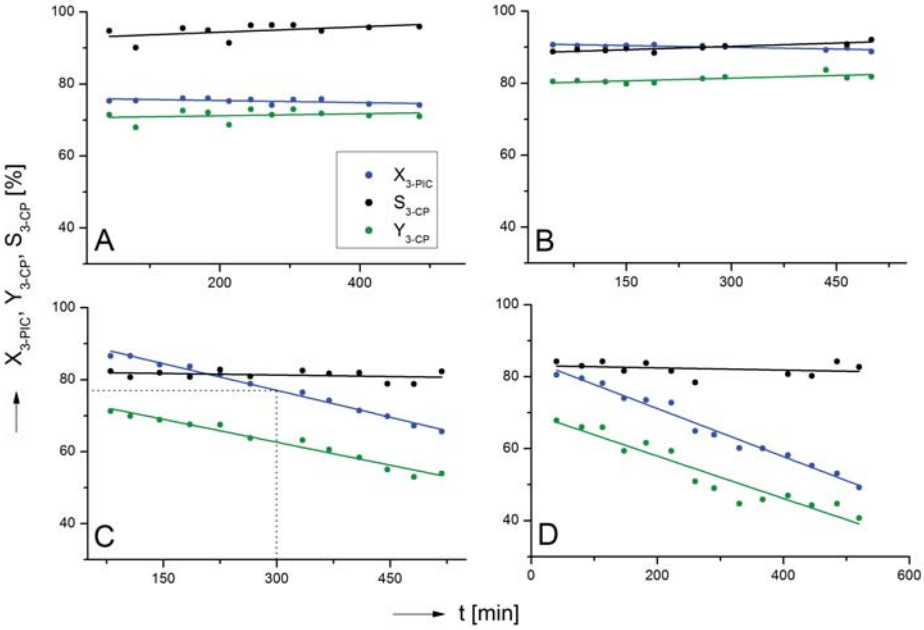

Figure 3.45.: Catalytic performance for precalcined VSbON oxynitrides as a function of the V/Sb ratio and time on stream at T_B = 360 °C and GHSV = 2713 h^{-1};
A) VSbON-0.2; B) VSbON-0.5; C) VSbON-1.0 and D) VSbON-2.0

Depending on this ratio the catalysts can be subdivided into deactivating and non-deactivating catalysts. At a ratio higher than 0.5 the conversion X_{3-PIC} decreases with reaction time at almost constant selectivity S_{3-CP}. At ratios lower than 1.0 an almost constant conversion is observed with time, while S_{3-CP} increases slightly. In the precalcined VSbON series the best catalytic performance can be reached using a ratio of V/Sb = 0.5, since this catalyst has a stable catalytic activity over time and a yield of about 80 %. However, the highest selectivity of almost 100 % in the precalcined VSb oxynitride series can be observed for the lowest V/Sb ratio.

Two oxynitride catalysts with V/Sb = 0.5 and 1.0 were prepared without precalcination prior to nitridation (VSbON-0.5* and VSbON-1.0*) to elucidate the influence of the precalcination step on the catalytic performance of oxynitrides. Additionally the catalytic performance of a calcined VSbO oxide with V/Sb = 0.5 was investigated. A comparison for the results of this study is given by Fig. 3.46 A - D.

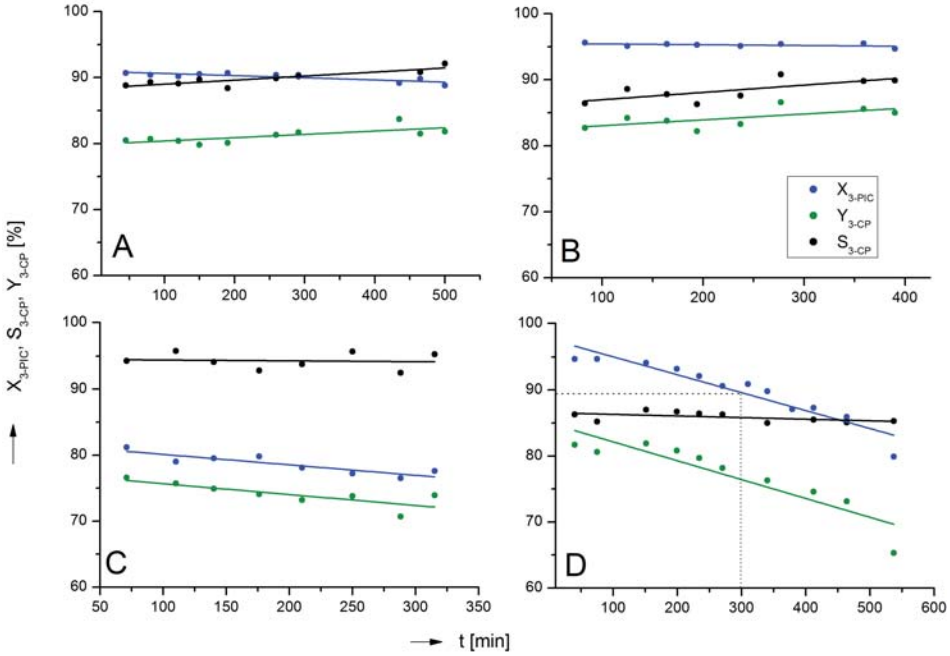

Figure 3.46.: Catalytic performance of different prepared VSb containing catalysts as a function of the time on stream at T_B = 360 °C and GHSV = 2713 h^{-1};
A) VSbON-0.5; B) VSbON-0.5*; C) VSbO-0.5 and D) VSbON-1.0*

By comparing Fig. 3.46 A - C it can be seen, that the precalcined VSbON-0.5 oxynitride and the non-precalcined VSbON-0.5* oxynitride as well as the corresponding calcined oxide VSbO-0.5 differ in their catalytic performance despite an almost identical bulk V/Sb ratio (see Tab. 3.18). Interestingly, for the oxide a slight decrease of the conversion is seen with time on stream, while the two corresponding oxynitrides possess an almost stable conversion with time on stream.

The highest and almost constant selectivity of $\approx 95\ \%$ can be observed for the VSbO-0.5 oxide. For the precalcined as well as for the non-precalcined VSb oxynitrides a slight increase of S_{3-CP} can be observed with time on stream, whereby the highest conversion is achieved by the non-precalcined VSbON-0.5* catalyst. The highest yield of 3-CP is obtained with VSbON-0.5*.

Moreover, by comparing Fig. 3.45 C and Fig. 3.46 D it can be seen, that omitting the calcination step is not avoiding the deactivation process. For both catalysts VSbON-1.0 and VSbON-1.0* a decline of X_{3-PIC} appears with time. However, also for these two catalysts a difference in the catalytic performance is detected. By comparing the catalytic performance at 300 min, a higher conversion and selectivity for the non-precalcined catalysts VSbON-1.0* can be observed (compare dotted lines in Fig. 3.45 C and Fig. 3.46 D). This trend is also valid for X_{3-PIC} of the catalysts VSbON-0.5 and VSbON-0.5* (see Fig. 3.46 A and 3.46 B).

For a better comparison of the catalytic performance of VSb catalysts, the initial values of X^0_{3-PIC}, S^0_{3-CP} and Y^0_{3-CP} at t = 0 are summarized in Tab. 3.17 for VSb containing catalysts [12]. Generally, all the already mentioned trends discussed for the relations given in Fig. 3.45 and 3.46 can be confirmed by comparing the initial catalytic performance listed in this table. The highest initial conversion and yield can be reached using a non-precalcined oxynitride catalyst with V/Sb = 1.0. The highest selectivity among VSb catalysts can be observed for the oxide VSbO-0.5 catalyst, but the initial conversion is significantly lower in comparison to the other VSb catalysts.

Table 3.17.: Initial catalytic performances for VSb containing catalysts

catalyst	X^0_{3-PIC}	S^0_{3-CP}	Y^0_{3-CP}	remark
VSbON-0.2	76	93	71	X_{3-PIC} = const., slight increase of S_{3-CP}
VSbON-0.5	88	91	80	X_{3-PIC} = const., slight increase of S_{3-CP}
VSbON-1.0	91	82	75	decrease of X_{3-PIC}, S_{3-CP} = const.
VSbON-2.0	85	83	70	decrease of X_{3-PIC}, S_{3-CP} = const.
VSbON-0.5*	96	86	82	X_{3-PIC} = const., slight increase of S_{3-CP}
VSbON-1.0*	98	87	85	decrease of X_{3-PIC}, S_{3-CP} = const.
VSbO-0.5	82	95	77	slight decrease of X_{3-PIC}, S_{3-CP} = const.

3.5.2. Structural characterization of VSbON catalysts

Chemical composition and BET surface areas The chemical composition derived by CHN and ICP-OES analysis of fresh and used VSbO oxides, precalcined VSbON oxynitrides and

---

[12] The values X^0_{3-PIC}, S^0_{3-CP} and Y^0_{3-CP} were calculated by finding the intercept of each line with the ordinate at t = 0 given in Fig. 3.45 and 3.46 via linear regression.

non-precalcined VSbON* oxynitrides are listed in Tab. 3.18. Additionally the N/V ratios and surface areas S_{BET} are given for each of these samples.

Table 3.18.: Chemical compositions, N/V bulk ratios and surface areas S_{BET} of fresh and used VSb catalysts derived by ICP-OES and CHN analysis

	Chemical compositions		N/V-ratio		S_{BET} $[m^2g^{-1}]$	
catalyst name	fresh	used	fresh	used	fresh	used
VSbO-0.25	$V_{0.21}SbO_{2.37}$	-	0	-	8.3	-
VSbO-0.5	$V_{0.50}SbO_{2.60}$	$V_{0.50}SbO_{3.23}N_{0.08}$	0	0.15	3.0	5.3
VSbO-1.0	$V_{1.06}SbO_{4.18}$	-	0	-	4.5	-
VSbO-2.0	$V_{1.98}SbO_{6.85}$	-	0	-	8.3	-
VSbON-0.25	$V_{0.26}SbO_{1.12}N_{0.04}$	$V_{0.24}SbO_{1.82}N_{0.03}$	0.14	0.15	12.8	10.9
VSbON-0.5	$V_{0.50}SbO_{1.26}N_{0.04}$	$V_{0.50}SbO_{2.25}N_{0.05}$	0.07	0.11	21.0	10.6
VSbON-1.0	$V_{1.01}SbO_{2.14}N_{0.05}$	$V_{1.02}SbO_{3.00}N_{0.18}$	0.05	0.17	33.0	8.0
VSbON-2.0	$V_{2.17}SbO_{4.07}N_{0.46}$	$V_{2.04}SbO_{5.27}N_{0.36}$	0.21	0.18	28.0	6.7
VSbON-0.5*	$V_{0.52}SbO_{1.41}N_{0.04}$	$V_{0.50}SbO_{2.40}N_{0.07}$	0.07	0.15	19.3	13.5
VSbON-1.0*	$V_{0.97}SbO_{1.32}N_{0.07}$	$V_{1.01}SbO_{3.51}N_{0.19}$	0.07	0.19	26.5	9.4

First of all, the highest N content among the fresh VSb oxynitrides can be detected for precalcined VSbON-2.0 oxynitride, while the N contents for the fresh precalcined VSbON catalysts with V/Sb < 2.0 are almost equal and much lower. Comparing the chemical composition of the fresh precalcined and fresh non-precalcined catalysts, it is evident for both V/Sb ratios of 0.5 and 1.0, that it is not possible to introduce more nitrogen into VSb containing catalysts via direct nitridation of the non-calcined oxide precursors.

When the fresh precalcined VSbON catalysts are used in the ammoxidation, a clear trend concerning the N content is visible. The bulk N content continuously increases with rising the V concentration. This phenomenon is also seen for the two used non-precalcined VSbON-0.5* and VSbON-1.0* samples. Moreover, the N content either increases or declines in dependence of the V/Sb ratio through use in ammoxidation. When a ratio of V/Sb = 0.5 and 1.0 is adjusted, the N content increases during ammoxidation in the precalcined and non-precalcined VSbON series. For the lower and higher ratios 0.25 and 2.0 a loss of nitrogen is observed.

A loss of volatile Sb during nitridation or ammoxidation can be excluded, since the ratios of V/Sb in the fresh and used catalyst are almost the same. Additionally, the C content in all used VSb catalysts ranges only between 0.05 and 0.1 wt.-%, suggesting that deposition of carbon species on the catalyst surface can be neglected. Thus, the observed deactivation is not caused by C deposition or leaching.

XRD In Fig. 3.47 A, B and C the XRD patterns of fresh calcined VSbO oxides as well as fresh and used precalcined VSbON oxynitrides are depicted as a function of the V/Sb ratio.

Depending on the V/Sb ratio different crystalline phases can be detected for the fresh calcined VSbO oxides (see Fig. 3.47 A). At low V concentration typical reflections for antimony oxide phases are dominating in the XRD pattern. According to the ICCD database mainly Sb_2O_4 is generated beside traces of SbO_2 and $SbVO_4$. By rising the V/Sb ratio the amount of crystalline $SbVO_4$ increases, while the crystalline antimony oxide phases are hardly observed.

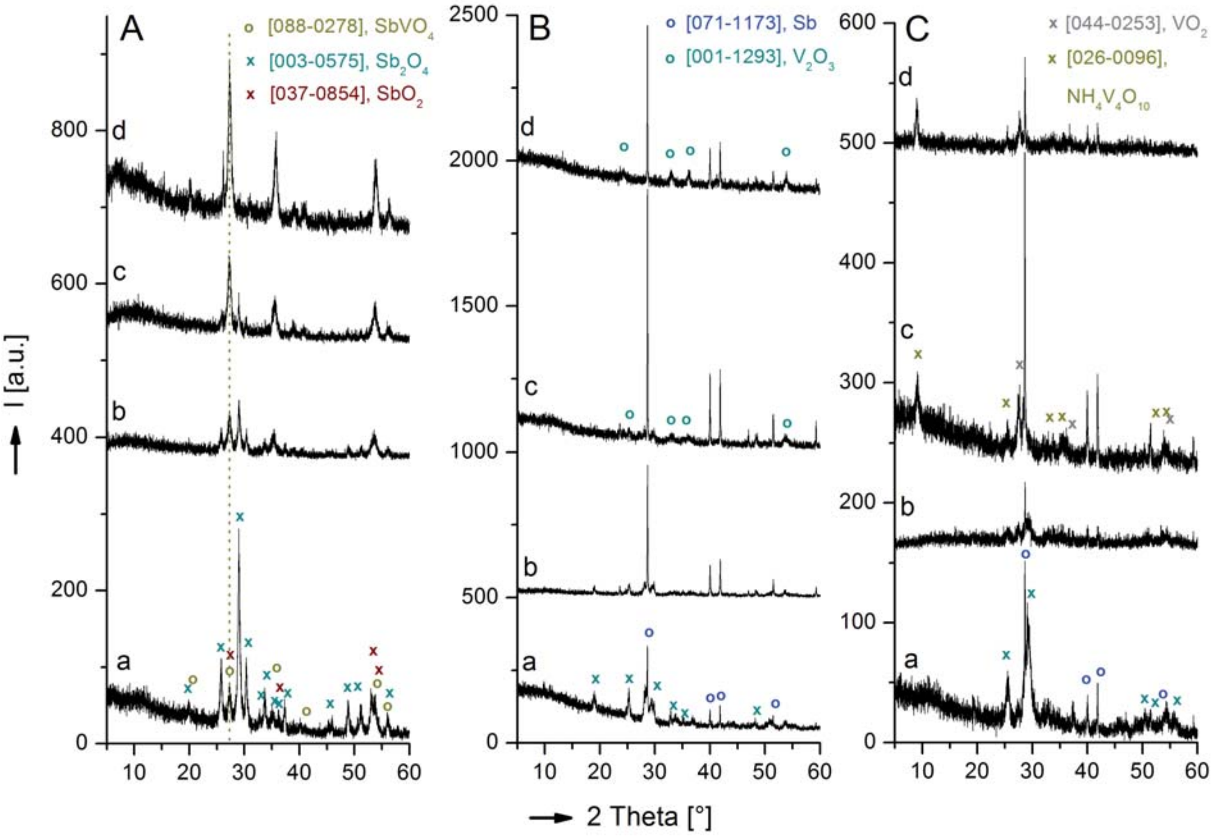

Figure 3.47.: Powder XRD pattern for VSb containing catalysts depending on the V/Sb ratio (a = 0.2, b = 0.5, c = 1.0 and d = 2.0); A) Fresh calcined VSbO oxides; B) Fresh precalcined VSbON oxynitrides and C) Used precalcined VSbON oxynitrides

The corresponding XRD patterns for the fresh precalcined oxynitrides VSbON are also given as a function of the V/Sb ratio in Fig. 3.47 B. Each pattern in this series is characterized by several strong narrow reflections, which can be assigned to elemental antimony. According to the most intense reflection of Sb at around 29 °, the highest amount of crystalline Sb is observed for the VSbON-1.0 catalyst, in which the bulk concentration of Sb and V is almost equal. For $V/Sb \geq 1.0$ the reflection intensity of elemental Sb decreases again. The lowest concentration of elemental crystalline Sb is surprisingly observed for the oxynitride catalysts with V/Sb = 0.2, in which the bulk concentration of Sb is five times higher than the V concentration. This trend is supported by calculating the area of the most intense reflection of the Sb phase at 28.6 ° in the XRD pattern of the fresh VSbON catalysts (see Fig. 3.48). Obviously, amorphous and crystalline antimony oxide phases are almost resistant to deep reduction during nitridation. Consequently, a substitution of O by N in these phases might not occur. Especially, $SbVO_4$ might be decomposed to elemental Sb and V_xO_y, V_xO_y and/or V_xN_y during nitridation. This would explain, why the fresh catalysts VSbON-1.0 contains the highest percentage of elemental Sb.

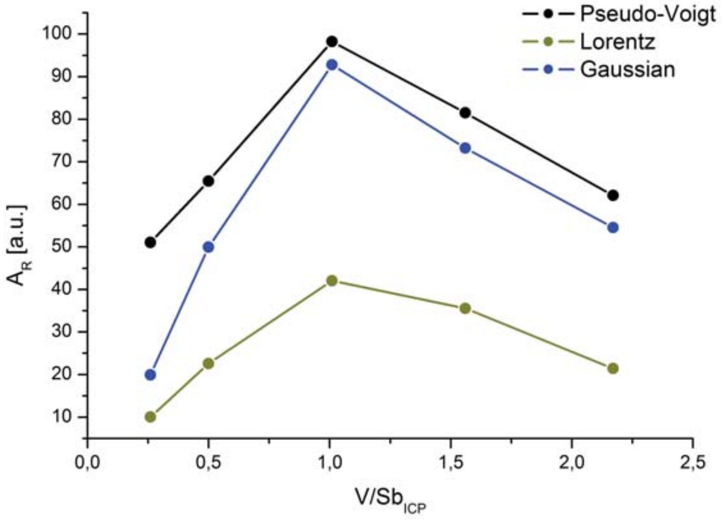

Figure 3.48.: Relative concentration of elemental Sb in fresh precalcined VSbON catalysts derived by calculation of the peak area A_R at 28.6 ° assuming a line shape based on pseudo-Voigt, Lorentz or Gaussian functions

Moreover, in the XRD patterns of the fresh precalcined oxynitride catalysts with V/Sb ratios ≥ 1.0 additional weak broad reflections are seen. These reflections can be assigned to reduced V_2O_3. Interestingly, traces of V_2O_3 can be detected only for those precalcined VSbON catalysts by XRD, which deactivate with time on stream.

By inspecting the XRD powder patterns of the used precalcined VSbON oxynitrides, which are given in Fig. 3.47 C, again marked changes can be observed, indicating that ammoxidation has also a strong impact on the crystalline phases in VSbON oxynitrides. First of all, the narrow reflections being typical for elemental Sb are strongly loosing intensity. Considering the feed composition during ammoxidation, which is more oxidizing than reducing, this effect can be understood easily. Moreover two new additional phases can be detected in the XRD pattern of the used VSb oxynitrides with V/Sb $\geq$ 1.0. According to the ICDD database these new phases are VO_2 and $NH_4V_4O_{10}$.

In Fig. 3.49 A the powder XRD patterns of the fresh precalcined and fresh non-precalcined oxynitride with V/Sb = 1.0 are shown to elucidate the impact of the precalcination step on crystalline phases. Without doubt, the formation of crystalline Sb can also be observed in the XRD pattern of the non-precalcined fresh VSbON-1.0* catalyst, yet in a significantly lower amount than for the precalcined VSbON-1.0 catalyst (see also Fig. 3.49).

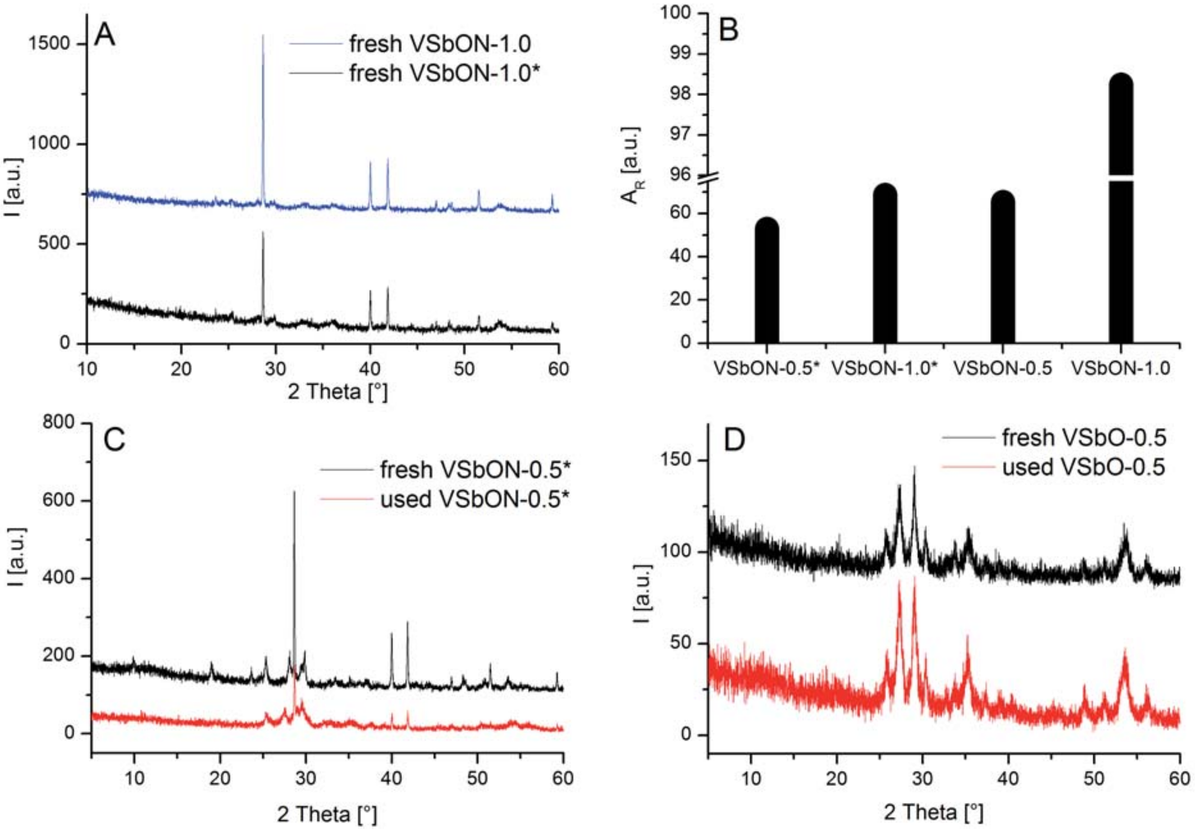

Figure 3.49.: Impact of calcination on crystalline phases of VSbON catalysts; A) Powder XRD pattern of fresh precalcined VSbON-1.0 and non-precalcined VSbON-1.0*, B) Peak area A_R of the Sb reflection at 28.6 ° for fresh precalcined VSbON and non-precalcined VSbON* oxynitrides with V/Sb = 0.5 and 1.0, C) XRD patterns of fresh and used non-precalcined VSbON-0.5* catalysts, D) XRD patterns of fresh and used calcined VSbO-0.5 oxide catalysts

Fig. 3.49 B compares the area of the most intense Sb reflection at 28.6 ° of precalcined and non-precalcined fresh oxynitrides. It is evident from this plot, that also for V/Sb = 0.5 the formation of elemental Sb is partially suppressed when precalcination prior to nitridation is omitted. However, the effect is more pronounced for the ratio V/Sb = 1.0 than for 0.5. Thus, it must be concluded that the precalcination of VSbO precursors prior nitridation favors the formation of elemental crystalline Sb during nitridation. This might be due to the fact, that the calcination prior nitridation generates a higher concentration of $SbVO_4$. From this compound elemental Sb is formed.

Moreover, the XRD patterns of the fresh and used oxynitrides VSbON-0.5* are depicted in Fig. 3.49 C. A dramatic loss of elemental Sb is indicated by the decrease of the Sb reflection intensity in the used sample, as it is also the case for precalcined VSbON catalysts.

Additionally the XRD patterns of fresh and used VSbO-0.5 oxide catalysts are given in Fig. 3.49 D. In contrast to the oxynitride catalysts, almost no changes can be observed for the reflection intensity and position. As mentioned above, beside traces of SbO_2 and $SbVO_4$ mainly Sb_2O_4 is detected by XRD in these samples.

Characterization by XPS More information about the chemical surface composition and N containing surface sites was gained by XPS. Among the precalcined VSbON series, the fresh and used catalysts VSbON-0.5 and VSbON-2.0 were investigated by XPS. Additionally, XPS results of fresh and used non-precalcined VSbON*-0.5 as well as calcined VSbO-0.5 are discussed. The binding energies E_B, the surface concentration c for each detected surface site in these catalysts and elemental ratios are given in Tab. 3.19.

XPS results of precalcined VSbON catalysts with V/Sb = 0.5 and 2.0: Results of the XPS analysis for the fresh and used catalysts of the precalcined VSbON series are discussed first. Among the precalcined VSbON catalysts the fresh and used VSbON-0.5 and VSbON-2.0 samples were analyzed.

First of all, from Tab. 3.19 it is evident, that the E_B values of the respective surface elements in the two fresh precalcined catalysts VSbON-0.5 and VSbON-2.0 are almost the same, however their surface concentrations c differ clearly. Three types of N sites can be observed for both fresh samples with E_B values between 397 and 402 eV. The site N^1 with the lowest N1s binding energy can be assigned to nitride-like sites, while N^2 might reflect NH_x sites (x = 1 or 2). N^3 sites are due to NH_4^+ species. Interestingly, the surface concentration c of the three N sites increases with their binding energies and site N^3 dominates in fresh VSbON-0.5 and VSbON-2.0 catalysts. The VSbON-2.0 catalyst contains a much higher surface N concentration than VSbON-0.5 which is consistent with the respective bulk N contents (see also Tab. 3.18).

Moreover, two distinct V sites are present on the surface of both catalysts. Their binding energies E_B and ΔE_B values are characteristic for a mean surface V valence state of 4.5 and 4.0 according ref. [79] and Fig. 3.4. Interestingly, the concentrations of both V sites differ clearly in the two fresh catalysts. For the fresh VSbON-2.0 catalysts the percentage of the higher oxidized V site V^2 is remarkably higher than that of the reduced site V^1. In VSbON-0.5 with the low V/Sb ratio the reduced site V^1 dominates on the surface. Therefore, it must concluded, that the mean V surface oxidation state is significantly lower for the fresh VSbON-0.5 than for the fresh VSbON-2.0.

Table 3.19.: Binding energies E_B, surface concentrations c [at.-%] and elemental surface ratios of fresh and used VSb containing catalysts derived by XPS; values in brackets: ΔE_B values

		Fresh VSbON-0.5		Fresh VSbON-2.0		Fresh VSbON-0.5*		Fresh VSbO-0.5	
XPS peak	site	E_B [eV]	c [at.-%]	E_B [eV]	c [at.-%]	E_B [eV]	c [at.-%]	E_B [eV]	c [at.-%]
N1s	N^1	396.9	0.16	397.2	0.72	396.6	0.09	-	0.0
N1s	N^2	400.3	0.19	400.0	0.49	399.6	0.10	-	0.0
N1s	N^3	401.7	0.42	402.0	3.30	401.5	0.43	401.9	0.17
V2p3/2	V^1	516.4 (14.6)	4.31	516.5 (14.3)	5.46	516.0 (14.7)	4.81	-	0.0
V2p3/2	V^2	517.3 (13.7)	1.29	517.8 (13.0)	13.07	517.2 (13.5)	3.68	517.6 (11.7)	3.64
O1s	O^1	529.8	46.86	-	-	529.5	14.26	527.4	0.62
O1s	O^2	531.0	36.14	530.8	60.78	530.7	60.79	531.2	70.55
Sb3d3/2	Sb^1	539.0	5.24	-	-	538.6	2.31	-	0.0
Sb3d3/2	Sb^2	540.3	5.38	540.5	3.020	540.1	7.03	540.5	8.38

		Used VSbON-0.5		Used VSbON-2.0		Used VSbON-0.5*		Used VSbO-0.5	
XPS peak	site	E_B [eV]	c [at.-%]	E_B [eV]	c [at.-%]	E_B [eV]	c [at.-%]	E_B [eV]	c [at.-%]
N1s	N^1	-	0.0	397.3	0.06	-	0.0	395.9	0.34
N1s	N^2	398.9	0.18	399.6	0.31	399.7	0.34	398.2	0.43
N1s	N^3	400.9	0.42	401.3	0.45	400.9	0.69	400.2	0.24
V2p3/2	V^1	516.1 (14.0)	1.99	517.0 (13.6)	2.25	516.4 (14.1)	1.91	513.2 (16.9)	1.28
V2p3/2	V^2	-	0.0	-	-	516.9 (13.6)	0.28	516.1 (14.0)	1.71
O1s	O^1	528.8	18.07	-	-	-	0.0	527.0	35.03
O1s	O^2	530.6	68.40	530.6	80.19	530.5	85.48	530.1	46.52
Sb3d3/2	Sb^1	538.7	2.88	-	-	-	0.0	536.0	2.48
Sb3d3/2	Sb^2	540.0	8.11	539.9	10.27	539.9	11.3	539.3	6.86

Elemental surface ratios

fresh catalyst	V/Sb ratio	N/V ratio	used catalyst	V/Sb ratio	N/V ratio
fresh VSbON-2.0	6.14	0.24	used VSbO-0.5	0.22	0.36
fresh VSbON-0.5	0.53	0.14	used VSbON-0.5	0.18	0.30
fresh VSbON-0.5*	0.91	0.07	used VSbON-0.5*	0.19	0.47
fresh VSbO-0.5	0.43	0.05	used VSbO-0.5	0.32	0.34

Remarkably, the VSbON-0.5 catalyst possesses also two types of Sb and O sites, in contrast to VSbON-2.0. This might be due to the presence of an additional antimony oxide phase, which could be detected by XRD for VSbON-0.5, but not for the VSbON-2.0 catalyst.

In addition, the surface V/Sb ratios differ dramatically for the two fresh catalysts. A very high surface V/Sb ratio of 6.14 in VSbON-2.0 indicates, that the near surface region of this catalyst is rich of V and poor of Sb. On the contrary, the surface V/Sb ratio of the fresh VSbON-0.5 catalyst is almost identical to the bulk V/Sb ratio, meaning that this catalyst provides more Sb than V on its surface. The surface N/V ratios are slightly higher than the bulk N/V ratios for VSbON-0.5 and VSbON-2.0. This suggests, that N sites are enriched on the surface in the fresh catalysts.

The surface characteristics of the two precalcined VSbON catalysts are changed after use in the ammoxidation. First of all, in both samples a decrease of the surface V/Sb ratio occurs. This effect is especially pronounced for the catalyst VSbON-2.0, in which V/Sb drops from 6.14 to 0.22. Indeed, this might be the main reason for the observed deactivation process in VSbON catalysts with V/Sb $\geq$ 1.0, since active V sites seem to migrate into the bulk to a considerable extent. A closer look to the V2p3/2 region shows, that for both used precalcined catalysts only one V surface site remains, which differs in its oxidation state for the two catalysts as indicated by the difference in binding energy and ΔE_B value. This V site possesses a higher mean surface oxidation state in the VSbON-2.0 than in the VSbON-0.5 catalyst.

Interestingly, the surface concentration of the remaining V surface site in the used catalysts is only slightly higher for VSbON-2.0 compared to VSbON-0.5. Also the V/Sb ratios do not differ much. Nevertheless the 3-PIC conversion values of both catalysts clearly differ (compare Fig. 3.45 B and D). After around 450 min time on stream, the VSbON-2.0 sample converts only 40 % of 3-PIC, while VSbON-0.5 still converts 80 % of the 3-PIC. This suggests, that the nature of the surface Sb site might have an important impact on the conversion, too. Indeed, two types of surface Sb sites are detected by XPS for the fresh and used catalyst VSbON-0.5, which differ significantly in their oxidation state, since the difference in binding energies between Sb^1 and Sb^2 amounts to 1.3 eV. Typically, as reported in literature the binding energies of the Sb3d3/2 peak in the series of the antimony oxides Sb_2O_3, Sb_2O_4 and Sb_2O_5 increase with the oxidation state of Sb from 539.5 eV (Sb^{3+}) up to 540.4 eV (Sb^{5+}) [156, 157]. This points to the fact, that site Sb^2 in both VSbON catalysts possesses a valence state close to +5, while the site Sb^1 might be threevalent. Moreover, a partial reoxidation of Sb^{3+} to Sb^{5+} is indicated in the catalysts VSbON-0.5, because the concentration of Sb^1 decreases, while the concentration of Sb^2 increases during ammoxidation.

Changes in the N1s region also occur, when using these two catalysts for ammoxidation. The amount of the N species with the low binding energy value N^1 assigned to N^{3-} surface sites drops markedly for both catalysts. This suggests, that nitride-like nitrogen species are not stable during ammoxidation in VSbON-0.5 and VSbON-2.0 catalysts. The surface concentrations of the nitrogen sites N^2 (assigned NH_2^- or NH^{2-}) and N^3 (assigned to NH_4^+) stay almost constant for the VSbON-0.5 catalysts during ammoxidation, while the surface concentration of N^2 and N^3 decreases during ammoxidation for VSbON-2.0. This effect is surprising, since it indicates that the N^{3-} surface sites in VSbON catalysts are not converted into N^2 and N^3 during ammoxidation as it is suggested for VZrAlON-0.5 catalyst in chapter 3.1. However, it should be noted, that also the V concentration is changed during ammoxidation; thus the N/V ratios increase during ammoxidation for both catalysts.

XPS results of fresh and used VSbO-0.5 and VSbON-0.5 compared to VSbON-0.5:* To learn more about the impact of N sites on the catalytic performance in VSb containing catalysts, also the fresh and used VSbO-0.5 oxide as well as non-precalcined VSbON-0.5* catalyst were investigated by XPS. Results of this study are also listed in Tab. 3.19.

For the non-precalcined fresh catalyst VSbON-0.5* almost no changes are visible in the N1s region in comparison to the results of the fresh precalcined VSbON-0.5 sample. Also three N sites can be detected in almost identical amounts. This is also in agreement with the bulk N content, which is almost identical for both catalysts (see Tab. 3.18). However, a clear difference can be observed for the surface V/Sb ratios for the two fresh samples. A ratio of V/Sb of 0.91 in the fresh non-precalcined catalyst VSbON-0.5* indicates a stronger enrichment of V on the surface compared to VSbON-0.5. However, the percentage of the sites V^1 and V^2 in the latter sample is almost equal. Moreover the amount of the reduced Sb sites Sb^1 is lower for the fresh non-precalcined catalysts than for the precalcined sample. This suggests, that the calcination step prior to nitridation promotes the reduction of V and Sb sites in VSbON catalysts. This is surprising since calcination in air in principle depletes the reduction degree of redox-active metal sites. However, in agreement with XPS results, the stronger reduction of the precalcined VSbON-0.5 sample in comparison to the non-precalcined sample is also indicated by XRD results, in which the amount of elemental crystalline Sb is lower for the non-precalcined sample than for the precalcined one.

The surface Sb sites of the used VSbON-0.5 and VSbON-0.5* catalysts differ in their nature, as well. In the catalyst VSbON-0.5* only one Sb surface site can be observed, which possesses an E_B value characteristic of an oxidation state close to +5. On the other hand, two different V sites can be still well distinguished in the used sample of the latter non-precalcined catalyst. In contrast to the precalcined catalyst, the amount of the nitrogen sites N^2 and N^3 increases in the course of ammoxidation for VSbON-0.5*, while the nitrogen site N^1 totally disappeared in the VSbON-0.5* catalyst after use in the ammoxidation. In addition, also a slight reoxidation of both V sites can be observed and the V/Sb ratio drops from 0.91 to 0.19 indicating also in this sample a partial migration of V into the bulk during catalysis.

Interestingly the chemical surface nature of the VSbO-0.5 catalyst differ significantly from that of VSbON-0.5 and VSbON-0.5* before and after use in ammoxidation. For the fresh calcined VSbO-0.5 oxide only one V site can be detected at around 517.6 eV, corresponding to an oxidation state of +5. Also, only one Sb site with a binding energy being characteristic for Sb^{5+} is exposed in the near-surface region of the fresh oxide catalyst. Additionally, a small peak in the N1s region can be seen for NH_4^+ sites, which originates from the synthesis of the oxide precursor, in which NH_4VO_3 was used. Only for this catalyst three N sites with distinct different binding energies are formed during ammoxidation. Furthermore one of the two V sites has a remarkable low binding energy (E_B = 513.2 eV), which is typical for V-N bonds. Likewise, two different sites are detected for Sb with a high difference in their binding energies (E_B (Sb^2) - E_B (Sb^1) = 3.3 eV). The E_B value of the second Sb site Sb^2 is the lowest detected E_B value among all the investigated VSb samples.

These results suggest, that only the VSbO-0.5 oxide catalyst is able to form stable Sb-N and V-N bonds during ammoxidation. Possibly, also Sb-N-V sites are created during ammoxidation resulting in a stronger reduction of V and Sb sites.

Relationship between catalytic performance of VSbO-0.5, VSbON-0.5 & VSbON-0.5 and their surface N and V species:* To understand in-depth the impact of the three surface nitrogen sites on the catalytic performance, N/M ratios (M = V or Sb) were calculated from the XPS results of the used VSbO-0.5, VSbON-0.5 and VSbON-0.5* catalysts. These ratios are presented in Tab. B.4, while the catalytic performance of these catalysts at the end of the catalytic test is presented in Fig. 3.50 A.

Interestingly, no direct correlation can be found between the catalytic performance of the three catalysts and the surface N_s/V_s, N_s/Sb_s, N_s/M_s ($M = Sb_s + V_s$) and bulk N/V_{bulk} ratios indicating that it is not the total amount of surface N species which is important for the catalytic performance, but rather the nature of N sites and metal sites to which they are bound. Therefore, the idea arose to correlate the surface $(N^x+N^y)/V_s$ and $(N^x+N^y)/Sb_s$ ratios with the corresponding catalytic performance. [13]

In Fig. 3.50 B and C the $(N^x+N^y)/V_s$ and $(N^x+N^y)/Sb_s$ ratios are presented for the used VSbO-0.5, VSbON-0.5 and VSbON-0.5* catalysts. It turned out, that only for the ratios $(N^x+N^y)/V_s$

---

[13] x and y denotes the N sites 1, 2 or 3 ($x \neq y$).

a correlation to the S_{3-CP} and X_{3-PIC} can be found. With declining $(N^1+N^2)/V_s$ and rising $(N^2+N^3)/V_s$ ratios the selectivity S_{3-CP} declines and the conversion X_{3-PIC} rises in the catalyst series VSbO-0.5, VSbON-0.5 and VSbON-0.5*. Such relationship is not found for the $(N^x+N^y)/Sb_s$ ratios.

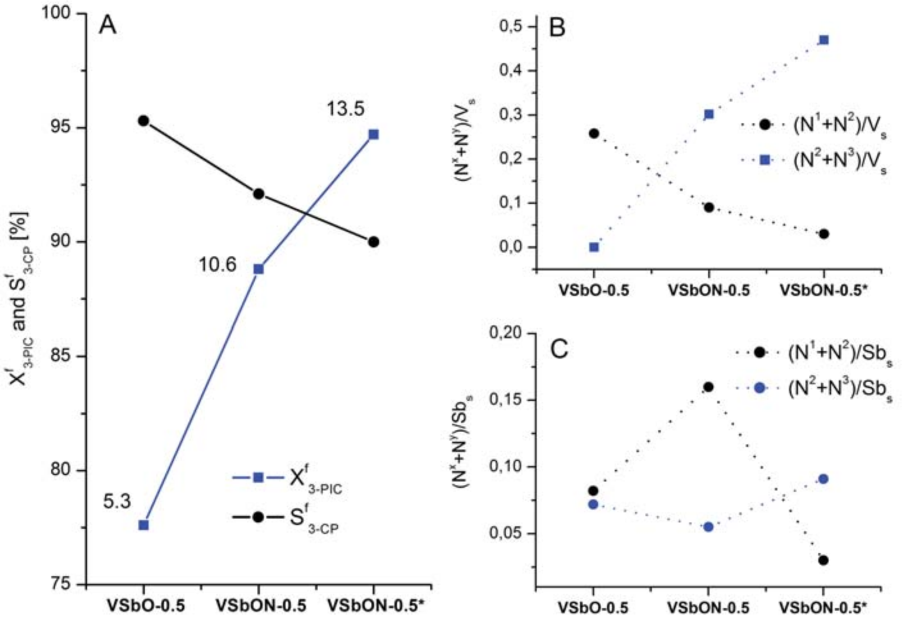

Figure 3.50.: A) Catalytic performance of VSbO-0.5, VSbON-0.5 and VSbON-0.5* catalysts at the end of the catalytic test (numbers: corresponding surface areas S_{BET} of used catalysts in m^2/g); B) Surface $(N^x + N^y)/V_s$ ratios and C) Surface $(N^x + N^y)/Sb_s$ ratios of used VSbO-0.5, VSbON-0.5 and VSbON-0.5* catalysts calculated from XPS results

The chemical meaning of $(N^1+N^2)/M$ and $(N^2+N^3)/M$, respectively, is significantly different. This is due to the fact that the electrophilic character of the three N sites increases in the order $N^1 < N^2 < N^3$ according to their E_B values. This means that the sum of N^1+N^2 has a more nucleophilic character, while the sum of N^2+N^3 reflects a more electrophilic character. From the catalytic performance it is evident, that electrophilic N sites such as NH_4^+ bound to V sites are highly active, but poorly selective. Moreover, N sites with nucleophilic character like N^{3-} bound to V sites are more selective, but less active. Obviously, these N sites must be locally bound to V sites since for the $(N^x+N^y)/Sb_s$ ratios no correlation can be found to the catalytic performance.

Note that the conversion increases, while selectivity decreases with rising surface area of the used catalysts (shown in Fig. 3.50). Thus, it has to be considered that the difference in catalytic performance for these three catalysts may simply due to the difference in surface area. However, the catalytic performance of VSbON-0.5, VSbON-0.5* and VSbO-0.5 changes with time on stream (see again Fig. 3.46 A, B and C). While S_{3-CP} increases slightly at constant X_{3-PIC}

values for the two oxynitrides VSbON-0.5 and VSbON-0.5* with time on stream, X_{3-PIC} decreases slightly at constant S_{3-CP} values for the VSbO-0.5 catalyst. These changes in catalytic performance suggest, that the impact of the chemical nature of V and N containing surface species on the catalytic performance dominates on the surface area effect. Additionally, the surface area of VSbO-0.5 increases in the course of the ammoxidation from 3 to 5 m^2/g, while conversion decreases slightly with time on stream. If the surface area would have an important effect on the catalytic performance, one would expect, that X_{3-PIC} increase with reaction time. This also supports that the difference in catalytic performance is mainly due to the difference of V and N containing surface sites and not due to different surface areas.

Finally, it should be emphasized that this correlation does not mandatorily disagree with the mechanism postulated earlier for the ammoxidation of heteroaromatics on oxide catalysts since in each of the three catalysts NH_4^+ sites are detected on the surface, which helps to insert N into the benzyl-like intermediate to form 3-CP. Rather the catalyst VSbO-0.5 might incorporate gaseous ammonia from the reaction stream as nitride-like sites near to the coordination of V, which can be also transformed to NH_4^+ in the course of the ammoxidation. This incorporation goes along with reduction of surface V species.

3.5.3. Conclusions to VSbON catalysts

VSb containing catalysts are a complex catalytic system. The catalytic performance of these catalysts is sensitive to the adjusted V/Sb ratio and the thermal treatment (nitridation, calcination and a combination of precalcination and nitridation). Three different types of VSb containing catalysts were catalytically and structurally characterized: Oxynitrides being calcined prior nitridation (VSbON-x.x), oxynitrides being directly nitrided without a precalcination step (VSbON-x.x*) and oxides being only calcined in air (VSbO-x.x).

For the VSbON catalyst type the catalytic performance and structure has been investigated for different V/Sb ratios ranges from 0.25 up to 2.0. It turned out that VSbON oxynitrides with V/Sb $\leq$ 0.5 show a constant conversion with time on stream, while for ratios higher than 0.5 a rapid loss of conversion was detected with time on stream. This loss of X_{3-PIC} might be due to the fact that the surface of VSbON catalysts is initially rich of V, but poor of Sb at high V/Sb ratios as it is evident from XPS results. During ammoxidation a considerable high V concentration moves to the bulk; thus the number of catalytically active V sites decreases with reaction of time. Simultaneously, elemental crystalline Sb formed by nitridation in VSbON catalysts is reoxidized. By XRD it was found, that $SbVO_4$ is destroyed by nitridation, whereby the VSbON oxynitride with a V/Sb ratio of 1.0 contains the highest amount of elemental Sb. This indicates that the elemental Sb originates from the decomposition of $SbVO_4$. As a consequence of this decomposition process, V from $SbVO_4$ might be enriched as V_xO_y and/or $V_xO_yN_z$ on the surface for catalysts with V/Sb > 0.5 as indicated from XRD and XPS results. Omitting the calcination step prior nitridation decrease the concentration of elemental Sb and therefore decline the enrichment of V_xO_y species on the surface, maybe due to the fact that the percentage concentration of $SbVO_4$ is lower compared to the precalcined oxynitrides. However, as a consequence the catalytic deactivation is rather not that fast as for precalcined VSbON catalysts, but can be still observed. On the contrary, Sb_xO_y phases being exclusively present in oxide samples prior nitridation with V/Sb $\leq$ 0.5, seems to be resistant to reduction by nitridation.

The comparison of the catalytic performances and structural properties of differently prepared VSb catalysts with V/Sb = 0.5 shows that unexpectedly for VSbO-0.5 catalysts nitride like V-N and probably Sb-N units are formed in the near-surface region during ammoxidation, which goes along with a decline of the mean surface V oxidation state. Nitride like sites introduced into VSbON-0.5 and VSbON-0.5* catalysts diminish during nitridation, instead NH_x sites (x = 1-4) remain on the surface. For this reasons, the VSbO-0.5 catalyst is more selective but less active than VSbON-0.5 and VSbON-0.5*.

4. General Conclusions

4.1. Catalytic performance of oxynitrides

Ternary VAlZrON and VZrPON as well as binary VMoON and VSbON oxynitrides and VMON/$Mo_xO_yN_z$ (M = Al or Zr) catalysts have been catalytically tested as a function of the V concentration in the ammoxidation of 3-PIC to 3-CP.

The catalytic performance (X_{3-PIC}, S_{3-CP}, Y_{3-CP} and STY) of the best catalysts in the VAlZrON, VZrPO, VMoON and VSbON oxynitride series is compared in Fig. 4.1 A. The highest conversion X_{3-PIC} is detected for VZrAlON-0.5, whereby X_{3-PIC} decreases in the following order: VZrAlON-0.5 ≈ VSbON-0.5* > VMoON-1.5 » VZrPON-0.5. The highest selectivity S_{3-CP} is observed for VMoON-1.5, whereby S_{3-CP} decreases in the following order: VMoON-1.5 > VSbON-0.5* > VZrAlON-0.5 > VZrPON-0.5. For comparison also an industrial catalysts, called CPCAT, has been catalytically characterized as reference to classify the catalytic potential of oxynitrides precisely. In Fig. 4.1 B and C the catalytic activity of this benchmark catalyst is compared to that of VZrAlON-0.5 and VZrON-0.25. Although the industrial catalyst is more selective than VZrAlON-0.5 and VZrON-0.25, it is clearly seen that due to a much higher activity of VZrAlON-0.5 and VZrON-0.25 the space-time yield is significantly improved. Moreover, the combination of highly-active VZrON catalysts with selective VAlON oxynitrides improves the selectivity at slightly lower conversion at T_B = 360 °C. Interestingly, for both catalysts CPCAT and VZrAlON-0.5, the selectivity is almost not changed when increasing T_B by 18 °C, while X_{3-PIC} increase for both. By comparing the catalytic performance of VZrAlON-0.5 and VSbON-0.5* in Fig. 4.1 A, it is evident that also VSb containing oxynitrides bear a great potential in the ammoxidation of 3-PIC since a high conversion at a high selectivity is reached with the latter catalyst at T_B = 360 °C and GHSV = 2713 h^{-1}. Thus it is expected that at higher space velocities such as 5728 h^{-1}, the space-time yield might be higher for VSbON-0.5* than that of VZrAlON-0.5. This suggests additionally that probably a combination of highly active VZrON catalyst with VSbON catalysts might be also a beneficial route to improve STY in the ammoxidation of heteroaromatics.

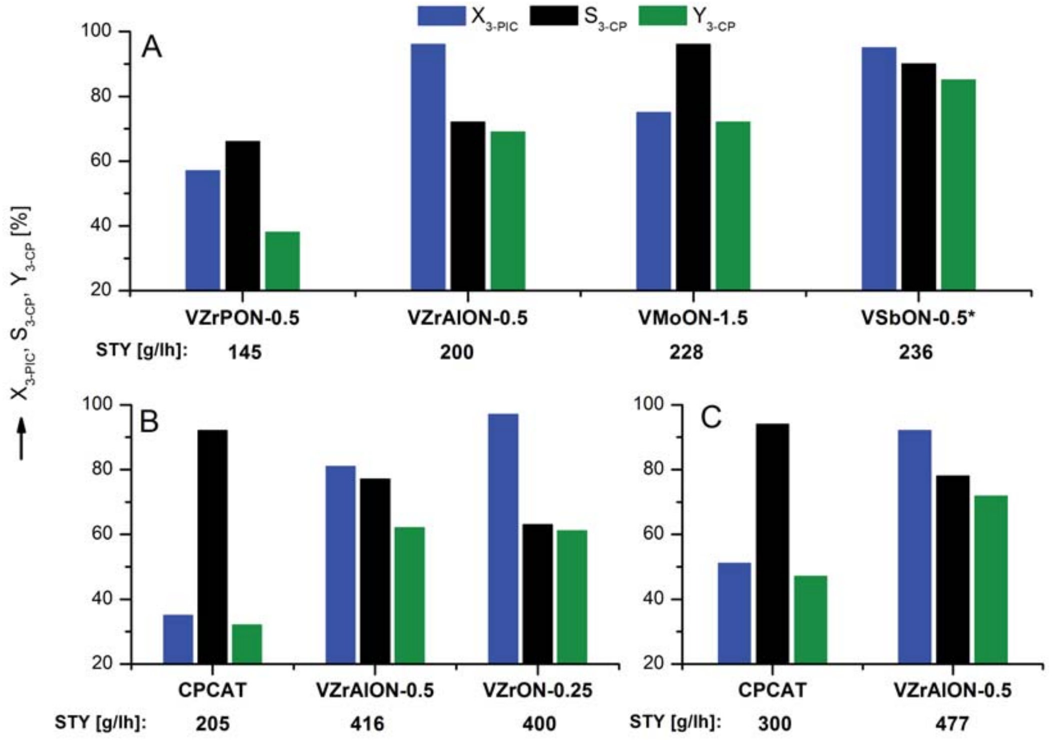

Figure 4.1.: Comparison of the catalytic performances (X_{3-PIC}, S_{3-CP}, Y_{3-CP}) of oxynitrides with an industrial catalyst CPCAT including STY (given as numbers);
A) Catalytic performance at T_B = 360 °C (GHSV = 3242 h^{-1} for VZrPON-0.5; GHSV = 2713 h^{-1} for VZrAlON-0.25, VMoON-1.5 and VSbON-0.5*); B) Catalytic performance at T_B = 360 °C of CPCAT, VZrAlON-0.5 and VZrON-0.25 (GHSV = 5728 h^{-1}); C) Catalytic performance at T_B = 378 °C of CPCAT and VZrAlON-0.5 (GHSV = 5728 h^{-1})

4.2. Structure-reactivity relationships

Structural changes during nitridation of the oxide precursors and during ammoxidation have been elucidated using a variety of characterization methods (e. g. ICP-OES, XRD, XPS, TPO, FTIR, UV-vis, Raman). In situ EPR and Raman spectroscopy were applied during ammoxidation and nitridation including also simultaneously coupled in situ-EPR/UV-vis/Raman spectroscopy to enlighten relationships between catalyst structure and the catalytic performance.

In previous studies it turned out that VAlON catalysts were more selective, but less active than VZrON catalysts, due to a lower mean V valence state and a higher dispersion of V sites. With the ternary VAlZrON material the selectivity S_{3-CP} of VAlON could be almost maintained, yet at significantly higher conversions. Thus space-time yields higher than those for VZrON, VAlON and the benchmark catalysts could be achieved. This successful improvement is attributed to the exposure of proper V-N sites on the surface of VAlZrON, in which V obeys a mean valence state close to +4, as well as to the formation of anion defects close to V^{5+} species in VAlZrON.

In contrast, crystalline ZrO_2 and highly oxidized V_xO_y clusters are formed on the nitrogen free surface of binary VZrON catalysts [7, 8]. These structural properties are supposed to be responsible for high activity but low selectivity of VZrON. This distinct V_xO_y site agglomeration is not observed for VAlON materials and also not for VZrAlON. Thus it can be suppressed by combining VZrON and VAlON to VZrAlON.

Incorporating phosphorus into VZrON catalysts has a detrimental impact on the catalytic performance. This effect of P in VZrPON catalysts is due to the strong dilution of active V sites (low activity) and the incorporation of N in the neighborhood of P, but not of V. This leads to low selectivity since a beneficial synergism between the redox-active V sites and the N incorporation sites via V-N junctions is not achieved. At V/Zr and Zr/P ratios close to 1.0 the formation of crystalline $ZrV_{2-x}P_xO_7$ phase occurs, in which tetrahedrally V sites are even highly diluted.

The combination of VMON and high-surface area $Mo_xN_yO_x$ to VMON/$Mo_xN_yO_x$ (M = Al or Zr) catalysts does not lead to an improvement of the activity compared to that of pure VAlON and VZrON catalysts. This is due to the fact that VMON and $Mo_xN_yO_x$ are not structurally interacting, rather $Mo_xN_yO_x$ is retransformed to MoO_3. During this reoxidation not only N sites of $Mo_xN_yO_x$ get lost but also the surface area decreases. Besides the loss of surface area it has to be considered that MoO_3 and the higher percentage of ZrO_2 might merely dilute the more active VMON catalyst part or/and even deactivates VMON due to covering active sites of VMON by MoO_3 or ZrO_2.

The highest selectivity of S = 96 % is shown by VMoON catalysts. This might be due to an in situ formed surface structure during ammoxidation, which resembles that of the solid solution $V_6Mo_4O_{25}$. The change of the oxynitride structure is accompanied by a partial release of nitrogen incorporated during preceding nitridation and a short activation period. In contrast to VMoO oxide catalysts containing mainly V_2MoO_8 and being less active and seletive than VMoON catalysts, $V_6Mo_4O_{25}$ contains long-range ordered edge-shared $V^{4+/5+}$-O-$Mo^{5+/6+}$ surface units that enable an effective electron transport. These surface units provide active N species in the immediate vicinity of a redox-active site for incorporation into the substrate.

Also oxynitrides containing V and Sb as redox-active components are efficient catalysts in the ammoxidation if a ratio of V/Sb ≤ 0.5 is adjusted. VSb containing catalysts being nitrided in pure ammonia are more active and slightly less selective than the corresponding calcined VSb oxide catalysts. Most remarkably, VSbO oxides are able to form V-N in the course of ammoxidation accompanied by V surface reduction, while oxynitrides do not contain nitride-like V surface species after ammoxidation, but V-NH_x units (x = 1-4). However, oxynitrides and oxide catalysts as well provide surface V-N junctions, as it is also true for VAlON, VZrAlON and VMoON catalysts.

Conclusively, highly effective V containing ammoxidation catalysts must contain tailored V-N surface sites with moderately reduced V species. V_xO_y clusters are highly active but favor total oxidation to CO and CO_2. Highest selectivity is realized by edge-sharing V-O-Mo units with optimum redox potential for effective electron transport without promoting over oxidation. High selectivities can be reached also with VSb containing catalysts, which are also able to generate surface V-N junctions. Besides surface V-N junctions, defect sites in the anionic lattice helps to improve selectivities, as it is exclusively the case for VZrAlON.

Therefore, the presence of direct V-N junctions as well as anionic defects on the surface are essential for high nitrile selectivity. This is fulfilled the best for VZrAlON, VSbON and VAlON catalysts, but not for VZrON or VZrPON catalysts.

5. Experimental part

5.1. Catalyst syntheses

In general, the catalyst preparation strategy for oxynitrides and nitrides is almost identical. The preparation starts with the synthesis of an mixed metal oxide, so called oxide precursor, which was subsequently converted into the oxynitride or nitride by thermal treatment of the oxide precursor in a stream of pure ammonia at high temperatures.

In general, the nomenclature is as follows in this work: Predried compounds obtained directly from a liquid route are called oxide precursors. Samples being thermally treated in air are generally designated as oxides or calcined oxides. In contrast, directly processed oxide precursors via nitridation are called oxynitrides, although some of those compounds are not any more oxyitrides after catalysis. Mostly, catalysts before and after ammoxidation are designated as fresh and used catalysts, respectively. x.x attached to the abbreviated catalysts compounds denotes always a V to metal ratio.

Synthesis of mixed VZrAlON compounds Oxide precursors VZrAlO with V/(Al+Zr) ratios ranging from 0.1 to 0.6 were synthesized using the co-precipitation method. The Al/Zr ratio was adjusted to 1.5 and for one sample to 0.8. NH_4VO_3 (Aldrich, 99 % +) was suspended in distilled water (0.1 M) and subsequently acidified with 65 % HNO_3 (Roth, pure) to pH = 3 at 70 °C under stirring (pH-Meter Seven Multi, Mettler Toledo). The colour of the solution turned from yellow to dark orange. Meanwhile, both salts, $Al(NO_3)_3 \cdot 9\,H_2O$ (Sigma Aldrich, 98 % +) and $ZrO(NO_3)_2$ (Aldrich, tech.), were dissolved at 70 °C in distilled water maintaining an entire concentration of 0.15 M. The acidified V solution was slowly added to the colourless Al-/Zr-solution. Dropwisely the pH of the final solution was raised to 7 at 70 °C under stirring using NH_4OH (Merck, 25 %). A yellow precipitate was formed, whereby the degree of gelefication depended strongly on the adjusted metal ratios. In all cases, high amounts of Zr assisted the formation of a gel-like state of the co-precipitated solid. The solid was filtered and washed twice with distilled water. Finally, the raw product was dried at 120 °C for 16 h. The predried yellow solids were crushed in a mill to get a fine powders. Approximately, 6 g of each VZrAlO precursor was directly nitrided in a calcination oven for 6 h at 600 °C using an ammonia (3.8, air liquide) flow of 30 l/h and a heating ramp of 5 K/min. By this treatement the colour changed from yellow to black, independently from the adjusted metal ratios. The resulting oxynitrides are denoted as VZrAlON-x.x with x.x being the V/(Al+Zr) ratio. After catalytic test the colour changed as a function of the chemical composition. For V/(Al+Zr) = 0.1 (Zr/Al = 1.5) the colour changed to dark green, while for higher ratios such as V/(Al+Zr) = 0.5 (Zr/Al = 1.5) the catalysts stay almost black.

Synthesis of VZrPO, VZrPON and ZrPO compounds VZrPO oxide precursors were synthesized by the citrate method with V/Zr ratios of 0.1, 0.5 and 0.9. Respective samples are denoted as VZrPO-x.x, with x.x being the V/Zr ratio. The atomic Zr/P ratio was adjusted to 0.9 (V + Zr = const.). The desired amount of NH_4VO_3 (Sigma Aldrich, 99%) was suspended in water under stirring at 70 °C (0.02 M) and subsequently acidified with HNO_3 (19 M) to pH = 3. A second solution was prepared by dissolving the appropriate amount of $ZrO(NO_3)_2$ (Sigma–Aldrich, tech.) in water under stirring at 70 °C (0.02 M). To this solution, the acidic NH_4VO_3 solution was added under stirring at 70 °C. After adding the corresponding amount of phosphoric acid (3 M), a gel was formed, which was stirred for 1 h at 70 °C, before 55 g of solid citric acid was added under stirring. These solutions were refluxed for 16 h under stirring at 70 °C. Different blue colours were observed depending on V concentration in the final solution. Then, water was evaporated using a rotating evaporator, and the resulting brown powder was dried at 120 °C for 16 h. After grinding, the powder was calcined in air (6 l/h) for 16 h at 500 °C and for another 6 h at 600 °C to remove the carbon. The resulting yellow powders, called VZrPO-x.x oxides, were carbon free. To obtain oxynitrides, the calcined VZrPO oxides were pressed and crushed to particles with a diameter between 0.8 and 1 mm. In a home-made shaking fluidized bed reactor, 6 ml of VZrPO particles were loaded. These particles were treated in flowing NH_3 (40 l/h) for 6 h at 500 °C. During this treatment, the sample colour turned from yellow to grey or black depending on the V concentration. The resulting oxynitrides are denoted as VZrPON-x.x with x.x being the V/Zr ratio.

Synthesis of VMON/$Mo_xO_yN_z$ catalysts (M = Zr or Al) The synthesis of VMON/$Mo_xO_yN_z$ catalysts (M = Zr or Al) included three steps. First of all, VMO oxide precursors were synthesized via co-precipitation with V/Al = 0.5 for VAlO and V/Zr = 0.25 for VZrO sample. During co-precipitation the appropriate amount of NH_4VO_3 (Sigma Aldrich, 99 %) was dissolved in distilled water at 70 °C. This solution was then acidified by adding dropwise 65 % HNO_3 (Roth, 65 %) until a pH of 3 (pH-Meter Seven Multi, Mettler Toledo) was adjusted. The V containing solution was mixed with an aqueous solution of 0.5 M $Al(NO_3)_3 \cdot 9\ H_2O$ (Sigma Aldrich, 98 % +) or of 0.5 M $ZrO(NO_3)_2$ (Aldrich, tech.). Subsequently, 2 M NH_4OH (Merck, 25 %) was added until a pH of 7 was reached (pH-Meter Seven Multi, Mettler Toledo), whereupon a yellow precipitate (VAlO-0.5) and a yellow gel (VZrO) was formed. The solids were removed by filtration, washed twice with distilled water, and dried for 16 h at 120 °C. These dried VMO oxide precursors were mixed with MoO_3 (Sigma Aldrich, 99,5 % +) in a mortar adjusting different ratios of VMoO/MoO_3 for several minutes. Finally, 10 g of each of these mixtures were nitrided in an ammonia stream of 26 l/h. The nitridation temperatures was first rised from RT to 350 °C and hold for 30 min (10 K/min), then from 350 °C to 450 °C (1 K/min) and hold for 30 min, and subsequently from 450 °C to 700 °C (3 K/min). The latter nitridation temperature was hold for 1 h. Finally, samples were cooled in Ar to RT. At RT it was switched from Ar to 2 l/h air. This condition was kept for 1 h. Pure VMON catalysts and $Mo_xO_yN_z$ were nitrided by the same procedure. During nitridation the colour of each sample was turned from yellow to black.

Synthesis of VMoO and VMoON catalysts VMoO (V/Mo = 0.25 - 2.0) precursors were synthesized via an aqueous route. The appropriate amount of NH_4VO_3 (Sigma Aldrich, 99%) was dissolved under stirring in distilled water at 75 °C. To this yellow solution the appropiate amount of the salt $(NH_4)_6Mo_7O_{24} \cdot 4\ H_2O$ (Sigma Aldrich, ACS reagent) was added to adjust the desired V/Mo ratios. A clear red-orange coloured solution was observed, which was then acidified by adding dropwise with 65 % HNO_3 (Roth, pure) up to a pH of 2 (pH-Meter Seven Multi, Mettler Toledo). During this treatment, a yellow or red solid was formed. Finally, this suspension was stirred for at least 2 h at 75 °C. Water was evaporated using a rotating evaporator, and the resulting brown powder was dried at 120 °C for 12 h. After grinding, these oxide precursors were calcined in air (5.0, air liquide) at 500 °C for 6 h using a heating ramp of 5 K/min to obtain VMoO oxides. These calcined VMoO oxides were subsequently nitrided at 500 °C for 5 h using a ammonia flow (3.8, air liquide) of 30 l/h and a heating ramp of 5 K/min. The latter samples are called VMoON-x.x oxynitrides or in some cases precalcined VMoON-x.x oxynitrides. x.x denotes the V/Mo ratio.

Synthesis of VSbON catalysts VSbO oxide precursors were synthesized by long-term refluxing. Sb_2O_3 (Sigma Aldrich, 99.9 %) and NH_4VO_3 (Aldrich, 99 % +) were added as powder into distilled water at RT (0.2 M). The initially inhomogeneous suspension was refluxed at 90 °C for 20 h. During refluxing the colour of the suspension turned from dirty white to deep grey. The water was removed using an rotating evaporator. Finally, the glittery black powder was dried for 2 h at 75 °C. These predried VSbO oxide precursors were processed in three different routes resulting in threed different catalyst classes: 1) VSbO oxide precursors were calcined in air (5.0, air liquide) at 500 °C for 6 h using a heating ramp of 5 K/min and a flow of 5 l/h. Subsequently, those calcined compounds were nitrided at 500 °C for 6 h with 5 K/min using an ammonia (3.8, air liquide) flow of 30 l/h. This catalyst class is abbreviated with VSbON-x.x and called precalined oxynitrides. 2) VSbO oxide precursors were directly nitrided at 500 °C for 6 h with 5 K/min using an ammonia (3.8, air liquide) flow of 30 l/h. This catalyst class is abbreviated with VSbON-x.x* and called non-precalined oxynitrides. 3) VSbO oxide precursors were calcined in air (5.0, air liquide) at 500 °C for 6 h using a heating ramp of 5 K/min and a flow of 5 l/h. This catalyst class is abbreviated with VSbO-x.x and called oxides. x.x denotes the V/Sb ratio.

5.2. Catalytic tests

General remarks to the catalytic setup Catalytic tests were performed in a fixed bed glass reactor with an inner diameter of 1.5 cm. The liquid feed components were fed into the gas stream by continuous evaporation of an aqueous solution with a fixed molar ratio of 1:8 (3-PIC (Aldrich, 99 %) : water) using a syringe pump (74900 series, Cole-Parmer Instument Company). Gaseous feed components air (5.0, air liquide) and NH_3 (3.8, air liquide) were dosed by pre-calibrated mass flow controller (Bronkhorst). The respective gaseous space velocities GHSV are given for each presented test result in chapter 3. The catalyst bed temperature T_B inside the reactor was measured by an additional thermocouple. The products were collected in a cooling trap and analyzed off-line using a GC-17A (Shimadzu) equipped with an auto sampler (AOC-20i) and a WCOT fused Silica CP-SIL 8CB column (Varian). The GC was callibrated by the external method using solutions of EtOH containing 3-CP (98 %, Acros Organics) or 3-PIC (99 %, Aldrich). Carbon oxides (CO_2 and CO) as by-products were quantified on-line by a non-dispersive infrared analyser (BINOS100 2M, Rosemount). The calibration of the latter analyser was carried out using test gas mixture CO/CO_2/He (4 %/4 %/92 %; vol.-%; air liquide). The zero point was adjusted using N_2 (5.0, air liquide). The carbon balance B_C was determined for each test (B_C = 97 - 100 %).

The industrial catalyst CPCAT ($VTiSbSiO_x$) was used as received. General information about this catalyst can be found in [34].

General implementation of the catalytic tests Catalyst powder was pressed to pellets, chrushed and sieved to obtain particles with a diameter of 1.0 - 1.25 mm. These catalyst particles were diluted with glass beads possessing a diameter of 1.25 - 1.55 mm. The volumetric ratio of catalyst particles : glass beads was adjusted to 1 : 1.7. This catalyst mixture in the reactor was embedded in addition in glass beads. This loaded reactor was connected to the catalytic setup. A common catalytic test was designed in the following way. First of all, the filled reactor was heated under air/NH_3 to 190 °C using a heating ramp of 10 K/min. Subsequently, the desired amount of 3-PIC/H_2O was added to the air/NH_3 flow. The molar ratio of 3-PIC : air : NH_3 : H_2O was adjusted to 1 : 28 : 5 : 8. This condition was maintained at least for one our. Afterwards products were collected at 190 °C in a cooling trap filled with EtOH for a half an hour. The latter solution was transfered to 50 ml standard flask, which was then analyzed via off-line by GC to monitor the real concentration of 3-PIC in the reaction flow. Then it was heated to the desired reaction temperature (> 300 °C, 10 K/min). In general, the oven temperature T_O was always lower than the measured bed temperature T_B. After ca. 20 min a new cooling trap with EtOH was connected to the reactor exit and 3-PIC as well as 3-CP were collected also for a half an hour. The concentration of 3-PIC and 3-CP related to 50 ml EtOH were determined also off-line by GC. CO_x contents in the stream were measured afterwards connecting a cooling trap filled with 10 % H_2SO_4/EtOH solution to the exit of the reactor. After passing this cooling trap the gas mixture was sent to the infrared analyser (BINOS100 2M, Rosemount), where CO and CO_x contents were measured. Finally, after taking several catalytic data the reaction temperature was cooled to 190 °C, the 3-PIC/H_2O stream was turned off and it was cooled to RT.

Examination of catalytic data The conversion X_{3-PIC}, yield Y_{3-CP} and selectivity S_{3-CP} were calculated from:

$$X_{3-PIC} = \frac{n^0_{3-PIC} - n_{3-PIC}}{n^0_{3-PIC}} \cdot 100; \tag{5.1}$$

$$n_{3-PIC} = \frac{2 \cdot A_{n_{3-PIC}}}{f_{3-PIC}} \quad and \quad n^0_{3-PIC} = \frac{2 \cdot A_{n^0_{3-PIC}}}{f_{3-PIC}}; \tag{5.2}$$

$$Y_{3-CP} = \frac{n_{3-CP} - n^0_{3-CP}}{n^0_{3-CP}} \cdot \frac{\upsilon_{3-PIC}}{\upsilon_{3-CP}} \cdot 100; \tag{5.3}$$

$$n_{3-CP} = \frac{2 \cdot A_{n_{3-CP}}}{f_{3-CP}}, \quad n^0_{3-CP} = \frac{2 \cdot A_{n^0_{3-CP}}}{f_{3-CP}} \quad and \quad \frac{\upsilon_{3-PIC}}{\upsilon_{3-CP}} = 1; \tag{5.4}$$

$$S_{3-CP} = \frac{Y_{3-CP}}{X_{3-PIC}} \cdot 100. \tag{5.5}$$

The value n^0 describes the used molar flux. A_n denotes the peak area of the respective GC peak and f as calibration factor was derived from external calibration using known concentrations of 3-PIC and 3-CP. The carbon balance B_C for each catalytic experiment ranges from 97 to 100 %. It was calculated according to:

$$B_C = \frac{C^{out}_{3-PIC} + C^{out}_{3-CP} + C^{out}_{CO} + C^{out}_{CO_2}}{C^{in}_{3-PIC}}; \tag{5.6}$$

$$C^{in}_{3-PIC} = n^0_{3-PIC} \cdot M^C_{3-PIC}, \quad C^{out}_{3-PIC} = n_{3-PIC} \cdot M^C_{3-PIC}; \tag{5.7}$$

$$C^{out}_{3-CP} = n_{3-CP} - n^0_{3-CP} \cdot M^C_{3-CP}; \tag{5.8}$$

$$C^{out}_{CO_x} = \frac{V_{CO_x} \cdot V_M \cdot M^C_{CO_x} \cdot \sum_{i=1}^{z} V^{out}_g}{100}. \tag{5.9}$$

The space-time yield STY characterize the effectiveness of a catalyst and is given by:

$$STY = \frac{n_{3-CP} \cdot M_{3-CP}}{V_C}. \tag{5.10}$$

V_C denotes the catalyst volume, while m_{3-CP} stands for the mass of generated 3-CP per hour.

5.3. Characterization methods

Elemental analysis ICP-OES measurements were performed with a Varian 715-ES spectrometer calibrated for the required elements. All values were verified by double determination. Ten milligrams of catalyst was dissolved in 4 ml HF and 4 ml aqua regia in a microwave oven (Anton Paar/Perkin-Elmer) at ca. 60 bar and ca. 120 °C. The obtained solution was filled up to 100 ml with distilled water and measured.

CHN analysis was performed with an EA 1110 CHN analyzer (CE Instrumenta) calibrated for the required elements and equipped with an auto sampler. In a home-made tin crucible, 10–30 mg of each catalyst powder was placed. Measured data were evaluated with Eager 200 for windows software. All values were verified by double determination.

MAS NMR ^{31}P and ^{51}V MAS NMR spectra were recorded on a Bruker AVANCE 400 spectrometer (Larmor frequencies: ν_{31P} = 161.9 MHz; ν_{51V} = 105.2 MHz) using a 2.5 mm magic angle spinning (MAS) probe (Bruker Biospin). ^{51}V MAS NMR (I = 7/2) spectra were recorded with a sweep width of 1 MHz and an excitation pulse duration of 0.8 μs ensuring a linear irradiation regime for reducing the distortion of the spectra. $VOCl_3$ was used as reference for the chemical shift of ^{51}V. The recycle delay was chosen as 1 s, and accumulation numbers of 10,060 (sample VZrPO-0.9, ν_{rot} = 28 kHz) and 62,800 (sample VZrPON-0.9, ν_{rot} = 25 kHz), respectively, were used for an acceptable signal-to-noise ratio. ^{31}P MAS NMR measurements (ν_{rot} = 25 kHz) were performed with a recycle delay of 120 s, a π/2 pulse length of 6 μs and 180 (sample VZrPO-0.9) or 623 (sample VZrPON-0.9) transients. ^{31}P chemical shifts are referenced against H_3PO_4.

Surface area Surface areas of the samples were determined according to BET method [158, 159]. The BET surface area of VZrPO and VZrPON catalysts was determined by nitrogen adsorption at 77 K (ASAP2010). For all other samples the surface area was determined by krypton adsorption at 77 K.

UV/Vis-DRS UV/Vis-DRS spectra were recorded on a Varian Cary 400 spectrometer equipped with an praying mentis and heatable in situ-cell (Harrick) [160]. Gas supply was realized by mass flow controllers (Bronkhorst). All spectra were measured against the baseline of the white standard $BaSO_4$ (Merck) in diffuse reflection mode from 200 to 800 nm with a scan rate of 300 nm/min. A dilution of dark samples with $BaSO_4$ was necessary to decrease the absorbance.

The redox properties of VMoO samples were investigated with UV/Vis-DRS technique using a kinetic approach. The diluted sample ($BaSO_4$: sample = 6 : 1) was first heated in 9 % O_2/Ar (55 ml/min) to 300 °C using a heating ramp of 10 K/min. UV-Vis spectra were recorded until steady state conditions were reached under these conditions (preoxidation). After stopping the O_2 flow and flushing the loaded in situ-cell with pure Ar, the flow was switched to 9 % H_2/Ar (55 ml/min) at 300 °C. The change of the absorbance was followed at 700 nm as a function of time using the kinetic program of Varian software. The time-dependent absorbance change functions for the reduction of preoxidized VMoO compounds could be only fitted successfully by the following equation:

$$[V^{4+}] = [^aV^{5+}] \cdot [1 - exp(-^ak_{red} \cdot t)] + [^bV^{5+}] \cdot [1 - exp(-^bk_{red} \cdot t)]. \tag{5.11}$$

Then the flow of H_2 was stopped and the cell was again flushed with Ar. For reoxidation it was again switched to 9 % O_2/Ar (55 ml/min). The time-dependent absorbance change functions for the reoxidation of prereduced VMoO compounds could be only fitted successfully by the following equation:

$$[V^{5+}] = [{}^aV^{4+}] \cdot exp(-{}^ak_{reox} \cdot t) + [{}^bV^{4+}] \cdot exp(-{}^bk_{reox}) \cdot t. \tag{5.12}$$

XRD analysis XRD powder patterns were recorded in transmission geometry with Cu Kα_1 radiation on a Stoe STADI P diffractometer, equipped with a position sensitive detector (PSD). Processing and assignment of the powder patterns was done using the software Win Xpow (Stoe) and the powder diffraction file (PDF) database of the International Center of Diffraction Data (ICDD).

The diffractogram in Fig. A.9 was obtained at the μ-spot beam line of the Berlin synchrotron facility BESSY. Details of the beam line can be found in [161]. The sample was fixed in a borosilicate capillary of a diameter of 0.7 mm. A double crystal monochromator was used to provide highly monochromatic X-rays (E = 15 kV). The scattered intensities were collected 20 cm behind the sample with a two-dimensional X-ray detector (MarMosaic CCD; 3072 x 3072 pixel). The scattering data were converted to diagrams of scattered intensities as a function of the scattering vector using the algorithm of the software package Fit2D [162].

XPS analysis X-ray photoelectron spectra (XPS) were recorded on a VG ESCALAB 220iXL instrument with Mgα_1 radiation (E = 1253.6 eV). The samples were fixed with a double-adhesive carbon tape on a stainless steel sample holder. The peaks were fitted by Gaussian–Lorentzian curves after Shirley background subtraction. The electron binding energy was referenced to the carbon 1s peak at 284.8 eV. For quantitative analysis of the near-surface region, the peak areas were determined and divided by the element-specific Scofield factor and the analysator-depending transmission function.

FTIR spectroscopy FTIR spectra at ambient conditions of VZrPO, VZrPON and VZrAlON catalysts were recorded in attenuated total reflection (ATR) mode using an Alpha-P FTIR spectrometer (Bruker).

Spectra of VZrPON (V/Zr = 0.1; 0.5; 0.9) were recorded at room temperature in transmission mode on a Nicolet 6700 FTIR spectrometer equipped with a heatable and evacuable IR cell and CaF$_2$ windows. In this case, 50 mg of each catalyst powder was pressed to a self-supporting wafer and heated to 300 °C under vacuum before collecting the spectrum.

Surface acidity was analyzed by transmission FTIR spectroscopy (Bruker IFS 66) of pyridine adsorbed at 20 °C on self-supporting wafers after pretreatment in flowing He at 250 °C. Desorption spectra were recorded stepwise during heating the catalyst with preadsorbed pyridine to 350 °C. Band areas at 1540 cm^{-1} for Brønstedt and at 1450 cm^{-1} for Lewis acid sites were used to elucidate the surface acidity.

Ex situ and in situ EPR spectroscopy In situ-EPR and ex situ-EPR spectra in X-band ($\nu \approx$ 9.5 GHz) were recorded with the cw-spectrometer ELEXSYS 500-10/12 (Bruker) using a microwave power of 6.3 mW, a modulation frequency of 100 kHz and a modulation amplitude of 0.5 mT. The magnetic field was measured with respect to the standard 2,2-diphenyl-1-picrylhydrazyl (DPPH). For the in situ-EPR measurements a home-made quartz plug-flow reactor connected to a gas-dosing system containing mass flow controllers (Bronkhorst) was implemented in the rectangular cavity of the spectrometer.

For all in situ EPR experiments during ammoxidation using VZrAlON (V/(Zr+Al) = 0.1; 0.25 and 0.5), 100 mg of the catalyst particles (d_P = 315 - 710 μm) were used. Spectra were recorded at RT before any treatment. After heating the respective catalysts in air/NH_3 (4.5 : 1) to 350 °C water was added via a saturater to the air/NH_3 stream at 350 °C. Subsequently it was switched to the complete feed at 350 °C (3-PIC : air : NH_3 : H_2O = 1 : 30 : 6 : 8) at 350 °C. That followed by stopping the 3-PIC stream at 350 °C, so that the catalyst was again exposed to air/NH_3 at 350 °C, then the gaseous stream was changed again from air/NH_3 (4.5 : 1) to N_2 (10 ml/min) at 350 °C and finally the sample was cooled from 350 °C to RT in N_2. Spectra at elevated temperatures were recorded as a function of time for at least 1 h. For qualitative analysis via off-line GC (see section: General implementation of the catalytic tests), the exit of the reactor was connected to a cooling trap filled with EtOH to collect 3-PIC and 3-CP from the reaction stream at 350 °C.

For the in situ EPR experiments during ammoxidation using VMoON-1.5 and VMoO-1.5, 45 mg of the catalyst particles (d_P = 315 - 710 μm) has been used. The sample was first heated in 10 ml/min N_2 to 350 °C. Then it was switched to air/NH_3 (4.5 : 1) at this temperature. After ca. 1 h, 3-PIC was added to the latter stream (molar ratio of 3-PIC : air : NH_3 = 1 : 30 : 6). Finally, the sample was cooled to RT in N_2.

For the in situ EPR experiments during nitridation of VZrAlO-0.5 precursor, 112 mg of the catalyst particles (d_P = 315 - 710 μm) were used. The sample was first heated from RT to 120 °C in N_2 (10 ml/min) and was cooled after 1 h again to RT. Then it was switched to 20 % NH_3/N_2 (37.5 ml/min) at RT and it was stepwise heated to 410 °C. After cooling the sample from 410 °C to RT in NH_3/N_2, it was finally switched from NH_3/N_2 to N_2 at RT. The sample was exposed to latter condition for 14 h. Spectra at elevated temperatures were recorded as a function of time for at least 30 min.

Computer simulation of EPR spectra was performed with the program SIM14S of Lozos et al. [163] using the spin Hamiltonian

$$H = \mu_B \cdot S \cdot g \cdot B_0 + SAI. \tag{5.13}$$

μ_B reflects the Bohr magneton, g the g tensor, S the electron spin operator, B_0 the magnetic field vector, A the hyperfine tensor, and I is the nuclear spin operator.

TPO experiments TPO experiments on VMoON oxynitride were performed on a chemisorption apparatus (Autochem 2910, Micromeritics) which was coupled to quadrupole mass spectrometer (Omnistar, Pfeiffer-Vacuum). 100 mg of the sample was used. Before any heating, the sample space was rinsed with He for 30 min. Then it was switched to the gaseous mixture 5 % O_2/He at 40 °C. After 10 min the sample was heated with 10 K/min in 50 ml/min 5 % O_2/He to 500 °C. Mass traces in Fig. A.22 are scaled and summarized as groups.

Simultaneous in situ-EPR/UV–vis/Raman measurements Simultaneous in situ-EPR/UV–vis/Raman studies during nitridation of VZrPO catalysts were performed using the equipment described in-depth in [164]. 115 mg of the VZrPO oxide particles (d_P = 315 - 710 μm) were heated in N_2 flow (10 ml/min) to 120 °C, before switching to 20 % NH_3/N_2 (50 ml/min) at the same temperature.

In situ Raman microscopy studies The Raman investigations were performed with a UV/Vis/NIR Raman spectrometer (LabRam HR, Horiba-Jobin Yvon) equipped with a confocal microscope, Notch filters and a CCD detector. The laser was focused on the sample by a long working distance objective (x 100) using a Ar^+-K^+ laser (2018 RM, Spectra physics). The green exciting line at 514 nm was taken for each measurement, while the laser power was never higher than 1 mW. Exposition times ranged typically between 1 min and 15 min. The Raman setup included a heatable oven equipped with a home-made quartz reactor including a thermocouple hollow. Heating ramps were usually set to 3 K/min. 0.7 ml of the undiluted catalyst particles were loaded into the reactor (d_P = 315 - 710 μm). A liquid mixture containing water and 3-PIC was dosed via a syringe pump (74900 series, Cole-Parmer Instument Company), while gas flows of NH_3, O_2 and He were controlled by mass flow controllers (Bronkhorst). The molar ratio of the feed components 3-PIC : 20% O_2 in He : NH_3 : H_2O during reaction conditions was adjusted to

1 : 28 : 5 : 8. The GHSV was set to 2713 h^{-1}. Condensable products (unconverted 3-PIC and 3-CP) were collected in EtOH, while the rest gas was analyzed via on-line mass spectrometry (VG ProLab, Thermo Electron Corporation). A qualitative analysis of 3-PIC and 3-CP was done using off-line gas chromatography Shimadzu GC-2014 equipped with a Shimadzu auto sampler AOC-20i, a FID detector and column Nukol.

A. Supporting Figures

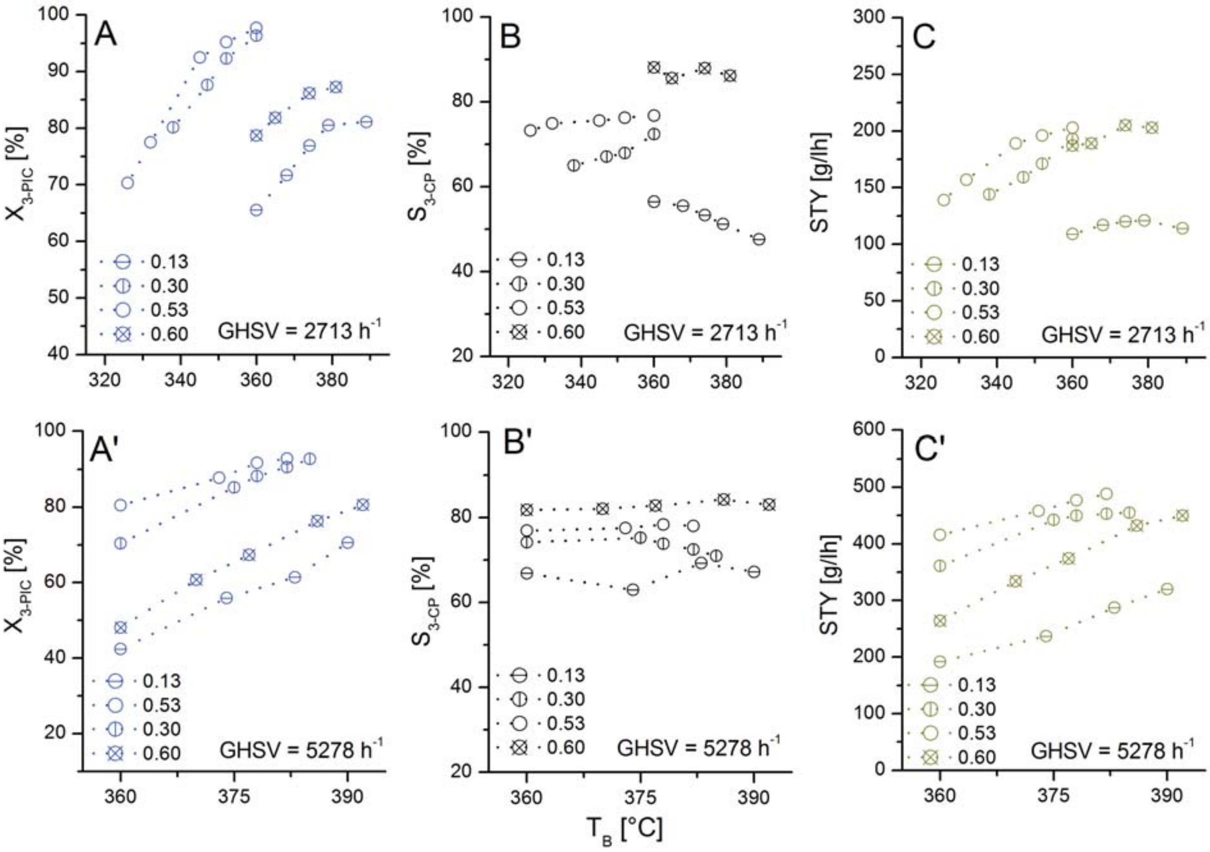

Figure A.1.: Catalytic performance of VZrAlON catalysts with Al/Zr = 1.5 as a function of the bed temperature T_B; GHSV as indicated

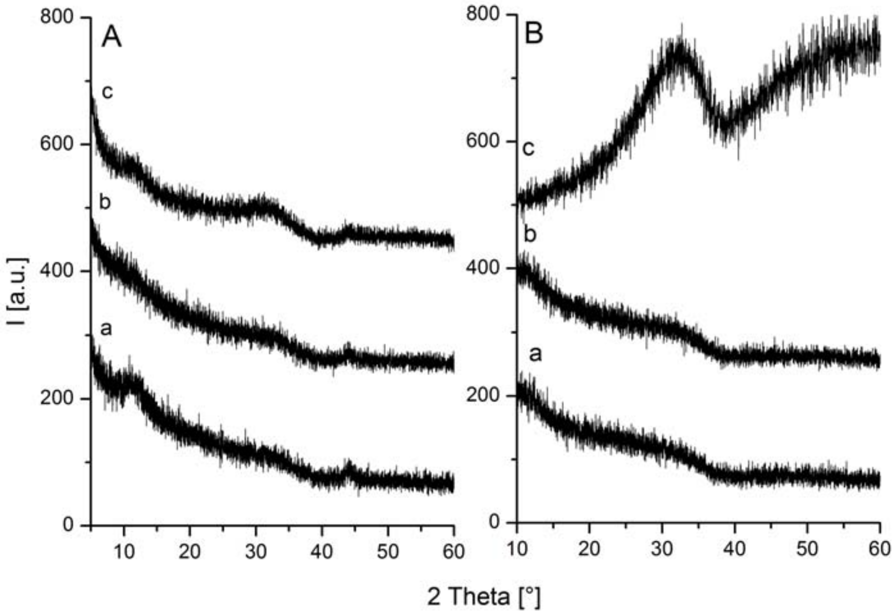

Figure A.2.: Powder XRD pattern of A) fresh VZrAlON and B) used VZrAlON with Al/Zr = 1.5 depending on the V/(Zr+Al)); a = 0.5, b = 0.25, c = 0.12

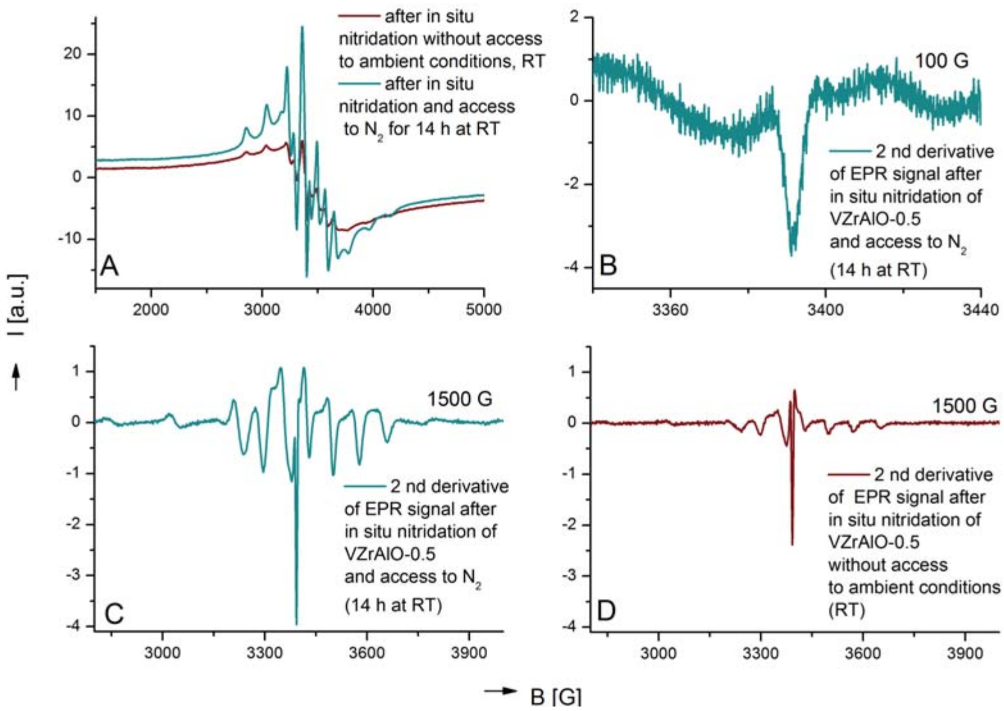

Figure A.3.: In situ EPR signals derived during nitridation of the VZrAlO-0.5 oxide precursor (Al/Zr = 1.5); A) obtained after in situ nitridation at RT, B) - D) 2nd derivatives of EPR signals given in A)

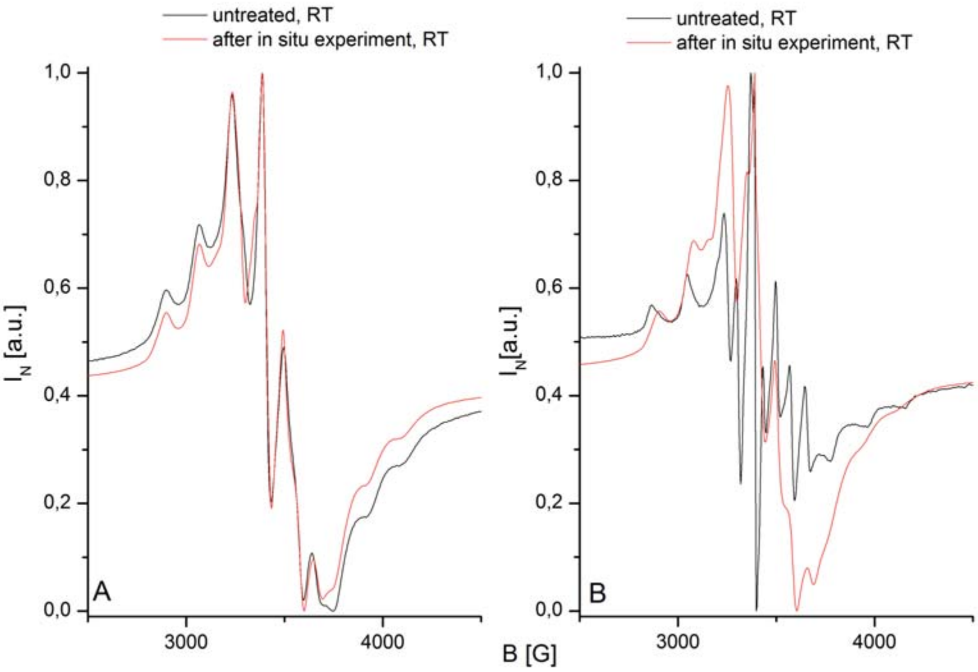

Figure A.4.: Comparison of normalized EPR spectra measured at RT for untreated VZrAlON and after the in situ experiment; A) VZrAlON-0.1, Al/Zr = 1.5; B) VZrAlON-0.5, Al/Zr = 1.5

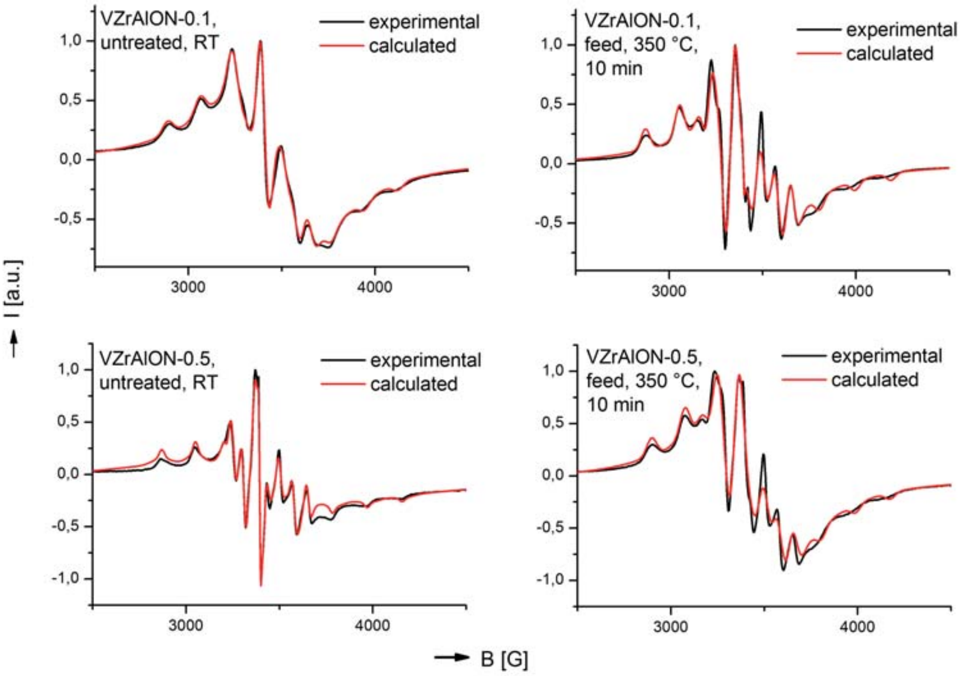

Figure A.5.: Experimental EPR signals compared to calculated EPR signals of VZrAlON catalysts derived by spectra simulation

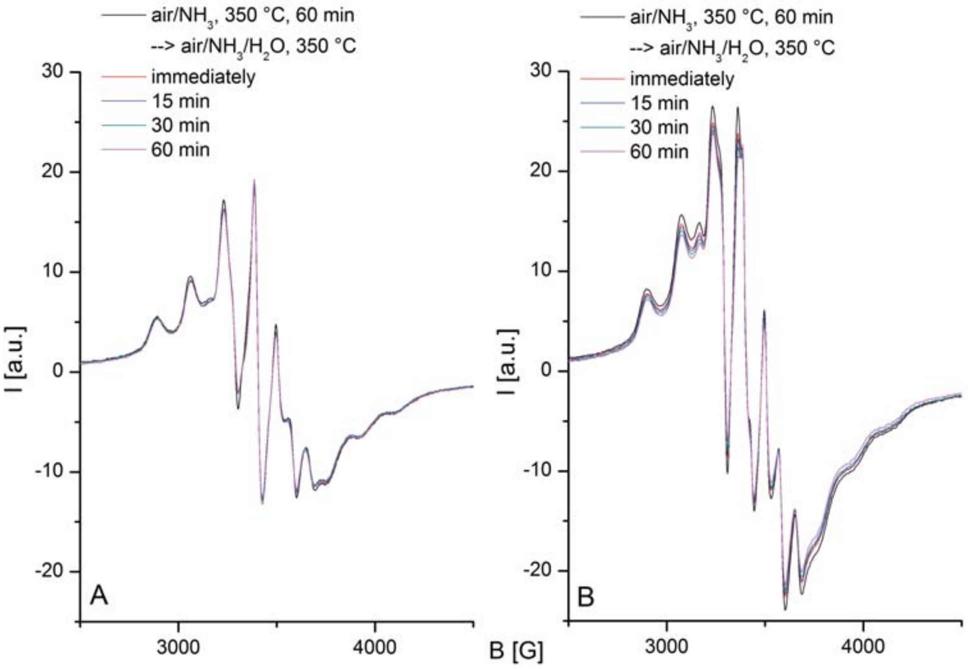

Figure A.6.: In situ EPR signals for VZrAlON under air/NH_3/H_2O at 350 °C with time on stream; A) VZrAlON-0.1, Al/Zr = 1.5 ; B) VZrAlON-0.5, Al/Zr = 1.5

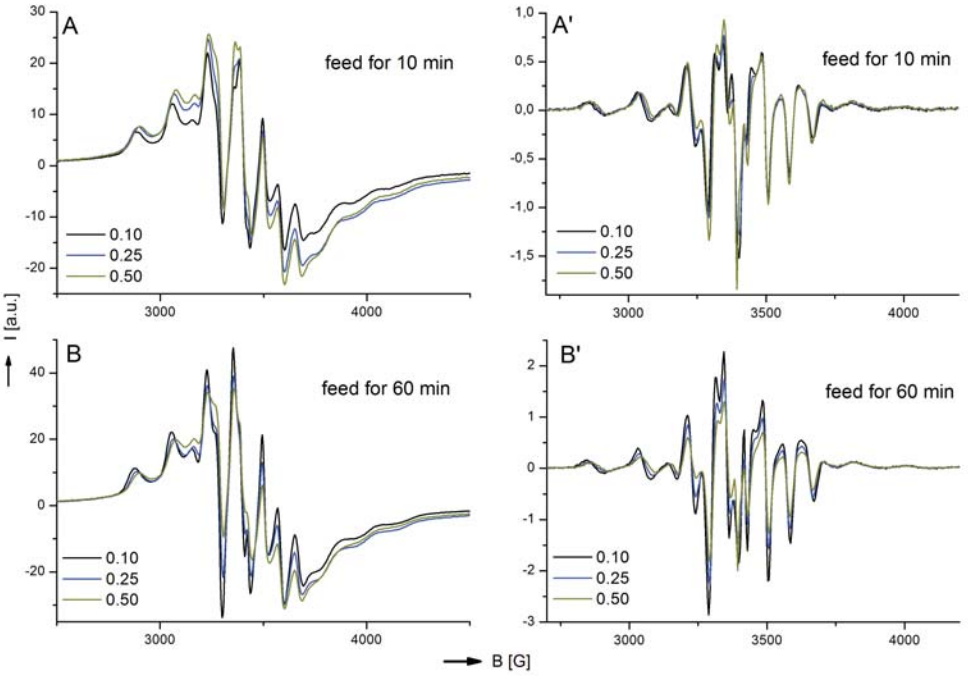

Figure A.7.: In situ EPR signals and their 2nd derivatives (') for VZrAlON under feed conditions (3-PIC, H_2O, air, NH_3) after 10 and 60 min, Al/Zr = 1.5

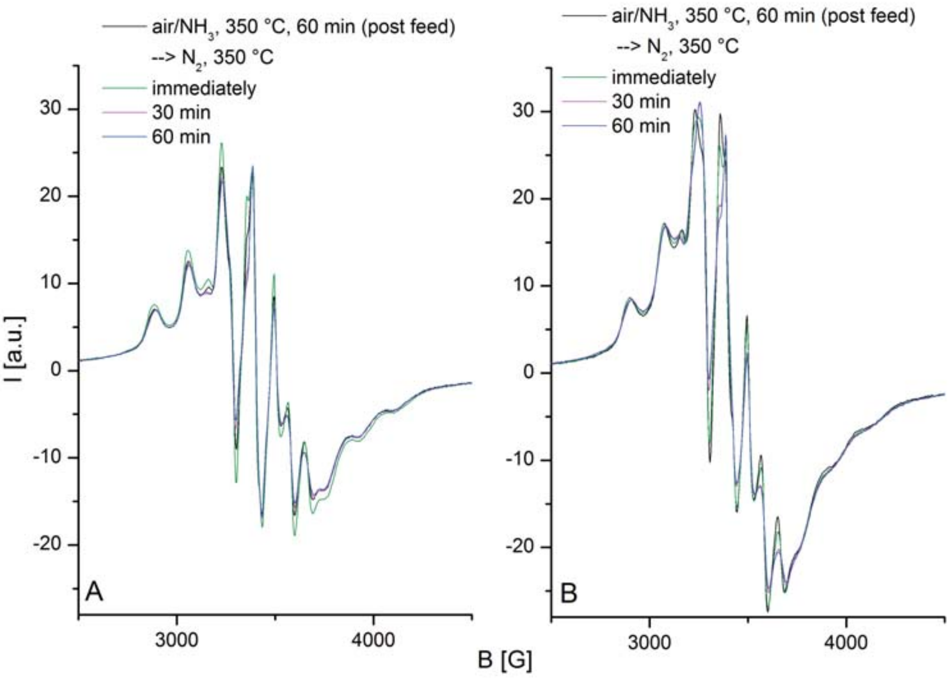

Figure A.8.: In situ EPR signals measured at 350 °C after switching from air/NH_3 to N_2; A) VZrAlON-0.1, Al/Zr = 1.5; B) VZrAlON-0.5, Al/Z r= 1.5

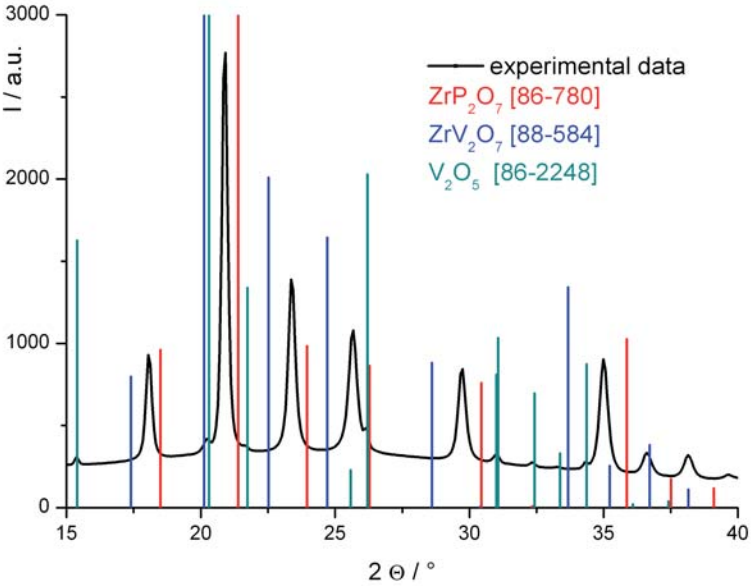

Figure A.9.: Powder pattern for the fresh calcined VZrPO-0.9 oxide measured at μ spot beam line of the Berlin synchrotron facility BESSY placed over by reflections of ZrP_2O_7, ZrV_2O_7 and V_2O_5

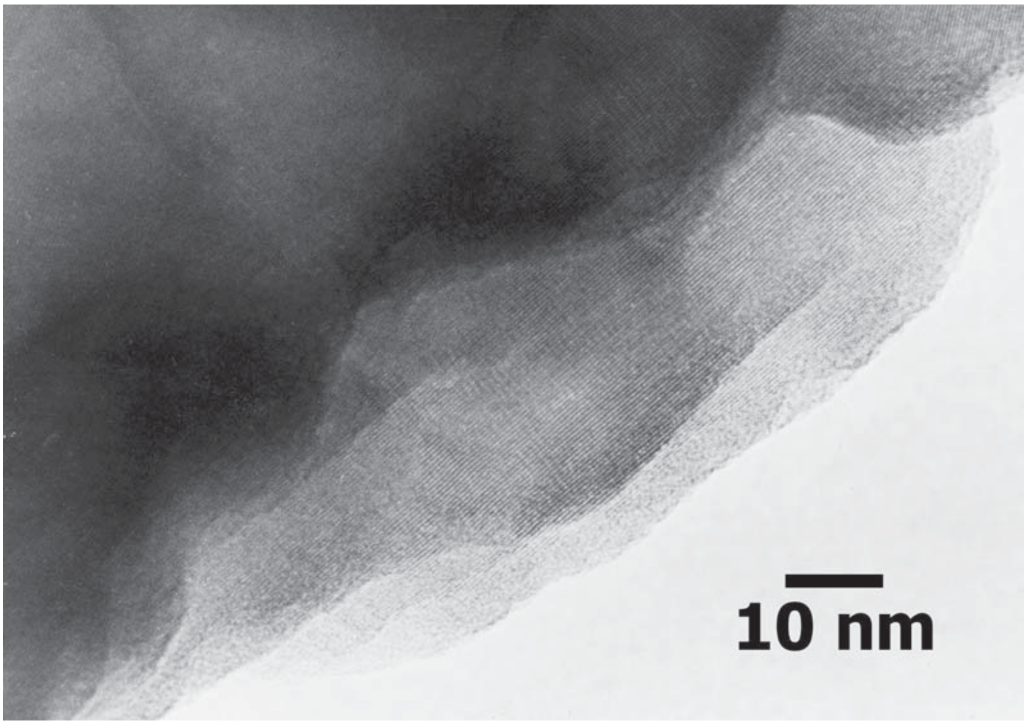

Figure A.10.: TEM image of VZrPO-0.9 sample

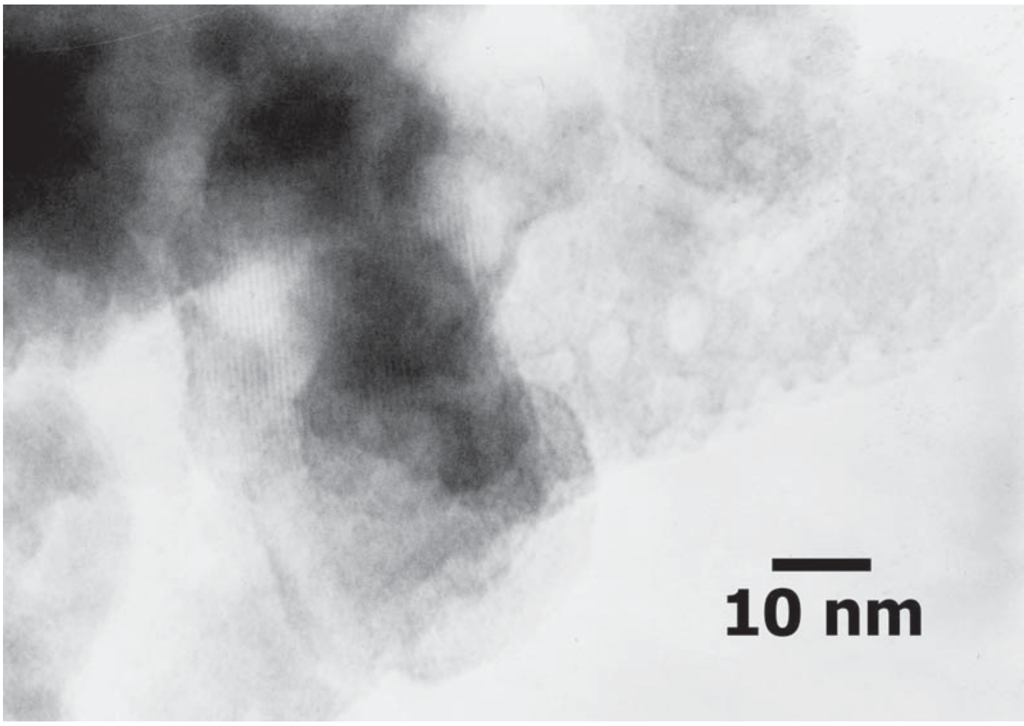

Figure A.11.: TEM image of VZrPO-0.5 sample

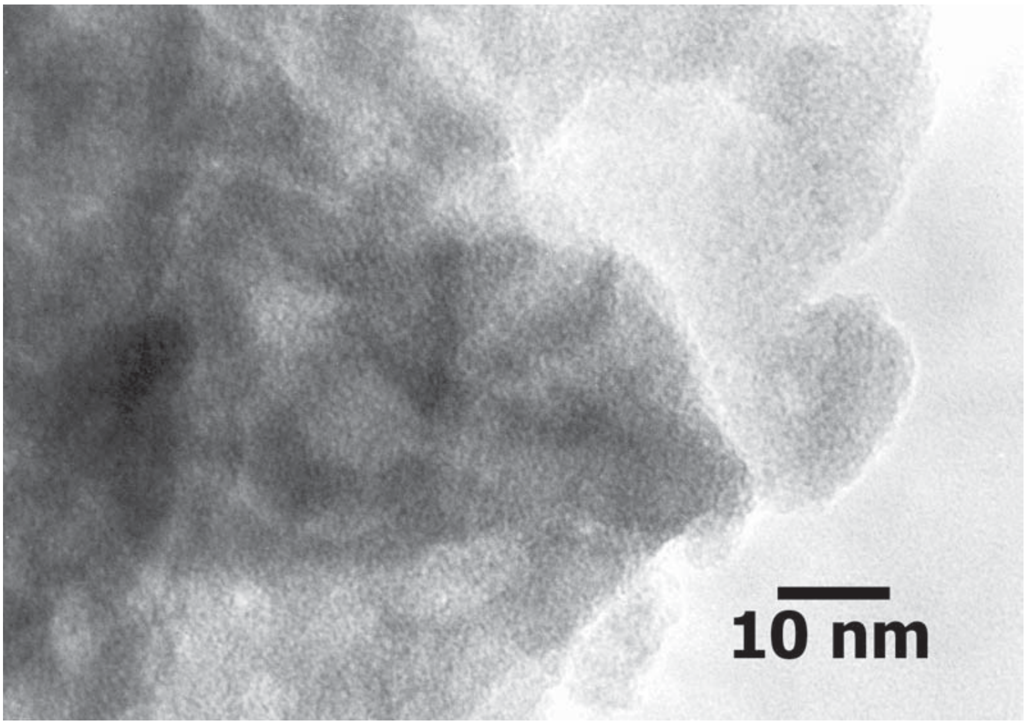

Figure A.12.: TEM image of VZrPO-0.1 sample

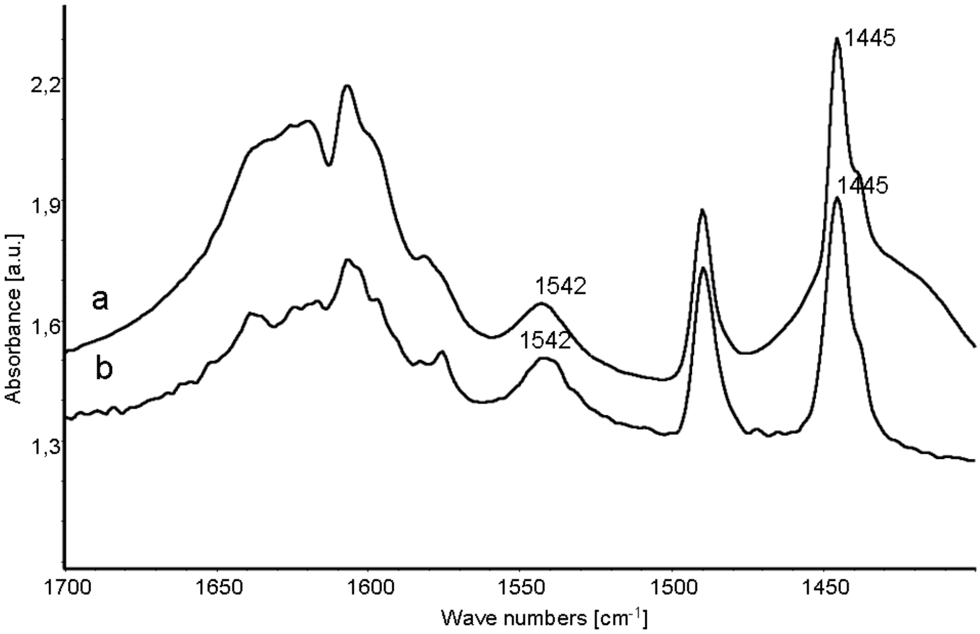

Figure A.13.: FTIR spectra of pyridine adsorbed on VZrPON-0.1 (a) and VZrPO-0.1 (b) at RT

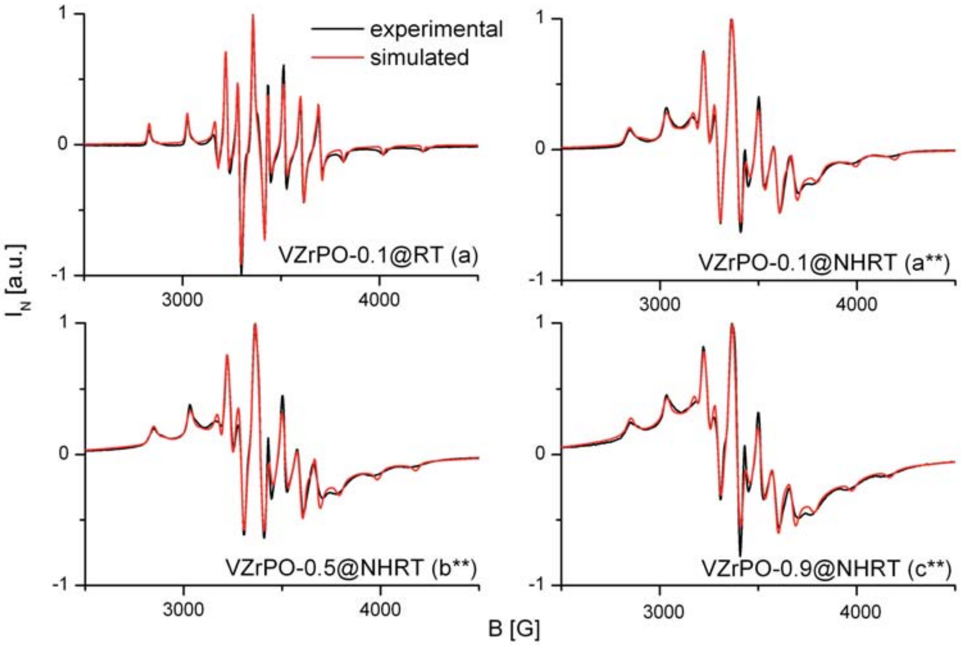

Figure A.14.: Comparison of experimental EPR spectra and calculated EPR spectra (a** - c**: spectra after treatment in NH_3 at RT, a: spectrum for untreated sample VZrPO-0.1)

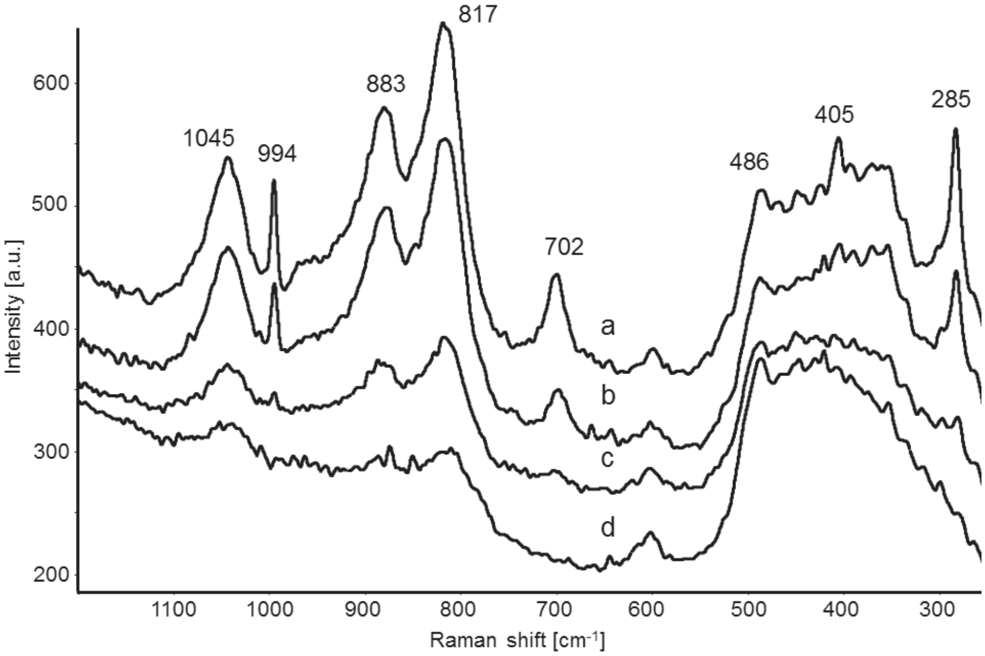

Figure A.15.: In situ Raman spectra of sample VZrPO-0.9 a) Measured at room temperature after heating in N_2 flow for 90 min at 120 °C; b) Recorded after heating in NH_3/N_2 flow for 30 min at 110 °C and c) for 90 min at 160 °C d) and for 30 min 300 °C

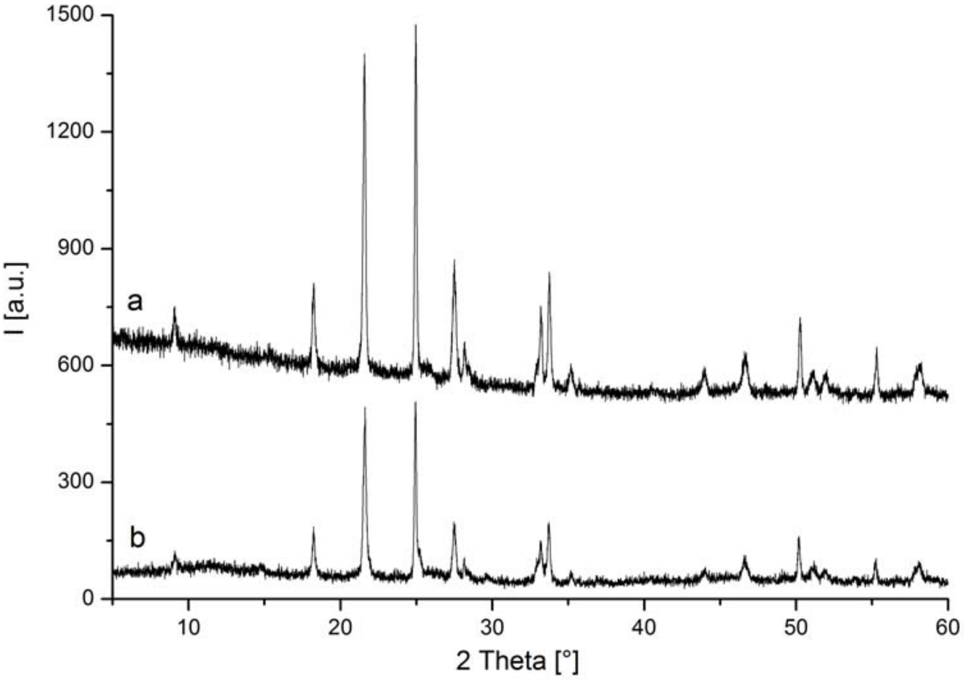

Figure A.16.: Comparison of XRD patterns measured for the fresh (a) and used (b) VMoO-1.5 oxide catalyst

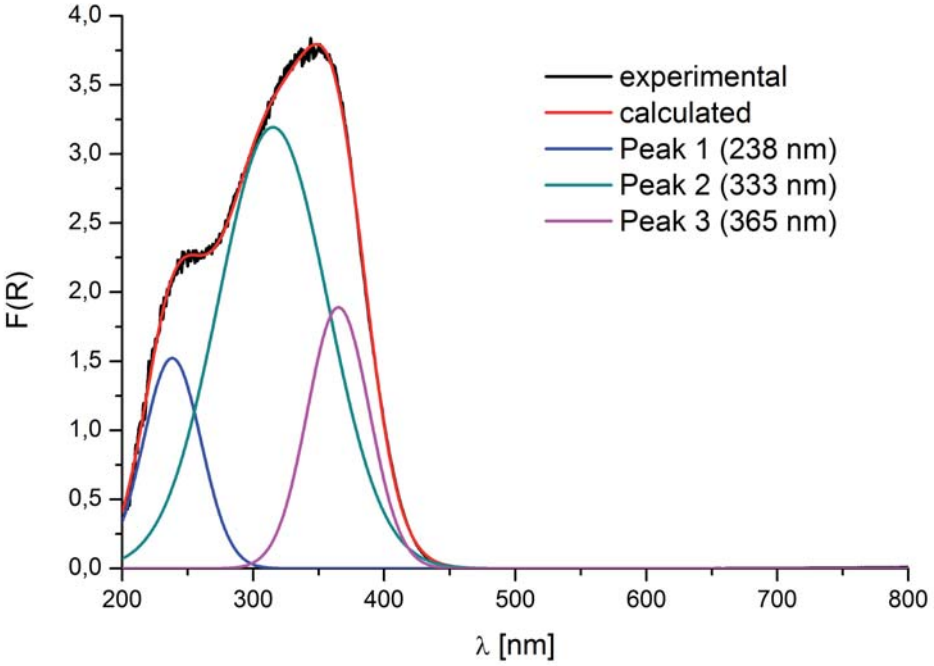

Figure A.17.: Experimental UV/Vis spectrum at RT of MoO_3 (Aldrich) including results of deconvolution

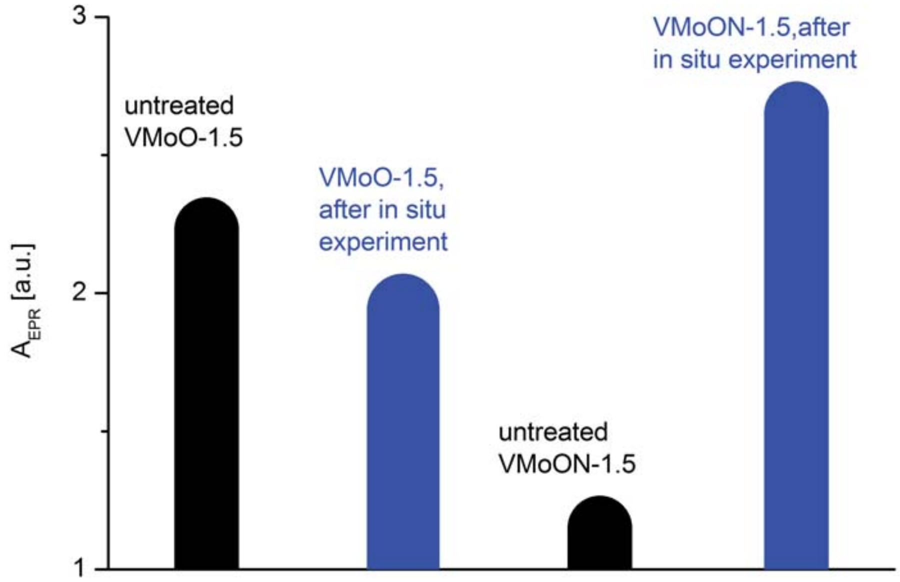

Figure A.18.: Double integral intensity A_{EPR} of EPR signals derived at RT before and after in situ ammoxidation experiment

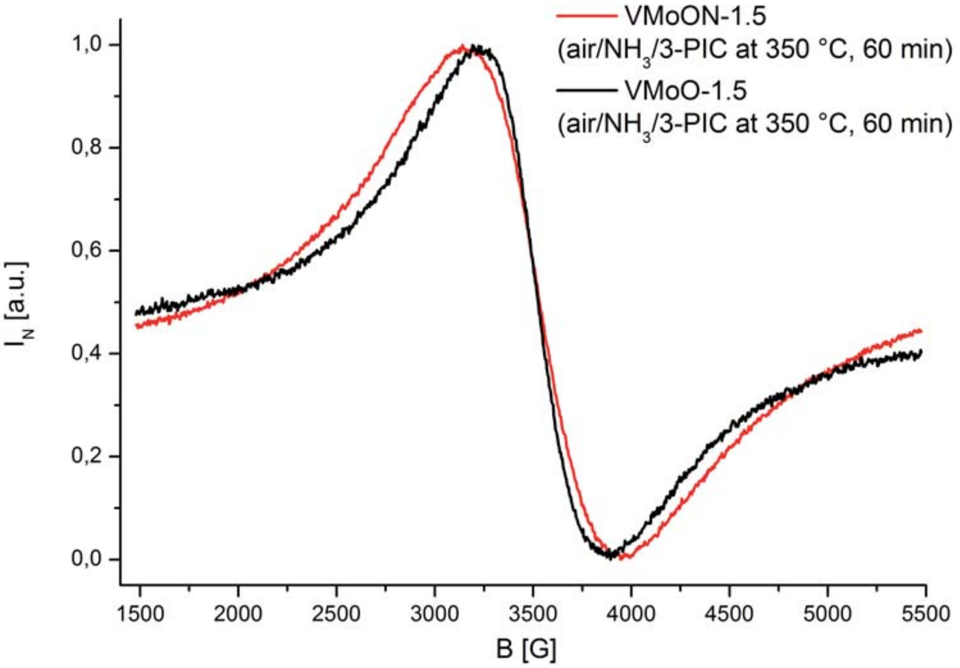

Figure A.19.: Normalized EPR spectra of VMoO-1.5 and VMoON-1.5 derived under feed conditions (air/NH$_3$/3-PIC) at 350 °C after 60 min

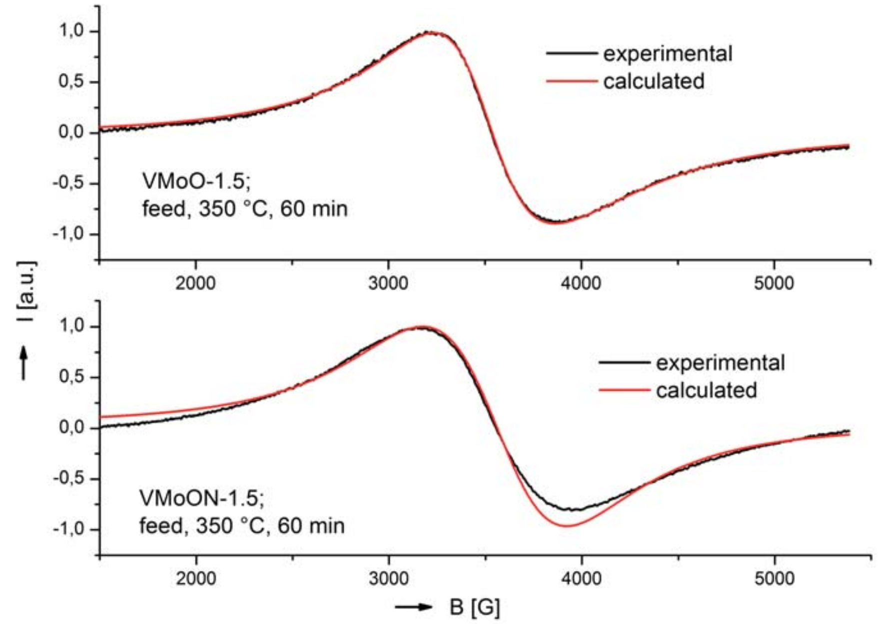

Figure A.20.: Experimental and calculated EPR signals of VMoO-1.5 and VMoON-1.5 derived under feed (air/NH_3/3-PIC) conditions at 350 °C after 60 min

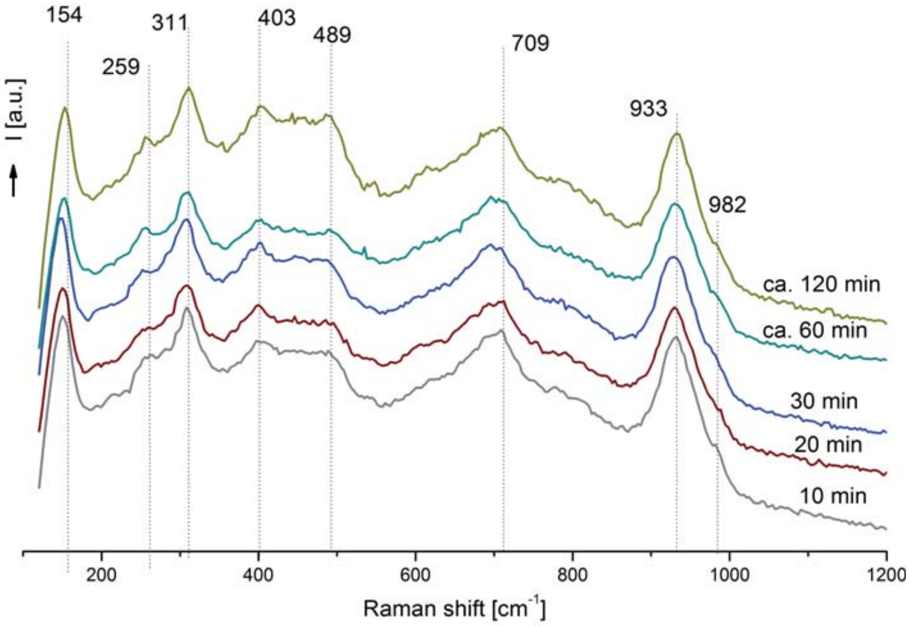

Figure A.21.: In situ Raman spectra taken as a function of time under reaction stream at 360 °C using VMoO-1.5 catalyst

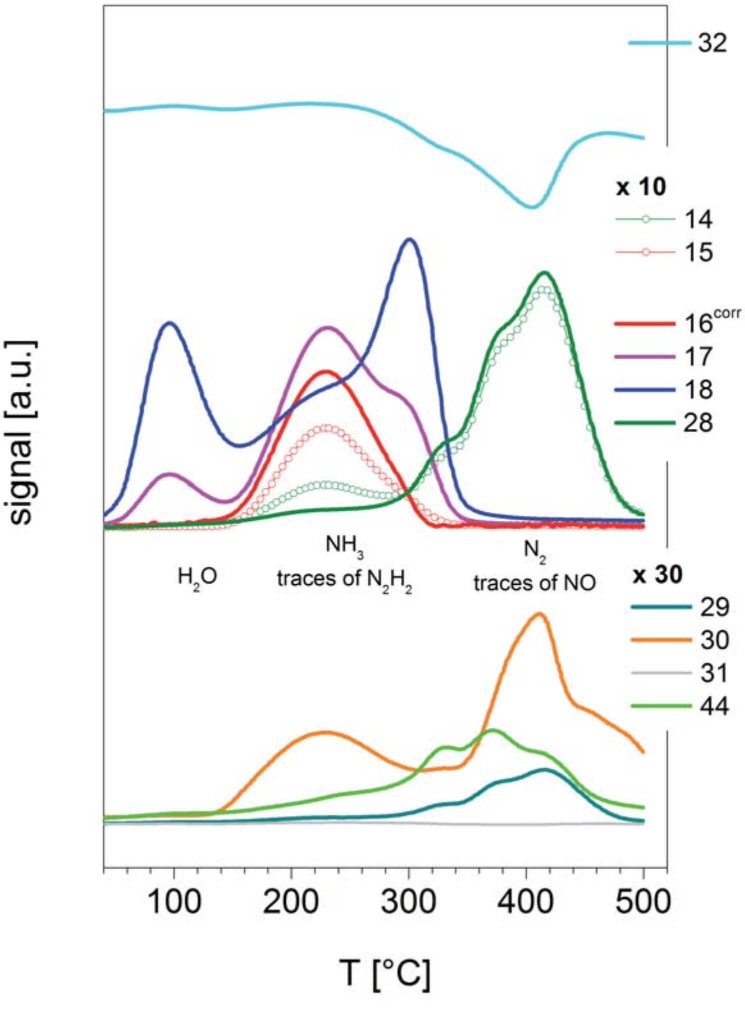

Figure A.22.: Scaled mass traces derived from temperature programmed oxidation (TPO) of fresh VMoON-1.5 catalyst in 5 % O_2/He - followed by MS; different scaling factors as indicated in the legend (x 10 and x 30)

B. Supporting Tables

Table B.1.: Nitrogen containing species in $HPO_2(NH_2)_2$ and their vibration modes at 120 °C according to [97]

wave number [cm^{-1}]	assignment	wave number [cm^{-1}]	assignment
3074	ν_s (P)-NH-(P)	1467	δ NH_4^+
870; 696	ν_{as}; ν_s P-NH-P	830-750	ν_s P=N-
3385; 3269; 1586	ν_{as}; ν_s; δ (P)-NH_2	690	ν_s P-N(P)-P

Table B.2.: Peak positions and peak areas of Gaussian peaks derieved by deconvolution of normalized UV/Vis spectra

VMoO-0.25		VMoO-0.5		VMoO-1.0		VMoO-1.5	
λ [nm]	A_p [a.u.]	λ [nm]	A_p [a.u.]	λ [nm]	A_p [a.u.]	λ [nm]	A_p [a.u.]
260	27.4	254	15.1	251	7.9	240	6.9
305	76.6	296	75.8	278	66.7	275	44.8
395	64.2	392	106.7	379	108.0	378	186.0
568	14.4	564	11.2	560	17.6	561	12.8
736	2.4	737	35.2	737	31.5	737	109.6

Table B.3.: A selection of ammoxidation reactions using heteroaromatics; *: catalyst precursor

substrate	product	catalyst	T [°C]	X [%]	S [%]	Lit.
3-picoline	3-cyanopyridine	20 wt.-% $VOHPO_4 \cdot 0.5\ H_2O$*/TiO_2	360	100	81	[18]
3-picoline	3-cyanopyridine	$V_2O_5/MoO_3/P_2O_5$ (VMPO)	425	98	98	[165]
3-picoline	3-cyanopyridine	VMPO/SiO_2	425	80	91	[165]
3-picoline	3-cyanopyridine	V_2O_5	385	30	60	[38]
3-picoline	3-cyanopyridine	V_6O_{13}	385	98	78	[38]
3-picoline	3-cyanopyridine	V_xO_y/30 mol-%TiO_2 (rutile)	385	100	79	[166]
3-picoline	3-cyanopyridine	V_xO_y/90 mol-%TiO_2 (rutile)	385	40	58	[166]
3-picoline	3-cyanopyridine	V_2O_5/SnO_2 (1:1.5 mole ratio)	385	82	74	[167]
2-picoline	2-cyanopyridine	α-$VOPO_4$*	430	87	65	[20, 168]
4-picoline	4-cyanopyridine	α-$VOPO_4$*	430	98	93	[20, 168]
toluene	benzonitrile	10 % V_2O_5/TiO_2	340	100	80	[47]
toluene	benzonitrile	5 % Mo/Nb_2O_5-TiO_2	400	54	90	[169]
toluene	benzonitrile	α-$(NH_4)_2[(VO)_3(P_2O_7)_2]$	440	21	99	[19]
3-chlorotoluene	3-chlorobenzonitrile	$VOHPO_4 \cdot 0.5\ H_2O$*	430	62	57	[20, 168]
4-chlorotoluene	4-chlorobenzonitrile	$VOHPO_4 \cdot 0.5\ H_2O$*	430	98	95	[20, 168]
2,4-dichlorotoluene	2,4-dichlorobenzonitrile	$VOHPO_4 \cdot 0.5\ H_2O$*	415	85	54	[20, 168]
2,6-dichlorotoluene	2,6-dichlorobenzonitrile	$VOHPO_4 \cdot 0.5\ H_2O$*	415	55	28	[20, 168]
3-methoxytoluene	3-methoxybenzonitrile	$VOHPO_4 \cdot 0.5\ H_2O$*	430	50	21	[20]
4-methoxytoluene	4-methoxybenzonitrile	$VOHPO_4 \cdot 0.5\ H_2O$*	430	98	74	[20]
2,3-dimethoxytoluene	2,3-dimethoxybenzonitrile	$VOHPO_4 \cdot 0.5\ H_2O$*	415	28	> 5	[20]
2,6-dimethoxytoluene	2,6-dimethoxybenzonitrile	$VOHPO_4 \cdot 0.5\ H_2O$*	415	20	> 2	[20]

Table B.4.: Surface and bulk N/V ratios of fresh and used VSb catalysts

catalyst	N^1/V_s	N^2/V_s	N^3/V_s	$(N^1 + N^2)/V_s$	$(N^1 + N^3)/V_s$	$(N^2 + N^3)/V_s$	N^s/V_s
fresh VSbO-0.5	0.0	0.0	0.047	0.0	0.047	0.047	0.047
fresh VSbON-0.5	0.029	0.034	0.075	0.063	0.104	0.109	0.138
fresh VSbON-0.5*	0.011	0.012	0.051	0.022	0.061	0.062	0.073
fresh VSbON-2.0	0.039	0.026	1.093	0.065	0.898	0.205	0.205
used VSbO-0.5	0.114	0.144	0.080	0.258	0.224	0.0	0.338
used VSbON-0.5	0.0	0.090	0.211	0.090	0.221	0.302	0.302
used VSbON-0.5*	0.0	0.155	0.315	0.030	0.155	0.470	0.470
used VSbON-2.0	0.027	0.138	0.200	0.164	1.787	0.347	0.364
catalyst	N^1/Sb_s	N^2/Sb_s	N^3/Sb_s	$(N^1 + N^2)/Sb_s$	$(N^1 + N^3)/Sb_s$	$(N^2 + N^3)/Sb_s$	N^s/Sb_s
fresh VSbO-0.5	0.0	0.0	0.020	0.0	0.020	0.020	0.020
fresh VSbON-0.5	0.015	0.018	0.040	0.033	0.055	0.057	0.073
fresh VSbON-0.5*	0.010	0.011	0.046	0.020	0.056	0.057	0.066
fresh VSbON-2.0	0.283	0.162	1.093	0.401	1.331	1.255	1.493
used VSbO-0.5	0.036	0.046	0.026	0.082	0.062	0.072	0.108
used VSbON-0.5	0.0	0.016	0.038	0.016	0.038	0.055	0.055
used VSbON-0.5*	0.0	0.030	0.061	0.030	0.061	0.091	0.091
used VSbON-2.0	0.006	0.030	0.044	0.036	0.050	0.074	0.080
catalyst	N^1/M_s	N^2/Sb_s	N^3/M_s	$(N^1 + N^2)/M_s$	$(N^1 + N^3)/M_s$	$(N^2 + N^3)/M_s$	N^s/M_s
fresh VSbO-0.5	0.0	0.0	0.014	0.0	0.014	0.014	0.014
fresh VSbON-0.5	0.010	0.012	0.026	0.022	0.036	0.038	0.047
fresh VSbON-0.5*	0.005	0.006	0.024	0.011	0.029	0.030	0.035
fresh VSbON-2.0	0.040	0.027	0.185	0.068	0.029	0.213	0.253
used VSbO-0.5	0.028	0.035	0.019	0.062	0.047	0.054	0.082
used VSbON-0.5	0.0	0.014	0.032	0.014	0.032	0.046	0.046
used VSbON-0.5*	0.0	0.025	0.051	0.025	0.051	0.076	0.076
used VSbON-2.0	0.005	0.025	0.036	0.030	0.041	0.061	0.065

Bibliography

[1] v. Hippel, L., Neher, A., and Arntz, D. *EP 0726092B1* (1996).

[2] Wiame, H., Bois, L., L'Haridon, P., Laurent, Y., and Grange, P. *Journal of the European Ceramic Society* **17**(15-16), 2017–2020 (1997).

[3] Bois, L., L'Haridon, P., Wiame, H., and Grange, P. *Materials Research Bulletin* **33**(1), 9–19 (1998).

[4] Florea, M., Prada-Silvy, R., and Grange, P. *Catalysis Letters* **87**(1), 63–66 (2003).

[5] Florea, M., Silvy, R. P., and Grange, P. *Applied Catalysis A: General* **255**(2), 289–300 (2003).

[6] Florea, M., Silvy, R. P., and Grange, P. *Applied Catalysis A: General* **286**(1), 1–10 (2005).

[7] Janke, C. *Diploma Thesis - Struktur und Wirkung von Vanadium-Oxynitrid-Katalysatoren in der Ammoxidation von 3-Picolin* (2008).

[8] Janke, C., Radnik, J., Bentrup, U., Martin, A., and Brückner, A. *ChemCatChem* **1**(4), 485–491 (2009).

[9] Wohl, A. *Angewandte Chemie* **35**(83), 593 (1922).

[10] Andrussow, L. *Angewandte Chemie* **48**(37), 593–595 (1935).

[11] Martin, A. and Kalevaru, V. N. *ChemCatChem* **2**(12), 1504–1522 (2010).

[12] Grasselli, R. K. and Tenhover, M. A. *Handbook of Heterogeneous Catalysis*, 3489–3517. Wiley-VCH Verlag GmbH and Co. KGaA (2008).

[13] Jackson, S. D. and Hargreaves, J. S. J. *Metal Oxide Catalysis, 1. Edition*, 771–818. Wiley-VCH, Weinheim (2008).

[14] Rizayev, R. G., Mamedov, E. A., Vislovskii, V. P., and Sheinin, V. E. *Applied Catalysis A: General* **83**(2), 103–140 (1992).

[15] Kalevaru, V. N., Raju, B. D., Rao, V. V., and Martin, A. *Catalysis Communications* **9**(5), 715–720 (2008).

[16] Narayana, K. V., David Raju, B., Khaja Masthan, S., Venkat Rao, V., Kanta Rao, P., Subrahmanian, R., and Martin, A. *Catalysis Communications* **5**(8), 457–462 (2004).

[17] Narayana, K. V., Raju, B. D., Masthan, S. K., Rao, V. V., Rao, P. K., and Martin, A. *Journal of Molecular Catalysis A: Chemical* **223**(1-2), 321–328 (2004).

[18] Kalevaru, V. N., Madaan, N., and Martin, A. *Applied Catalysis A: General* **391**(1-2), 52–62 (2011).

[19] Berndt, H., Büker, K., Martin, A., Rabe, S., Zhang, Y., and Meisel, M. *Catalysis Today* **32**(1-4), 285–290 (1996).

[20] Martin, A. and Lücke, B. *Catalysis Today* **32**(1-4), 279–283 (1996).

[21] Martin, A., Hannour, F., Brückner, A., and Lücke, B. *Reaction Kinetics and Catalysis Letters* **63**(2), 245–251 (1998).

[22] Manohar, B. and Reddy, B. M. *Journal of Chemical Technology and Biotechnology* **71**(2), 141–146 (1998).

[23] Barnett, C. and Dewing, J. *US 3818066* (1974).

[24] Barnett, C., Dewing, J., and Jubb, A. H. *US 3624125* (1971).

[25] Barnett, C., Dewing, J., and Jubb, A. H. *US 3627817* (1971).

[26] Spitz, P. H. *Petrochemicals - The Rise of an Industry*. John Wiley and Sons, Inc. (1988).

[27] Idol Jr., J. D. *US 2904580* (1959).

[28] Cavani, F., Ballarini, N., and Cericola, A. *Catalysis Today* **127**(1-4), 113–131 (2007).

[29] Moro-Oka, Y. and Ueda, W. *Partial oxidation and ammoxidation of propane: Catalysts and processes*, volume 11, 223–245. The Royal Society of Chemistry (1994).

[30] Centi, G., Grasselli, R. K., and Trifiro, F. *Catalysis Today* **13**(4), 661–666 (1992).

[31] Grasselli, R. K. *Catalysis Today* **49**(1-3), 141–153 (1999).

[32] Prada Silvy, R., Florea Popescu, M., and Grange, P. *WO 03/053913 A1* (2003).

[33] Weissermel, K. and Arpe, H.-J. *Industrielle Organische Chemie*, 211. Wiley-VCH, Weinheim (1998).

[34] Martin, A., Narayana Kalevaru, V., Lücke, B., and Brückner, A. *Applied Catalysis A: General* **335**(2), 196–203 (2008).

[35] Chuck, R. *Applied Catalysis A: General* **280**(1), 75–82 (2005).

[36] Kertesz, S. G. *Mayo Clinic Proceedings* **76**(3), 315–318 (2001).

[37] Brown, T. M. *Psychosomatics* **51**(2), 93–97 (2010).

[38] Andersson, A. and Lundin, S. T. *Journal of Catalysis* **58**(3), 383–395 (1979).

[39] Brückner, Andreas Martin, N. S. G.-U. W. and Lucke, B. *J. Chem. Soc., Faraday Trans.* **92**, 4257–4263 (1996).

[40] Brückner, A. *Catalysis Reviews: Science and Engineering* **45**(1), 97 – 150 (2003).

[41] Prasad, R. and Kar, A. K. *Industrial & Engineering Chemistry Process Design and Development* **15**(1), 170–175 (1976).

[42] Sanati, M. and Andersson, A. *Industrial & Engineering Chemistry Research* **30**(2), 320–326 (1991).

[43] Zhang, Y., Martin, A., Berndt, H., Lücke, B., and Meisel, M. *Journal of Molecular Catalysis A: Chemical* **118**(2) (1997).

[44] Baiker, A. and Zollinger, P. *Applied Catalysis* **10**(2), 231–249 (1984).

[45] M. Albert, V. *Catalysis Today* **123**(1-4), 18–22 (2007).

[46] Andersson, A. *Journal of Catalysis* **100**(2), 414–428 (1986).

[47] Busca, G., Cavani, F., and Trifirò, F. *Journal of Catalysis* **106**(2), 471–482 (1987).

[48] Martin, A., Brückner, A., Zhang, Y., and Lücke, B. *Ammoxidation of methylaromatics over NH_4^+-containing vanadium phosphate catalysts—New mechanistic insights*, volume 108, 377–384. Elsevier (1997).

[49] Olea, M., Florea, M., Sack, I., Prada Silvy, R., Gaigneaux, E. M., Marin, G. B., and Grange, P. *Journal of Catalysis* **232**(1), 152–160 (2005).

[50] Bentrup, U., Brückner, A., Martin, A., and Lücke, B. *Journal of Molecular Catalysis A: Chemical* **162**(1-2), 391–399 (2000).

[51] Lietti, L., Forzatti, P., Ramis, G., Busca, G., and Bregani, F. *Applied Catalysis B: Environmental* **3**(1), 13–35 (1993).

[52] Toda, Y., Ohno, T., Hatayama, F., and Miyata, H. *Applied Catalysis A: General* **207**(1-2), 273–280 (2001).

[53] Scheurell, K., Scholz, G., and Kemnitz, E. *Journal of Solid State Chemistry* **180**(2), 749–758 (2007).

[54] Wiame, H., Cellier, C., and Grange, P. *Journal of Catalysis* **190**(2), 406–418 (2000).

[55] Fripiat, N., Parvulescu, V., Parvulescu, V. I., and Grange, P. *Applied Catalysis A: General* **181**(2), 331–346 (1999).

[56] Wu, G., Jiang, S., Li, L., and Guan, N. *Applied Catalysis A: General* **391**(1-2), 225–233 (2011).

[57] Lerch, M., Janek, J., Becker, K. D., Berendts, S., Boysen, H., Bredow, T., Dronskowski, R., Ebbinghaus, S. G., Kilo, M., Lumey, M. W., Martin, M., Reimann, C., Schweda, E., Valov, I., and Wiemhöfer, H. D. *Progress in Solid State Chemistry* **37**(2-3), 81–131 (2009).

[58] Glasson, D. R. and Jayaweera, S. A. A. *Journal of Applied Chemistry* **18**(3), 65–77 (1968).

[59] Lévy, F., Hones, P., Schmid, P. E., Sanjinés, R., Diserens, M., and Wiemer, C. *Surface and Coatings Technology* **120-121**, 284–290 (1999).

[60] Oyama, S. *Catalysis Today* **15**(2), 179–200 (1992).

[61] Krawiec, P. and Kaskel, S. *Topics in Catalysis* **52**(11), 1549–1558 (2009).

[62] Yu, C. C., Ramanathan, S., and Oyama, S. T. *Journal of Catalysis* **173**(1), 1–9 (1998).

[63] Chen, L., Gu, Y., Shi, L., Yang, Z., Ma, J., and Qian, Y. *Inorganic Chemistry Communications* **7**(5), 643–645 (2004).

[64] Kroke, E. and Schwarz, M. *Coordination Chemistry Reviews* **248**(5-6), 493–532 (2004).

[65] Kojima, R. and Aika, K.-i. *Applied Catalysis A: General* **215**(1-2), 149–160 (2001).

[66] Jacobsen, C. J. H. *Chemical Communications* (12), 1057–1058 (2000).

[67] Anderson, R. B., Shultz, J. F., Seligman, B., Hall, W. K., and Storch, H. H. *Journal of the American Chemical Society* **72**(8), 3502–3508 (1950).

[68] Yuhong, W., Wei, L., Minghui, Z., Naijia, G., and Keyi, T. *Applied Catalysis A: General* **215**(1-2), 39–45 (2001).

[69] Yu, C. C., Ramanathan, S., Sherif, F., and Oyama, S. T. *The Journal of Physical Chemistry* **98**(49), 13038–13041 (1994).

[70] Ramanathan, S., Yu, C. C., and Oyama, S. T. *Journal of Catalysis* **173**(1), 10–16 (1998).

[71] Rodrigues, J. A. J., Cruz, G. M., Bugli, G., Boudart, M., and Djéga-Mariadassou, G. *Catalysis Letters* **45**(1), 1–3 (1997).

[72] Fuertes, A. *Dalton Transactions* **39**(26), 5942–5948 (2010).

[73] Zhu, J. and Zäch, M. *Current Opinion in Colloid & Interface Science* **14**(4), 260–269 (2009).

[74] Fripiat, N., Conanec, R., Marchand, R., Laurent, Y., and Grange, P. *Journal of the European Ceramic Society* **17**(15-16), 2011–2015 (1997).

[75] Volpe, L. and Boudart, M. *The Journal of Physical Chemistry* **90**(20), 4874–4877 (1986).

[76] Volpe, L. and Boudart, M. *Journal of Solid State Chemistry* **59**(3), 332–347 (1985).

[77] McGee, R. C. V., Bej, S. K., and Thompson, L. T. *Applied Catalysis A: General* **284**(1-2), 139–146 (2005).

[78] Andersson, A., Andersson, S. L. T., Centi, G., Grasselli, R. K., Sanati, M., and Trifirò, F. *Applied Catalysis A: General* **113**(1), 43–57 (1994).

[79] Mendialdua, J., Casanova, R., and Barbaux, Y. *Journal of Electron Spectroscopy and Related Phenomena* **71**(3), 249–261 (1995).

[80] Chenakin, S. P., Prada Silvy, R., and Kruse, N. *The Journal of Physical Chemistry B* **109**(30), 14611–14618 (2005).

[81] Crist, B. V. *Handbook of Monochromatic XPS Spectra - Commercially Pure Binary Oxides (Demo Version)*, 43–49. XPS International, LLC (2005).

[82] Crist, B. V. *Handbook of Monochromatic XPS Spectra - The Elements and Native Oxides (Demo Version)*, xx–xx. XPS International, LLC (1999).

[83] Liu, H., Bertolet, D. C., and Rogers Jr, J. W. *Surface Science* **340**(1-2), 88–100 (1995).

[84] Rosenberger, L., Baird, R., McCullen, E., Auner, G., and Shreve, G. *Surface and Interface Analysis* **40**(9), 1254–1261 (2008).

[85] Crist, B. V. *Handbook of Monochromatic XPS Spectra - Commercially Pure Binary Oxides (Demo Version)*, 829–837. XPS International, LLC (2005).

[86] Valov, I. *Nitrogen doped zirconia (N-YSZ): preparation, characterization and electrode processes*. PhD thesis, (2006).

[87] Prieto, P., Galán, L., and Sanz, J. M. *Surface and Interface Analysis* **21**(6-7), 395–399 (1994).

[88] Milošev, I., Strehblow, H. H., Gaberšcek, M., and Navinšek, B. *Surface and Interface Analysis* **24**(7), 448–458 (1996).

[89] Zhang, Y. *Journal of Materials Science Letters* **21**(20), 1603–1605 (2002).

[90] Hendrickson, D. N., Hollander, J. M., and Jolly, W. L. *Inorganic Chemistry* **8**(12), 2642–2647 (1969).

[91] Wiame, H., Bois, L., Lharidon, P., Laurent, Y., and Grange, P. *Solid State Ionics* **101-103**(Part 2), 755–759 (1997).

[92] Wiame, H., Centeno, M.-A., Picard, S., Bastians, P., and Grange, P. *Journal of the European Ceramic Society* **18**(9), 1293–1299 (1998).

[93] Le Gendre, L., Marchand, R., and Laurent, Y. *Journal of the European Ceramic Society* **17**(15-16), 1813–1818 (1997).

[94] Bielanski, A. and Haber, J. *Oxygen in Catalysis*. Marcel Dekker Inc. (1991).

[95] Davydov, A. *Molecular Spectroscopy of Oxide Catalyst Surfaces*, 78–81. John Wiley and Sons (2003).

[96] Burcham, L., Deo, G., Gao, X., and Wachs, I. *Topics in Catalysis* **11-12**(1), 85–100 (2000).

[97] Parent, Y., Montagne, L., and Palavit, G. *Journal of Materials Science* **31**(13), 3583–3587 (1996).

[98] Busca, G. *Phys. Chem. Chem. Phys.* **1**, 723–736 (1999).

[99] Griffith, J. S. *The Theory of Transition Metal Ions*. Cambridge University Press (1961).

[100] Occhiuzzi, M., Tuti, S., Cordischi, D., Dragone, R., and Indovina, V. *Journal of the Chemical Society, Faraday Transactions* **92**(21), 4337–4345 (1996).

[101] Adamski, A., Zapala, P., Jakubus, P., and Sojka, Z. *Journal of Alloys and Compounds* **442**(1-2), 302–305 (2007).

[102] Adamski, A., Spalek, T., and Sojka, Z. *Research on Chemical Intermediates* **29**(7), 793–804 (2003).

[103] Adamski, A., Sojka, Z., Dyrek, K., and Che, M. *Solid State Ionics* **117**(1-2), 113–122 (1999).

[104] Sharma, V. K., Wokaun, A., and Baiker, A. *The Journal of Physical Chemistry* **90**(12), 2715–2718 (1986).

[105] Concepción, P., Knözinger, H., López Nieto, J. M., and Martínez-Arias, A. *The Journal of Physical Chemistry B* **106**(10), 2574–2582 (2002).

[106] Chary, K. V. R., Kumar, C. P., Naresh, D., Bhaskar, T., and Sakata, Y. *Journal of Molecular Catalysis A: Chemical* **243**(2), 149–157 (2006).

[107] Dhachapally, N., Kalevaru, V. N., Radnik, J., and Martin, A. *Chemical Communications* **47**(29), 8394–8396 (2011).

[108] Fripiat, N., Conanec, R., Auroux, A., Laurent, Y., and Grange, P. *Journal of Catalysis* **167**(2), 543–549 (1997).

[109] Morgan, W. E., Van Wazer, J. R., , and Stec, W. J. *Journal of the American Chermical Society* **95**(3), 751–755 (1973).

[110] Fripiat, N., Centeno, M.-A., and Grange, P. *Chemistry of Materials* **11**(6), 1434–1445 (1999).

[111] Evans, J. S. O., Hanson, J. C., and Sleight, A. W. *Acta Crystallographica Section B* **54**(6), 705–713 (1998).

[112] Dusold, S., Kummerlen, J., and Sebald, A. *The Journal of Physical Chemistry A* **101**(33), 5895–5900 (1997).

[113] King, I. J., Fayon, F., Massiot, D., Harris, R. K., and Evans, J. S. O. *Chemical Communications* (18), 1766–1767 (2001).

[114] Khosrovani, N., Sleight, A. W., and Vogt, T. *Journal of Solid State Chemistry* **132**(2), 355–360 (1997).

[115] Khosrovani, N., Korthuis, V., Sleight, A. W., and Vogt, T. *Inorganic Chemistry* **35**(2), 485–489 (1996).

[116] Hudalla, C., Eckert, H., and Dupree, R. *The Journal of Physical Chemistry* **100**(39), 15986–15991 (1996).

[117] Shubin, A. A., Lapina, O. B., Bosch, E., Spengler, J., and Knözinger, H. *The Journal of Physical Chemistry B* **103**(16), 3138–3144 (1999).

[118] Nakamoto, K. *Infrared and Raman Spectra of Inorganic and Coordination Compounds, Part A*. John Wiley & Sons, Inc. (1997).

[119] Baran, E. J. *Journal of Molecular Structure* **48**(3), 441–443 (1978).

[120] Nakamoto, K. *Infrared and Raman Spectra of Inorganic and Coordination Compounds, Part A*, 236–237. John Wiley & Sons, Inc. (1997).

[121] Bues, W., Bühler, K., and Kuhnle, P. *Zeitschrift für anorganische und allgemeine Chemie* **325**, 8–14 (1963).

[122] Brown, R. G. and Ross, S. D. *Spectrochimica Acta Part A: Molecular Spectroscopy* **28**(7), 1263–1274 (1972).

[123] Siebert, H. *Anwendung der Schwingungsspektroskopie in der Anorganischen Chemie*. Springer-Verlag, Berlin (1966).

[124] Ballutaud, D., Bordes, E., and Courtine, P. *Materials Research Bulletin* **17**(4), 519–526 (1982).

[125] R'Kha, C., Vandenborre, M. T., Livage, J., Prost, R., and Huard, E. *Journal of Solid State Chemistry* **63**(2), 202–215 (1986).

[126] Klokishner, S., Melsheimer, J., Ahmad, R., Jentoft, F. C., Mestl, G., and Schlögl, R. *Spectrochimica Acta Part A: Molecular and Biomolecular Spectroscopy* **58**(1), 1–15 (2002).

[127] Kumar Rana, R. and Viswanathan, B. *Catalysis Letters* **52**(1), 25–29 (1998).

[128] Ballhausen, C. J. and Gray, H. B. *Inorganic Chemistry* **1**(1), 111–122 (1962).

[129] Gao, X. and Wachs, I. E. *The Journal of Physical Chemistry B* **104**(6), 1261–1268 (2000).

[130] Catana, G., Rao, R. R., Weckhuysen, B. M., Van Der Voort, P., Vansant, E., and Schoonheydt, R. A. *The Journal of Physical Chemistry B* **102**(41), 8005–8012 (1998).

[131] Blasco, T. and Nieto, J. M. L. *Applied Catalysis A: General* **157**(1-2), 117–142 (1997).

[132] Rybarczyk, P., Berndt, H., Radnik, J., Pohl, M. M., Buyevskaya, O., Baerns, M., and Brückner, A. *Journal of Catalysis* **202**(1), 45–58 (2001).

[133] McKay, D., Hargreaves, J. S. J., Rico, J. L., Rivera, J. L., and Sun, X. L. *Journal of Solid State Chemistry* **181**(2), 325–333 (2008).

[134] Ganin, A. Y., Kienle, L., and Vajenine, G. V. *Journal of Solid State Chemistry* **179**(8), 2339–2348 (2006).

[135] Thielemann, J. P., Ressler, T., Walter, A., Tzolova-Müller, G., and Hess, C. *Applied Catalysis A: General* **399**(1-2), 28–34 (2011).

[136] Dieterle, M., Weinberg, G., and Mestl, G. *Physical Chemistry Chemical Physics* **4**(5), 812–821 (2002).

[137] Tian, H., Ross, E. I., and Wachs, I. E. *The Journal of Physical Chemistry B* **110**(19), 9593–9600 (2006).

[138] Mestl, G., Verbruggen, N. F. D., and Knoezinger, H. *Langmuir* **11**(8), 3035–3041 (1995).

[139] Sperlich, G., Zimmermann, P. H., and Keller, G. *Zeitschrift für Physik A Hadrons and Nuclei* **270**(3), 267–275 (1974).

[140] Chary, K. V. R., Bhaskar, T., Kishan, G., and Reddy, K. R. *The Journal of Physical Chemistry B* **105**(19) (2001).

[141] Cordischi, D., Indovina, V., and Occhiuzzi, M. *Applied Surface Science* **55**(4), 233–237 (1992).

[142] Labanowska, M. *Physical Chemistry Chemical Physics* **1**(23), 5385–5392 (1999).

[143] Plyasova, L. M., Solov'eva, L. P., Tsybulya, S. V., Kryukova, G. N., Zabolotnyi, V. A., and Olen'kova, I. P. *Journal of Structural Chemistry* **32**(1), 89–93 (1991).

[144] Slade, R. C. T., Ramanan, A., West, B. C., and Prince, E. *Journal of Solid State Chemistry* **82**(1), 65–69 (1989).

[145] Slade, R. C. T., Ramanan, A., Nicol, J. M., and Ritter, C. *Materials Research Bulletin* **23**(5), 647–651 (1988).

[146] Eick, H. A. and Kihlborg, L. *Acta Chemica Scandinavica* **20**, 1658–1666 (1966).

[147] Lucarelli, C., Moggi, P., Cavani, F., and Devillers, M. *Sol-Gel synthesis and characterization of Nb-Mo and Nb-Mo-V mixed oxides as potential catalysts for the selective oxidation of propane*, volume 162, 841–848. Elsevier (2006).

[148] Zazhigalov, V., Khalameida, S., Litvin, N., Bacherikova, I., Stoch, J., and Depero, L. *Kinetics and Catalysis* **49**(5), 692–701 (2008).

[149] Pouchan, C., Dargelos, A., and Chaillet, M. *Journal of Molecular Spectroscopy* **76**(1-3), 118–130 (1979).

[150] Breda, S., Reva, I. D., Lapinski, L., Nowak, M. J., and Fausto, R. *Journal of Molecular Structure* **786**(2-3), 193–206 (2006).

[151] Harris, W. C., Yang, D. B., and Wilcox, P. M. *Spectrochimica Acta Part A: Molecular Spectroscopy* **31**(12), 1981–1991 (1975).

[152] Bañares, M. A. and Khatib, S. J. *Catalysis Today* **96**(4), 251–257 (2004).

[153] Guerrero-Pérez, M. O., Al-Saeedi, J. N., Guliants, V. V., and Bañares, M. A. *Applied Catalysis A: General* **260**(1), 93–99 (2004).

[154] Dieterle, M., Mestl, G., Jäger, J., Uchida, Y., Hibst, H., and Schlögl, R. *Journal of Molecular Catalysis A: Chemical* **174**(1-2), 169–185 (2001).

[155] Mestl, G., Linsmeier, C., Gottschall, R., Dieterle, M., Find, J., Herein, D., Jäger, J., Uchida, Y., and Schlögl, R. *Journal of Molecular Catalysis A: Chemical* **162**(1-2), 463–492 (2000).

[156] Delobel, R., Baussart, H., Leroy, J.-M., Grimblot, J., and Gengembre, L. *Journal of the Chemical Society, Faraday Transactions 1: Physical Chemistry in Condensed Phases* **79**(4), 879–891 (1983).

[157] Xu, W., Wang, H., Liu, R., Zhao, X., and Qu, J. *Journal of Colloid and Interface Science* **363**(1), 320–326 (2011).

[158] Brunauer, S., Emmett, P. H., and Teller, E. *Journal of the American Chemical Society* **60**(2), 309–319 (1938).

[159] Do, D. D., Do, H. D., and Nicholson, D. *Chemical Engineering Science* **65**(10), 3331–3340 (2010).

[160] Weckhuysen, B. M. and Schoonheydt, R. A. *Catalysis Today* **49**(4), 441–451 (1999).

[161] Paris, O., Li, C., Siegel, S., Weseloh, G., Emmerling, F., Riesemeier, H., Erko, A., and Fratzl, P. *Journal of Applied Crystallography (special session)* **40**, 466–470 (2007).

[162] Hammersley, A. P., Svensson, S. O., Hanfland, M., Fitch, A. N., and Hausermann, D. *High Pressure Research* **14**(4), 235–248 (1996).

[163] Lozos, G. P., Hofman, B. M., and Franz, C. G. *Quantum Chemistry Program Exchange* , 265 (1973).

[164] Brückner, A. *Chemical Communications* **13**, 1761–1763 (2005).

[165] Roy, S. K., Dutta, P., Nandi, L. N., Yadav, S. N., Mondal, T. K., Ray, S. C., Mitra, S., and Samuel, P. *Journal of Molecular Catalysis A: Chemical* **223**(1-2), 211–215 (2004).

[166] Andersson, A. and Lundin, S. T. *Journal of Catalysis* **65**(1), 9–15 (1980).

[167] Andersson, A. *Journal of Catalysis* **69**(2), 465–474 (1981).

[168] Martin, A. and Lücke, B. *Catalysis Today* **57**(1-2), 61–70 (2000).

[169] Chary, K. V. R., Reddy, K. R., Kumar, C. P., Naresh, D., Rao, V. V., and Mestl, G. *Journal of Molecular Catalysis A: Chemical* **223**(1-2), 363–369 (2004).